

MICROSCOPIC STUDIES OF THE FATE OF CHARGES IN
ORGANIC SEMICONDUCTORS: SCANNING KELVIN PROBE
MEASUREMENTS OF CHARGE TRAPPING, TRANSPORT,
AND ELECTRIC FIELDS IN P- AND N-TYPE DEVICES

A Dissertation

Presented to the Faculty of the Graduate School

of Cornell University

in Partial Fulfillment of the Requirements for the Degree of

Doctor of Philosophy

by

Louisa Marion Smieska

August 2015

© 2015 Louisa Marion Smieska

ALL RIGHTS RESERVED

MICROSCOPIC STUDIES OF THE FATE OF CHARGES IN ORGANIC
SEMICONDUCTORS: SCANNING KELVIN PROBE MEASUREMENTS OF CHARGE
TRAPPING, TRANSPORT, AND ELECTRIC FIELDS IN P- AND N-TYPE DEVICES

Louisa Marion Smieska, Ph.D.

Cornell University 2015

Organic semiconductors could have wide-ranging applications in lightweight, efficient electronic circuits. However, several fundamental questions regarding organic electronic device behavior have not yet been fully addressed, including the nature of chemical charge traps, and robust models for injection and transport. Many studies focus on engineering devices through bulk transport measurements, but it is not always possible to infer the microscopic behavior leading to the observed measurements. In this thesis, we present scanning-probe microscope studies of organic semiconductor devices in an effort to connect local properties with local device behavior.

First, we study the chemistry of charge trapping in pentacene transistors. Working devices are doped with known pentacene impurities and the extent of charge trap formation is mapped across the transistor channel. Trap-clearing spectroscopy is employed to measure an excitation of the pentacene charge trap species, enabling identification of the degradation-related chemical trap in pentacene.

Second, we examine transport and trapping in perylene diimide (PDI) transistors. Local mobilities are extracted from surface potential profiles across a transistor channel, and charge injection kinetics are found to be highly sensitive to electrode cleanliness. Trap-clearing spectra generally resemble PDI absorption spectra, but one derivative yields evidence indicating variation in trap-clearing mechanisms for different surface chemistries. Trap formation rates are measured and found to be independent of surface chemistry, contradicting a proposed

silanol trapping mechanism.

Finally, we develop a variation of scanning Kelvin probe microscopy that enables measurement of electric fields through a position modulation. This method avoids taking a numeric derivative of potential, which can introduce high-frequency noise into the electric field signal. Preliminary data is presented, and the theoretical basis for electric field noise in both methods is examined.

BIOGRAPHICAL SKETCH

Louisa was born in Buffalo, New York on June 14, 1987 to two math teachers, Charles and Alice Brown. She grew up in East Aurora, New York, where her parents encouraged her to explore the natural world through observation. Her interest in science as a future path was sparked by two years at the Horizons summer camp at Potsdam, a chance for middle school girls to explore engineering. She was the valedictorian of her high school graduating class of 2005.

Louisa attended Hamilton College in Clinton, New York where her studies were supported by a Bristol fellowship. She spent the summers of 2005, 2006, and 2008 as a chemistry research student, working on inorganic and organic synthesis projects. She spent the academic year 2007-2008 studying chemistry, literature, and art history in Paris, France. In a drawing class in Paris, she met John Smieska, whose intellectual passion and generous spirit have been inspiring her ever since. Louisa graduated from Hamilton summa cum laude in 2009 with a Bachelor of Arts in chemistry and fine arts. She received several awards during her undergraduate studies, including induction into the Sigma Xi and Phi Beta Kappa societies, the Underwood Prize for Excellence in Chemistry, and the Elihu Root Fellowship for Graduate Study in the Sciences.

Louisa began her graduate study at Cornell in August 2009 and joined the Marohn lab that fall. She was awarded a National Science Foundation Graduate Research Fellowship that supported her research from summer 2010 to summer 2013. She passed her A-exam on March 29, 2012. On August 11, 2012, John and Louisa were married in East Aurora, NY.

Louisa has enjoyed leading outreach activities at Cornell. She helped adapt the activity “Juice from Juice: Berry Solar Cells” into a workshop for Expanding Your Horizons, a one-day annual conference designed to encourage middle school girls to pursue science. The workshop has been popular since its first run in 2012. Louisa served as the evaluations chair for EYH in 2015. She also helped develop a lending library kit on “Juice from Juice” with

the Cornell Center for Materials Research.

During her graduate study, Louisa contributed numerous conference talks and posters; her presentation entitled “Directly Measuring Local Electric Fields via Tip Potential- and Position-Modulated Scanning Kelvin Probe Microscopy” was selected for a student award in symposium PP, Scanning Probe Microscopy, at the fall 2014 Materials Research Society meeting. Louisa has enjoyed research in the Marohn lab as well as extracurricular classes in art history and in the Johnson Museum of Art. In the future, she hopes to apply her passion for art, her love of chemistry, and her skills in thoughtful measurement to the technical study of cultural heritage materials.

To my family, for all their encouragement,
and especially to my husband, for his unwavering support.

ACKNOWLEDGEMENTS

Funding I am grateful for the support of an NSF graduate research fellowship as well as funding from grants NSF-DMR 1006633 and NSF-DMR 1309540. Support for each chapter is noted throughout the dissertation.

Cornell

First and foremost, many thanks to Professor John Marohn for his guidance throughout my graduate work. He is an outstanding mentor, and his leadership fosters an environment where students can independently and rigorously pursue difficult inquiries with the support of the team. Through his passion for research and his commitment to lifelong learning, he leads by example. His eagerness to take on new fields demonstrates an unforgettable intellectual fearlessness. His contagious enthusiasm for new ideas is unmatched, and his do-it-yourself attitude leads to a group dynamic that cultivates creativity and collaborative, continuous learning.

Prof. Marohn has provided constant opportunities to work on challenging research projects, learn new skills, and share findings, always advocating for individual growth. I cannot imagine a better learning environment for the pursuit of graduate study. John, thank you for all your patient hours of meetings, derivations, pep talks, and last-minute revisions, and thank you for taking a chance on an interested first-year student. I will carry the skills and scientific integrity I have learned from you into all my future endeavors.

Many thanks to the members of my committee: Prof. Will Dichtel, Prof. Richard Hennig, and Prof. Nandini Ananth. Your thoughtful questions and advice helped me to overcome research challenges and to improve my explanations of my work. It was a privilege to learn from you all.

Enormous thanks also to all the members of the Marohn group, past and present. This research lab is a wonderful place to work because you make it that way. Eric, Justin, Nik, Joni, Robert, and Andrew, thank you for welcoming me and teaching me the ropes. Eric,

I appreciated learning from your skepticism, and thank you for backing me up when Justin was being impossible. Nik, thank you for all your help learning Matlab, and for your patient training in CNF. It was so much fun working with you. Justin, thank you especially for your careful training and attention to detail as I learned how to run the EFM rig. I didn't break it! Joni, thank you for passing on your wisdom about the group, Cornell, and life in general. Your friendship is one of the best things to come out of this whole graduate school experience.

Jimmy, Lei, Ryan, Paméla, Christine, Sarah, Hoang, Corinne, Beth, Michael, Ali, Alex, Joseph, and Sherry, I am so glad I had the chance to work with you. You are all such talented scientists. Thank you for sharing your skills so generously and continuing to make the lab a friendly and cooperative environment. Jimmy, I so admire your thorough research skills, your eagerness to teach what you know, and your passion for making science accessible. Watching you and Joni grow as leaders while John was on sabbatic taught me so much. Ryan, I don't know how you find the time to experiment with code, but thank you for answering all my questions and teaching me so much about Python and EAGLE. Sarah, you have a great capacity for persistence when you take on challenges, in lab and beyond (as well as an uncanny ability to get all the sales rep goodies!). Keep it up and I'm sure you will go far. Ali, best of luck as you take over EFM operations. Between your thoughtful approach and your access to interesting materials, I think you are poised for success.

To all my collaborators at Cornell, thank you for the chance to learn about what you do. Vladimir, thank you especially for all your advice on successfully evaporating organic thin films. Katie, since you left Ithaca, I've missed both your chemical insights and your company over lunch.

Personal

To my friends at SewGreen and the Johnson Museum, thank you for all your encouragement, and for keeping me optimistic about life outside of school.

Julia MacDougall, thank you so much for all the mutual venting sessions and for always rooting for me. Your well-timed care packages lifted my spirits so many times. It is so good to know that I always have such a loyal friend (and tenacious woman in science) in my corner!

Finally, to my amazing husband John Smieska, your support throughout this experience has been so essential. Thank you for listening to my gripes and anxieties with empathy, and also for not letting me wallow in any of them. Your confidence in me helps me to rediscover my motivation and my own curiosity. Thank you for encouraging me to forge my own path inside and outside the chemistry department. You continue to teach me so much about myself, and about how to understand and support others. I would not be where I am today without your irreplaceable partnership.

TABLE OF CONTENTS

Biographical Sketch	iii
Dedication	v
Acknowledgements	vi
Table of Contents	ix
List of Tables	xiii
List of Figures	xiv
1 Introduction	1
1.1 Organic semiconductors and the need for local measurements	1
1.1.1 Scanning probe measurements of organic semiconductors	2
1.2 Methods	4
1.2.1 Microscope	4
1.2.2 Electric force microscopy	5
1.2.3 Tip-modulated electric force microscopy	6
1.3 Thesis Outline	7
2 Chemical Charge Traps in Pentacene	10
2.1 Introduction	10
2.2 Results	17
2.2.1 Results: Topography and potential maps	17
2.2.2 Results: Trap-clearing spectra	19
2.3 Control samples	26
2.4 Discussion	31
2.4.1 Discussion: Charge trapping maps	31
2.4.2 Discussion: Trap-clearing spectra	32
2.5 Deposition control experiments	35
2.5.1 NMR	35
2.5.2 Mass spectrometry	37
2.5.3 Infrared absorption spectroscopy	38
2.6 Experimental	43
2.6.1 Sample Preparation	43
2.6.2 Electric Force Microscopy (EFM)	45
2.6.3 Trap-clearing spectra: data fitting	48
2.6.4 Pentacene Device Characterization	49
2.7 Conclusions	50
2.8 Acknowledgements	51
3 Charge transport in perylene diimide derivatives	53
3.1 Introduction	53
3.1.1 Scanning-probe microscopy of PDIs	54
3.2 Charge transport in Braunschweig PDIs	56
3.2.1 Current-voltage measurements	57

3.3	Short channel effects in PDIF-CN ₂	58
3.4	Extracting local mobilities using electric force microscopy	60
3.5	Charge injection kinetics in perylene diimides	67
3.6	Conclusions	73
3.7	Experimental	74
3.7.1	PDI transistor substrates	74
3.7.2	Thermal deposition of PDI films	76
3.7.3	Drop-casting of PDI films	77
3.8	Acknowledgements	77
4	Charge trapping in perylene diimide derivatives	78
4.1	Introduction	78
4.1.1	Trapping mechanisms in PDIs	79
4.1.2	Hückel predictions of PDI HOMO-LUMO electron densities	83
4.2	Trap-clearing spectroscopy of perylene diimides	85
4.2.1	Spatially uniform charge trapping in PDI transistor channels	86
4.2.2	Trap-clearing spectra: results	90
4.2.3	Trap-clearing spectra: discussion	94
4.3	Trap formation kinetics and surface treatments	98
4.3.1	Trap formation rate experiment	99
4.3.2	Trap formation rate results and discussion	100
4.4	Conclusions	105
4.5	Acknowledgements	106
5	Position-modulated FM-Kelvin Probe Force Microscopy	108
5.1	Introduction	108
5.1.1	Motivation	108
5.2	Concept: Position Modulated FM-KPFM	112
5.3	Data workup process	114
5.4	Experimental details	117
5.4.1	Instrument settings	118
5.4.2	Choosing a position modulation frequency and amplitude	120
5.4.3	Feedback gains	122
5.4.4	Choosing a tip-sample separation	127
5.4.5	Scanning speed and spatial grid	129
5.5	Interconverting signals and noise measured as functions of time and position	130
5.6	Overview of electric field noise derivations	133
5.7	Electric field noise in the potential derivative from standard FM-KPFM	134
5.7.1	Signal and voltage noise in terms of frequency noise	134
5.7.2	Defining a lock-in operator	135
5.7.3	Potential noise in FM-KPFM feedback	136
5.7.4	Relationship between power spectra of electric field noise and voltage noise in <i>k</i> -space	138
5.7.5	Electric field noise in derivative of FM-KPFM potential	140

5.8	Electric field noise in position-modulated FM-KPFM	144
5.8.1	Definition of position modulated signal and voltage noise in terms of frequency noise	144
5.8.2	Electric field noise in position-modulated FM-KPFM	146
5.9	Discussion: comparing electric field noise in standard and position-modulated KPFM	150
5.10	Varying size of position modulation	152
5.11	Conclusions and future directions	154
5.12	Acknowledgements	155
6	Collaborative work: Preliminary EFM measurements on photovoltaic materials	156
6.1	Introduction	156
6.2	EFM of Covalent Organic Frameworks	156
6.2.1	Introduction: Chemistry of COFs	156
6.2.2	Characterization Techniques for COFs	157
6.2.3	COFs for Devices	159
6.2.4	Scanning-Probe Microscopy for COFs	159
6.2.5	Conductive-Probe AFM for COFs	160
6.2.6	Electric Force Microscopy for COFs	161
6.2.7	Future COF Experiments	166
6.2.8	COF Acknowledgements	167
6.3	EFM of Perovskites	167
6.3.1	Perovskite performance pros and cons	168
6.3.2	Previous scanning probe microscopy of perovskites	168
6.3.3	Preparing a perovskite transistor	169
6.3.4	EFM of a perovskite transistor	171
6.3.5	Future experiments	172
6.3.6	Perovskite Acknowledgements	173
A	Glove Box and Evaporator Protocols	174
A.1	Glove box and evaporator requirements	174
A.2	Glove box and evaporator operation	175
A.2.1	Operating the transfer antechamber	175
A.2.2	Evacuating, venting, and baking out the evaporator	177
A.2.3	Depositions in the Trovato evaporator	180
A.3	Maintenance and parts	186
A.3.1	Glove box and evaporator upkeep	186
A.3.2	Glove box parts: setup, repairs, and upgrades	186
A.3.3	Replacing the pressure switches	188
A.4	Recommended upgrades	190

B Microscope Upgrades	192
B.1 Laser diode replacement	192
B.2 Summing circuit	194
B.3 Temperature diode	196
B.4 Monochromator Labview Code	197

LIST OF TABLES

LIST OF FIGURES

2.1	Schematic of samples used in pentacene study	11
2.2	Pentacene trap precursors, calculated absorption spectra, and proposed reaction mechanisms.	14
2.3	Surface potentials and topography of pentacene transistor channels with different trap precursors.	18
2.4	Schematic of molecular energy levels involved in trap clearing processes.	20
2.5	Representative raw trap-clearing data set.	21
2.6	Fitting procedure for trap-clearing potential transients.	23
2.7	Potential drop vs. wavelength.	25
2.8	Trap-clearing spectra.	27
2.9	Exponential trap-clearing rates at two locations in a pentacene + PHO device.	28
2.10	Pristine pentacene transistor, AFM and EFM.	29
2.11	Topography and trapping in pentacene + thin DHP transistor.	29
2.12	Topography and trapping in pentacene + PHO transistor.	30
2.13	^1H NMR spectra of trap precursors before and after deposition.	36
2.14	Mass spectrometry of co-deposited films.	38
2.15	Infrared absorption spectra.	39
2.16	Calculated and measured IR spectra.	41
2.17	Pentacene transistor curves.	50
3.1	Molecular structures of PDI derivatives.	55
3.2	Schematic of tip, transistor channel, and transistor cross-section.	57
3.3	Bulk current-voltage curves for dCH dBr PDI and dEO PDI.	57
3.4	Bulk current-voltage curves for PDIF-CN ₂	59
3.5	Surface potentials and E fields for dEO PDI on bare and HMDS/SiO ₂	62
3.6	Surface potentials, E fields, charge densities, and local mobilities for dCH dBr PDI.	63
3.7	Surface potentials, E fields, and local mobilities for PDIF-CN ₂	66
3.8	Schematic illustrating injection barrier lowering.	67
3.9	Sketch of charge injection kinetics experiment and sample data.	68
3.10	Raw charge injection surface potential transients.	69
3.11	Topography of dEO PDI transistor and locations where charge injection measurements were made.	70
3.12	Charge injection rates and steady-state surface potentials in dEO PDI.	71
3.13	Charge injection rates for two dEO PDI samples.	72
4.1	Hückel theory model of PDI core electron density.	84
4.2	AFM topography of drop-cast PDI transistors.	86
4.3	AFM topography of thermally deposited PDI transistors.	87
4.4	Representative mass spectrometry of PDI transistors.	87
4.5	Trapping maps and transients in dCH dBr PDI and dEO PDI transistors.	89
4.6	Trapping maps in dEO PDI and PDI FCN ₂ transistors.	89

4.7	State diagram of light-enhanced (k_1-k_4) and thermal (k_5) trap-clearing processes in <i>n</i> -type semiconductors. k_1-k_2 : excitation of neutral PDI leads to electron transfer from trap to neutral PDI. k_3-k_4 : excitation of charged trap leads to electron transfer from trap to neutral PDI. k_5 : thermally activated electron transfer from trap to neutral PDI. Once the electron is transferred to the neutral PDI, it is mobile and can be transported to the electrode.	91
4.8	Trap-clearing in light-insensitive PDI derivatives.	92
4.9	Trap-clearing spectra in dCH dBr PDI and dEO PDI transistors.	93
4.10	Trap-clearing spectrum for evaporated dEO PDI on bare SiO ₂ , linear fits.	95
4.11	Solution absorption spectrum of dEO PDI anion radical.	97
4.12	Water contact angles of transistor substrates.	99
4.13	Schematic illustrating trap formation kinetics measurements.	100
4.14	Raw trap formation surface potential transients for different surface treatments.	101
4.15	Trap formation rates for different surface treatments.	102
4.16	Summary of all trap formation rates for different surface treatments.	104
5.1	Electric fields help evaluate quality of contacts.	109
5.2	Injection processes into organic semiconductors.	110
5.3	Noise amplification due to derivative.	111
5.4	Schematic sketch of position modulation experiment.	113
5.5	Data workflow: transformation of raw signal.	115
5.6	Data workflow: Isolation of DC peak.	116
5.7	Data workflow: isolation of AC signal.	117
5.8	Block diagram of position modulated FM-KPFM experiment.	118
5.9	Frequency power spectrum and mechanical noise.	121
5.10	Height dependence of E field for poor feedback.	124
5.11	Tip voltage dependence of E field for poor feedback.	125
5.12	Block diagram for feedback network frequency analysis (Bode plots).	126
5.13	Bode plots for optimized feedback settings.	127
5.14	Height independence of E field for correct feedback.	128
5.15	FT of position modulated surface potential for different scanning step sizes.	129
5.16	Comparison of derivative and position modulated electric fields for different size modulations.	153
6.1	Schematic of conductive-probe AFM on a COF film.	160
6.2	Preliminary cp-AFM data on a COF/graphene/fused silica sample.	162
6.3	Schematic of EFM on a COF film.	163
6.4	Preliminary EFM on HHTP-DPB COF on graphene.	164
6.5	Preliminary EFM on COF-5 on ITO.	165
6.6	Perovskite data.	171
A.1	Parts of the glove box and evaporator system.	176
B.1	Single summing circuit, schematic.	194
B.2	Single summing circuit, board layout.	195

B.3	Dual summing circuit, schematic.	195
B.4	Dual summing circuit, board layout.	196
B.5	PCB summing circuit.	197
B.6	Temperature diode.	198
B.7	New monochromator Labview code.	198

CHAPTER 1

INTRODUCTION

1.1 Organic semiconductors and the need for local measurements

Organic semiconductors hold promise in a range of devices, including complementary circuits [1–4], molecular sensors [5], and photovoltaics [6, 7]. Unlike their inorganic counterparts, establishing reliable models for organic device performance has proven difficult. Although bulk device characterization techniques such as current-voltage measurements have been used to brute-force engineer improved devices, these bulk measurements rarely shed light on underlying microscopic processes limiting device performance. These limiting processes include charge trapping, charge injection, and charge transport.

In the case of chemical degradation, it would be helpful to connect specific degradation products to decreased device performance. Measurements of current-voltage curves in different atmospheres can suggest possible reactions, but do not identify specific defects [8]. However, spectroscopy techniques often are not sensitive enough to detect the low concentrations of impurities that influence performance. Even when bulk spectroscopic techniques have high sensitivity, they do not always provide the direct connection to performance [9, 10]. For example, mass spectrometry is often used to identify all degradation products in aged devices [11, 12], but the presence of a molecule does not necessarily implicate it in performance issues [13].

In inorganic semiconductors, ideal charge injection is modeled as an activated process that depends on the energy level alignment of the electrode work function and the semiconductor band. By contrast, charge injection in organic semiconductors can range from barrier-limited (activated) to essentially barrier-less, depending on disorder in the organic material and the

alignment of organic tail states with the electrode work function [14, 15]. Even contacts that can appear ideal, *i.e.* contacts with little to no potential drop, can actually have significant local electric fields that indicate different degrees of charge injection non-ideality [16]. These non-ideal contacts are typically only evaluated in terms of contact resistance for bulk device measurements [17, 18], but are directly accessible in local measurements of surface potential and electric fields.

Charge transport is usually reported in terms of mobility, measured on a bulk scale. However, extracting mobility, threshold voltage, and contact resistance, of which the mobility and contact resistance may have a gate bias dependence, requires several assumptions regarding the density of states in the organic, the density and distribution of traps, and the modeling of the contact resistance as a series resistance with the semiconductor film [19]. Although it is well known that local features such as variations in morphology can have a large impact on device mobility [20, 21], local variations in mobility are ignored when a single value is reported for a device. In addition, apparent device mobility can be impacted by contact effects. Other measurements such as time-resolved microwave conductivity (TRMC) yield a “contact-less” mobility, but these values can be overestimates since film morphology effects like grain boundaries are not expected to impact charge transport on the nanosecond and picosecond timescales probed in a TRMC measurement [22]. Measurements of local mobility can help evaluate uniformity of transport in a material, as well as disentangle material performance from contact effects [23].

1.1.1 Scanning probe measurements of organic semiconductors

Although scanning-probe measurements excel at discerning connections between local physical and electronic properties, few experiments to date have directly connected local device performance to local degradation chemistry. One exception is a study of surface poten-

tial charging rates as a function of photodegradation in a polymer donor:acceptor solar cell blend; this work demonstrated that microscopic charging rates were more sensitive to the concentration of ketone defect than infrared spectroscopy [24]. In this thesis, we employ scanning-probe microscopy techniques to examine *local* electronic properties in conjunction with local morphology and chemistry. A measurement which we term “trap-clearing spectroscopy” is employed to examine chemical species at specific charge trap locations in working *p*- and *n*-channel transistors [13, 25].

With scanning probe microscopy, charge traps can be mapped, and the spatial distribution of traps can distinguish grain boundary and morphology traps from other mechanisms [26]. Another angle for evaluating charge trap chemistry is to study the trap formation kinetics. Trapping kinetics can be measured by following the amount of trapped charge as a function of available free charge using electric force microscopy [27, 28]. Here, we examine trap formation kinetics in *n*-channel devices with different surface chemistries.

Charge injection theories have been tested in *p*-type materials with great success using scanning-probe microscopy [15, 16, 29]. In this thesis, we observe and measure injection-barrier lowering in *n*-channel transistors. We also find that energetic barriers to charge injection in *n*-channel materials are extremely sensitive to the electrode work function.

Local measurements of mobility via scanning-probe measurements of surface potentials have been employed to study both *p*- and *n*-channel transistors for several years [30–33]. However, the independent parameter in microscopic theories of charge injection is the electric field, not the voltage. The electric field is usually obtained by taking a numeric derivative of the local potential [30, 34]. Since derivatives can introduce noise into the resulting electric field, we developed a new variation of FM-KPFM to measure electric fields while avoiding the need for a spatial derivative.

1.2 Methods

1.2.1 Microscope

The scanning-probe measurements discussed in this dissertation were performed using a custom-built, high-vacuum Kelvin probe microscope. Platinum-coated silicon cantilevers with resonance frequencies of 75 ± 15 kHz were purchased from MikroMasch, model number HQ:NSC18/PT. The cantilever displacement was monitored using a fiber-optic interferometer at either 1310 or 1490 nm (see Appendix B.1 for a discussion of the new laser diode). Frequency demodulation was achieved using an RHK PLLPro 1.0 cantilever controller. Biases were applied to samples and currents measured using a Keithley 2400 source meter for the gate/ground and a Keithley 6430 source meter with a remote pre-amplifier for the source-drain connections.

Lateral scanning was achieved using a custom-built sample stage comprised of four s-bending piezos. The design of this stage can be found in other Marohn group theses [35, 36]. Vertical scanning of the cantilever used a slip-stick mechanism for coarse motion up and down with fine piezo motion in a $3 \mu\text{m}$ range near the sample surface. The design of this slip-stick positioner is discussed in Bill Silveira's thesis [37]. A tabling circuit adds a scaling factor to the z extension for every lateral position, $A \times x + B \times y = z$.

The microscope is equipped with two modes of top-down visible light sample illumination: a white LED (InGaN, LiteOn model LTW-1KHC5) ~ 1 cm away from the cantilever and ~ 5 mm above the sample, and an optical fiber pointing below the cantilever. The optical fiber provides variable-wavelength visible illumination: light from a 150 W tungsten-halogen bulb in a Dolan-Jenner Fiber-Lite source is collected by a $50 \mu\text{m}$ wide-core fiber and passed through a Micropak Monoscan 2000 scanning monochromator and an OzOptics

motor-controlled attenuator to adjust for constant power. We estimate the incident power from the optical fiber to be $\sim 0.5 \text{ mW/cm}^2$ [38].

1.2.2 Electric force microscopy

The idea behind our electric scanning probe measurements is somewhat like a hair attracted to a charged balloon. Like a thin hair, our tiny metal-coated silicon cantilever bends in response to electrostatic forces on a charged sample surface. Unlike a hair, however, our cantilevers are vibrating at high frequencies of $\sim 60 \text{ kHz}$; in addition, our cantilevers are electrically conductive, while hairs can hold charge because they are electrically insulating. Instead of measuring a large physical displacement, we measure tiny shifts in the cantilever resonance frequency that contain information about the sample surface sensed by the probe [39].

In electric, non-contact, scanning-probe measurements, we can write the cantilever frequency, f , as:

$$f = f_0 - \frac{f_0}{4k_0} C_{zz}(V_{\text{DC}} - \phi)^2 \quad (1.1)$$

where f_0 is the cantilever resonance frequency, k_0 is the cantilever spring constant, C_{zz} is the tip-sample capacitance second derivative relative to height z , V_{DC} is the cantilever tip bias, and ϕ is the contact potential difference. This expression assumes that charge moves on and off the cantilever without dissipation on the same timescale of the cantilever oscillation period. The derivation of this relationship is presented in greater detail in reference 40.

Eq. 1.1 assumes that the charge on the cantilever equilibrates with charge on the sample as the cantilever vibrates closer and further from the sample surface. It also assumes that the contact potential difference ϕ is height-independent; as shown in Ch. 5 this is a fair assumption for the samples studied here. It is also important to note that the contact

potential difference is composed of an electrostatic and a chemical potential term:

$$\phi = \phi(x) - \frac{\mu}{e} \quad (1.2)$$

where $\phi(x)$ is the local electrostatic potential, μ is the chemical potential difference between the tip material and the electrode material in the device under study, and e is the elementary charge. In generally μ is assumed to be constant across a sample surface, and most of the variation we see in images of the contact potential difference arise from electrostatic forces [36, 40]. This assumption is especially accurate in the case of charge trapping in transistors.

As shown in Eq. 1.1, the cantilever frequency shift $f - f_0$ depends quadratically on the tip voltage. If the tip voltage is swept from low to high, the tip of the parabola will be located at $\phi = V_T$. This is a relatively slow method of obtaining surface potential data since one can feasibly gather only one or two parabolas per second. However, the method is reasonable for measuring slow surface potential transients over a single point.

1.2.3 Tip-modulated electric force microscopy

Most surface potential measurements presented in this thesis were acquired via tip-modulated electric force microscopy (EFM), also known in the literature as frequency-modulated Kelvin probe microscopy (FM-KPFM) [39]. Here, we review the frequency-modulation method for feeding back on the cantilever tip voltage to measure the surface potential. This derivation is discussed in greater detail in Michael Jaquith's thesis [36].

When an oscillating voltage is applied to the tip, so that $V_T = V_{DC} + V_{AC}$, the cantilever frequency is defined as:

$$f = f_0 - \frac{f_0}{4k_0} C_{zz} (V_{DC} - \phi + V_{AC} \cos(\omega_v t))^2 \quad (1.3)$$

where f_0 is the cantilever resonance frequency, k_0 is the cantilever spring constant, C_{zz} is the tip-sample capacitance second derivative relative to height, (V_{DC}) is the DC tip voltage applied during feedback, ϕ is the surface potential, V_{AC} is the AC tip voltage, and ω_v is the frequency of the AC tip voltage. Expanding this expression, we find:

$$f = f_0 - \frac{f_0}{4k_0} C_{zz} [(V_{DC} - \phi)^2 + 2(V_{DC} - \phi)V_{AC} \cos(\omega_v t) + V_{AC}^2 \cos^2(\omega_v t)] \quad (1.4)$$

$$f = f_0 - \frac{f_0}{4k_0} C_{zz} [(V_{DC} - \phi)^2 + 2(V_{DC} - \phi)V_{AC} \cos(\omega_v t) + \frac{1}{2}V_{AC}^2 + \frac{1}{2}V_{AC}^2 \cos(2\omega_v t)] \quad (1.5)$$

We use lock-in detection at ω_v and $2\omega_v$ to detect the first and second Fourier components of the frequency shift signal:

$$\Delta \hat{f}(\omega_v) = \frac{f_0}{2k_0} C_{zz} V_{AC} (V_{DC} - \phi) \quad (1.6)$$

$$\Delta \hat{f}(2\omega_v) = \frac{f_0}{8k_0} C_{zz} V_{AC}^2 \quad (1.7)$$

In typical frequency-modulated Kelvin probe force microscopy (FM-KPFM), or what this group has previously referred to as tip-modulated electric force microscopy (EFM), the $\Delta \hat{f}(\omega_v)$ component of the frequency shift is tracked and set to zero by adjusting V_{DC} with a PID loop. $V_{DC} = \phi$ when $\Delta \hat{f}(\omega_v)$ equals zero, so the output of the PID loop yields the surface potential ϕ directly. The assumptions detailed in section 1.2.2 regarding charge equilibration of the tip, height-independence of ϕ , and the dominance of the electrostatic potential term in ϕ are all assumed to apply here as well. This lock-in method is a much faster way to obtain the surface potential than the parabola method, and enables collection of line-scans and 2D images of ϕ at 16 or 32 points per second.

1.3 Thesis Outline

Chapter 2 presents the results of impurity-doping experiments in working pentacene transistors. Three known impurity molecules are co-deposited with pentacene, and extensive

spectroscopic characterization confirm that the impurities are deposited as expected. The devices are examined in high vacuum, and the charge traps resulting from gate biases are mapped. Trap-clearing spectroscopy is validated as a method for measuring internal photoexcitations of charge trap species. We find that an oxygen-defect, rather than the literature favorite hydrogen-defect, is a potent trap-precursor. We caution that thermodynamic predictions of degradation chemistry do not always reflect the chemistry that goes on in the solid-state.

In [Chapter 3](#), we report on transport studies in perylene diimide (PDI) *n*-channel transistors. We observe firsthand that bulk transport measurements cannot always yield reliable mobility information. Instead, we turn to scanning-probe methods of local mobility measurements using surface potential profiles at different gate and drain biases. We confirm that local electric fields can be extremely noisy when calculated from numeric derivatives, in part motivating our work in Ch. 5. We also measure highly variable barriers for charge injection into a low-LUMO PDI.

[Chapter 4](#) details our experiments exploring charge trapping mechanisms in low-LUMO PDIs. We measure the first-ever trap-clearing spectra in *n*-channel semiconductors. These spectra show that the main species involved in trap-clearing is most likely the neutral PDI, consistent with a non-chemical-degradation trap mechanism. We measure trap formation rates in transistors with bare and passivated SiO₂ dielectrics, but we do not find a reproducible trend in trap formation rates for different surface chemistries. This data refutes the popularly cited silanol-based trapping mechanism in *n*-channel devices.

In [Chapter 5](#), we describe a new variation of Kelvin probe microscopy that measures electric fields without requiring a numeric derivative of the surface potential. We employ a spatial modulation in the scanning direction to obtain a surface potential signal that oscillates in time; the amplitude of these oscillations is proportional to the local electric

field. We demonstrate the importance of careful tip-voltage feedback in performing position-modulated FM-KPFM, and we present preliminary data comparing the new method and the derivative method. We also present derivations describing the expected noise in each method, and suggest improvements that would allow our new method to be even more useful.

Chapter 6 summarizes data from two important internal collaborations during this dissertation period. We discuss photovoltage measurements on covalent organic framework (COF) films, and describe how future experiments could contribute to ongoing research efforts. We describe preliminary photovoltage measurements on a lead-halide perovskite photovoltaic film, and outline the methods for fabricating these samples.

A major upgrade to the Marohn lab capabilities during this dissertation period was the addition of a glove box and evaporator. **Appendix A** describes the parts of the glove box and evaporator and outlines operation protocols. Repairs and maintenance that were performed on the glove box are discussed, and future upgrades are recommended.

Finally, **Appendix B** details changes that have been made to the microscope during this dissertation period. The laser diode, a critical component of the interferometer, was replaced; the selection criteria are outlined here. Other upgrades and repairs, including printed circuit board summing circuits, a temperature-measurement diode, and monochromator software are also described in this chapter.

CHAPTER 2

CHEMICAL CHARGE TRAPS IN PENTACENE

2.1 Introduction

Degradation is an acknowledged issue in organic semiconductors that decreases the amount of active material and creates impurities. However, the distinction between degradation alone and degradation that affects performance is often lacking. In many cases, impurities in organic semiconductors are proposed as a source of charge trapping. Intentional doping with impurities for controlled charge trapping is important for optimizing applications like photorefractive materials [41, 42] and organic transistor memory [43]. Conversely, in organic transistors and most other applications of organic semiconducting materials, charge trapping is detrimental to device performance because it increases operating voltages and decreases mobility.

There are hundreds of characterized organic semiconducting materials, but only a few systems in which the chemical degradation product responsible for decreased performance has been spectroscopically identified [44, 45]. Even the most sensitive bulk materials characterization techniques can only demonstrate the *presence* of impurities and may not be capable of detecting defects at concentrations relevant to device performance [24]. Few characterization techniques can draw a direct connection between the presence of impurities and regions of decreased performance. For example, although XPS is an extremely sensitive surface analysis technique, it does not necessarily yield information about the semiconductor-dielectric interface, where most of charge transport occurs. There is a need for techniques that can provide *local* information correlating threshold voltage and chemical composition.

The work presented in this chapter is designed to deepen our understanding of chemical

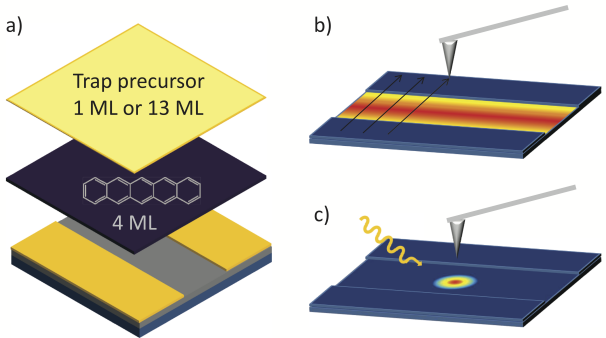


Figure 2.1: (a) Schematic of samples investigated in this study: 4 monolayers (4 ML) of pentacene were deposited on bottom-contact transistor substrates and subsequently layered with 1 ML or 13 ML of a trap-precursor defect species. (b) Schematic of electric force microscopy (EFM) surface potential mapping. The local threshold voltage is measured as the contact potential difference between the cantilever tip and the sample surface while the cantilever is scanned in-plane above the sample. (c) Schematic of time- and wavelength-resolved EFM trap-clearing experiments. The cantilever is positioned above a single point of interest and the local contact potential difference is measured as a function of time while the sample is illuminated from above with monochromatic light. The cantilever is not scanned in the lateral plane during this measurement. The cantilever does not contact the sample in either (b) or (c).

charge trapping in pentacene. First, I directly deposited possible chemical trap-precursor molecules on top of very thin pentacene films in a bottom-contact transistor geometry (Figure 2.1a). I then measured the resulting spatial distribution of charge trapping in the transistor channel (Figure 2.1b). Finally, I spectroscopically probed the electronic energy levels in the cationic trap species by introducing variable-wavelength sample illumination (Figure 2.1c). This experiment allows us to directly microscopically and spectroscopically investigate the charge-trapping efficacy of various chemical defects in pentacene. We find that the charged species responsible for charge trapping in aged pentacene is very likely PHO^+ .

To perform the charge trapping characterization described above (Figure 2.1b, c), we employ electric force microscopy (EFM). EFM is a non-perturbative scanning-probe tech-

nique that measures the contact potential difference between a metallic cantilever tip and the sample below [46]. (The techniques I refer to as EFM can also be described as frequency-modulated Kelvin probe force microscopy, or FM-KPFM.) EFM has been used to image charged traps in thin films of pentacene and pentacene derivatives [27, 28].

Recently, Luria *et al.* have demonstrated that EFM can also be used to spectroscopically measure the energy levels of the charged trap species in aged pentacene [25]. Charged traps in pentacene are neutralized by electron transfer from neighboring molecules. This process is very slow (many hours) when driven by thermal energy, but it can occur at a faster rate (seconds) under illumination [47]. This rate enhancement is usually attributed to photoexcitation of pentacene followed by electron transfer to the trap. Luria *et al.* measured the local surface potential of a charged trap in aged pentacene as a function of time while illuminating the sample from above. By extracting the trap-clearing rate as a function of illuminating wavelength, Luria *et al.* revealed that the rate of trap-clearing in pentacene is enhanced at 500 nm. 500 nm does not correspond to a strong pentacene absorption, indicating the existence of a second trap-clearing mechanism. The peak at 500 nm in the spectrum of light-induced trap-clearing rate was smooth and symmetrical, which suggested that it might arise from excitation of a single chemical species, consistent with other observations that hole traps in pentacene arise from a discrete oxygen-related defect [48, 49].

To explain these observations, a new internal photoexcitation mechanism of trap-clearing was proposed, involving direct absorption by the charged trap species (rather than pentacene) followed by electron transfer from pentacene and neutralization of the trap [25]. The trap-clearing spectrum thus measures an electronic transition in the cationic trap species. In the present work, we add chemical defect species to pristine pentacene transistors and compare their trap-clearing spectra to the spectrum obtained from aged pentacene.

In the following two paragraphs, we evaluate the numerous possibilities for the proposed

chemical charged trap species. Exposure of pentacene films to humidity leads to charge trapping [8] and produces a variety of oxygenated species observable by mass spectrometry [12]. In solution, the reaction of pentacene with oxygen to form the endoperoxide has been known for decades, [50] and many computational studies affirm this reactivity [51, 52]. However, the pentacene endoperoxide is highly distorted out of plane, [53] and calculations indicate that it is not the most stable oxygen-related defect in the pentacene crystal [54]. Although the analogous endoperoxide has been proposed in rubrene single crystals as a product of exposure to light and oxygen, [55] this species is unstable in the crystal by at least 1.1 eV compared to other oxygen related defects [56, 57]. It has been shown that pentacene stability and photochemistry is very different in solution versus in thin films, [51] and XPS studies of pentacene photooxidation in thin films suggested that the endoperoxide in pentacene films is probably converted to a more stable species [58]. To our knowledge, the pentacene endoperoxide has not been spectroscopically observed as a degradation product in polycrystalline pentacene thin films. For these reasons, the endoperoxide was not considered as a trap precursor in this study, but we do consider two other oxygenated species as trap precursors, discussed below (pentacen-6(13H)-one, PHO; 6,13-pentacenequinone, PQ; Figure 2.2a).

Hydrogenated pentacene defects have been predicted computationally [59] and observed experimentally as byproducts of pentacene sublimation via mass spectrometry [60, 61], and possible mechanisms for the process of hydrogenation have also been studied computationally [62]. Northrup and Chabinyc noted that pentacene is energetically likely to have a dihydrogen defect ($C_{22}H_{16}$, or DHP, Figure 2.2a), and they also suggested several oxygenated traps and neutral defects ($C_{22}H_{13}O$, $C_{22}H_{15}O$ and $C_{22}H_{16}O$, not pictured), predicting that defects like these will give rise to gap states and could form charged defects in the presence of pentacene cation radicals [59]. Considerable attention has also been paid to the impurity 6,13-pentacenequinone ($C_{22}H_{12}O_2$, PQ, Figure 2.2a) identified in commercial pentacene [63]. The presence of PQ in pentacene films has been shown to have a significant effect on

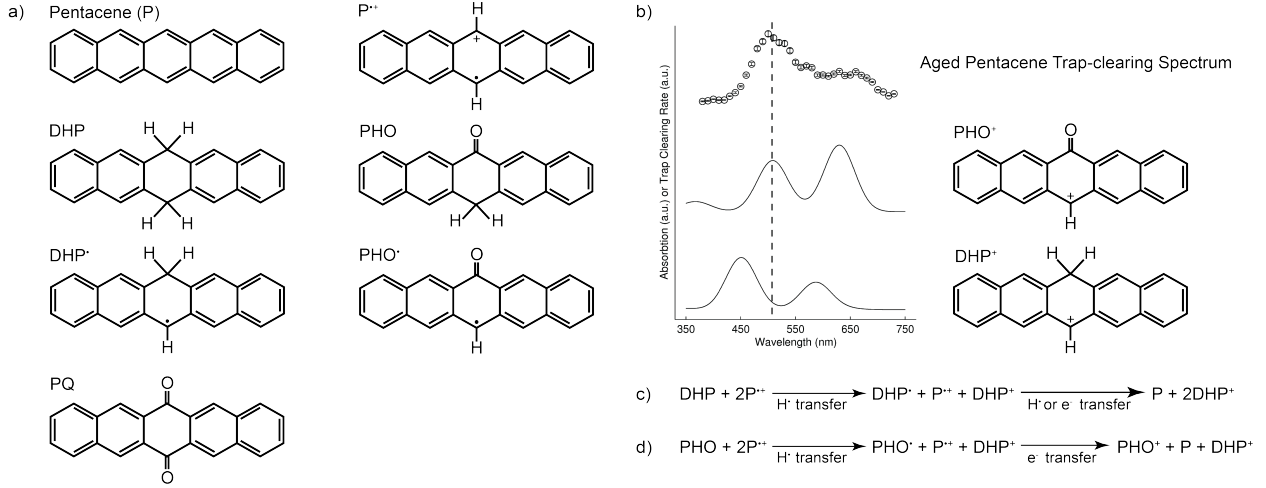


Figure 2.2: (a) Molecules, intermediates, and charged species. $\text{P}^{\cdot+}$ is a pentacene hole carrier. DHP and PHO are neutral trap-precursor candidates that may undergo hydrogen atom loss followed by electron loss. PQ is a major impurity in commercial pentacene. (b) Trap-clearing spectrum obtained from aged pentacene compared with calculated absorption spectra for the proposed charged trap species, PHO^+ and DHP^+ , reproduced from Ref. 25 (c) Proposed mechanism for the formation of DHP^+ from DHP. (d) Proposed mechanism for the formation of PHO^+ from PHO. Note that DHP^+ is formed in both mechanisms (c) and (d). For the calculated thermodynamics and proposed mechanisms for processes (c) and (d), see the Supporting Information of Ref. 25.

mobility, [63, 64] island nucleation, [65] and thin film morphology [64, 66, 67]. However, the precise role of PQ in these effects remains unclear. PQ’s energy levels suggest that it behaves as a scattering center rather than a charged trap species, [63] but its geometry and distribution in the film are consistent with the possibility of charged traps due to structural defects [64]. Finally, the so-called “butterfly” photodimer of pentacene has been characterized by UV/Vis spectroscopy in solution and in PMMA films [68]. Analogous dimers of trialkylsilylalkynyl-functionalized pentacene have been characterized in solution and thin films, [11] and silylethyne-substituted hexacenes are known to undergo dimerization in solution and in the solid state [69]. To the best of our knowledge, the pentacene dimer has not been spectroscopically observed in thin films. For this reason, and because we did not observe any species of such high molecular weight by mass spectrometry of our samples, we did not consider the pentacene butterfly dimer as a possible trap precursor.

Luria *et al.* assessed several charged trap species by considering the electronic transition measured in the trap-clearing spectrum of aged pentacene. Challenging time-dependent density functional theory calculations of the charged species' absorbance spectra were performed by Schwarz and Hennig [25]. By comparing the experimental pentacene trap-clearing spectrum with the calculated absorbance spectra (Figure 2.2 b), Luria *et al.* found that pentacen-6(13H)-one (PHO) and 6,13-dihydropentacene (DHP) were likely candidates for chemical trap-precursors in pentacene. Proposed mechanisms for the formation of the charged trap species from the neutral precursors are summarized in Figure 2.2c-d [25, 59]. Note that the degradation of DHP (Figure 2.2b) results only in DHP^+ , while the degradation of PHO (Figure 2.2c) is expected to produce *both* DHP^+ and PHO^+ .

The literature suggests two possible methods for intentionally adding impurities to sublimed pentacene thin films. Impurity molecules can be co-deposited with pentacene by physically mixing them as solids and then depositing the mixture itself [64]. Alternatively, impurity molecules can be sequentially deposited on top of very thin layers of pentacene (4 monolayers, 4 ML) [66]. We chose to sequentially deposit the impurities on the pentacene since this allowed us to separately analyze the success of each deposition as well as to monitor the condition of the added precursor compound before and after being heated for deposition.

Both deposition methods are intended to incorporate the additive precursor into the first few critical monolayers where charge is transported so it can react with pentacene cation radicals (charge carriers) to form a charged trap species. The critical thickness at which mobility saturates is thought to represent the number of monolayers that contribute to charge transport; this thickness is also known as the Debye length. In pentacene, measurements of this thickness range from 2 ML to 6 ML [70–74]. For deposition conditions nearly identical to ours, Shehu *et al.* measured a critical thickness of 4 ML, suggesting that our 4 ML films should be saturated with pentacene cation radicals when a negative gate bias is applied

[75]. In this case, we would expect the reaction of the neutral trap precursor with pentacene hole carriers to take place uniformly throughout the transistor channel; this hypothesis is supported by the uniform trapping by PHO in Figure 2.3d. Our samples are thus designed such that trap precursors are not required to intercalate into the pentacene layer to react with the hole carriers; *i.e.*, pentacene cation radicals are expected to be available at the interface between the pentacene and the trap precursor.

In the present work, we layer pristine pentacene transistors with three different possible trap-precursors. We study PHO and DHP based on the predictions of Luria *et al.* and also PQ (despite its unfavorable trapping energetics) since it is the starting material for the synthesis of PHO. We note that although the tautomer of PHO considered as a trap-precursor by Northrup and Chabinyc may be more likely to form in aged pentacene films than PHO since it does not break resonance, both precursors are expected to yield PHO^+ in the presence of pentacene cation radicals [25, 59].

The goal of this work is to compare the trap-clearing spectra in these intentionally “doped” samples with the theoretical predictions of Luria *et al.* and with the trap-clearing spectrum in undoped aged pentacene to reveal the chemical identity of the charged trap species. Below, we use EFM to measure spatial distribution of charge trapping and trap-clearing spectra of pentacene transistors with the three trap-precursors of interest. We use mass spectrometry and IR spectroscopy to corroborate the presence of the impurities in the transistor channel. Our data strongly supports PHO^+ as the charged trap species in aged pentacene.

2.2 Results

2.2.1 Results: Topography and potential maps

Before interpreting my EFM results, it is also important to note that I performed several chemical characterization techniques to confirm that the trap-precursors are indeed intact on the transistor substrate. Please see section 2.5 for a discussion of the ^1H NMR, mass spectrometry, and infrared spectroscopy data collected in this study.

Figure 2.3 shows the results of our AFM and modulated EFM imaging measurements. In the AFM images, Figure 2.3g-i, different morphologies are apparent for the different trap precursors. The most obvious difference is that a greater thickness of DHP (13 ML) was deposited in comparison with the other precursors (1 ML each). This thicker layer was required to confirm the chemical identity of DHP in the transistor channel since 1 ML DHP was not detectable by mass spectrometry, micro-Raman spectroscopy, or transmission IR spectroscopy. The EFM results for 1 ML DHP were identical to those obtained with 13 ML DHP. When deposited thickly, DHP formed needle-like, apparently crystalline features (Figure 2.3f). The single monolayers of PHO and PQ did not form visible crystalline structures on the sample surface. The uniformity of the PHO deposition is confirmed by the trapping throughout the transistor channel seen in Figure 2.3d. For all samples, the thin 4 ML films of pentacene show incomplete coverage of the transistor channel and poor wetting of the gold electrodes, yielding tall spire features as in Figure 2.3g (spires to left and right of the channel). The stars in Figure 2.3d-f represent the locations where trap-clearing spectra were acquired (discussed below).

In the EFM images, Figure 2.3d-f, charge trapping is observed as regions of positive potential. The 4 ML P + 1 ML PHO sample shows strikingly uniform charge trapping

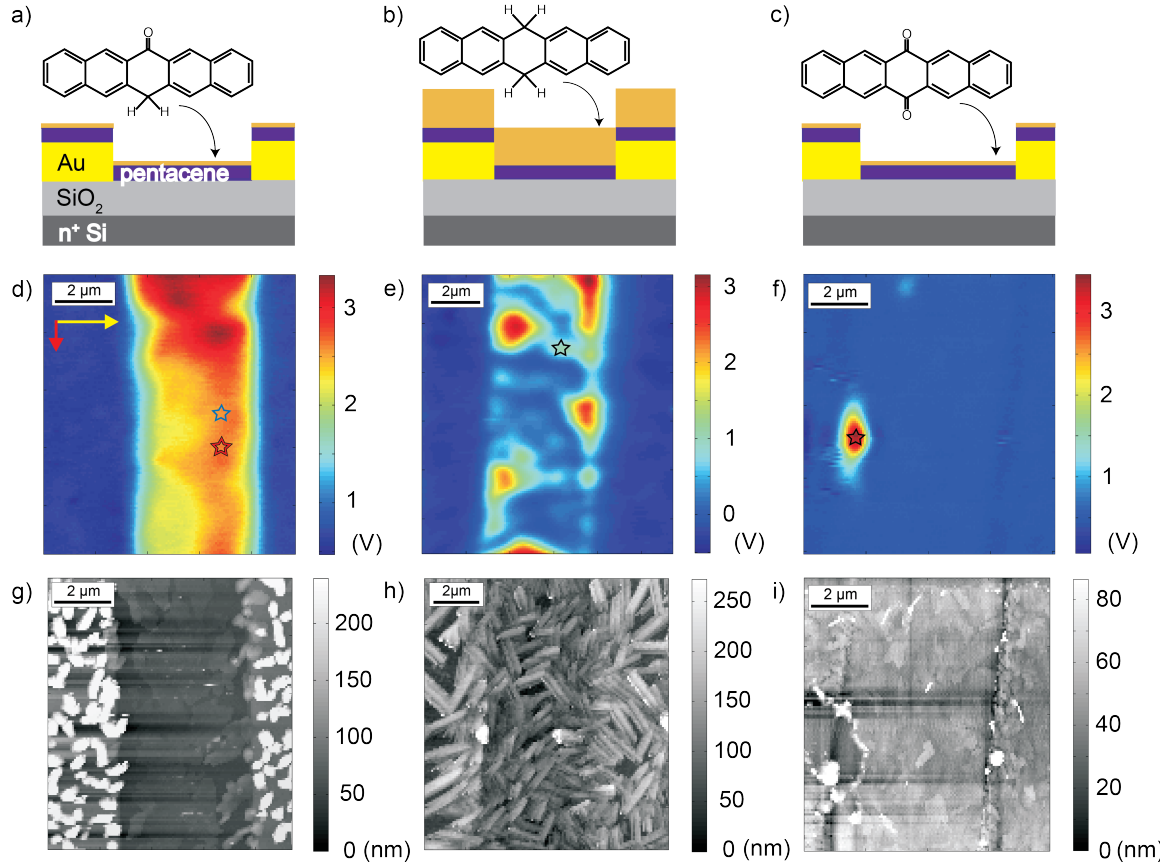


Figure 2.3: (a-c) Schematic side views of the sequentially deposited bottom-contact transistor substrates used in this work. The trap-precursor molecules shown are (a) 1 ML PHO, (b) 13 ML DHP, and (c) 1 ML PQ deposited on top of a thin, 4 ML pentacene film. (d-f) Electric force microscopy (EFM) surface potential images of charge trapping in transistor channels with 4 ML pentacene after application of (d) -5 V, (e) -15 V, and (f) -40 V to the gate for two minutes. (g-i) Corresponding AFM images, taken before EFM experiments. The yellow arrow represents the direction of each line scan and the red arrow shows the direction of the overall scan progress. Stars mark the locations where the trap-clearing data presented in Figure 4.9 was gathered. Charge does not accumulate in the source and drain electrodes, visible as blue regions in the left and right portions of the EFM images. Charged traps are expected to form in the channel between the electrodes and are visible as regions of positive surface potential. In (e) and (f), the traps are scattered and non-uniform, but in (d) trapping is uniform throughout the channel, as we would expect for traps arising from the blanket-deposited precursor (decrease in voltage from top to bottom is due to slow trap-clearing during the scan.)

throughout the transistor channel (Figure 2.3d). This unprecedented uniform trapping everywhere in the transistor channel is clear evidence for the presence of a trap-precursor in the channel. The change in potential from top to bottom of the scan is due to traps clearing over the course of the scan, *not* an overall trapping “hot spot” in the transistor channel: each line scan in the image proceeds from left to right (yellow arrow) and the overall progress of the scan is from top to bottom (red arrow). The lateral nonuniformities in trapping magnitude within the channel can be attributed to variations in coverage (Figure 2.3g). Note that this level of trapping required only a -5 V gate bias.

The 4 ML P + 13 ML DHP sample has traps scattered throughout the transistor channel (Figure 2.3e), very different from the uniform trapping seen with the PHO precursor. This degree of trapping, which arose from a -15 V gate bias, is similar to that seen in 4 ML P alone with a -15 V gate bias (Fig. 2.10) and also similar to that seen in 4 ML P + 1 ML DHP (Figure 2.11). The 4 ML P + 1 ML PQ shows very little trapping (Figure 2.3f) even with a -40 V gate bias; these traps are clearly related to major topographic defects (Figure 2.3i).

2.2.2 Results: Trap-clearing spectra

As discussed in the introduction, trap clearing in pentacene can be accelerated by illumination with visible light. Optical absorptions in both pentacene and the trapped species can speed up trap clearing. Measuring surface potential as a function of time at a trap site for different illuminating wavelengths can reveal these optical absorption peaks through the resulting enhanced rates of trap clearing.

In Figure 2.4 we sketch the relative energy levels of pentacene and PHO^+ and illustrate the two trap-clearing mechanisms (excitation of pentacene or excitation of a charged trap)

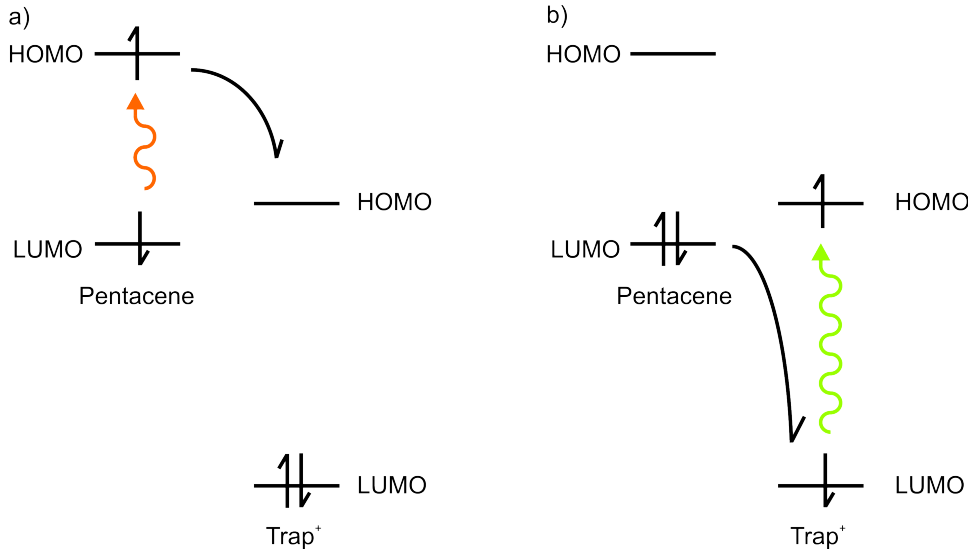


Figure 2.4: Sketches of (a) trap-clearing process due to pentacene absorption and (b) trap-clearing process due to PHO^+ absorption.

discussed below. The HOMO–LUMO energy level splitting is greater in PHO^+ than in pentacene [25]. Since PHO^+ is a hole trap, we expect the HOMO level to be relatively close in energy to the pentacene LUMO. Our sketches illustrate that charge transfer to excited PHO^+ (2.4 b) is expected to be more exothermic than charge transfer from excited pentacene (2.4a), which may explain the enhanced trap-clearing rate at 500 nm, where PHO^+ absorbs. However, exothermicity is not the only factor leading to fast electron transfer, and our calculations do not address electron-transfer reorganization energy or orbital overlap. We also note that these general sketches do not show absolute energy level alignment between pentacene and PHO^+ , nor can this information be obtained from our trap-clearing data. We can only sketch a general picture of energy level alignment, observing that shifting the relative energies up or down still results in the same relative exothermicities of trap-clearing.

A representative set of trap-clearing surface potential transients (36 in all, one for each wavelength investigated) is shown in Fig. 2.5. Each plot represents the surface potential (V) over 1200 seconds above the same trap location. This data was taken from trapped charge in the pentacene + PHO transistor. Different rates of trap-clearing are clearly evident for

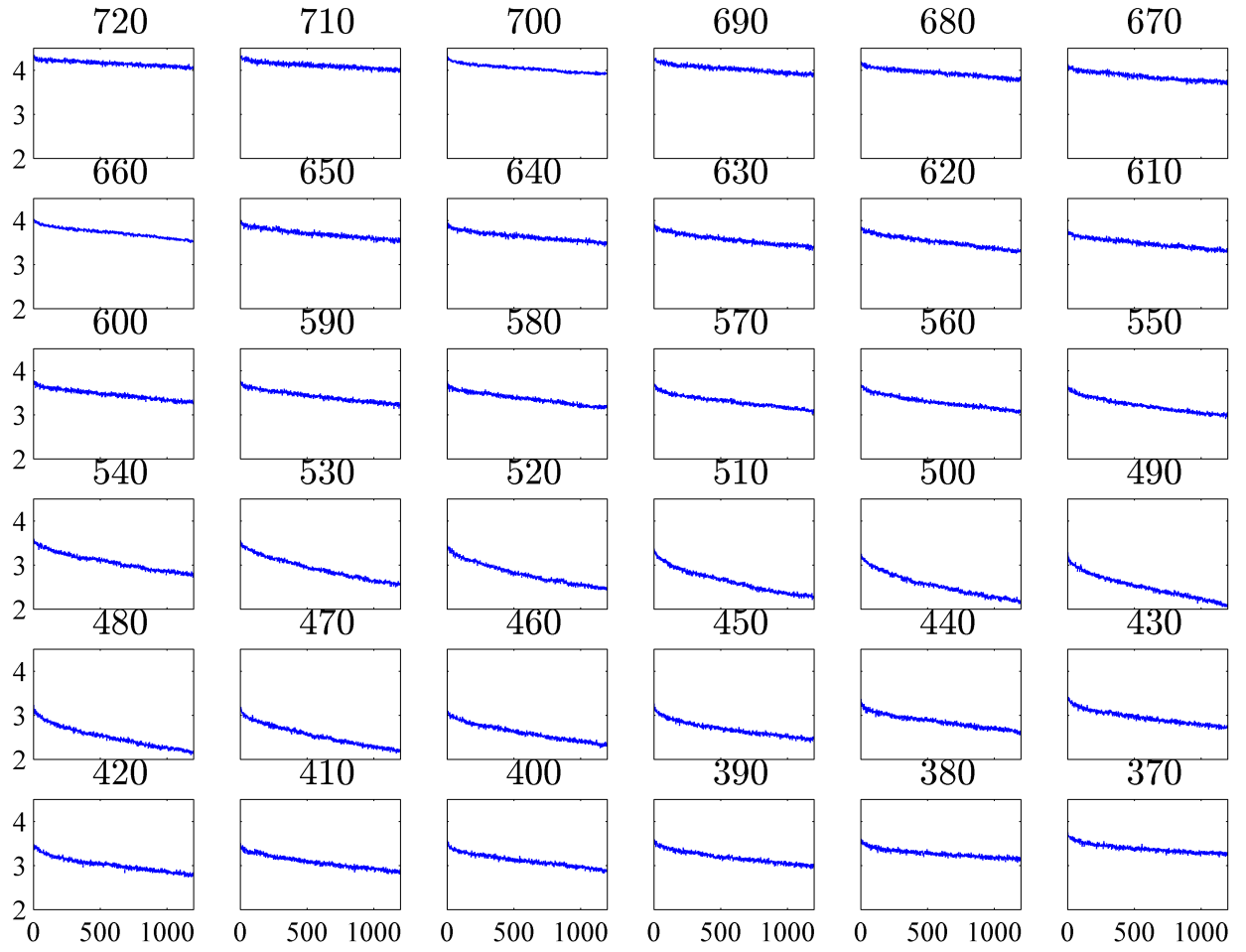


Figure 2.5: A sample set of decay transients [Contact potential (V) vs. time (s)] for charged trap clearing in the PHO-layered device. Each plot represents the data taken with a single wavelength of illumination; plots are titled with this wavelength (nm).

different illuminating wavelengths.

Choosing the appropriate fitting procedure for this data was critical because these decays contain information about the trap-clearing mechanism(s) at play. Fitting the surface potential decay transients to only a single exponential yielded poor results, showing no trend vs. wavelength and large error bars. This is not surprising given that the trap decay is too slow for the sample to reach a common “fully cleared” potential at every wavelength. We can understand this behavior mathematically by considering the expression needed to fit a

single exponential decay, Equation (2.1), where ϕ_i is the initial surface potential and ϕ_f is the final, “fully cleared” surface potential. Expanding Equation (2.1) yields Equation (2.2), which would describe the slope of a line approximating a very slow exponential decay.

$$\phi(t) = \phi_f + (\phi_i - \phi_f)e^{-kt} = \phi_i e^{-kt} + (1 - e^{-kt})\phi_f \quad (2.1)$$

$$\phi(t) \simeq \phi_i + (\phi_f)kt \simeq \phi_i + (\phi_f k)t \quad (2.2)$$

The fundamental ambiguity in Equation (2.2) lies in the fact that differences in either ϕ_f or k can alter the slope. If only short-time data is recorded, ϕ_f and k cannot be determined independently. Since the trap-clearing behavior that we measure here is so slow (hundreds of seconds per transient), measuring times long enough for independent determination of ϕ_f and k at 36 wavelengths cannot be practically achieved.

To address this issue, we consider these decays as a sum of two exponentials:

$$\phi(t) = \phi_i - rt + \Delta\phi e^{-k_{\text{exp}}t} \quad (2.3)$$

where we have assumed one of the exponential decays to be very slow compared to the measurement time. In writing Equation (2.3), we have replaced the $\phi_f k$ term in Equation (2.2) with the slope r . As we later discuss, this separation of the potential decay into a fast and a slow term implies that at least two different mechanisms are responsible for charged trap-clearing in our samples; we will show that the fast exponential decay is mostly light-independent, while the slow (approximately linear) decay is very light-sensitive.

To separate these decays in practice, we fit the later two-thirds of the data to the first two terms in Equation (2.3). Subtracting this best-fit line, the data decayed to zero and was fit to the third term in Equation (2.3), with $\Delta\phi$ the change in potential due to the fast exponential component and k_{exp} the exponential decay rate. This line-subtraction procedure effectively separates the trap-clearing behavior at short times (fast, light-insensitive, exponential decay) from the behavior at long times (slow, light-sensitive, linear decay).

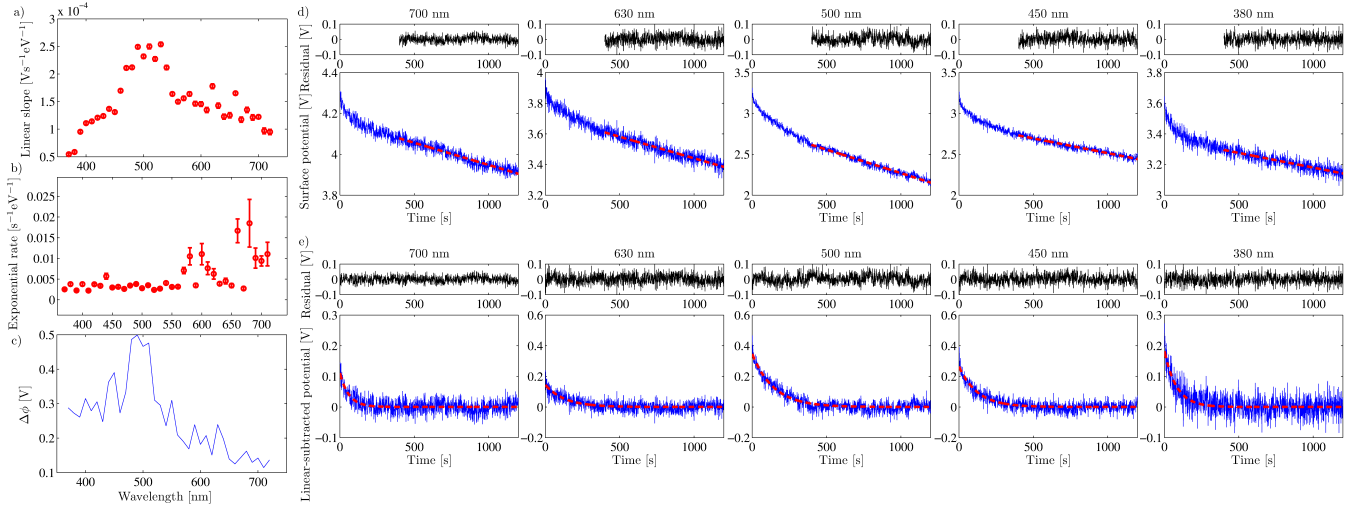


Figure 2.6: We demonstrate our fitting procedure using this sample set of transients at various wavelengths for charged trap-clearing in the PHO-layered device. The last two-thirds of the decay transient is fit to a line and the best-fit line is subtracted from the entire transient. The resulting decay curve is fit to a single exponential function. The rates of these two processes (slow linear and fast exponential) are normalized to the energy of the illumination and plotted vs. wavelength in (a) slow linear decay, displayed in units of $V s^{-1} eV^{-1}$, and (b) fast exponential decay, in units of $s^{-1} eV^{-1}$. The difference between the initial potential and the y-intercept of the best-fit line is plotted in (c) as $\Delta\phi$ vs. wavelength. The apparent variation in $\Delta\phi$ vs. wavelength is likely an artificial measure of device history. Sample fits and residuals for various wavelengths are shown for the linear fit in (d) and for the exponential fit to the linear subtracted data in (e).

The fitting procedure is summarized in Figure 2.6 for the 4 ML P + 1 ML PHO sample. Different surface potential decay speeds (trap-clearing rates) are clearly evident for different wavelengths of illumination. The wavelength dependence of the linear slopes and exponential rates is readily extracted and plotted. Note that in Figure 2.6a-b, we have normalized the slopes and rates by dividing by the energy of the illuminating wavelength in eV. This correction converts the units of the experiment, which was performed at constant incident power, into units that reflect the photon-dependence of the trap-clearing process.

We also plot $\Delta\phi$ vs. wavelength in Fig. 2.6c. The wavelength dependence of this value would be of interest if it represented the amount of surface potential drop due to the exponential decay. However, the traps are not completely cleared during the experimental

period of single-wavelength illumination, so this drop appears relatively larger and larger as the experiment progresses and the traps are filled closer to saturation. $\Delta\phi$, the difference between the initial surface potential ϕ at $t = 0$ s and the y-intercept of the best-fit line used for the later portion of the decay, is plotted vs. wavelength in Figure 2.7 for all the samples investigated. We report this data to emphasize that under our experimental conditions, $\Delta\phi$ does not independently represent the potential drop due to the exponential portion of the decay. Instead, as we discussed, this quantity is likely influenced by both the exponential decay and the relative saturation of the charged trap.

The results of all the trap-clearing experiments are summarized in Figure 4.9. All slopes (Figure 4.9c,e,f) are normalized to the energy of the illuminating wavelength in eV, as in Figure 2.6; note that the rate plotted in Figure 4.9d is *not* normalized, for direct comparison with the dark trap-clearing rate. The slow linear slopes for trap-clearing in the 4 ML P + 1 ML PHO are plotted as a function of wavelength in Figure 4.9c. The red and blue spectra represent detrapping experiments performed at two of the several different locations studied in the sample; they agree well. The slow portion of the P + PHO trap-clearing shows a large peak at 500 nm and two smaller features at 660 and 620 nm.

In contrast, the fast exponential rates for the P + PHO sample trap-clearing plotted vs. wavelength in Figure 4.9d do not show a rate enhancement at 500 nm. Instead, the exponential rates are enhanced only at wavelengths where pentacene absorbs. After the light-dependent experiment, a dark decay transient was collected; this decay was exponential and had no linear component. The dark rate for the P + PHO sample is plotted as the dashed line in Figure 4.9d. However, the P + PHO sample was the only one to show a clear wavelength dependence in the exponential portion of the decay. The fast rates are significantly above the dark rate at 630 nm, but the rate enhancements near 675 nm may not be significant when data taken at multiple locations is compared.

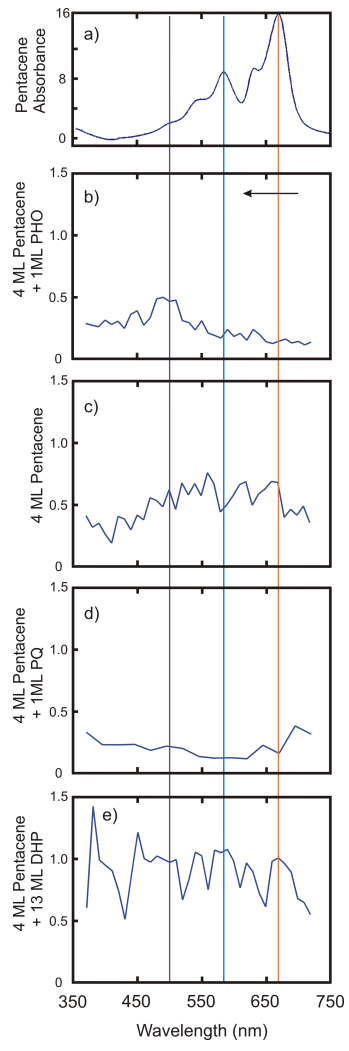


Figure 2.7: (a) Absorption spectrum of pentacene. (b-f) Change in surface potential (V) due to exponential decay as a function of wavelength (nm). These values are obtained by subtracting the y-intercept of the linear-fit from the initial surface potential. This data is plotted for (b) 4 ML P + 1 ML PHO, (c) 4 ML P only, (d) 4 ML P + 1 ML PQ, (e) 4 ML P + 13 ML DHP. The black arrow in (b) represents the direction in which the wavelength was scanned in (b-e).

The slow linear slopes for trap-clearing in the 4 ML pristine pentacene are plotted in Figure 4.9e. This spectrum shows some finer features in the pentacene absorption region, but more importantly, it does not show a relatively large peak at 500 nm. Likewise, the slow linear slopes for 4 ML P + 13 ML DHP are plotted in Figure 4.9f; this spectrum strongly resembles the analogous pristine pentacene spectrum, and does not show a major peak at 500 nm. The sloping shoulder present at 500 nm in Figure 4.9e-f is consistent with minor sample aging during sample loading, as discussed below. The traps in the P + PQ sample did not show wavelength dependence in either the fast or slow parts of the decay.

We noted that the slow linear trap-clearing spectra are spatially reproducible in Fig. 4.9c. In Figure 2.9 we plot the exponential trap-clearing spectra from two locations in the P + PHO transistor channel. This comparison shows that the exponential rate enhancement of trap-clearing about 600 nm may be considered reproducible, but that there is probably no enhancement at shorter or longer wavelengths. It is unclear at this point whether or not the exponential decay in the P + PHO sample is related to an optical absorption in pentacene or to some other process.

2.3 Control samples

As a control, we measured the surface potential and topography on a 4 ML pentacene-only transistor sample (Fig. 2.10). The trap-clearing spectrum collected at the starred location is shown in Fig. 4.9e. Trapping in this sample is plainly nonuniform and related to the sample topography. As noted above, the magnitude and distribution of traps are comparable to the P + DHP sample; both EFM scans were taken after a 2 minute gate bias of -15 V. The region of highest surface potential in Fig. 2.10a is directly related to a region with obvious morphological defects, similar to the P + PQ case. This trap did not show any light

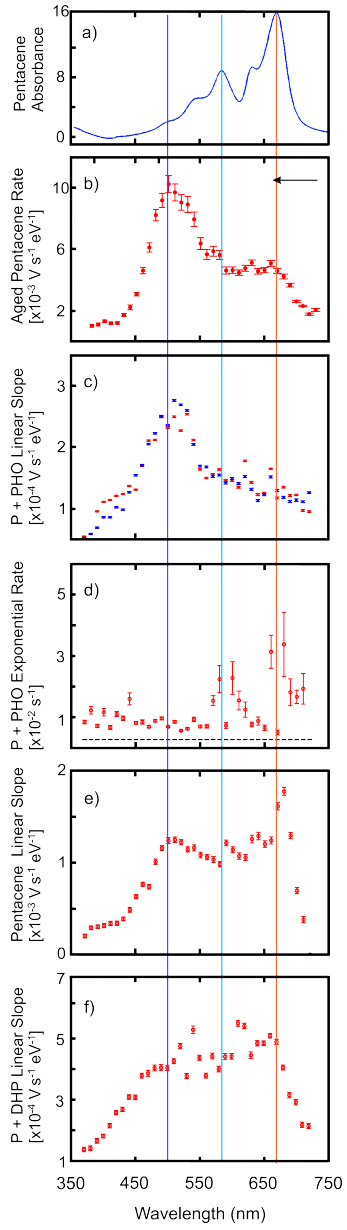


Figure 2.8: (a) Absorption spectrum of pentacene (a.u.) [25]. (b) Trap-clearing spectrum (exponential rates) in aged pentacene obtained by Luria *et al* [25]. (c) Slope of the slow linear decay vs. wavelength for traps in 4 ML pentacene + 1 ML PHO. The blue and red spectra are taken at different locations on the same sample. (d) Fast exponential rates vs. wavelength for traps in 4 ML pentacene + 1 ML PHO. With no illumination, the trap-clearing in 4 ML pentacene + 1 ML PHO is a single exponential decay; the associated decay rate in units of s^{-1} is plotted in black. Note that this trap-clearing spectrum is not normalized, for direct comparison with the dark rate. (e) Slope of the slow linear decay vs. wavelength for traps in 4 ML pentacene alone. (f) Slope of the slow linear decay vs. wavelength for traps in 4 ML pentacene + 13 ML DHP. The vertical colored lines are a guide to the eye for comparison with the absorption spectrum of pentacene. The arrow in (b) represents the direction of wavelength scanning for spectra (b-f).

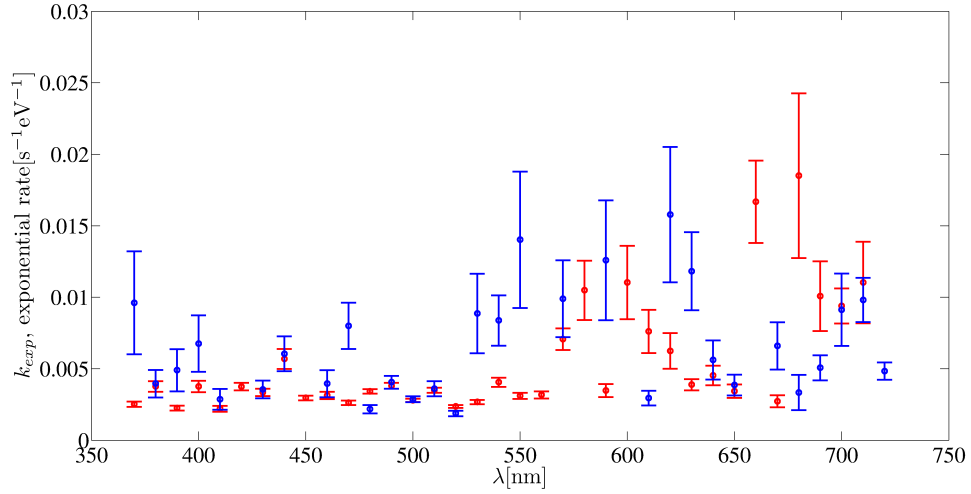


Figure 2.9: Reproducibility of exponential portion of wavelength-dependent detrapping in the P + PHO sample. These spectra were acquired at the starred locations in the P + PHO sample EFM image (see full text). These are the two best-resolved spectra.

sensitivity. Other traps of lesser magnitude are clearly related to regions of low coverage. This suggests that the analogous traps in the P + DHP sample may also arise from incomplete pentacene coverage, but this speculation cannot be verified since we cannot measure the pentacene morphology beneath the DHP layer.

We also prepared a transistor with 4 ML pentacene + a nominal 1 ML DHP as a control for comparison with the 13 ML thick DHP sample. In Fig. 2.11, we show the measured topography, corresponding EFM image, and trap-clearing spectrum for this control. Like the other samples layered with 1 ML defect and unlike the 13 ML DHP sample, the DHP layer is not distinctly visible in the topography image. The charge trapping distribution in this 4 ML P + 1 ML DHP sample was similar to that of the pristine pentacene and that of the 4 ML P + 13 ML DHP samples, suggesting that DHP is not a charged trap precursor in pentacene. Most importantly, the trap-clearing spectrum in this sample matches the spectrum observed in pristine pentacene *and* that observed in 4 ML P + 13 ML DHP, showing that the additional DHP in the 13 ML sample did not significantly change the chemical nature of the charged traps. We could not prove spectroscopically that this thin

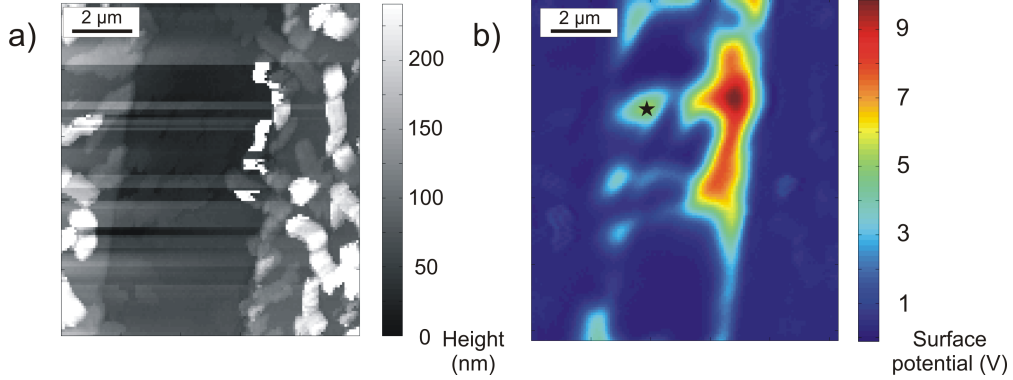


Figure 2.10: (a) AFM topography in nm for 4 ML pentacene only. (b) EFM data in volts for 4 ML pentacene only after a -15 V gate bias. The black star marks the location where the trap-clearing data for pentacene presented in Fig. 4.9e was collected. The traps with the greatest surface potential magnitude are light-insensitive and morphology-related.

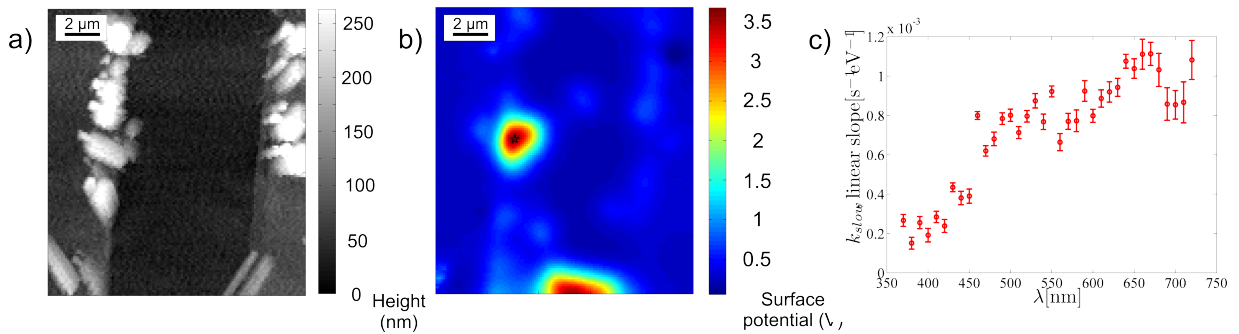


Figure 2.11: (a) Topography of 4 ML pentacene + 1 ML DHP sample. (b) EFM data for 4 ML pentacene + 1 ML DHP after -25 V gate bias. (c) Trap-clearing spectrum for the location marked with a star in (b). This spectrum qualitatively matches the spectra observed in both pristine pentacene and in the 4 ML P + 13 ML DHP sample (Fig. 4.9e-f).

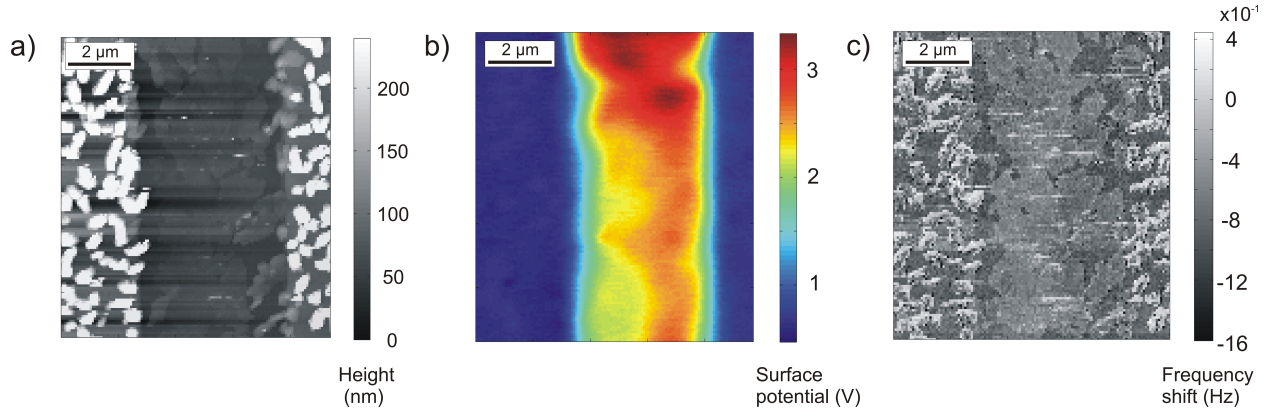


Figure 2.12: (a) Topography of 4 ML pentacene + 1 ML PHO sample. (b) EFM data for 4 ML pentacene + 1 ML PHO after -5 V gate bias. (c) Frequency shift (material phase contrast) image of 4 ML pentacene + 1 ML PHO sample.

layer of DHP was in the transistor channel; the layer was too thin to obtain an IR spectrum. Without this independent spectroscopic confirmation we could not conclude which charged species, PHO^+ or DHP^+ , was responsible for trapping in the 4 ML P + 1 ML PHO sample. From this point forwards we focus on the 13 ML thick DHP sample since it exhibits similar trapping behavior and we can prove that DHP is present.

I have mentioned that some traps seem to be due to low pentacene coverage, but in the pentacene + PHO sample, this is not the case. In Fig. 2.12, we show the relationship between pentacene/PHO coverage and surface potential by comparing the topography and cantilever frequency shift (material phase) alongside the EFM data. This direct comparison shows that some of the small, lateral variations in surface potential across the channel are clearly due to differences in material coverage. In contrast with the pentacene-only and P + DHP samples, the charge trapping is relatively *lower* in magnitude in regions of low coverage. The major regions of trapping in this sample correspond to the *presence*, not the absence of material in the channel.

2.4 Discussion

2.4.1 Discussion: Charge trapping maps

We first consider the interpretation of the electric force microscopy 2D images in Figure 2.3. If a defect species/trap-precursor blanket-deposited onto one of our pentacene transistor reacts to form charged traps, then uniform charge trapping throughout the transistor channel is expected in our EFM results. This trapping pattern was only present in the P + PHO sample (Figure 2.3d). The application of only a -5 V gate bias led to 3V of charge trapping, meaning that 60% of the holes induced in the channel became trapped — an enormous effect. This finding establishes PHO as a potent charged trap-precursor. Although mass spectrometry showed that both PHO and PQ were present on this transistor, PQ has been used as the dielectric in a pentacene transistor [76], is energetically not likely to form charged traps in pentacene [64], and the P + PQ transistor exhibits only morphology-defect-related trapping. Therefore, the trapping effect most likely arises from the addition of PHO. However, the proposed reaction of PHO with pentacene charge carriers to form charged defects leads to *two* different charged species: PHO⁺ and DHP⁺ (Figure 2.2c) [25].

In order to differentiate between the effects of these two charged species, the charge trapping in the P + DHP transistor must be considered. We used 13 ML DHP for this experiment because 1 ML DHP on 4 ML pentacene was not detectable with mass spectrometry, micro-Raman spectroscopy, or transmission IR spectroscopy, and it was crucial that we confirm the chemical identity of the precursor spectroscopically since DHP is predicted to yield only DHP⁺ upon reaction with pentacene charge carriers. The P + DHP transistor did not show readiness or uniformity of trapping, suggesting that the traps formed in this sample arise from a mechanism besides formation of DHP⁺. Tello *et al.* observed irreversible trapping in regions of pentacene film discontinuity [77]; the traps in the P + DHP sample may arise from

similar effect since 4 ML pentacene on our transistor substrates does not form a completely continuous film (see Fig. 2.10), although we cannot be certain of this since the thick layer of DHP obscures the pentacene morphology in our AFM measurement. Nevertheless, the trapping observed in the P + DHP transistor is not consistent with traps arising from a blanket-deposited trap-precursor. This strongly suggests that PHO⁺ is responsible for the trapping induced by addition of PHO to pentacene, and that DHP⁺ is not.

2.4.2 Discussion: Trap-clearing spectra

The results of the trap-clearing spectra, Figure 4.9, support the assignment of PHO⁺ as the chemical trap species and yield further evidence for multiple trap-clearing mechanisms in pentacene [25]. First, we consider the wavelength dependence of the slow, linear portions of the decay transients (Figure 4.9c,e,f). Consistent with our interpretation of the EFM data, only the P + PHO sample (Figure 4.9c) exhibited strongly enhanced trap-clearing rates at 500 nm. We attribute this rate enhancement to the excitation of the charged trap species, followed by neutralizing charge transfer from pentacene [25]. This behavior was reproducible in multiple locations in the transistor channel, consistent with the trapping uniformity implied by the EFM data. Furthermore, the peak at 500 nm in the P + PHO trap-clearing spectrum reproduces both the peak observed by Luria *et al.* in aged pentacene (Figure 4.9b) and the TD-DFT calculated absorption spectrum of PHO⁺ (Figure 2.2b) [25]. PHO⁺ is therefore likely both the cause of the charge trapping we observe and the electronically active degradation defect in aged pentacene.

In contrast, the P + DHP (4.9f) trap-clearing spectrum strongly resembled that of freshly deposited pristine pentacene (4.9e). Instead of a dramatic rate enhancement at 500 nm, both of these spectra have a “shoulder” at or near 500 nm, which we attribute to the presence of a trace amount of PHO⁺ in the samples. A small amount of pentacene oxidation in such

thin films is not surprising since the samples were all briefly exposed to ambient conditions while they were loaded into our custom AFM/EFM microscope. These spectra support our assertion that DHP^+ is not a chemical charged trap in pentacene. The P + PQ sample did not show any wavelength dependent trap-clearing behavior, consistent with non-chemical trapping. Other mechanisms, such as grain boundaries or morphology defects, may be at play.

Besides the feature at 500 nm, the slow-portion trap-clearing spectra (Figure 4.9c,e,f) exhibit some fine structure at longer wavelengths. We tentatively assign these features to enhancements in trap-clearing rate due to excitation of pentacene leading to excited-electron transfer that neutralizes the charged trap species. The trap-clearing spectra thus provide evidence for the operation of both proposed light-induced trap-clearing mechanisms (excitation of pentacene or of the charged trap species, followed by neutralizing charge transfer to the trap). The larger magnitude of the peak at 500 nm implies that excitation of PHO^+ is more effective than excitation of pentacene in initiating trap-clearing. Although this rate enhancement is qualitatively reasonable since the charge transfer to excited PHO^+ is expected to be more exothermic, as discussed above, we caution that the rate of electron transfer also depends on reorganization energy and an orbital overlap integral, the calculation of which are beyond the scope of this work. We further note that this charge transfer is only the first step in fully stabilizing the charged defect (to return to PHO , the reactions in Figure 2.2c must be reversed).

A fast, exponential decay component is observed in all the samples, but only in the P + PHO sample was this component wavelength-dependent. The P + PHO sample had enhanced exponential decay rates at wavelengths where pentacene absorbs (see Fig. 4.9d and Fig. 2.9). This is puzzling because if the exponential component of the trap-clearing is due to pentacene absorption, we would expect to see the same pentacene-related wavelength depen-

dence of the exponential rates in *all* the samples, not just one. In contrast, the exponential decay component does not depend on illuminating wavelength in the pentacene-only, P + DHP, and P + PQ samples.

This fast (a few tens of seconds), wavelength-independent decay cannot be attributed to trap clearing via thermal excitation of pentacene, which is expected to be very slow (many hours) [47]. Trap-clearing in intergrain traps has been shown to be light-insensitive, but the time scale for intergrain trap-clearing is much slower (greater than 24 hours) than the fast exponential clearing we observe [77]. Recently, evidence has been reported for proton migration into SiO₂ [78, 79] and for hole states in amorphous dielectrics [80]; trap-clearing of charges near the surface *in* the dielectric might explain the light-independent fast clearing we observe in these samples.

However, none of these cases explains why only P + PHO would exhibit a pentacene-absorption-dependent exponential decay. One possibility could be that there really is an additional and distinct fast trap-clearing mechanism in this sample. Perhaps PHO accepts electrons from optically excited pentacene more readily in some configurations or local environments than others; a scenario like this could yield two light-sensitive trap-clearing processes. At this point, it is unclear whether or not a third trap-clearing mechanism (beyond optical absorption by pentacene or the charged trap species) is needed to fully explain the fast single-exponential decay portion of the data.

2.5 Deposition control experiments

2.5.1 NMR

First, to be sure that PHO and DHP did not break down when exposed to the high temperatures required for deposition, I compared the ^1H NMR spectra of material recovered from the evaporator crucible post-deposition with the corresponding spectra of the fresh material. ^1H NMR spectra were measured for PHO and DHP at 499.76 MHz and 599.50 MHz, respectively. 16 scans of 2 seconds each with a 1 second relaxation decay were acquired for each sample, and the final spectra were zero-filled to 32k or 64k data points. An exponential window function (line broadening) of 0.3 to 1.0 Hz was applied prior to Fourier Transform. Chemical shift values are referenced relative to 7.26 ppm (CDCl_3). Peaks for PHO and DHP are listed in section [2.6.1](#).

^1H NMR data for the trap precursors PHO and DHP, as-synthesized and after deposition, is shown in Fig. [2.13](#). Fresh PHO (Fig. [2.13a](#)) and PHO recovered from the crucible after deposition (Fig. [2.13b](#)) are essentially identical; the recovered PHO may contain slightly more PQ. However, as I have discussed, this should not affect the conclusions we draw from our study of pentacene + PHO since PQ does not act as a chemical trap. Likewise, the spectra for fresh DHP (Fig. [2.13c](#)) and DHP recovered from the crucible (Fig. [2.13d](#)) are nearly identical, demonstrating that the trap precursors do not degrade during deposition. Some PQ is present in the PHO both before and after deposition; this is not surprising since it is the starting material for the PHO synthesis. For both PHO and DHP, we found that no new chemical species appeared as a result of heating.

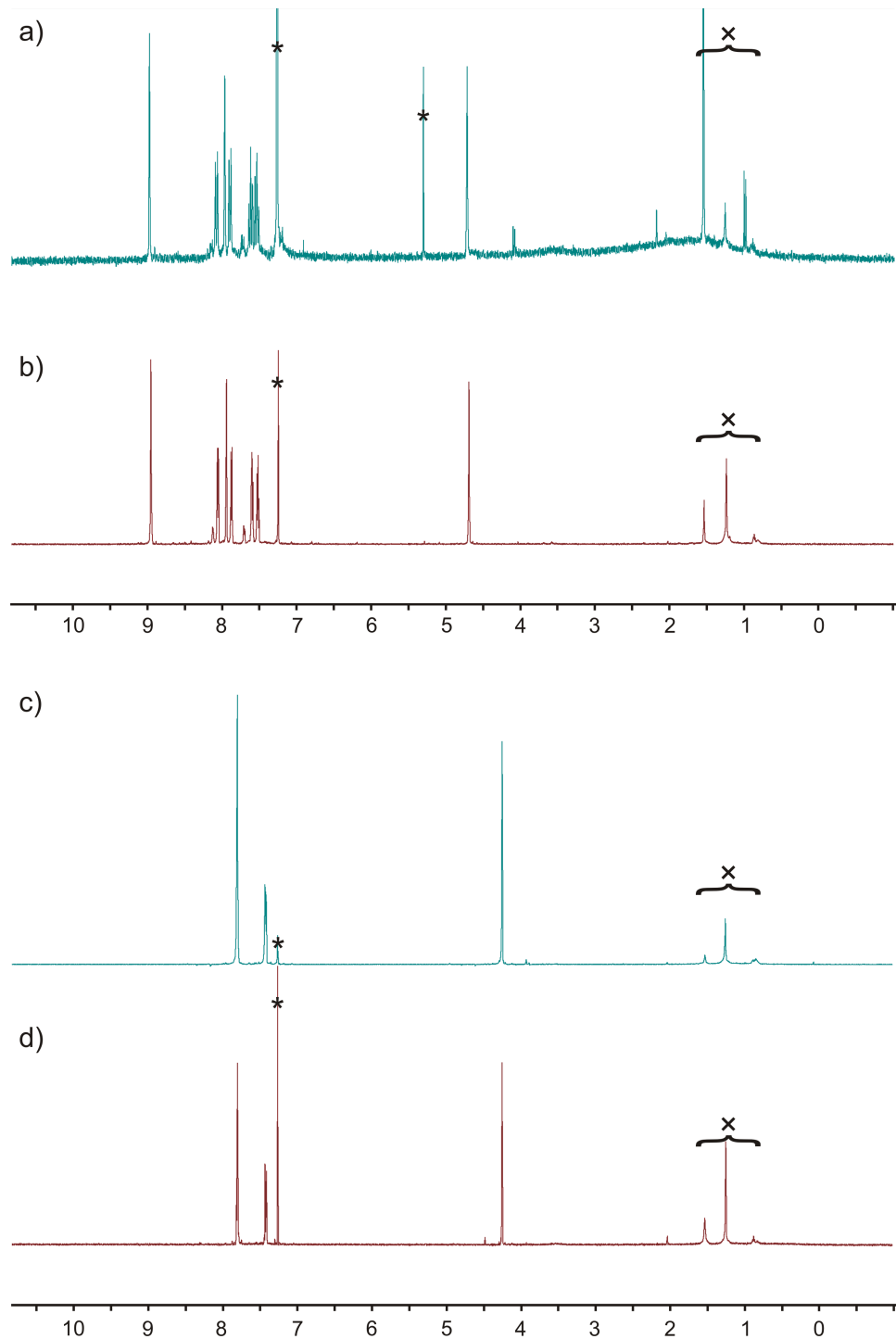


Figure 2.13: ^1H NMR spectra of (a) freshly purified PHO, (b) PHO recovered from the crucible after deposition, (c) freshly purified DHP, and (d) DHP recovered from the crucible after deposition. Starred (*) peaks are due to solvent impurities: CHCl_3 (7.26 ppm) and CH_2Cl_2 (5.29 ppm). The regions marked with an ‘ \times ’ contain peaks arising from residual solvents used in column chromatography (hexanes; ethyl acetate). Peaks for PHO and DHP are listed in section 2.6.1.

2.5.2 Mass spectrometry

Second, I considered the distribution and chemical identity of the trap-precursors on the sample surface. After AFM and EFM analysis, we performed laser desorption ionization (LDI) mass spectrometry on the active region of the sample. Mass spectrometry was performed using a MALDI Micro MX time-of-flight benchtop mass spectrometer (Waters) with a 10 Hz N₂ UV laser in positive ion reflectron detection mode. 50-70 individual spectra from each sample were combined for data analysis.

Mass spectrometry data from the active regions of the pentacene and the pentacene + PHO samples is shown in Fig. 2.14. The spectrum from the pentacene-only sample is quite clean (Fig. 2.14a), with no evidence of dimerization or other chemical decomposition. Consistent with the ¹H NMR data, the only chemical species present in the pentacene + PHO sample (Fig. 2.14b) were those expected: pentacene, PHO, and PQ. The presence of PQ, which is the starting material for PHO synthesis, is confirmed in the fresh PHO by ¹H NMR, so its presence is expected here as well. However, as we have seen, PQ is not responsible for the chemical charge trapping effect that we observe in the pentacene + PHO sample.

A limitation of my present work is that no further spectroscopy was performed on the P + PHO sample. This work therefore does not explicitly differentiate between the presence of PHO or its tautomer (pentacene with a central –OH group) on the sample surface. However, since both oxygenated defects are expected to form PHO⁺, our conclusions regarding the charged defect species are not affected [59].

In the case of the DHP-layered sample, the AFM topography clearly shows that a trap precursor layer extends throughout the transistor channel. However, mass spectrometry was unable to confirm that the deposited material was DHP. Since the chemical identity of this

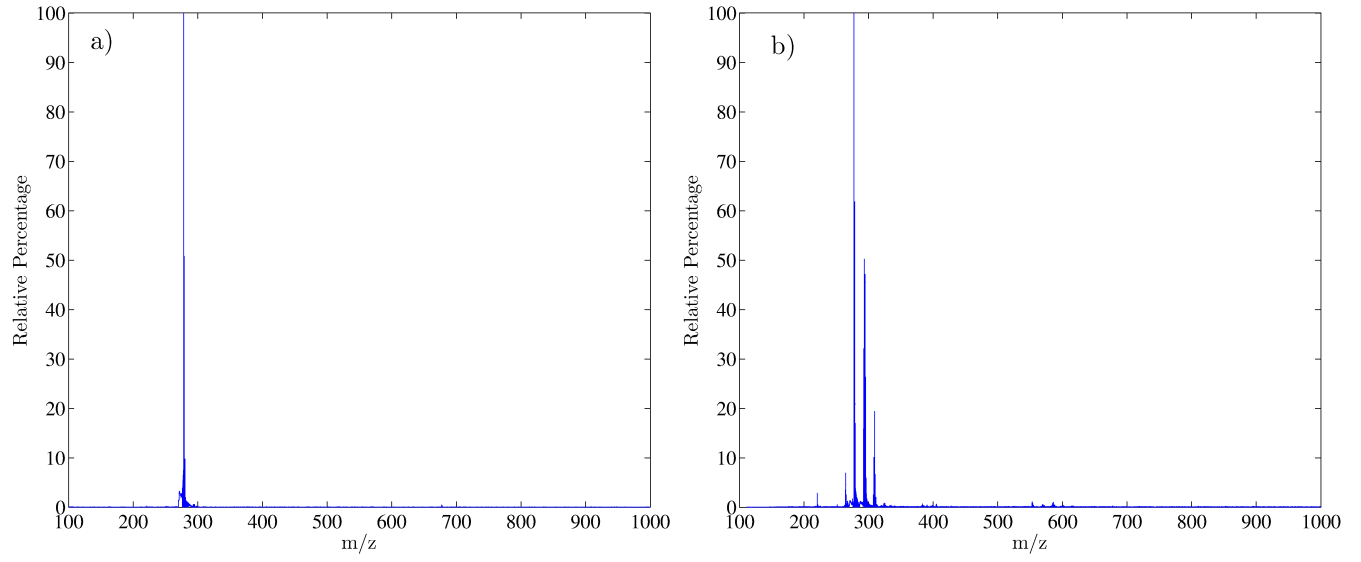


Figure 2.14: Mass spectrometry data for (a) 4 ML pentacene on bottom-contact transistor substrate and (b) 4 ML pentacene and 1 ML PHO on bottom-contact transistor substrate. Note the presence of pentacene ($m/z = 278$) in both spectra, and the additional presence of PHO ($m/z = 294$) and PQ ($m/z = 308$) in (b). Based on the charge trapping and trap clearing data for the PQ-layered device, PQ is not responsible for the chemical trapping in the PHO-layered device.

precursor is crucial in the interpretation of the P + PHO trapping results (Figure 2.2c-d), I collaborated with the Hines group to perform infrared spectroscopy on the co-deposited P + DHP transistor. Additional characterization techniques were not performed on the P + PQ sample since its codeposition with pentacene is well established, and it is not expected to break down under deposition conditions [64].

2.5.3 Infrared absorption spectroscopy

To identify infrared transitions characteristic of P and DHP, 4 ML (6 nm) of pentacene, 10.7 ML (16 nm) of DHP, or sequential layers of the two materials (4 ML pentacene + 10.7 ML DHP) were deposited on a 520-nm-thick thermal oxide grown on 500- μm -thick, single-side-polished, *n*-type Si samples. It was important that the silicon was not too heavily doped;

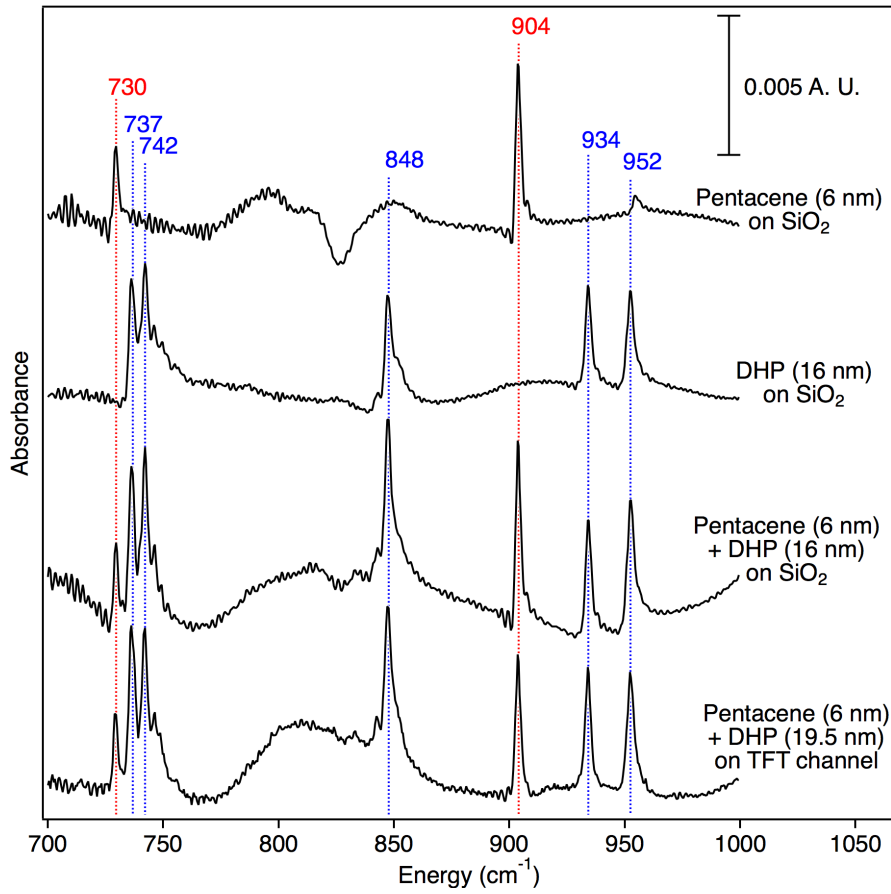


Figure 2.15: Infrared absorption spectra for, from top to bottom: 4 ML pentacene on SiO₂; 10.7 ML DHP on SiO₂; 4 ML pentacene + 10.7 ML DHP on SiO₂; 4 ML pentacene + 13 ML DHP on bottom-contact transistor substrate. The vertical dotted lines mark the characteristic transitions for pentacene (red; 730 and 904 cm⁻¹) and DHP (blue; 737, 742, 848, 934, and 952 cm⁻¹).

in highly-conductive silicon, the dopants block infrared transmission. Infrared spectra of an approximately 2.5 mm × 6 mm region of each sample were obtained at normal incidence and 1 cm⁻¹ resolution in transmission mode with a nitrogen-purged FTIR spectrometer equipped with a mercury-cadmium-telluride detector. The reported spectra consist of 2000 coadded scans referenced to spectra of a similarly prepared, film-free oxidized sample. Interference fringes in the spectra were removed computationally [81].

Infrared spectra of transistor structures were taken in a similar fashion, with the infrared

radiation only probing the active region of the device. This was ensured both by the design of the sample holder as well as the reflective nature of the 35-nm-thick gold electrodes. The reported spectra were referenced to a similarly prepared, film-free transistor structure. Codeposition of P and DHP is confirmed by the good agreement between the transition intensities and energies in infrared spectra of the active-region of the transistor structure and similarly prepared neat films, as shown by Figure 2.15. We believe the DHP is deposited with no or minimal degradation; traces of “tetrahydropentacene” (alternating aromatic and aliphatic rings) and 5,14-dihydropentacene may also be present. As our EFM data shows, none of these species appears to be an active trap precursor since uniform trapping is not observed in the DHP sample.

The thin films displayed a number of characteristic absorption bands in the 700-1000 cm^{-1} energy range, as shown by Fig. 2.15. Pentacene films, whether alone or in combination with DHP, displayed two moderately intense bands at 730 and 904 cm^{-1} . According to Prof. Melissa Hines, these transitions are assigned to the out-of-plane (oop) bend vibration of CH bonds on the outer rings (hydrogen quartet) and inner rings (hydrogen solo) of pentacene, respectively, by comparison to theoretical calculations [82, 83]. Analogous transitions are observed at 731.3 cm^{-1} and 899.9 cm^{-1} in matrix-isolated pentacene [84].

The spectra of the DHP films were more complex, displaying at least five moderately strong bands at 737, 742, 848, 934, and 952 cm^{-1} . The vibrational spectrum of DHP in this region has not been previously reported or simulated. The bands at 737 and 742 cm^{-1} were assigned by Prof. Hines to predominantly oop bend vibrations of quartet hydrogens in analogy to the pentacene spectrum and trends in the spectra of polyaromatic hydrocarbons (PAHs) [85]. However, the calculated IR absorption spectrum of DHP (see below, and Fig. 2.16) suggests that only the band at 737 cm^{-1} can be definitively assigned to the DHP quartet bend vibrations. The band at 742 cm^{-1} may indicate the presence

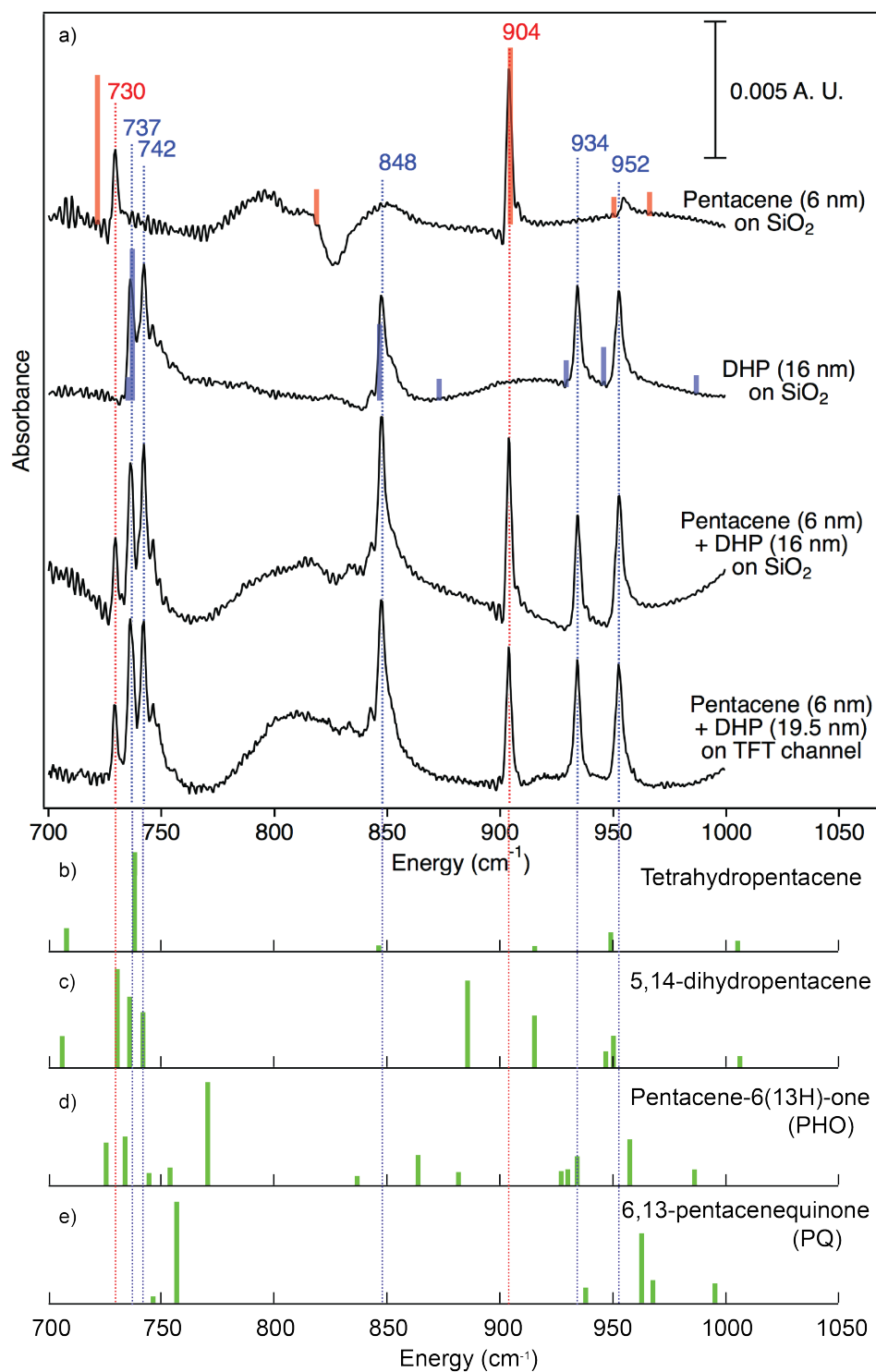


Figure 2.16: (a) Experimental infrared absorption spectra for pentacene and DHP, as shown in the text. Red and blue bars represent the calculated infrared absorption peaks for pentacene and DHP, respectively. (b-e) Calculated infrared absorption spectra for tetrahydropentacene (alternating aromatic and aliphatic rings), 5,14-dihydropentacene, PHO, and PQ, respectively.

of an impurity in the DHP. Based on the calculated bands for the alternating aromatic-aliphatic “tetrahydropentacene” defect, the main impurity we would expect based on our synthetic route to DHP, our data does not exclude this species; however, DHP is a much better match in terms of relative intensities [86]. The calculated spectrum for an asymmetric 5,14-dihydropentacene reproduces the band at 742 cm^{-1} , but also includes several bands at higher energy that are not observed experimentally. The calculated spectra for oxygenated pentacene defects PHO and PQ are not good matches for any of the experimentally observed peaks in the pentacene + DHP infrared absorption spectrum. We conclude that the band at 737 cm^{-1} arises from DHP, and that there may be some tetrahydropentacene and asymmetric 5,14-dihydropentacene present in the film. The bands at 934 and 952 cm^{-1} were assigned to predominantly oop bend vibrations of solo hydrogens by analogy to similar changes between the calculated spectra of anthracene ($\text{C}_{14}\text{H}_{10}$) and pentacene [82]. This assignment is supported by the calculated IR absorption spectrum for DHP. The band at 848 cm^{-1} was assigned by comparison with the calculated spectrum of DHP to a complex motion that combines the oop bend vibration of the four hydrogen atoms adjacent to the central aliphatic ring with a moderate CH_2 rocking motion. No similar band was observed in the calculated IR spectra of any of the impurities discussed here, so we consider this strong absorption to be diagnostic of the presence of DHP in our sample.

Absorption bands associated with CH stretch vibrations were not observed, although a broad structured band in the $3000\text{-}3100\text{ cm}^{-1}$ range was observed in previous studies of pentacene thin films taken in the more sensitive multiple-internal-reflection (MIR) geometry [87]. The broad nature of this band likely prevented detection. An intense absorption band near $1000\text{-}1200\text{ cm}^{-1}$ (not shown), characteristic of SiO_2 phonons, [88] was also observed.

For comparison with the experimental IR data, IR spectra for pentacene and dihydropentacene were calculated by Prof. Richard Hennig using Gaussian 09 [89], [90] with the B3LYP

functional [91] and the 6-311G basis set. The basis set was converged for the IR frequencies in the range of 700 to 1000 cm⁻¹. For the 6-311G basis the relative position of the peaks is converged to within 5 cm⁻¹. Molecular geometries, ground state energies and IR frequencies were found by optimizing single molecule geometries with the 6-311G basis. To approximate the chemical environment of the pentacene molecular solid, the calculations were performed with solvation in a dielectric medium, using the Polarizable Continuum Model [92] with a dielectric constant of 4.82, as suggested by previous calculations [93]. Figure 2.16b-c shows the calculated IR spectra for the pentacene and dihydropentacene for the energy range of 700 to 1050 cm⁻¹. The intensities and frequencies of the calculated IR modes of both molecules closely agree with the measured IR spectra. The largest deviation in IR intensity occurs for dihydropentacene for the doublet of peaks at 737 and 742 cm⁻¹; the calculation shows a larger difference in the IR intensity of these peaks compared to the measurement. This may be due in part to preferred molecular orientations in the sample. We would also like to thank Dr. Alessandra Ricca and the group from the NASA Ames Research Center for their calculation of the IR spectrum of DHP; this spectrum was calculated using the B3LYP functional and the 4-31G basis set and was made available on the PAH IR spectral database in October 2012.

2.6 Experimental

2.6.1 Sample Preparation

Pentacene for deposition was obtained from Kintec, HK (triple sublimed grade). 6,13-pentacenequinone (PQ) for deposition and for synthesis of pentacen-6(13H)-one (PHO) was obtained from Aldrich. Pentacene used for synthesis of 6,13-dihydropentacene (DHP) was

obtained from VWR International. All commercially obtained chemicals were used without further purification.

Synthesis of pentacen-6(13H)-one (PHO) was based on procedures from the literature: PQ was heated to reflux in dry THF with sodium borohydride to yield 6,13-dihydroxypentacene (13% after column chromatography) [94]; 6,13-dihydroxypentacene was then heated to reflux in 100:1 THF:HCl to give PHO (18%) [95]. ^1H NMR (CDCl_3 , 500 MHz): δ 8.97 ppm (s, 2H); 8.07 ppm (d, 2H); 7.96 (d, 2H); 7.89 ppm (d, 2H); 7.61 ppm (t, 2H); 7.53 ppm (t, 2H); 4.71 ppm (s, 2H). Monitoring a sample of the purified PHO by thin film chromatography over the course of a day revealed the appearance of an unidentified second species. The PHO used in these experiments was therefore prepared fresh on the day of sample preparation. The freshly purified compound was stored under argon and cold for less than 2 hours before being transferred to the glove box housing the evaporator for sample preparation.

Synthesis of 6,13-dihydropentacene (DHP) was based on procedures [86] and characterization data [96] from the literature. Pentacene was mixed with HI and glacial acetic acid and heated to reflux for 24 hours in dark under N_2 . The reaction was quenched with sodium bisulfite and DHP was separated from the reaction mixture by column chromatography (17%). ^1H NMR (CDCl_3 , 600 MHz): δ 7.82 ppm (t, 8H); 7.44 ppm (dd, 4 H); 4.27 ppm (s, 4H).

Bottom-contact transistor substrates were fabricated by thermally growing 315 nm SiO_2 on an *n*-type Si wafer (1-10 Ωcm) and patterning interdigitated gold source and drain electrodes (5 μm channel length, 150 cm channel length, 15 μm electrode width, 3×6 mm total active area) using standard photolithography techniques. The cleaning protocol for substrates is as follows: Bottom-contact substrates were rinsed with acetone and IPA, sonicated in acetone, and soaked in microposit remover fluid 1165 (Shipley) for at least 8 hours to remove the protective coating of photoresist; they were then rinsed with acetone and IPA

before undergoing 10 minutes UV-ozone cleaning and additional sonication in acetone and IPA. All substrates were then sonicated in nonionic detergent (Aquet), dried, and UV-ozone cleaned 10 minutes more.

Substrates were heated to 60 °C during PHO deposition and all pentacene depositions except for the pentacene + PQ trial and the IR control sample. Substrates were not heated for PQ or DHP deposition. Source material was resistively heated in a ceramic crucible to achieve deposition rates of approximately 0.1 Å/s. 60 Å (nominally 4 monolayers, 4 ML, measured by quartz crystal microbalance) pentacene was deposited first. For trap-precursor candidates PQ and PHO, ~1 ML (nominally 15 Å) trap candidate was deposited next; for DHP, ~13 ML (nominally 195 Å) was deposited on the pentacene film. Vacuum was broken and samples were exposed to the glove box N₂ atmosphere between deposition of pentacene and the trap-precursor in order to remove the pentacene-only samples and place clean substrates for trap-precursor-only controls.

2.6.2 Electric Force Microscopy (EFM)

Atomic force microscopy (AFM), EFM, and wavelength-dependent trap-clearing measurements were performed under high vacuum ($1\text{--}2\times10^{-6}$ mbar) with transistor source , drain, and gate grounded. Samples were briefly exposed to ambient light and atmosphere (less than 30 minutes) while they were loaded into the microscope. A Ti-Pt coated Si cantilever was used (MikroMasch, NSC18 series, resonant frequency $f = 75$ kHz, spring constant $k = 3.5$ N m⁻¹). Cantilever deflection was measured using a fiberoptic interferometer with operating wavelength 1310 nm. Frequency demodulation was achieved using a PLLPro AFM controller (RHK), providing a voltage output proportional to the cantilever frequency shift δf .

Bottom-contact transistor substrates with sequentially deposited pentacene and a trap-

precursor were characterized by tapping-mode AFM and EFM. Two-dimensional scan data (AFM and EFM) was processed in Matlab to produce images. For AFM scans, the background plane was adjusted to be flat and a threshold was applied to the most extreme topographical features for better contrast in the transistor channel. The resulting minimum topography value was subtracted from all the data points, rescaling the topography so that the new minimum was zero. For EFM scans, no processing was applied to the image.

Immediately prior to EFM measurements, traps were populated by applying a negative gate bias for two minutes; neither a gate bias nor a source-drain bias was applied during all AFM and EFM imaging. Modulated EFM was used to image surface potential (Figure 2.1b), and swept-voltage EFM was used to measure surface potential during trap-clearing experiments (Figure 2.1c) [28]. Traps were populated by applying a negative bias to the gate for 2 minutes; upon returning gate to ground, remaining trapped holes appeared as regions of positive surface potential.

In modulated EFM (used in Figure 2.1b), both an AC modulation voltage (ω , 2-3 V rms) and a DC potential were applied to the cantilever. The first (ω) and second (2ω) Fourier components of the cantilever frequency shift due to the modulation frequency were monitored by lock-in detection (Stanford Research Systems, 30 ms time constant, and Perkin Elmer, 50 ms, respectively) with a sensitivity of 1V. The first component of the cantilever frequency with applied AC and DC potential is related to the DC potential and the tip-sample contact potential through the relationship:

$$\hat{f}(\omega) = \frac{f_0 V_{T,AC}}{2k_0} \frac{\partial^2 C}{\partial z^2} (V_{T,DC} - \phi) \quad (2.4)$$

where f_0 is the cantilever resonance frequency, k_0 is the cantilever spring constant, $V_{T,AC}$ and $V_{T,DC}$ are the AC and DC components of the tip potential, $\partial^2 C / \partial z^2$ is the second derivative of tip-sample capacitance with respect to cantilever position, and ϕ is the tip-sample contact potential difference. The output of a PID (Stanford Research Systems SIM960 Analog PID

Controller, $P = -0.1$, $I = 80$ Hz, $D = 5 \times 10^{-4}$ sec) feeding back on the DC potential ($V_{T,DC}$) to nullify the first component of the frequency shift in Equation (2.4) is equal to the tip-sample contact potential as mapped in Figure 2.3. The cantilever was scanned in the plane 60 nm above the sample plane (topography is not followed).

In swept voltage EFM (used in Figure 2.1c), a series of DC potentials (usually -3 to 3 V) was applied to the cantilever and the cantilever frequency shift was measured at each point. This produced a parabolic frequency shift-tip voltage curve with a maximum where the applied voltage is equal to the tip-sample contact potential, through the relationship:

$$\delta f(V_T) = f_0 - \frac{f_0}{4k_0} \frac{\partial^2 C}{\partial z^2} (V_T - \phi)^2 \quad (2.5)$$

with f_0 the cantilever resonance frequency, k_0 the cantilever spring constant, V_T the cantilever tip potential, $\partial^2 C / \partial z^2$ the second derivative of tip-sample capacitance with respect to cantilever position, and ϕ the tip-sample contact potential difference. The surface potential was measured by extracting the maxima of these frequency shift-tip voltage parabolas. This process is quite slow compared to modulated EFM. Modulated EFM was used for 2D imaging. Swept-voltage EFM was used for measuring the surface potential over a single location over time (trap-clearing experiments).

In the trap-clearing experiments, the swept-voltage EFM measurement of the surface potential was repeated at 2 Hz for up to 1200 seconds, producing a surface potential decay transient. After measurement of the transient, traps were freshly repopulated by biasing the gate at -5 , -10 , -20 , or -40 V (PHO, DHP, pentacene, and PQ samples, respectively) for 120 seconds before beginning the next transient measurement. The charged traps in the PHO and DHP samples were so slow to clear that traps were further cleared by a white-light LED (10 seconds and 8 seconds, respectively) between transient measurements and before trap repopulation. This procedure did not yield a consistent initial surface potential for each measurement. If the traps are not sufficiently cleared by the single-wavelength light (or by

additional LED illumination), a different initial surface potential will be produced by the next gate bias.

A decay transient was measured for each of 36 wavelengths between 370 and 750 nm. The cantilever was maintained in position 60-120 nm (dependent on the sample topography) above the charged trap site under study during transient measurement. A “dark” spectrum was obtained for each sample by measuring the surface potential as a function of time without illumination. The magnitude of this dark decay rate is strongly dependent on when the scan is performed relative to the light-dependent trap-clearing experiment: if performed first, traps may not be fully saturated for the given gate voltage, resulting in an artificially fast clearing rate. The dark clearing data shown in Figure 4.9c was collected after the light-dependent experiment.

The light source for variable-wavelength illumination was a Dolan-Jenner Fiber-Lite with a 150W bulb (Ushio) connected to a scanning monochromator (Monoscan 2000, Micropack) and attenuator (Oz Optics). The sample was illuminated with visible light from a $50 \mu\text{m}$ fiber with numerical aperture 0.22 angled 30° away from horizontal towards and roughly $200 \mu\text{m}$ away from the cantilever tip. The illumination had a measured bandwidth of 5 nm and a measured power of $0.015 \mu\text{W cm}^{-2}$. We estimate the intensity of the illumination to be 0.05 mW cm^{-2} at the sample.

2.6.3 Trap-clearing spectra: data fitting

Trap-clearing data was processed in Matlab. As discussed in the results section (2.2.2), the later two-thirds of the data was fit to a line and the slopes were plotted vs. wavelength. Then, the best-fit line was subtracted from the raw surface potential decay data and the resulting data was fit to a single exponential. These rates were also plotted vs. wavelength.

Both fits were performed using a nonlinear least squares method in Matlab. The values of the fit parameters were checked by finding the minima of the χ^2 surfaces for each fit type. The 95% confidence limits for each parameter were established by first plotting $\Delta\chi^2 = \chi^2 - \chi^2_{\min}$ vs. fit parameter, where χ^2_{\min} is the minimum value of the χ^2 surface calculated with uniform error in the data, and then finding the values of the fit parameter where $\Delta\chi^2 = \chi^2(95\%, M = 2)$, the χ^2 value expected for 95% probability and 2 degrees of freedom in the fit.

2.6.4 Pentacene Device Characterization

Transistor characterization was performed under high vacuum in the same apparatus as AFM and EFM measurements with the cantilever far removed from the sample surface. Current-voltage characteristics were measured by varying the drain current from 10 V to -30 V and keeping source grounded. These measurements were repeated for sixteen gate biases spaced between 10 V to -50 V. Current-voltage curves for the control pentacene transistor used in this study are shown in Figure 2.17.

We expect low performance in our devices due to the bottom-contact geometry, untreated SiO_2 , and low material coverage. For the pentacene transistor used in this study, we observed a clear gating effect, but the device had nonlinear turn-on behavior (usually indicating poor contacts) and did not reach saturation. The low coverage required for our charge-trapping experiments is likely responsible for these non-idealities, especially the contact effects. Although neither the saturation nor the linear-mobility regime was achieved, we calculated the mobilities μ_{sat} and μ_{linear} and from these we estimate a hole mobility on the order of $10^{-4} \text{ cm}^2\text{V}^{-1}\text{s}^{-1}$ in our 4 ML pentacene device.

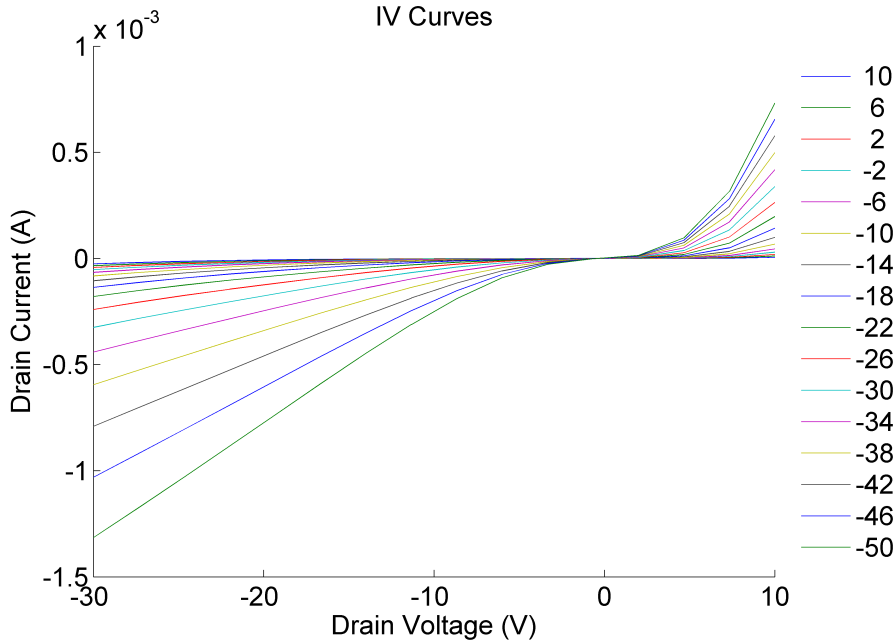


Figure 2.17: Current-voltage curves for the bottom-contact, 4 ML pentacene transistor used in this study. Gate voltage is indicated in the right hand legend.

2.7 Conclusions

In summary, we have layered thin pentacene films with pentacene trap-precursor candidates, imaged the trapped charge concentration in these samples, and detected light-dependent trap-clearing rates at selected sample locations with time- and wavelength-resolved electric force microscopy. We have demonstrated that PHO is capable of readily producing large charge trapping effects in pentacene that exhibit striking and direct verification of the predicted charge clearing spectrum [25]. These observations, coupled with the control experiments in DHP, strongly indicate that PHO^+ (and *not* DHP^+) is responsible for chemical, light-responsive charge trapping in pentacene thin film devices. The agreement between the trap-clearing spectra of the P + PHO sample and aged pentacene also strongly suggests that the trapping effects are the same, *i.e.*, PHO^+ is likely the charged defect that forms in aged pentacene devices. This result contradicts the general understanding of charged traps

in pentacene as arising from DHP or PQ, and is also surprising because DHP^+ is expected to be a thermodynamically more stable trap species than PHO^+ [59].

More generally, this result should be of interest in the design of new organic semiconductors. Strategies for developing new *n*-channel materials are strongly based in meeting specific electron affinities predicted to limit reaction with oxygen [97, 98]. For example, the growing family of naphthalene and perylene diimides are not expected to undergo degradation under atmospheric conditions, especially with electron-withdrawing core substituents to lower the LUMO level and stabilize the radical anion. However, positive threshold voltage shifts indicating charge trapping are still observed in these materials, and neither the chemical nature of this trapping nor the role of impurities due to degradation during deposition has yet been spectroscopically investigated [3, 99]. Our work demonstrates that in predicting and understanding air sensitivity, reactivity, and degradation-related charge trapping processes, thermodynamic considerations alone may not be sufficient. Our work also shows that EFM is a potentially useful tool in studying these issues.

2.8 Acknowledgements

I would like to thank Anthony Condo for acquisition of ^1H NMR spectra and assistance with mass spectrometry. Thanks to Kun Bao and Prof. Melissa Hines for assistance with collecting and processing the infrared spectroscopy data. This work made use of the soft matter characterization facility of the Cornell Center for Materials Research (CCMR) with support from the National Science Foundation Materials Research Science and Engineering Centers (MRSEC) program (DMR 1120296). A portion of this work was performed at the Cornell NanoScale Facility, a member of the National Nanotechnology Infrastructure Network, which is supported by the National Science Foundation (Grant ECS-0335765). I

acknowledge support from an NSF Graduate Research Fellowship and NSF-DMR 1006633. V. A. Pozdin acknowledges the support of the CCMR, NSF-DMR 1120296. J. L. Luria and J. A. Marohn acknowledge the support of NSF-DMR 1006633.

I prepared samples, gathered most and processed all of the AFM and EFM data, performed mass spectrometry and IR spectroscopy experiments, and coordinated the project. V. A. Pozdin provided instruction in substrate and sample preparation and prepared control samples. J. L. Luria gathered the P + PQ AFM and EFM data and provided instruction and assistance in gathering the rest of the AFM and EFM data. R. G. Hennig calculated the IR absorption spectra. M. A. Hines processed the IR spectroscopy data and assisted in its interpretation. C. A. Lewis synthesized the PHO and DHP used in this study. J. A. Marohn supervised the project and assisted with EFM data processing.

Text and figures in this chapter are reproduced from Ref. [13](#) with permission from John Wiley and Sons, license number 3637611365809.

CHAPTER 3

CHARGE TRANSPORT IN PERYLENE DIIMIDE DERIVATIVES

3.1 Introduction

Although a number of high-performing hole-transporting organic semiconductors are known, robust organic electron-transporting (n -channel) materials are also needed to realize complementary circuits and enable devices with high operating speeds and low power consumption. The family of perylene-3,4:9,10-tetracarboxylic diimides (PDIs) have relatively high n -channel mobilities compared with other small-molecule semiconductors and are well-known in transistor applications [3, 99–101]. PDIs can also serve as the electron acceptor in donor-acceptor photovoltaic systems [102, 103].

The Prof. Adam Braunschweig lab at the University of Florida is developing macromolecular self-assembled donor-acceptor systems for photovoltaics using custom-synthesized PDI derivatives [104, 105]. In collaboration with the Braunschweig lab, we set out to measure mobilities of these PDIs in field-effect transistors (FETs). In this chapter, we outline our attempts to fabricate working FET devices using these specialized PDIs. We attempted to measure bulk current-voltage curves for these custom high-LUMO PDIs (Section 3.2), and for a commercially available PDI derivative (PDIF-CN₂, Section 3.3). Bulk current-voltage curves were unsatisfactory measurements for mobility in each of these systems, leading us to explore methods for extracting local mobilities from scanning-probe experiments (Section 3.4) [30]. Since the charge injection barrier from gold into the Braunschweig high-LUMO PDIs was so large, we also investigated injection kinetics as a function of injection barrier lowering via gate voltage (Section 3.5).

The PDI derivatives (and their abbreviations) mentioned in this thesis are illustrated

in Fig. 3.1. The HOMO and LUMO levels for these derivatives are listed in Table 3.1. The HOMO and LUMO levels reported in the table for the custom-synthesized PDIs were measured by the Braunschweig group, using cyclic voltammetry versus ferrocene in CH_2Cl_2 with 0.1 M TBAPF₆ as the electrolyte. The reduction of dEO PDI is also reported in Ref. 105. The HOMO and LUMO levels for the commercially available PDIs (PDI-8, PDI8-CN₂, and PDIF-CN₂) are reported by Jones *et al.* from cyclic voltammetry (saturated calomel electrode, CH_2Cl_2 , 0.1 M TBAPF₆) [106]. We focussed attention on two materials: dEO PDI, a high-LUMO (predicted unstable) derivative synthesized by the Braunschweig group, and PDIF-CN₂, a commercial, air-stable PDI derivative.

Molecule	LUMO [eV]	HOMO [eV]	Source
dPyr PDI	-3.113	-4.759	Braunschweig group
dCH dPyr PDI	-3.451	-5.217	Braunschweig group
dEO PDI	-3.607	-5.392	Braunschweig group
dCH dEO PDI	-3.618	-5.096	Braunschweig group
dCH dBr PDI	-3.863	-6.109	Braunschweig group
PDI-8	-3.9	-6.3	Sigma Aldrich 663913 (CAS 78151-58-3)
– onset of stability to oxygen –			
PDI8-CN ₂	-4.3	-6.7	Polyera ActivInk N1200
PDIF-CN ₂	-4.5	-6.8	Polyera ActivInk N1100

Table 3.1: HOMO and LUMO levels for PDI derivatives mentioned in this thesis.

3.1.1 Scanning-probe microscopy of PDIs

Although scanning-probe experiments have routinely been used to evaluate PDI film topography, there is little precedent for applying scanning-probe microscopy to study charge transport in these materials. Palermo *et al.* used Kelvin-probe force microscopy (KPFM)

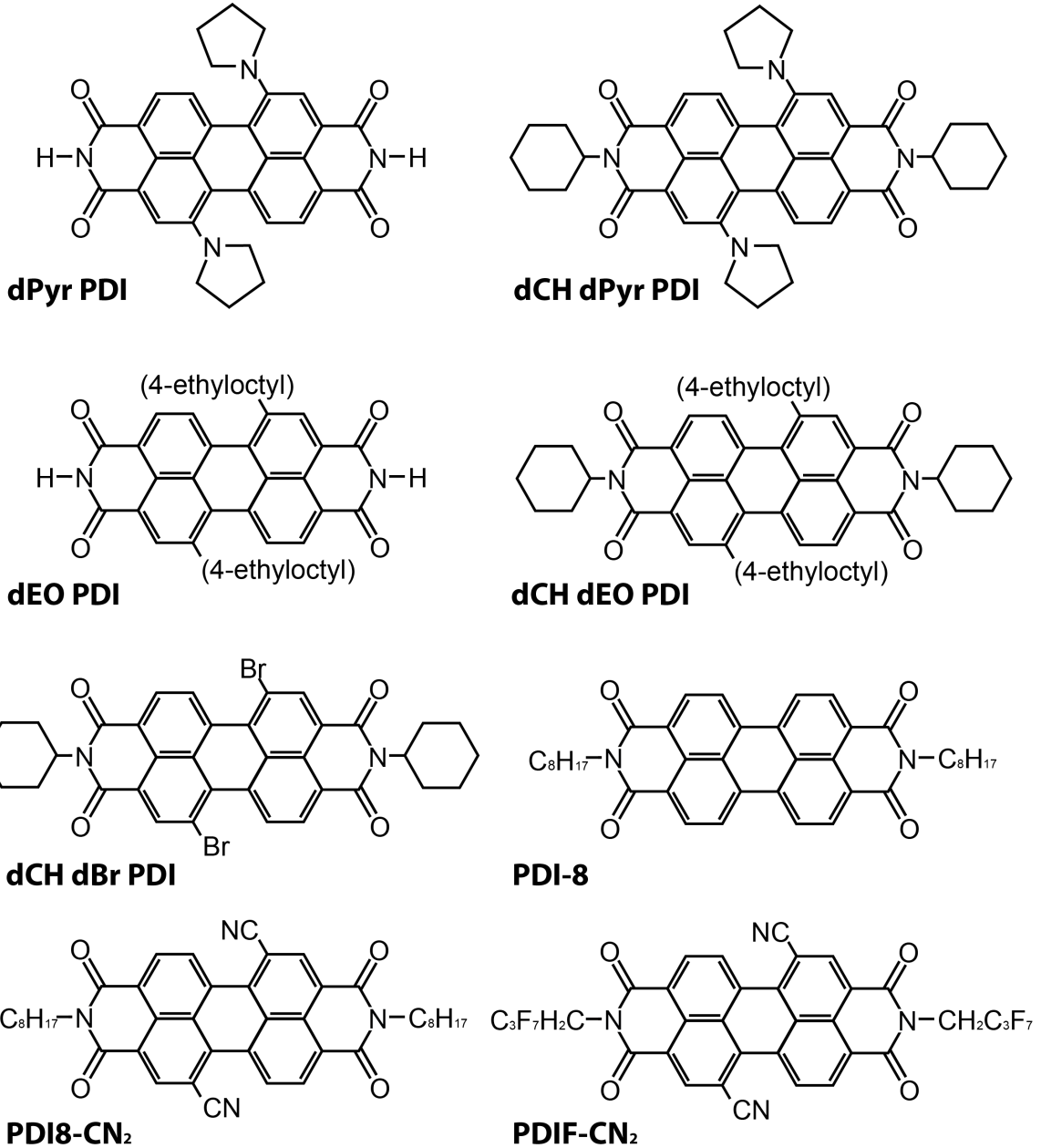


Figure 3.1: Molecular structures and abbreviations for PDI derivatives mentioned in this thesis.

to study the surface potential of PDI on mica as part of a photovoltaic donor-acceptor blend [107]. Liscio *et al.* studied the film thickness-dependent surface potential of unsubstituted PDI molecules on graphite to elucidate band bending at the PDI-graphite interface [108].

KPFM has been used to measure surface potential line-scans across 50 μm channel working transistors of PDI8-CN₂ on bare and OTS-treated SiO₂, similar to the experiments we present in section 3.4 [32, 33]. These studies also used numeric derivatives of the surface potential to obtain electric fields across the transistor channel, but since the measurements were performed in air, the surface potential measurements and hence the calculated electric fields had a much lower signal-to-noise ratio than the measurements presented here. Nevertheless, the electric field profiles observed by Luettich *et al.* had sufficient signal-to-noise to reveal decreased electron injection and extraction barriers at the contacts for the OTS-treated substrates. As discussed below in section 3.4, we employ a similar scanning-probe method to extract local electric fields, and in one case, local mobilities, from surface potential linescans and device currents.

3.2 Charge transport in Braunschweig PDIs

We prepared PDI transistors following the substrate cleaning and thermal deposition procedures given below (section 3.7). Cross-sections of the PDI transistors are sketched in Fig. 3.2. Figure 3.2a illustrates the position of our scanning probe cantilever above the transistor channel in our scanning probe measurements. Figure 3.2b-c shows labeled material cross-sections and electrical connections for bottom- and top-contact transistors, respectively, studied in this thesis. Most data was collected from 5 μm channel bottom-contact transistors in high vacuum in the dark; exceptions are noted.

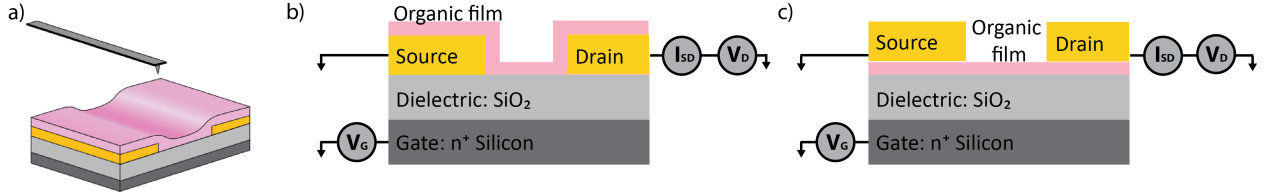


Figure 3.2: (a) Sketch of cantilever above transistor channel with sample cross-section. (b) Schematic of bottom-contact and (c) top contact transistor cross-sections, illustrating connections to ground and voltage/current sources.

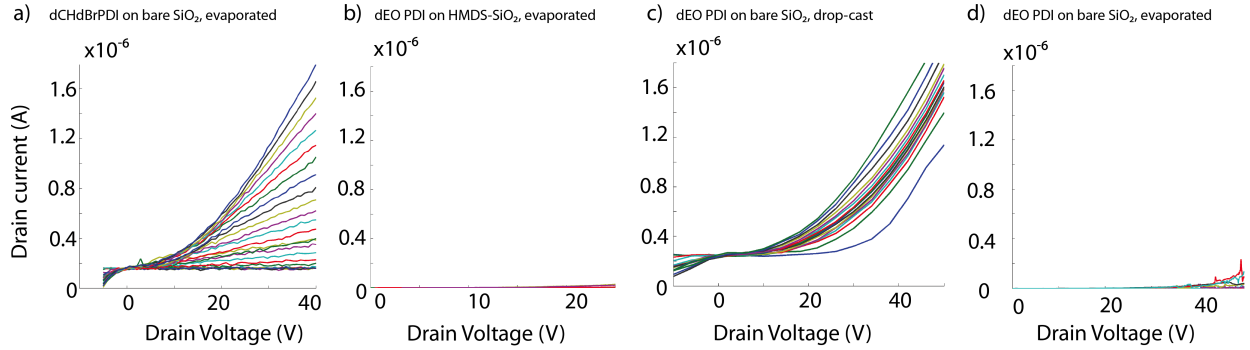


Figure 3.3: Current-voltage curves for PDI transistors. (a-c) are bottom-contact, 5 μm channel transistors, measured in high vacuum and dark in the EFM microscope. (a) Thermally deposited dCH dBr PDI on bare SiO₂. (b) Thermally deposited dEO PDI on HMDS-treated SiO₂. (c) Drop-cast dEO PDI on bare SiO₂. (d) Thermally deposited dEO PDI on a bottom-contact, 5 μm channel, bare SiO₂ transistor chip, measured in high vacuum and dark using the CCMR probe station.

3.2.1 Current-voltage measurements

We measured current-voltage curves for several transistors using different PDI derivatives (dCH dBr PDI; dEO PDI on bare and HMDS-treated SiO₂). The currents were generally very low, which was expected given the large energy gap between the work function of the gold contacts and the PDI LUMO levels. The results for the dCH dBr PDI and dEO PDI are shown in Figure 3.3. Transistor curves for PDIF-CN₂ on bare SiO₂ are shown in Figure 3.4 and discussed in section 3.3.

The dCH dBr PDI transistor exhibited low (microamp) currents that increased with increasing gate bias, but the device did not show saturation behavior (Fig. 3.3a). While

the measured currents were low for all the dEO PDI devices studied, the drop-cast dEO PDI device (Fig. 3.3c) had higher currents (microamps) than the thermally deposited dEO PDI devices (nanoamps, Fig. 3.3b,d). The higher currents in the drop-cast device may have arisen from its more crystalline film (Fig. 4.2 vs. Fig. 4.3).

In dCH dBr PDI and dEO PDI, the energy level alignment between the LUMO level (-3.6 eV or -3.8 eV, Table 3.1) and the gold (-5.2 eV) is particularly poor, so electron injection into the PDI from gold is expected to be especially difficult. In both PDIs, neither a clear linear nor saturation regime is achieved in the transistor current-voltage curves, so linear mobility and saturation mobility cannot be calculated. We conclude that device measurements of these high-LUMO PDI transistors are not an effective way to measure material mobility.

3.3 Short channel effects in PDIF-CN₂

Unlike the low currents in dEO PDI transistors, devices made with PDIF-CN₂ exhibit relatively large currents in the few milliamp range. The electron injection barrier from gold is expected to be extremely low in this system, as suggested by the LUMO level (-4.5 eV). Our measured surface potential profiles are also consistent with good electron injection in this system, as we measure very low voltage jumps at the contacts (Fig. 3.7a). The 5 μm channel bottom contact devices made with PDIF-CN₂ do not exhibit saturation (Fig. 3.4a) and have an almost supralinear shape, especially for devices tested in air (Fig. 3.4b). A 15 μm channel device tested in vacuum also exhibited this non-saturating behavior (Fig. 3.4c). However, if top contacts are added to the same film, a top-contact device with a 125 μm source-drain channel does exhibit gating and saturation, even when tested in air (Fig. 3.4d).

These observations could be consistent with short-channel effects. Short-channel effects arise in organic field-effect transistors when the gradual channel approximation breaks down,

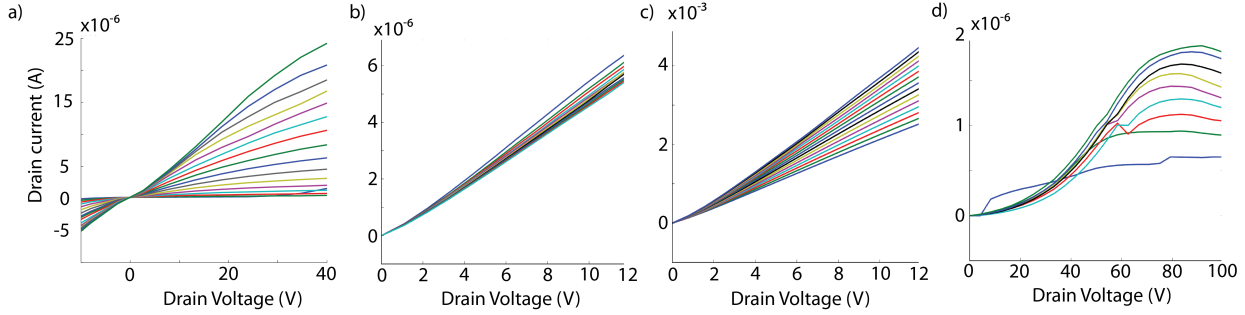


Figure 3.4: Current-voltage curves for thermally deposited PDIF-CN₂ transistors. (a) PDIF-CN₂ on a bottom-contact, 5 μm channel, bare SiO₂ transistor chip, measured in high vacuum and dark. (b) PDIF-CN₂ on a bottom-contact, 5 μm channel, bare SiO₂ transistor chip, measured in air and ambient room lighting. (c) PDIF-CN₂ on a bottom-contact, 15 μm channel, bare SiO₂ transistor chip, measured in high vacuum and dark. (d) Thermally deposited PDIF-CN₂ with 125 μm-channel top contacts on a bare SiO₂ transistor chip, measured in air and ambient room lighting.

and it can no longer be assumed that the electric field due to the gate voltage drop through the oxide is much larger than the source-drain electric field across the channel [109]. In a typical long-channel device, the depletion region at the drain electrode is small relative to the length of the channel, but in a device with short-channel effects, the depletion region approaches the physical length of the channel. When the physical length of the channel is entirely depleted, this scenario is called current punch-through; the punch-through current density is expected to have a quadratic dependence on the drain voltage [109]. Some of our 5 μm and 15 μm devices (Fig. 3.4b and c) appear to approach this limiting case. High off-currents are also a symptom of short-channel effects; our 5- and 15-μm channel transistors exhibited off-currents on the order of a few μA. Finally, short channel effects can decrease the measured mobility, which may explain our measured magnitudes on the order 10⁻⁴ cm²Vs⁻¹ (Fig. 3.7c); reported mobilities for this material are on the order of 0.1-1 cm²Vs⁻¹ [106, 110]. If we are seeing short channel effects, these observations are not without precedent: short-channel effects have been reported for *p*-channel organic transistors at channel lengths as long as 5 μm [111]. Most reported PDI transistors in the literature use channel lengths of 17 μm or greater.

However, our transport observations in PDIF-CN₂ transistors are also all consistent with a long depletion region in the channel, leading to a constant presence of injected charge in the channel. Long depletion regions arise from alignment of the injecting contact closer to the middle of the semiconductor band gap: there is less band bending in this case, but it extends further into the channel. We expected good alignment of gold with the PDI LUMO level, but a long depletion region would be consistent with a degraded or contaminated gold contact. Our first IV-curves were reasonable, but later IV-curves with these non-gating observations may have coincided with early stages of failure of our UV-ozone cleaner. In addition, for a small-grained morphology in PDIF-CN₂ films, contact resistances are known to be quite large [110]. Therefore we find it more likely that our non-gating observations are due to degraded gold contacts instead of short-channel effects. Although low-LUMO PDIF-CN₂ transistors yield overall much larger currents than the low-LUMO PDI devices, we did not find transistor curves to be a satisfactory method of measuring mobility in these small channel devices either.

3.4 Extracting local mobilities using electric force microscopy

To complement bulk charge transport measurements, we turned to a scanning-probe method pioneered by Bürgi *et al.* that can extract local mobilities from surface potential measurements, circumventing contact effects [30, 31]. In this experiment, surface potential profiles are measured using frequency-modulated Kelvin probe force microscopy (FM-KPFM, [39]) across working transistor channels at different gate and drain voltages. The device current at each gate and drain bias combination is also recorded.

The field-effect mobility can then be calculated using:

$$I_{ds} = en(x)W\mu(V'_g, E)E(x) \quad (3.1)$$

where I_{ds} is the device drain current, $en(x)$ is the gate-induced local charge carrier density, W is the channel width, $\mu(V'_g, E)$ is the field-effect mobility, V'_g is the effective local bias, and $E(x)$ is the local electric field [30].

$$V'_g = \phi(x) - V_g \quad (3.2)$$

$$en(x) = CV'_g \quad (3.3)$$

$$C = \frac{\epsilon_r \epsilon_0}{d} E(x) = -\frac{\partial \phi(x)}{\partial x} \quad (3.4)$$

The effective local bias, V'_g , is the difference between the measured surface potential and the applied gate bias. The local charge carrier density, $en(x)$, is calculated from the effective local bias V'_g and the dielectric capacitance per area, C , which is related to the dielectric constant of the insulator and the insulator thickness d . For our SiO_2 dielectric, $\epsilon_r = 3.9$ and $d = 315\text{nm}$. The electric field across the channel is calculated from the numeric spatial derivative of the surface potential.

The expression in Eq. 3.1 makes use of the gradual channel approximation, which assumes that the electric field across the channel is due only to the gate voltage. This assumption is generally assumed to be valid for channels longer than $2\ \mu\text{m}$ and for dielectric layers on the hundred-nm thickness and greater, or for a channel length-to-oxide thickness ratio greater than 10 [30, 112]. A major advantage of this scanning probe method is that it can distinguish the distinct contributions of the gate bias (*i.e.*, charge density) and transverse electric field to the charge mobility. Also, if a device has large contact resistances, the mobility across the channel may vary dramatically based on the varying local charge density. This method can demonstrate this spatial mobility variation, whereas bulk measurements only register an average mobility across the entire channel.

We measured surface potential profiles and device currents for bottom-contact PDI transistors at a range of gate and drain biases. All the thermally deposited films were very flat and amorphous. Since the surface potentials were found to be essentially independent of

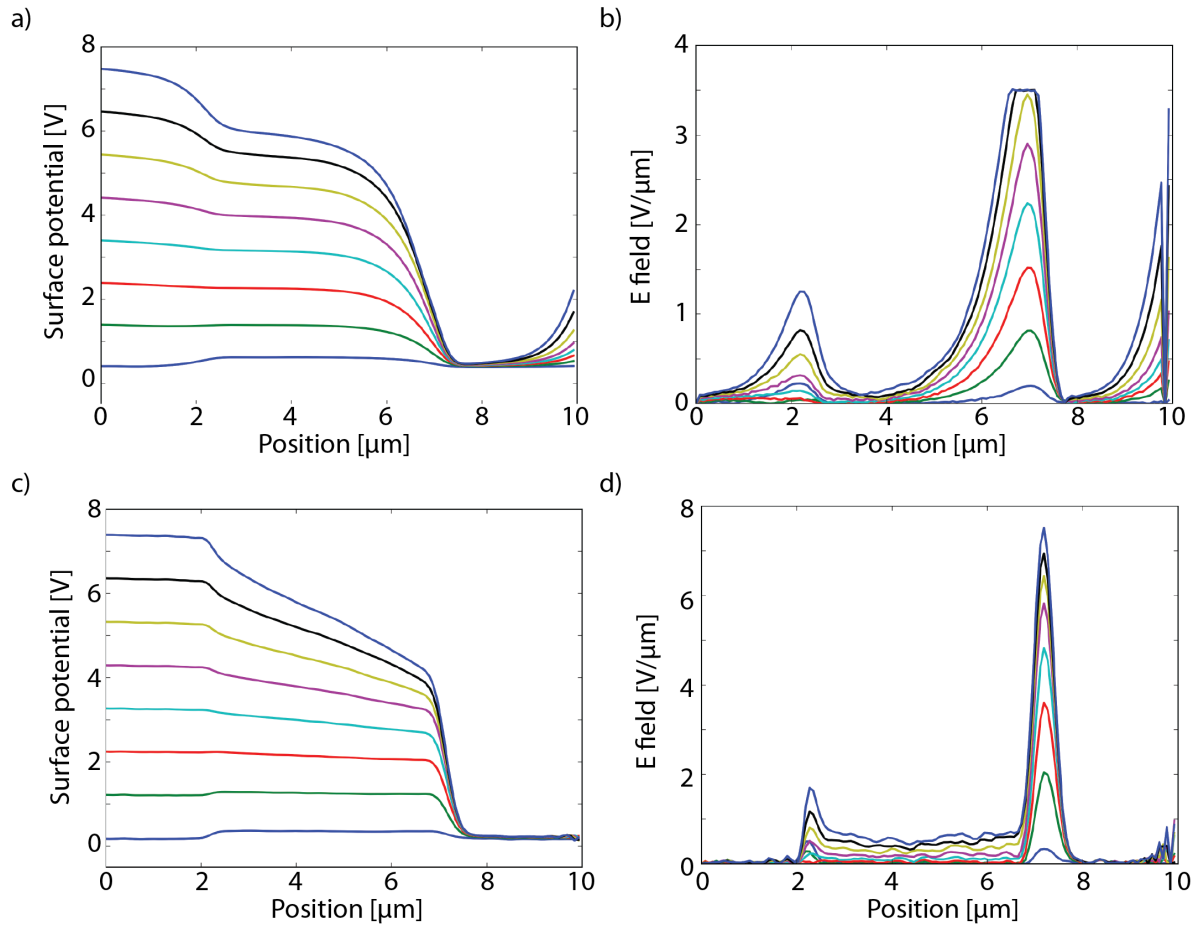


Figure 3.5: Surface potentials and E fields for dEO PDI on bare and HMDS/SiO₂. Top row: dEO PDI on HMDS-treated SiO₂; bottom row: dEO PDI on HNO₃-soaked SiO₂. (a,c) Surface potential profiles and (b,d) calculated E field profiles across the transistor channel. Drain voltages are 0 to +7V in steps of 1 V. Gate voltage is +15 V.

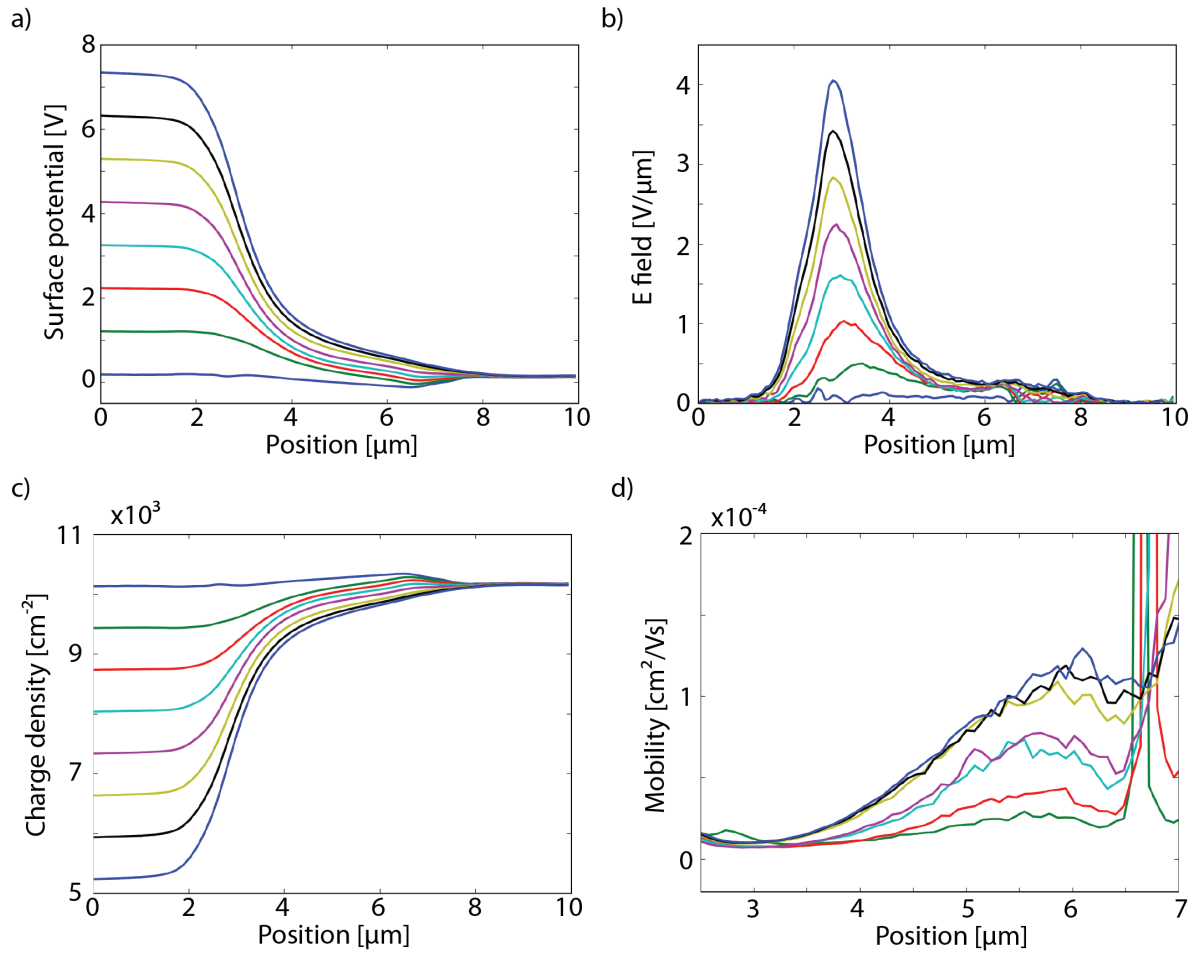


Figure 3.6: Linescan mobility measurements for dCH dBr PDI on bare SiO_2 . (a) Surface potential profiles, (b) calculated E field profiles, (c) calculated charge densities, and (d) calculated local mobilities across the transistor channel. Drain voltages are 0 to +7V in steps of 1V. Gate voltage is +15 V.

the lateral position along the channel, we present our scanning probe results in the form of line scans across the channel. The data is plotted in Figures 3.5 to 3.7. Fig. 3.5 shows the surface potentials and electric fields for dEO PDI transistors on HMDS-treated SiO₂ (a,b) and HNO₃-soaked (c,d). Fig 3.6 shows the surface potentials, electric field profiles, local charge densities, and local mobilities for dCH dBr PDI on bare SiO₂. Fig. 3.7 shows the surface potentials, electric fields, and local mobilities for PDIF-CN₂ on bare SiO₂. For the measurements on dEO PDI and dCH dBr PDI, 16 surface potential profiles were measured and averaged together for each drain voltage, while for the PDIF-CN₂, only one surface potential profile was measured for each drain voltage.

There is substantial variation in the shapes of the surface potential profiles for the different transistors studied. We observed a large voltage jump at the extracting contact for dCH dBr PDI (Fig. 3.6a), while for all dEO PDI samples studied, we measured a large voltage jump at the injecting contact (Figs. 3.5a,c). There was virtually no voltage jump at the injecting contact and only a small step at larger drain voltages at the extracting contact for PDIF-CN₂ (Fig. 3.7a). These observations are generally consistent with energy barriers to injection predicted from alignment of the LUMO with gold (*i.e.*, dCH dBr PDI should have better injection than dEO PDI, but PDIF-CN₂ should have far better injection than either of the high-LUMO PDIs).

The difference in the barrier to injection from gold between dEO PDI and dCH dBr PDI is probably sufficient to move from injection-limited to transport-limited devices. These differences in injection behavior could account for the substantial differences in bulk currents for evaporated films of dCH dBr PDI and dEO PDI (section 3.2.1, Fig. 3.3). Assuming that Arrhenius-type injection holds with similar prefactors for these systems, an energy barrier difference of 256 meV would yield a difference in injection rates of $e^{E_a/kT} = e^{10} = 2.2 \times 10^4$, sufficient to explain the observed difference in device currents (recall that $kT = 25$ mV

at room temperature). The reader should keep in mind that surprisingly small activation barriers to injection have been observed in polymer transistors, indicating that Arrhenius injection into organic materials does not always hold; instead, injection can be assisted by energetic “tail” states arising from molecular disorder at the injecting contact [15, 23].

Similarly, there is also variation in the electric field magnitude and distribution in the transistor channel (along the y-direction in Fig. 4.6) for each of these samples (Fig. 3.6b to 3.7b). Surface treatment of the channel dielectric influences the electric field distribution in dEO PDI transistors: the electric field peaks are broadened in the HMDS-treated, hydrophobic sample, while the field is large at the contacts but constant in the middle of the channel for the HNO₃-soaked, hydrophilic sample (Figs. 3.5b,d). Note that the electric fields in Figs. 3.5 and 3.6 are the derivative of an average surface potential profile compiled from 16 separate linescans, while the electric fields in Fig. 3.7 come from the derivative of one measured surface potential linescan. As a numeric derivative, the electric field can be quite noisy (even after averaging the surface potentials) since taking the derivative amplifies high-frequency noise in the surface potential data. This observation was a motivation for the work presented in Chapter 5.

Since satisfactory currents could not be measured in the dEO PDI devices, local mobilities were only calculated for dCH dBr PDI using currents measured in the microscope but separately from the linescan experiment (shown in Fig. 3.3a; the offset from zero was corrected before using the currents in the calculation of mobilities). The results are shown in Figure 3.6c. The calculated mobility is extremely noisy over the electrodes (since the electric field is small, we are nearly dividing by zero in these regions); results are shown for the channel region where the estimated mobility does not suffer from division-by-zero errors. The mobility laterally varies across the transistor channel. As expected from Eq. 3.1, the mobility is higher where the source-drain lateral electric field is lower. However, the mobility

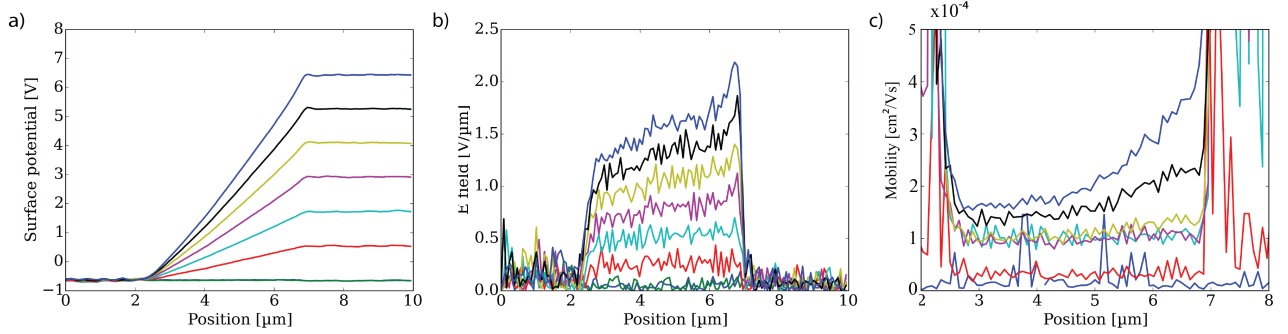


Figure 3.7: Linescan mobility measurements for PDIF-CN₂ on bare SiO₂. (a) Surface potential profiles, (b) calculated E field profiles, and (c) calculated local mobilities across the transistor channel. Drain voltages are 0 to +8 V in steps of 1.14 V. Gate voltage is +8 V.

does not appear to be strongly charge density dependent, since μ does not seem to follow an inverse proportionality with the charge density. Local mobilities for the PDIF-CN₂ device were calculated from currents measured concurrently with the scanning-probe measurement. In Fig. 3.7c, we plot only the channel region since the mobilities are again noisy over the electrodes. As suggested by the smooth surface potential profiles, the mobilities are relatively constant in the channel for low drain biases, but they shift to slightly higher values at the extracting contact for higher drain biases. Since the electric fields are higher at the extracting contact, this trend suggests a charge density dependent mobility, rather than an electric field dependent mobility (recalling that mobility should be inversely dependent on both charge density and electric field).

For PDIF-CN₂, we can compare the locally measured mobility in the device with the 5 μm channel (3.7c) with the saturation mobility calculated from a 125 μm long-channel device (3.4d). In the scanning-probe short-channel measurement, we find mobilities on the order $10^{-4} - 10^{-5}$ $\text{cm}^2\text{V}^{-1}\text{s}^{-1}$. For the long-channel device mobility, we measure $\mu_{\text{sat}} = 1.07 \times 10^{-7}$ $\text{cm}^2\text{V}^{-1}\text{s}^{-1}$. Decreasing mobility with increasing channel length has also been observed for PDIF-CN₂ in solution-deposited films [113]. This discrepancy in measured mobilities is consistent with short-channel effects in the 5 μm device, since these effects can artificially increase currents (and therefore the mobility inferred using the gradual-channel

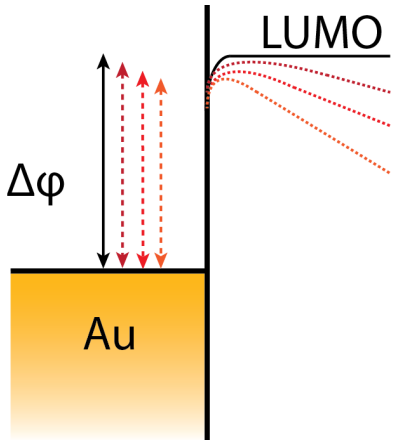


Figure 3.8: Schematic illustrating injection barrier lowering upon application of a gate voltage.

approximation) [114]. The mobility measured in air is also likely lowered by electron trapping, as evidenced by the substantial threshold voltage shift (+20 V, Fig. 3.4d).

In the data presented in this section, the source-drain biases were stepped sequentially from low to high voltage. For a more accurate measurement that avoids trends that might arise from device aging, this experiment can be improved by randomly varying the order in which gate and drain biases are applied, rather than simply varying the biases sequentially. Keeping track of these randomly ordered gate and drain biases allows us to distinguish between effects due to the specific applied biases and stress or degradation effects that vary with time.

3.5 Charge injection kinetics in perylene diimides

Because there is a substantial energy difference between the gold electrode work function and the dEO PDI LUMO level, these transistors provide a system where charge injection should be highly sensitive to shifts in the injection barrier [115]. As sketched in Fig. 3.8, one way to lower the injection barrier in a working transistor is to adjust the gate voltage. As

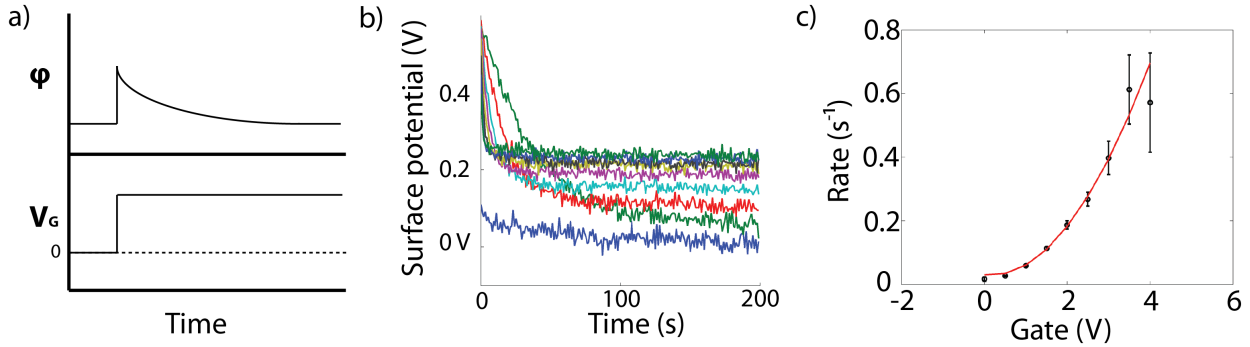


Figure 3.9: (a) Sketch of applied gate voltage and measured surface potential versus time.(b) Representative surface potential data measured at different gate voltages. (c) Rate of surface potential equilibration (*i.e.*, charge injection rate) versus gate voltage.

the gate is turned on, a lateral electric field is created that decreases the injection barrier, via the Schottky effect, thereby increasing the rate of charge injection. The greater the gate voltage, the greater the injection barrier lowering and the greater the charge injection rate (Fig. 3.9b-c).

In a scanning-probe context, this injection barrier lowering can be observed by measuring the surface potential as a function of time when the gate is turned on, for a range of different gate voltages. An applied gate pulse and expected surface potential profile are sketched in Fig. 3.9a. The surface potential peak is expected to increase with increasing gate voltage, but will not necessarily match the applied gate bias due to contact potential differences between the electrode and the semiconductor material in the transistor channel. We used frequency-modulated Kelvin probe force microscopy (FM-KPFM) to continuously monitor the surface potential, employing a LabView-triggered delay to turn on the gate bias a few seconds into the measurement.

We measured surface potential transients following gate turn-on in dEO PDI films on our usual transistors with bare SiO₂ and 5 μm channel, gold bottom-contact electrodes. Representative surface potential transients are shown in Fig. 3.10, where 3.10a is a closeup view of the short-time data in 3.10b. Note that as discussed above, it is similarly important in

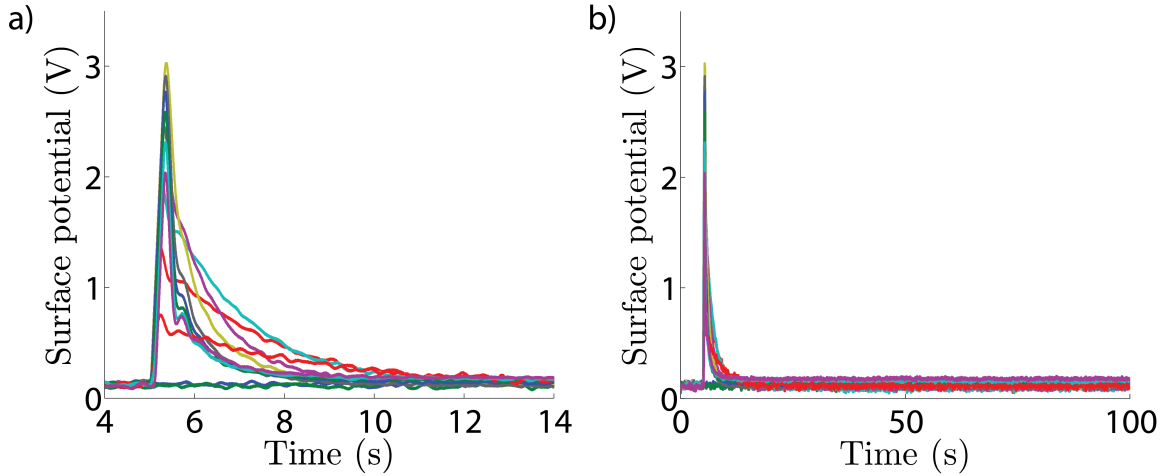


Figure 3.10: (a) Surface potential transients measured at different gate voltages for a dEO PDI transistor on bare SiO_2 . (b) Same data set as (a) shown to longer times.

these experiments to randomize the order of the gate voltages applied to distinguish between device aging and gate voltage-dependent effects. The sample data shown in Fig. 3.9b-c was measured while sequentially stepping through gate biases, while the data presented in Figs. 3.10 and 3.12 was collected using random gate bias steps.

We measured charge injection surface potential transients at three locations in the transistor channel, marked on the topography map in Fig. 3.11. We fit the surface potential transients to single exponential decays and extracted the rates from these fits. For the sample shown in Fig. 3.11, the injection rates for the three locations are shown in Fig. 3.12a. The data in Fig. 3.10 corresponds with the red dataset in Fig. 3.12. The fits are excellent and there is very good agreement in the injection rates from different locations in the same transistor channel.

We expect the injection rates to increase with the (time-dependent) gate-induced electric field, which depends on the applied gate voltage. This so-called Schottky barrier lowering can be written as: [116]

$$\Delta\phi = \sqrt{\frac{qE}{4\pi\epsilon_0\epsilon_r}} \quad (3.5)$$

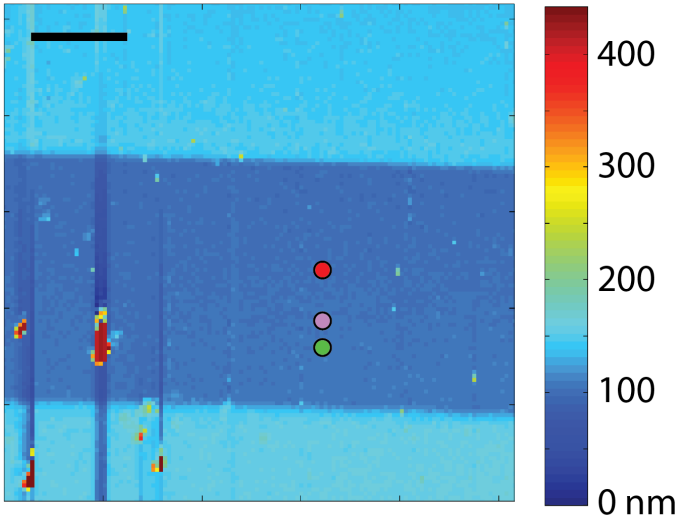


Figure 3.11: Topography of dEO PDI transistor and locations where charge injection measurements were made. The colors of the location dots correspond to the colors of the data in Figs. 3.12 and 3.13.

The charge injection rates we measure show a roughly quadratic dependence on the gate voltage for low V_G , then appear to level out at higher V_G . This effect is consistent at different locations in the same transistor channel. As a control measure, we plot the exponential charge injection rates versus time in Fig. 3.12b. As we expect, there does not appear to be a trend in the injection rate versus time. This control confirms that the dependence of rate on gate voltage is not in part due to any kind of device aging effect. The location independence of the rates also indicates that we are observing an injection process, not a transport process.

The steady-state surface potentials are also expected to have a gate voltage dependence, since the amount of free charge present in the channel should be related to the gate bias through the dielectric capacitance. However, our measured steady-state potentials are not strongly dependent on either gate voltage or time (Fig. 3.12c-d). The steady-state potentials do generally appear to increase linearly at larger gate biases, and this linear trend *may* start at the same gate bias where the injection rates start to slow down. However, the steady-

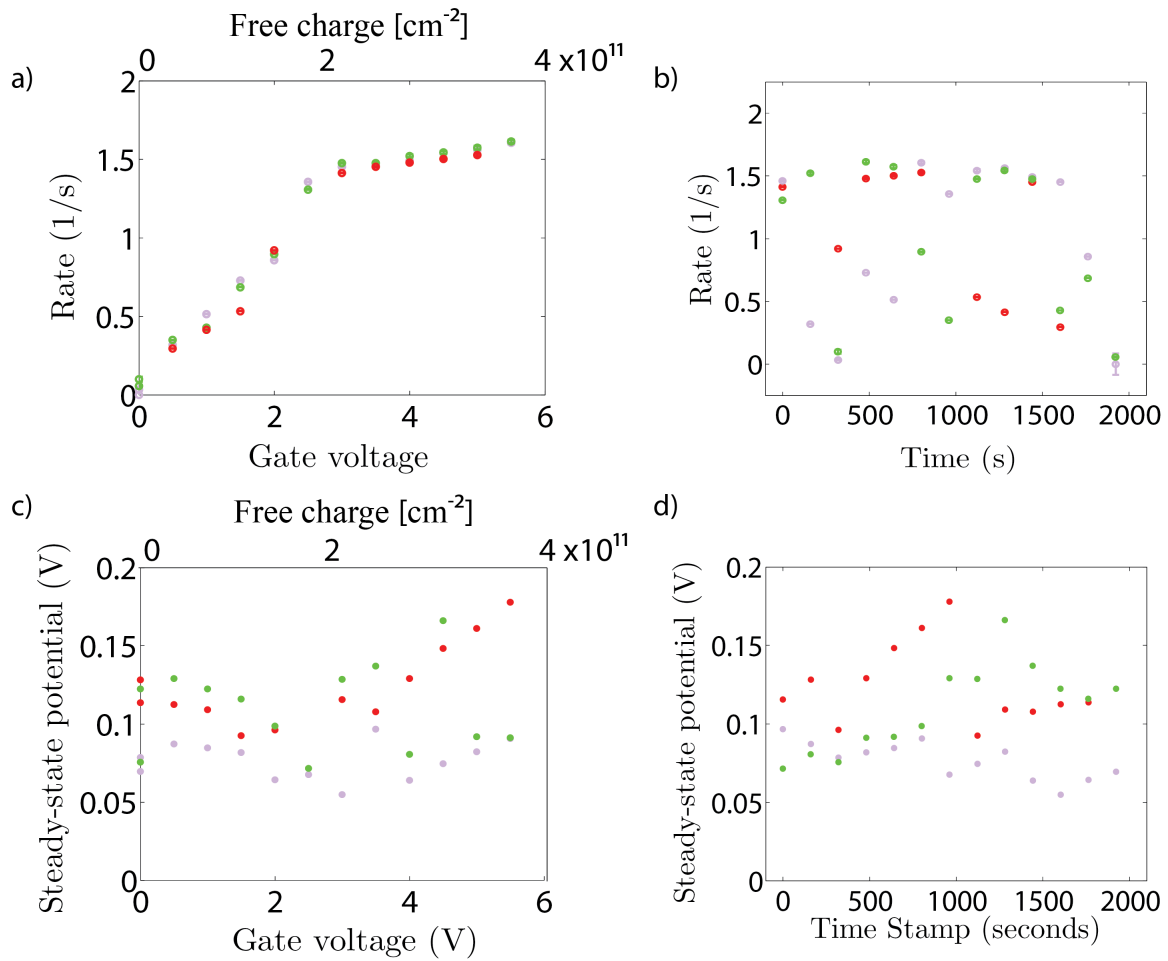


Figure 3.12: Charge injection rates versus gate voltage (a) and time (b). Steady-state surface potentials versus gate voltage (c) and time (d).

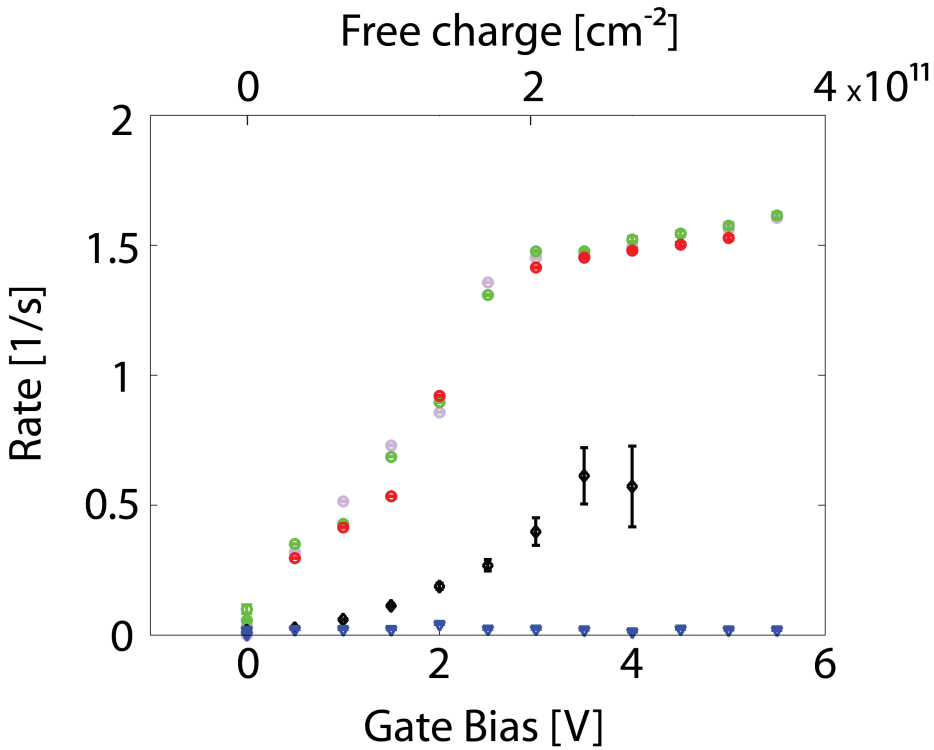


Figure 3.13: Charge injection rates versus gate voltage for two dEO PDI transistors. Rates are consistent within a single sample, but vary substantially between transistors. Circles, diamonds, and triangles represent three different devices.

state potential versus gate voltage trend is inconsistent between transistor locations, so we are hesitant to draw strong conclusions from these data. Overall, these observations suggest that trap-clearing is incomplete between transient measurements, so both the device history and the gate voltage are influencing measured steady-state potentials.

Although injection rates are fairly consistent within a single sample, when we compare the charge injection rates versus gate voltage for two different dEO PDI transistors, we find considerable variation in the absolute rates of charge injection between samples (Fig. 3.13). While both devices show an approximately quadratic dependence of charge injection rate on the gate voltage, the magnitude of these rates are quite different. In addition, it is unknown from our data whether the first sample, measured at fewer gate biases, would also have exhibited the transition in the shape of its gate bias dependence at larger V_G .

Unfortunately, a third dEO PDI sample prepared on the same bottom-contact transistors exhibited no charge injection whatsoever; the only difference in this sample was that it had not been UV-ozone cleaned *immediately* before deposition of the dEO PDI. Taken together, these observations lead us to conclude that the injection rates from gold into PDIs are extremely sensitive to the cleanliness of the gold contacts, and that we cannot expect the absolute values of charge injection rates between samples to be identical. Due to these concerns regarding irreproducibility, we chose not to pursue further temperature-dependent measurements of charge injection rates for this material.

In general, however, the reproducibility of these injection transients at different locations in a single sample, and for randomized gate biases, suggests a surprisingly robust effect—especially given that dEO PDI traps charge! Further study of injection rate dependence on gate bias will require careful modeling. The relevant electric field is the one between the injecting electrode and the semiconductor, at the semiconductor-dielectric interface [23]. How the gate bias influences the length of band bending into the channel from the electrode is not obvious. If this dependence could be modeled and/or measured, it would be interesting to study injection rates versus both gate bias and temperature.

3.6 Conclusions

In summary, we investigated charge transport properties in a variety of high- and low-LUMO PDIs. Bulk current-voltage characteristics were not useful for high-LUMO PDIs since the currents were extremely small due to the large electron injection barrier from gold into the LUMO. We measured bulk current-voltage curves in 5 and 15 μm -channel PDIF-CN₂ on bare SiO₂, and found a larger-than-expected mobility possibly consistent with short channel effects.

To circumvent the resulting difficulties interpreting transistor transport characteristics, we applied a scanning-probe method for measuring mobilities locally [30]. This method allowed us to estimate mobilities for devices that would not have been characterizable with transport measurements alone, and to comment on the electric field and charge density dependence of the mobility. We were able to evaluate the energetic barriers to charge injection and extraction for different PDIs. However, the electric field and mobility profiles obtained in this method were noisy, in part due to the inherent noise in the surface potential, and also in part to the amplification of this noise when taking the numeric derivative to obtain the electric field. This noise was a motivating factor for our work in Chapter. 5.

Finally, we explored charge injection from gold into dEO PDI films by measuring surface potential as a function of time upon application of a gate bias. We believe we have observed Schottky-barrier lowering in the dependence of the injection rate on the applied gate bias. The overall rates of charge injection varied substantially between samples, most likely due to variation in gold electrode cleanliness. However, the measurement is reproducible within a single sample, and with further theoretical work could yield new insights into charge injection for high-LUMO n -type semiconductors.

3.7 Experimental

3.7.1 PDI transistor substrates

For bottom-contact transistors, the substrates were fabricated in CNF and cleaned as follows. To remove dicing saw resist, the chips were rinsed with acetone and isopropanol (IPA), then sonicated for 10 minutes in acetone and then 10 minutes in IPA. The chips were soaked overnight (12-18 hours) in fluid 1165 microposit remover. For top-contact transistor sub-

strates, highly *n*-doped silicon with 315 nm thermally grown SiO₂ was prepared in CNF, cleaved in the lab by hand, and cleaned as below.

Both bottom-contact and top-contact substrate chips were cleaned in the following manner. The chips were gently scrubbed using a clean room swab in DI water with Aquet detergent, followed by 5 minutes of sonicating in DI water with Aquet detergent and 5 minutes in DI water. The chips were dried with a nitrogen gun and UV-ozone cleaned for 10 minutes. If the bottom-contact chips were cleaned well in advance, it was important to UV-ozone clean them again immediately before film deposition to ensure that the gold was as clean as possible.

Top-contact transistors were completed after deposition of the PDI film by thermally depositing 15 nm gold at a rate of 0.1 Å/s onto the film through a shadow mask. The shadow mask creates an array of devices with 75μm or 125μm channels. When depositing metals on top of organics, it is important to alternate depositing for 5Å and waiting with the shutter closed for 5Å. Dr. Vladimir Pozdin suggested that frequently pausing the metal deposition this way may help to prevent the hot metal from damaging the organic film; hot gold has been shown to penetrate into organic films, and the heat of the metal impacts the final contact resistance [117, 118].

For HMDS-treated bottom-contact transistor substrates, the chips were exposed to hexamethyldisilazane (HMDS) vapor in the CNF YES vapor prime oven following the standard tool recipe for silicon wafers. The samples were held in a glass dish during treatment. This treatment binds trimethylsilane groups to dangling Si-OH groups on the SiO₂ surface, rendering the transistor channel hydrophobic. For HNO₃-soaked bottom-contact transistor substrates, the chips were soaked in HNO₃ for 10 minutes, then rinsed with DI water. Contact angles for these and for standard SiO₂ transistors were measured using the Rame-Hart 500 Contact Angle Goniometer in the NBTC facility at CNF, Duffield 226.

3.7.2 Thermal deposition of PDI films

Thermally deposited thin films of PDI were prepared in a custom-built glove box evaporator housed in Baker 146. See Appendix A for further details of glove box operation. PDI powders were loaded into ceramic crucibles which were resistively heated until a deposition rate of 0.1 Å/s was achieved; the shutter was then opened and films deposited on the substrates. A copper substrate heater was used to hold the substrates at 125°C before, during, and for a few minutes after deposition. High substrate temperatures are important for achieving the highest possible degree of lateral motion of molecules at the sample surface when thermally depositing PDIs[17, 119–122]. These high temperatures promote molecular reorganization into crystalline domains during film deposition, generally yielding higher device mobilities [123].

Since PDIF-CN₂ is substantially more conductive than the other PDIs studied, precautions had to be taken to keep the material deposited on the transistor source-drain electrodes isolated from any material touching the edges of the chip. The highly conductive gate layer is exposed in cross-section on the chip edges, so if the material touching the electrodes also touches the sides of the chip, then the source and drain electrodes will be automatically shorted to the gate and the transistor will not work. The electrodes were isolated prior to deposition by painting a thin layer of QDope around the interdigitated region, taking care to be sure the gate pads were entirely covered. If the QDope layer is too thick, it will melt onto the active area when the substrates are heated. The QDope was allowed to cure overnight before a final UV-ozone cleaning and loading the chips into the evaporator. After depositing PDI, the QDope can be carefully pried and lifted up using a razor blade so that electrical contact can be made to the transistor pads with silver paint. Masking with Kapton tape is less effective. It is difficult to get the tape smoothly adhered to the surface of the chip, and after PDI deposition, it is extremely difficult to remove the tape without cracking or

flaking on the chip edges. These cracks may not necessarily ruin the chip, but are advisably avoided since they often send bits of conductive silicon flying, which can land on and short the transistor active region.

3.7.3 Drop-casting of PDI films

Drop-cast PDI films were prepared by the Braunschweig group from solutions in pyridine, used as received. The PDI concentration in solution was 10^{-5} M or approximately 6 mg/mL. A drop of PDI solution was placed on the transistor active area and the solvent was allowed to evaporate under ambient atmospheric conditions.

3.8 Acknowledgements

The PDI derivatives used for drop-casting were synthesized and purified by Dr. Zhong Li. The dCH dBr PDI used for thermal deposition was synthesized and purified by Dr. Zhong Li. The dEO PDI used for thermal deposition was synthesized and purified by Dr. David Ley. Drop-cast PDI transistors were prepared by Dr. Zhong Li. Electrochemical data for PDI derivatives was measured by the Braunschweig group. This work made use of the Cornell Center for Materials Research Shared Facilities which are supported through the NSF MRSEC program (DMR-1120296): some of the bulk transistor curves discussed in this chapter were collected in facilities managed by the CCMR. This work was supported by an NSF graduate research fellowship as well as funding from NSF-DMR 1006633 and NSF-DMR 1309540.

CHAPTER 4

CHARGE TRAPPING IN PERYLENE DIIMIDE DERIVATIVES

4.1 Introduction

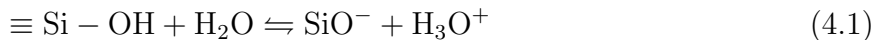
Our second interest in PDIs stemmed from a curiosity about the chemical stability of the PDI radical anion for derivatives of different LUMO levels. The enhanced stability of PDIs with lower LUMO levels (-4.0 to -4.3 eV, and below) has been argued from a thermodynamic perspective [98, 124]. However, as our work with pentacene demonstrated, thermodynamic predictions are not always an accurate reflection of the actual solid-state chemistry in organic electronics [13]. No specific trap species has been demonstrated in PDIs, and we hoped that the trap-clearing spectroscopy technique we developed with pentacene could offer insights into PDI trapping chemistry.

In this chapter, I describe the current understanding of charge trapping in PDIs, and review other scanning-probe microscopy studies on these materials. I then outline EFM experiments designed to shed light on charge trapping processes in a range of PDI derivatives. In these experiments, we used custom-synthesized “high-LUMO” PDI derivatives that were designed for macromolecular donor-acceptor photovoltaics by the Braunschweig group [104]. These molecules were not thermodynamically expected to be air-stable due to their higher LUMO levels (Table 3.1), and our aim was to evaluate their charge trap chemistry. I will discuss two efforts to investigate charge trap chemistry in these materials: the application of trap-clearing spectroscopy to several PDI derivatives, and attempts to measure trap formation rates in dEO PDI.

4.1.1 Trapping mechanisms in PDIs

For electron conductors like PDIs, the major source of charge trapping and performance instability is expected from thermodynamics to be reaction of the anion radical ($\text{PDI}^{\cdot-}$) with water and oxygen to form shallow, reversible traps [3, 98, 124, 125]. Permanent film degradation appears less likely, but has been observed in the presence of water for a related naphthalene diimide polymer [126]. To counter the oxidation of the anion radical, several strategies have been introduced. Lowering the PDI LUMO level via electron-withdrawing substituents such as cyano groups on the core “bay” positions and fluoroalkyl chains at the nitrogen positions have proven highly effective [100, 106, 127, 128]. These fluoroalkyl chains, such as those in PDIF-CN₂, are credited by some with providing a kinetic barrier to the penetration of oxygen and water into the PDI film [3, 106]; however, others have observed similar rates of mobility degradation in air for a range of film morphologies and fluorination patterns, suggesting that this kinetic barrier idea is insufficient to explain the high mobilities in fluorinated PDIs [120].

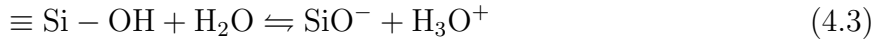
Substrate dielectric treatment also plays an important role in minimizing charge trapping in *n*–channel transistors. Yoon *et al.* observed from a broad study of several *n*–channel organic materials and a range of dielectrics that *n*–channel semiconductors on dielectrics with free hydroxyl or carbonyl groups were especially prone to electron trapping [129]. In particular, this study suggested that the silanol (-SiOH) groups on the silicon dioxide are acidic enough to sustain electron traps, regenerating the neutral semiconductor radical and releasing hydrogen:



In our case, the semiconductor is a single PDI molecule.

Many take this mechanism at face value despite its having been originally written to describe electron current flowing across bare hydrated SiO₂ [130]. The primary spectroscopic evidence for a silanol electron trapping mechanism is a report that during *n*-channel device operation, the silanol H-stretching and bending vibrational spectroscopic peak shifted from the slightly H–bonded state to the isolated state, finally disappearing altogether after many hours of device operation [131]. However, this IR spectroscopy signal is extremely small, and we consider this evidence weak on its own.

In addition, the mechanism as written in Eqs. 4.1-4.2 seems complex and thermodynamically unlikely. A rough back-of-the-envelope calculation of the reaction ΔG suggests this process would be significantly endothermic. For a silanol pKa of 5 [132], T = 298 K, and R = 8.314 kJ/mol · K:



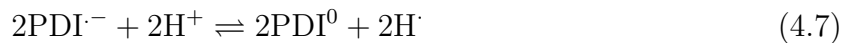
$$\Delta G = -RT \ln(K_a) = +28.5 \text{ kJ/mol} \quad (4.4)$$

With the pKa of H₃O⁺ = -1.74: [133]



$$\Delta G = -9.9 \text{ kJ/mol} \quad (4.6)$$

We next need to calculate the ΔG_{rxn} for the oxidation of the anion radical and the production of hydrogen:



For the first half of the reaction, we must convert the oxidation energy of the PDI anion radical versus ferrocene to an oxidation versus the normal hydrogen electrode (NHE). Here, I choose dEO PDI for the anion radical, whose reduction has been measured versus ferrocene by the Braunschweig group [105]. I adjust this measured reduction relative to NHE using

an offset of -0.64V [134].



$$E_{\text{ox}} = -E_{\text{red}} = +1.176\text{V} \text{ vs. ferrocene} \quad (4.9)$$

$$\text{Ferrocene } E_{\text{red}} \text{ vs. NHE } \sim -0.64\text{V} \quad (4.10)$$

$$E_{\text{ox}} \text{ dEO PDI vs. NHE } \sim +0.536\text{V} \quad (4.11)$$

The reduction of a proton vs. NHE is defined as zero volts:



$$E_{\text{red}} = 0\text{V} \quad (4.13)$$

So,

$$E_{\text{cell}} = E_{\text{red}} - E_{\text{ox}} = 0 - 0.536 = -0.536\text{V} \quad (4.14)$$

For $n = 2$ and $F = 96,485.3 \text{ C/mol}$, the ΔG_{rxn} is then:

$$\Delta G = -nFE_{\text{cell}} = 103.4\text{kJ/mol} \quad (4.15)$$

ΔG for the final step in the overall mechanism, the combination of two hydrogen radicals to give hydrogen gas, is defined as zero. The overall ΔG for the reactions outlined in Eqs. 4.1-4.2 is then:

$$\Delta G_{\text{tot}} = 28.5 - 9.9 + 103.4 + 0 + 0 = +122 \text{ kJ/mol} = +1.26 \text{ eV} \quad (4.16)$$

The numbers in Eqs. 4.3-4.16 should only be considered rough estimates, especially the conversion of the oxidation energy of $\text{PDI}^{\cdot-}$ from an energy vs. ferrocene to vs. NHE; converting electrochemical potentials between standard electrodes is an extremely suspect procedure since changes of solvents and electrolytes are usually involved. Even so, an estimated reaction energy of $+1.26 \text{ eV}$ suggests that a reaction between PDI anion radicals, water, and silanols to form electron traps is strongly thermodynamically unfavorable. If such traps do

form, this large reaction energy could explain why their supposed spectroscopic signature only occurs slowly over hours of device operation [131].

If the acidic silanol reaction *is* an important source of trapping, then other reasonably acidic alcohols should also lead to charge trapping. Yoon *et al.* pursue this line of reasoning in terms of dielectric chemistry, but oxygenated organic defects or impurities could also lead to trapping. Silanol groups have a pKa of either 5 or 8 depending on their microscopic environments [132], while organic alcohols have pKas that can range below 4, especially for aromatic substituents [133]. In addition, if acidic silanols or other alcohols are present, it seems that the $\text{PDI}^{\cdot-}$ could also react directly with a silanol group without introducing hydrogen formation.



However, this reaction would suffer a large energetic penalty for breaking the resonance of the PDI molecule.

In all these cases, importantly, the long-lived electron trap species resides at the SiO_2 dielectric-organic interface, not on the PDI molecule. A key difference between these proposed trapping mechanisms is that the Yoon *et al.* mechanism regenerates the neutral PDI radical (Eq. 4.2), while the mechanism in Eq. 4.17 yields a protonated PDI radical. Atmosphere-induced trapping in PDIs has been shown to be reversible by annealing or returning the device to vacuum, so it seems reasonable that a mechanism that does not involve loss of hydrogen would be more readily reversible [17, 135, 136].

Whether any or none of these trapping mechanisms plays a role in electron trapping in PDIs, dielectric chemistry clearly does influence PDI air stability. More hydrophobic dielectric surfaces seem to improve air stability, presumably by deterring the penetration of water into the charge-transporting interfacial organic layers [33, 137, 138]. The presence of water is expected to facilitate the Yoon *et al.* reactions discussed above. Multiple groups

have pointed out that adsorbed water could form a disordered dipole layer on the dielectric, a phenomenon that leads to gap states in hole conducting polyacenes such as pentacene and rubrene [139, 140]. Others have suggested that water confined in the film itself or at the dielectric interface is a source of charge trapping in *n*-channel devices [128, 141].

Dielectric chemistry also shapes the morphology of PDI films, which in turn influences charge trapping. For films with smaller grains, transport is expected to be poorer due to the increased number of grain boundaries [21, 115, 142] and the increased chance for diffusion of air into the film, leading to charge trapping [143]. Treatments such as HMDS or OTS can combine desirable hydrophobicity with larger grain sizes in PDIs, both of which are expected to increase mobilities [100, 110].

4.1.2 Hückel predictions of PDI HOMO-LUMO electron densities

In the discussion of PDI trap chemistry, above, we propose the possibility that the PDI anion radical might accept a proton from silanols or H_3O^+ , generating an electron trap SiO^- at the organic-dielectric interface. Curious what a protonated anion radical PDI might look like, we turned to simple Hückel theory. We generated a Hückel matrix for an unsubstituted PDI core, assuming that the carbon-carbon self interaction was zero, and assigning arbitrary interaction values to the remaining atomic interactions as shown in Table 4.1.

The Hückel matrix we generated is shown in Fig. 4.1a. As a check that we had correctly assigned and located all atoms, we used the matrix to generate a sketch of the molecule with color-coded atoms; this successful check is shown in Fig. 4.1b. We used our Hückel matrix to calculate relative atomic electron densities for different energy levels in the PDI core. The first two levels are shown in Fig. 4.1c-d; as we expect, the lowest energy level is a single phase, while the second energy level has one node. Since the PDI core has 32 π -electrons,

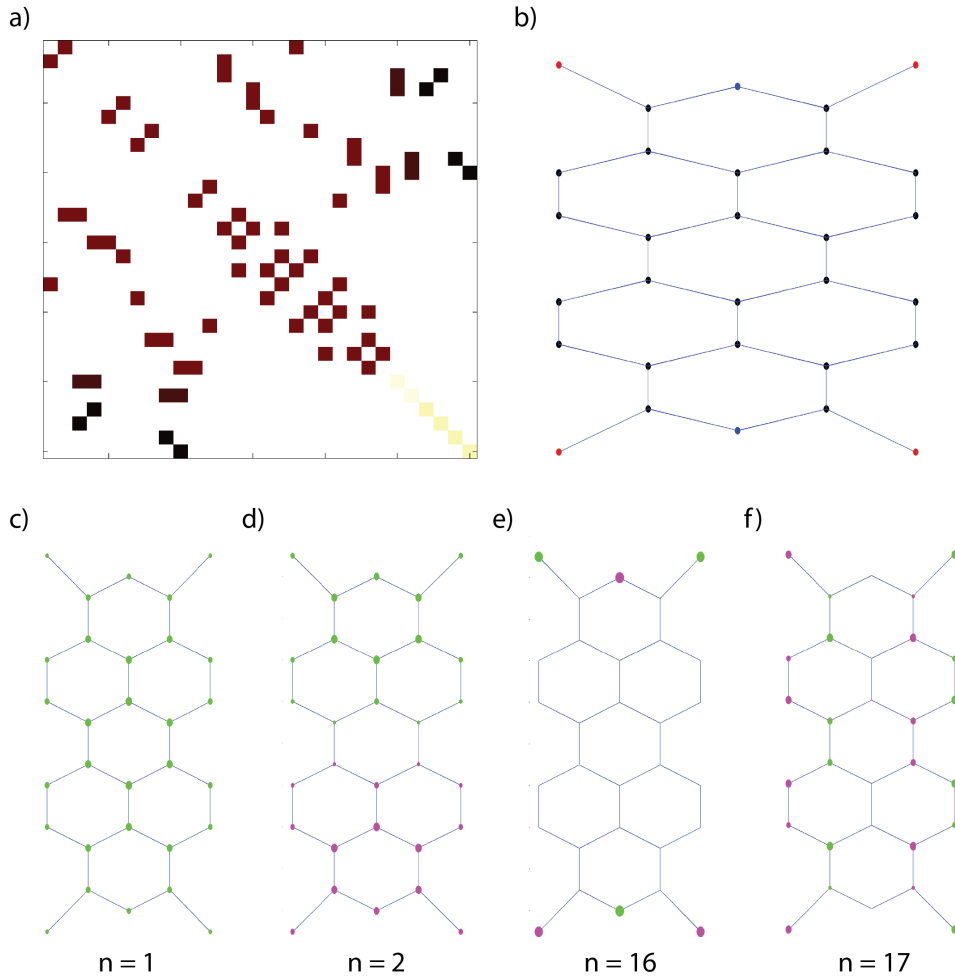


Figure 4.1: (a) Hückel matrix for PDI core. (b) PDI core generated by the Hückel matrix as a geometry check; black = carbon, blue = nitrogen, red = oxygen. (c-f) Electron density for energy levels n , where each level is filled by $2n$ electrons. Pink and green represent opposite phases. The PDI core HOMO and LUMO electron densities are shown in (e) and (f), respectively.

Atomic interaction	Symbol	Value
C (self)	α	0
C-C	β	-4.18
N (self)	α_N	-0.2
C-N	β_N	-4.5
O (self)	α_O	-0.4
C-O	β_O	-5

Table 4.1: Values used in generating a Hückel matrix for an unsubstituted PDI core.

the HOMO level is given by n=16 and the LUMO level is given by n = 17. These electron density maps are shown in Fig. 4.1e-f. The HOMO level shows that the nitrogen and oxygen atoms have the greatest electron density in the neutral PDI core, as we would expect from their relative electronegativity. When the PDI accepts an electron and becomes an anion radical charge carrier, the additional electron density can be found on any of the peripheral atoms, as shown in the LUMO. This calculation suggests that a PDI anion radical could be protonated (or undergo other reactions) at several different positions on the molecule, including core carbon atoms and the amide oxygen atoms, with similar probability.

4.2 Trap-clearing spectroscopy of perylene diimides

We prepared a variety of PDI transistors for trap-clearing spectroscopy measurements. We studied films of dPyr PDI, dEO PDI, and dCH dEO PDI drop-cast from pyridine onto bare SiO₂ bottom-contact transistors, prepared by the Braunschweig group on our transistor substrates as described in Ch. 3.7.3. AFM topography of these films is shown in Fig. 4.2. The drop-cast PDI films were polycrystalline, but the drop-casting method appeared to yield incomplete channel coverage and gave dramatic topography that was difficult to study with scanning-probe measurements.

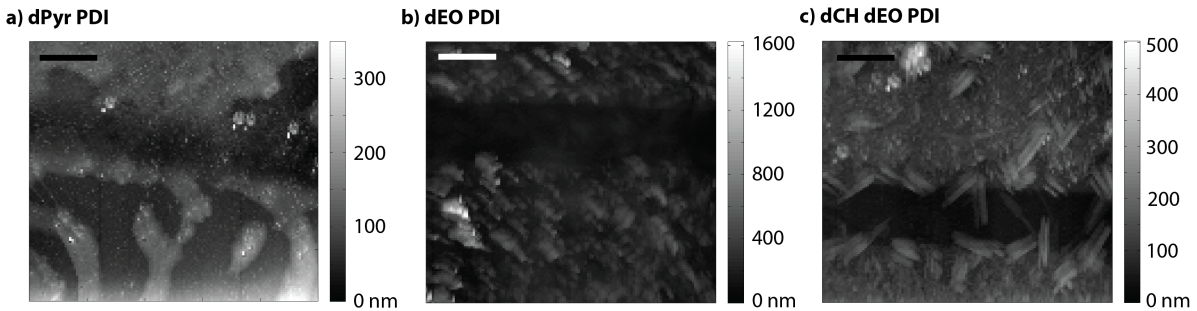


Figure 4.2: AFM topography of drop-cast transistors: (a) dPyr PDI, (b) dEO PDI, and (c) dCH dEO PDI. Solution preparation and drop-casting was performed by Dr. Zhong Li, Braunschweig group. Scale bar in (a-c) is $4 \mu\text{m}$.

We also studied thermally deposited films of dEO PDI and dCH dBr PDI, prepared as described in Ch. 3.7.2. These films were very amorphous and flat, as shown in Fig. 4.3. In fact, we found these AFM images disturbingly flat, despite the apparent color change (pink) on our transistor chips indicating the presence of a film. To confirm that depositions were successful, we used laser desorption ionization (LDI) mass spectrometry to examine which species were present. Representative mass spectroscopy results are shown in Fig. 4.4. In all cases, LDI mass spectrometry produced the molecular ion expected for the given PDI, reassuring us that the PDIs survived deposition despite their smooth films. (In one case, we even identified a PDI mislabeled by our collaborators through mass spec- we deposited dCH dBr PDI that had been labeled as dCH dEO PDI.)

4.2.1 Spatially uniform charge trapping in PDI transistor channels

We examined the distribution and lifetimes of traps in our PDI films by applying a positive gate bias for 2 minutes and then imaging the surface potential in a $10\mu\text{m}$ region. A typical gate bias is +5V. The gate must be off in order to image trapped charge, since free charged induced by the gate will screen the trapped charge [26]. The source and drain were grounded

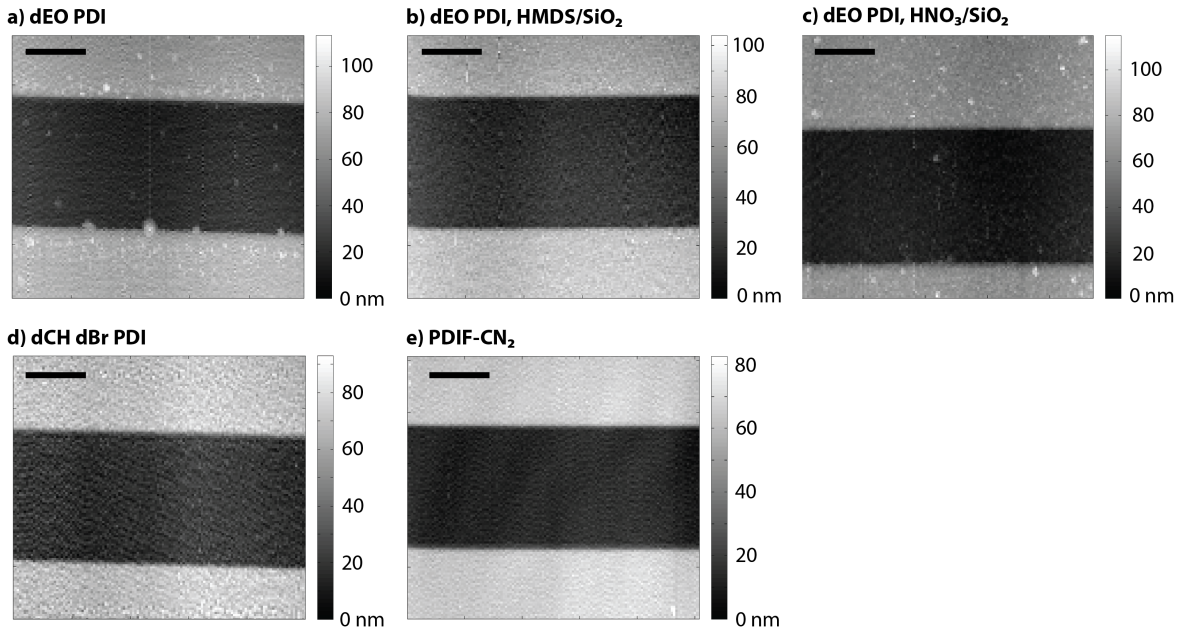


Figure 4.3: AFM topography of thermally-deposited transistors: (a) dEO PDI on bare SiO_2 , (b) dEO PDI on HMDS-treated SiO_2 , (c) dEO PDI on HNO_3 -soaked SiO_2 , (d) dCH dBr PDI on bare SiO_2 , and (e) PDIF- CN_2 on bare SiO_2 . Scale bar in (a-e) is $2 \mu\text{m}$.

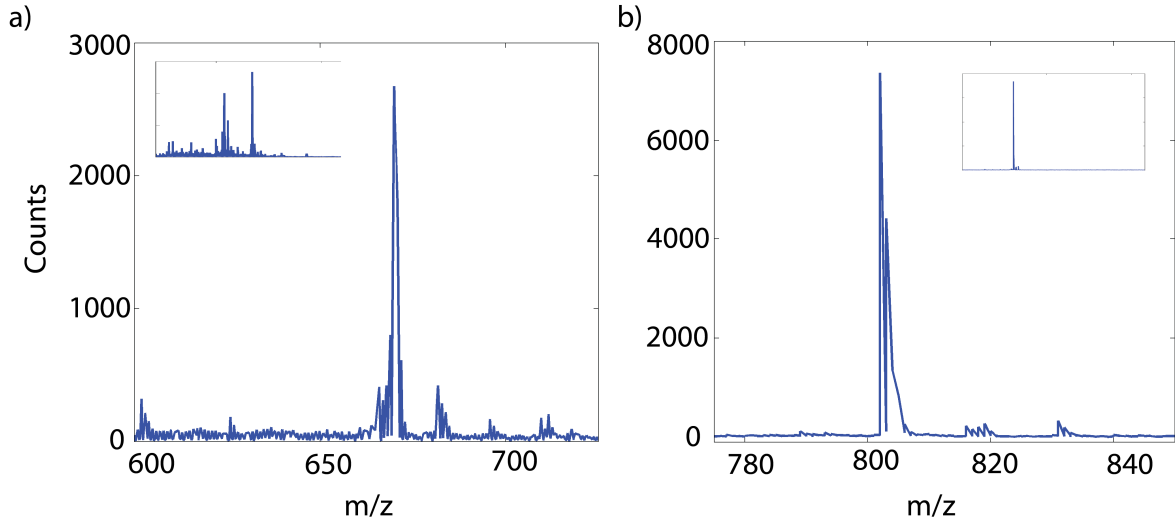


Figure 4.4: Representative LDI mass spectrometry results for thermally deposited (a) dEO PDI ($m/z = 670.9$) and (b) PDIF- CN_2 ($m/z = 804.4$) on bare SiO_2 . The insets show the same spectra on a larger m/z scale; we do not find any dimerization of our PDIs during deposition or laser desorption.

during the measurement. The samples are kept in the dark during these scans.

Charge trapping maps are shown in Fig. 4.5a-d and Fig. 4.6. Trapped charge appears as regions of negative potential (blue), while the more positive source and drain electrodes are visible above and below the transistor channel. The most negative regions at left are not trapping “hot spots” but rather represent the initial concentration of trapped charge after the gate is turned off.

In every high-LUMO sample studied, electron trapping was observed uniformly across the transistor channel. As the image progresses from left to right (slow scan direction, labeled x), the traps clear thermally over time on the order of \sim 5 minutes, suggesting that they may be relatively shallow in energy relative to the LUMO level. For a point of reference, traps in pentacene require 20 minutes or longer to clear to the same extent. Traps were not associated with obvious morphological features in any of the samples examined. These observations suggest that electron traps are not due to physical defects in the films. This uniformity across the channel width is consistent with traps forming everywhere due to a spatially independent process such as trapping at or in the dielectric, or a chemical reaction of the PDI anion radical. The PDIF-CN₂ film did not show any significant electron trapping.

Transient surface potentials obtained by averaging several rows of potential data in the channel are plotted below each transistor map (Fig. 4.5e-h, Fig. 4.6c-d). For the PDI derivatives studied, traps clear thermally in 5-10 minutes. In dEO PDI, which was studied on both bare and HMDS-treated SiO₂, the traps on the HMDS-treated sample exhibited a slightly slower thermal clearing while the traps in the evaporated film on bare SiO₂ cleared faster.

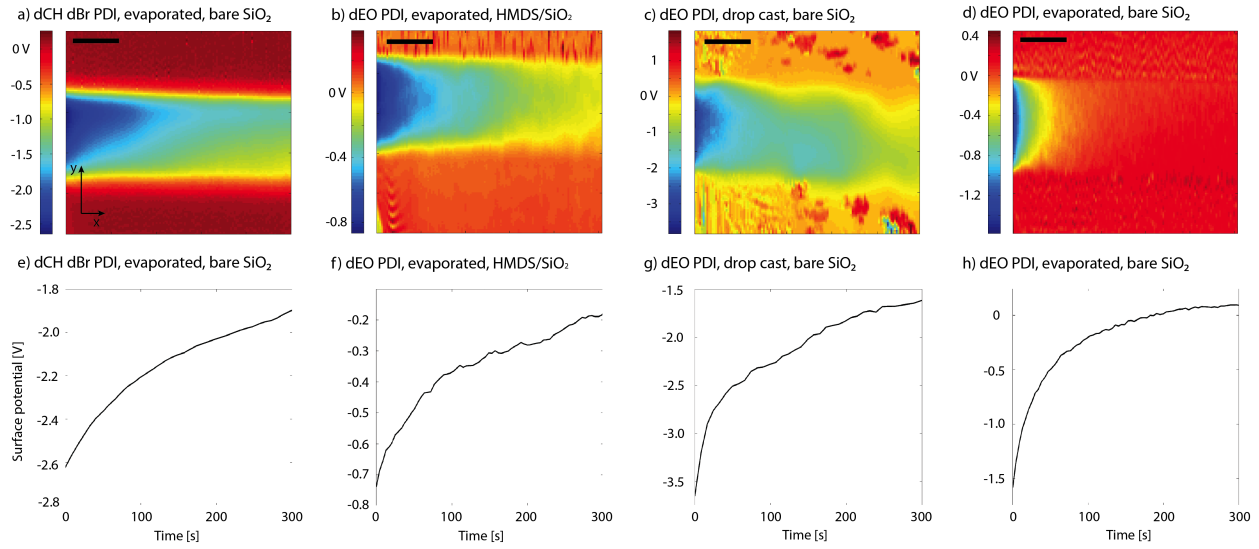


Figure 4.5: Top row: surface potential of PDI transistors after a 2 minute positive gate bias. The gate bias was +5 V prior to all images except (b) which was taken after +15 V. Bottom row: average surface potential transients from mid-channel, showing thermal trap-clearing. (a,e) dCH dBr PDI evaporated on bare SiO₂. (b,f) dEO PDI drop cast on bare SiO₂. (c,g) dEO PDI evaporated on HMDS-treated SiO₂. (d,h) dEO PDI on bare SiO₂. Scale bar is 2 μ m.

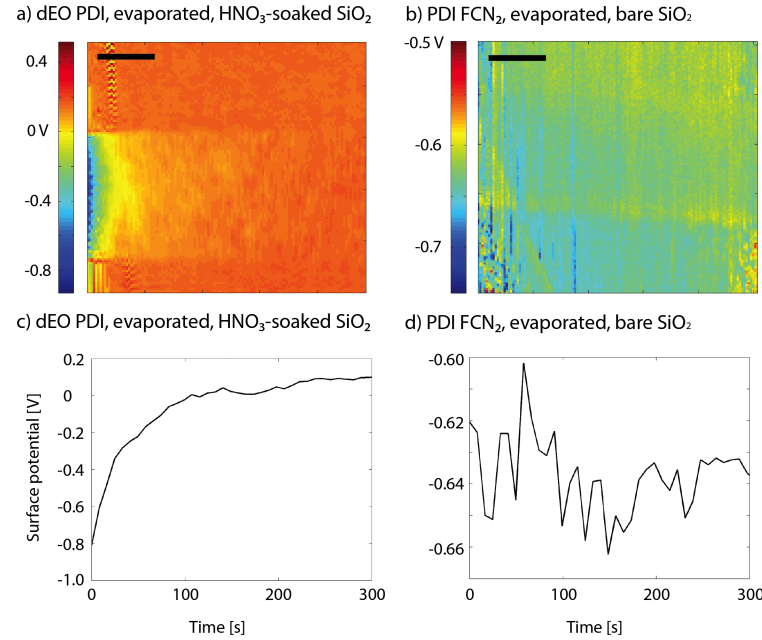


Figure 4.6: Top row: surface potential of PDI transistors after a 2 minute positive gate bias. The gate bias was +5 V prior to both images. Bottom row: average surface potential transients from mid-channel, showing thermal trap-clearing. (a,c) dEO PDI on HNO₃-soaked SiO₂. (b,d) PDIF-CN₂ evaporated on bare SiO₂. Scale bar is 2 μ m.

4.2.2 Trap-clearing spectra: results

We next examined the effects of visible illumination on traps in PDI derivatives. In *p*-type semiconductors such as pentacene, visible illumination can cause traps to clear more quickly [47]. In pentacene, measured rates of trap-clearing versus illuminating wavelength can reveal trap-clearing *spectra*, where absorptions in the neutral semiconductor or even a charged defect can lead to de-trapping faster than the thermal rate [13, 25]. A similar increase in trap-clearing rate due to light has also been observed in other PDI derivatives [17], but the wavelength dependence of this process has not been studied.

The relevant light-enhanced and thermal processes for the PDI case are sketched in Fig. 4.7. Traps can be cleared by visible light through two possible processes: excitation of the neutral semiconductor (Fig. 4.7, k_1) and excitation of the trap (k_3). In both cases, after excitation, the trapped electron is transferred to the neutral PDI (k_2 or k_4). These light-enhanced trap-clearing processes compete with the thermal trap-clearing process, where the electron is transferred directly from the trap to a neutral PDI molecule with no additional excitation (Fig. 4.7, k_5). When the PDI anion radical is formed ($\text{PDI}^{\cdot-}$, final state), the charge is mobile again and can be transported to an electrode and out of the film.

In our microscope, the visible light source is a halogen lamp fiber-optically coupled to a scanning monochromator and an attenuator. The intensity at the sample surface is low—approximately 0.5 mW/cm²—so competition between the light-dependent and the thermal processes is expected. In addition, we note that excitation of the neutral semiconductor (Fig. 4.7, k_1 - k_2) should be a more efficient trap-clearing process than excitation of the trap (k_3 - k_4). In processes k_1 - k_2 , any molecule within an exciton diffusion radius of the trap should be able to clear it, while only excitation of the trap itself would lead to the second light-enhanced process.

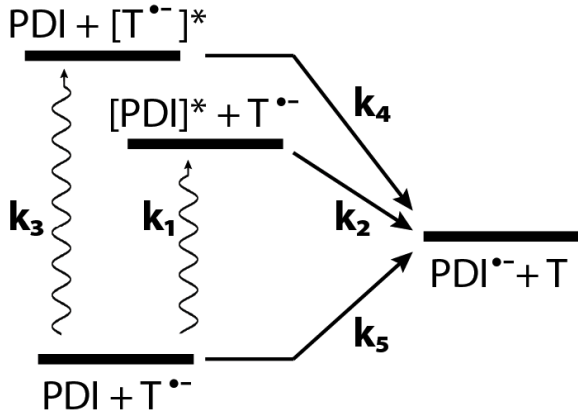


Figure 4.7: State diagram of light-enhanced (k_1-k_4) and thermal (k_5) trap-clearing processes in n -type semiconductors. k_1-k_2 : excitation of neutral PDI leads to electron transfer from trap to neutral PDI. k_3-k_4 : excitation of charged trap leads to electron transfer from trap to neutral PDI. k_5 : thermally activated electron transfer from trap to neutral PDI. Once the electron is transferred to the neutral PDI, it is mobile and can be transported to the electrode.

To obtain trap-clearing spectra, traps in the transistor channel were populated with a two-minute positive gate bias (typically $V_g = +5V$), then the surface potential was measured as a function of time while illuminating the sample from above with the optical fiber. Since trap-clearing spectroscopy is a point measurement, we collected frequency shift parabolas at a rate of 1 Hz to obtain the surface potential. Remaining traps were cleared as much as possible with the white LED followed by a dark wait of 1-3 minutes. This measurement was repeated for 36 different visible wavelengths (350-720 nm). The trap-clearing transients were fit to single exponential decays in Matlab. Finally, the rates were normalized by photon energy in eV since the experiment was carried out at constant power, not constant photon flux. This procedure is essentially identical to the experiments discussed in Ch. 2.2.2, except that the gate bias is positive here to induce electron trapping (rather than negative to induce hole trapping).

From our previous experiments in pentacene, we expected to find enhanced rates of trap clearing for illuminating energies absorbed by the neutral PDI, as well as possible rate

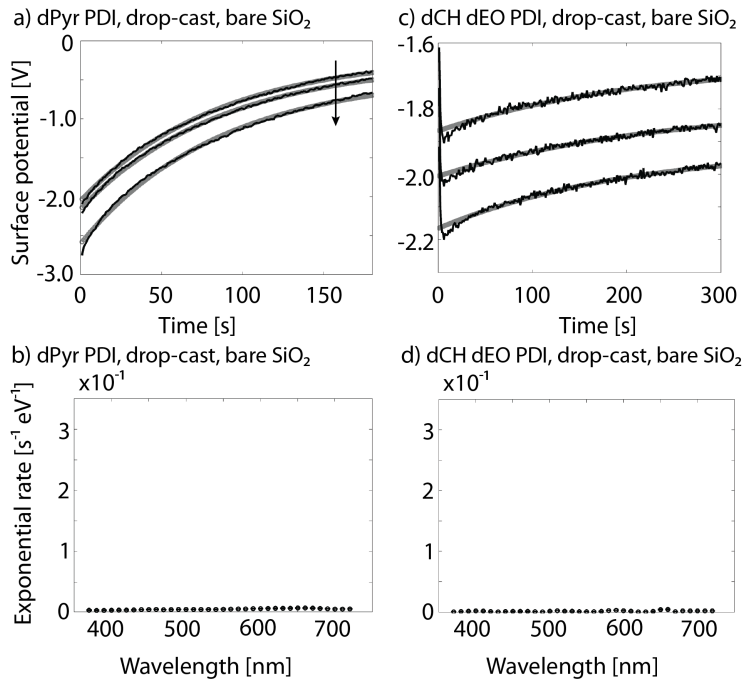


Figure 4.8: Top row: trap-clearing surface potential transients for several illumination wavelengths (black) with single exponential fits (gray); arrow indicates increasing energy. Bottom row: Trap-clearing rates versus wavelength. (a,b) Drop-cast dPyr PDI on bare SiO₂. (c,d) Drop-cast dCH dEO PDI on bare SiO₂. Rates are not enhanced above the thermal floor.

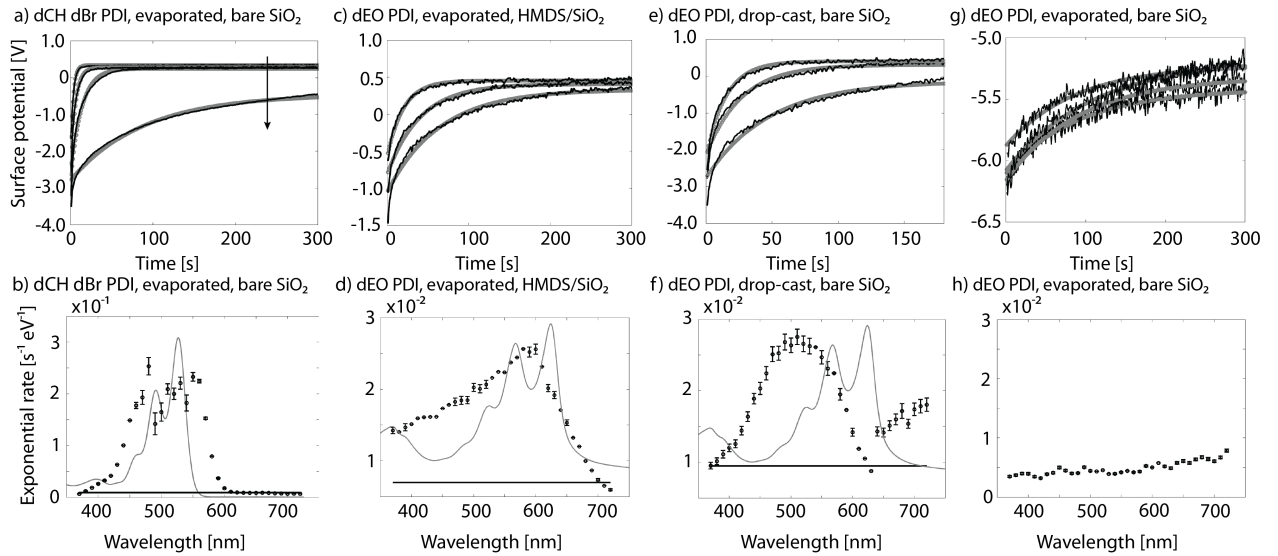


Figure 4.9: Top row: trap-clearing surface potential transients for several illumination wavelengths (black) with single exponential fits (gray); arrow indicates increasing energy. Bottom row: Trap-clearing rates versus wavelength (black open circles) with thermal floors indicated by black solid lines. Absorption spectra of the neutral PDIs overlaid in grey. (a,b) Thermally deposited dCH dBr PDI on bare SiO₂. (c,d) Thermally deposited dEO PDI on HMDS-treated SiO₂. (e,f) Drop-cast dEO PDI on bare SiO₂. (g,h) Thermally deposited dEO PDI on bare SiO₂.

enhancements due to absorption by other chemical species [13, 25]. In two of the PDI derivatives studied, dPyr PDI and dCH dEO PDI, both drop-cast on bare SiO₂, we found that light did not increase the rates of trap-clearing faster than the thermal process. The upper plots in Fig. 4.8 shows representative surface potential transients at long, medium, and short visible wavelengths (solid black lines) with single exponential fits (grey line with open circles), while the lower plots show all the trap-clearing rates measured versus wavelength for illumination across the visible spectrum. Although the concentration of trapped charge increases as the experiment proceeds, leading to the vertical offset between the transients for dPyr PDI and dCH dEO PDI, none of the measured trap-clearing rates are enhanced above the thermal rate by light. The y-axis in Figs. 4.8a,c is chosen to reflect this absence of light-enhancement for comparison with Fig. 4.9. The thermal trap-clearing rate for dPyr PDI is approximately 8E-4 s⁻¹eV⁻¹, and for dCH dEO PDI is 1E-3 s⁻¹eV⁻¹.

In contrast, traps in dEO PDI and dCH dBr PDI are cleared faster than the thermal rate when exposed to certain wavelengths of visible light. The plots in the upper row of Fig. 4.9 show representative surface potential transients with single exponential fits; the rates are clearly different for different illumination wavelengths. The plots in the lower row of Fig. 4.9 show the trap-clearing rates versus wavelength, which in this case appear to have spectral shape. For comparison, the thermal rates are plotted as solid horizontal lines and the optical absorption spectra are plotted in grey. In Fig. 4.9b,d,f,h, from left to right, thermal trap-clearing rates are $9\text{E-}3 \text{ s}^{-1}\text{eV}^{-1}$ for dCH dBr PDI, $9.5\text{E-}3 \text{ s}^{-1}\text{eV}^{-1}$ for dEO PDI evaporated on HMDS-treated SiO_2 , $1.1\text{E-}2 \text{ s}^{-1}\text{eV}^{-1}$ for dEO PDI drop-cast on bare SiO_2 , and $4.5\text{E-}3 \text{ s}^{-1}\text{eV}^{-1}$ for dEO PDI evaporated on bare SiO_2 .

The enhancement in trap-clearing rate closely tracks the absorption of the neutral semiconductor for dCH dBr PDI on bare SiO_2 (Fig. 4.9a,b) and roughly also for dEO PDI on HMDS-treated SiO_2 (Fig. 4.9c,d). However, the trap-clearing spectrum for dEO PDI drop-cast on bare SiO_2 is slightly blue-shifted relative to absorption by the neutral molecule, and there is a low-energy peak in the trap-clearing spectrum that is *absent* in the optical absorption spectrum of the neutral PDI (Fig. 4.9e,f). The same molecule evaporated onto bare SiO_2 (instead of drop-cast) exhibited slower thermal clearing rate and a slower light-enhancement: the single exponential rates are not wavelength-dependent in this sample (Fig. 4.9g,h), but the slopes of the transients at longer times do exhibit a wavelength dependence- although these “slope” rates are not strongly enhanced above the corresponding thermal rate either (Fig. 4.10).

4.2.3 Trap-clearing spectra: discussion

The thermal trap-clearing rates illustrated in Figs. 4.5e-h, 4.8b,d, and 4.9b,d,f,h exhibit variation in magnitude. For dPyr PDI and dCH dEO PDI, the thermal trap-clearing rate

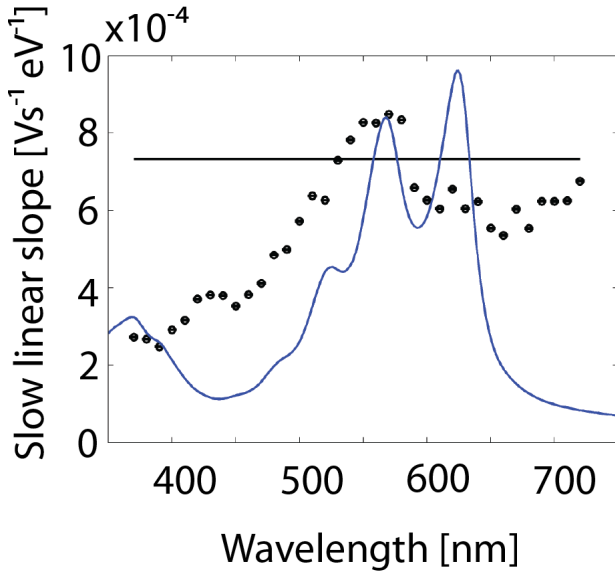


Figure 4.10: Trap-clearing spectrum for evaporated dEO PDI on bare SiO_2 . Linear fits to longer-time data (black open circles), linear fit to thermal transient at longer times (black horizontal line), optical absorption spectrum for dEO PDI (blue line).

is approximately ten times slower than thermal trap-clearing rates in dEO PDI and dCH dBr PDI. An exception to this trend is the sample of dEO PDI evaporated on bare SiO_2 , where the thermal trap-clearing rate is only five times faster than thermal clearing in dPyr PDI and dCH dEO PDI. These trends in thermal trap-clearing behavior do not appear to depend on PDI LUMO level, substrate dielectric, or film preparation method.

As shown in Figs. 4.8 and 4.9, the family of PDI derivatives studied exhibited a wide range of different trap-clearing behaviors when exposed to visible light. All the PDIs investigated strongly absorb visible light, but in only two of the four were electron trap clearing rates enhanced by light. Interestingly, the traps with the slower thermal trap-clearing rates (dPyr PDI and dCH dEO PDI) are the ones that do not exhibit a response to light, while the traps with faster thermal trap-clearing rates (dEO PDI and dCH dBr PDI) do respond to light.

For dPyr PDI and dCH dEO PDI, the unresponsiveness of trap-clearing to light could indicate that the thermal rate of trap-clearing (Fig. 4.7, k_5) is faster than any of the other

light-related electron transfer processes (Fig. 4.7, k_1 to k_4). However, since the thermal trap-clearing rates here are *slower* than the thermal rates in the light-responsive materials, this idea seems less likely. The other possible interpretation is that in these samples, electron transfer from the trap (Fig. 4.7, k_2 or k_4) is not the limiting process in trap-clearing. For example, transport in the neutral PDI could be slow to move free charge away from the trap site; this might be the case for dCH dEO PDI, given the somewhat discontinuous morphology of the film (Fig. 4.2c).

In contrast, dCH dBr PDI on bare SiO_2 and dEO PDI on HMDS-treated SiO_2 exhibited trap-clearing spectra close to the neutral PDI absorption spectra (Fig. 4.9a-d). This observation is consistent with trap-clearing processes k_1 and k_2 in Figure 4.7. We do not find evidence here for processes k_3 and k_4 ; however, this does not mean there are no chemically distinct traps in these samples. Processes k_3 and k_4 could simply be slower, or the energy required to drive k_1 and k_3 could be similar enough that a distinct peak is not visible in the trap-clearing spectrum. In addition, the process involving excitation of the neutral PDI (k_1 and k_2) should clear traps much more efficiently than excitation of the trap: any excitation within an exciton diffusion length of the trap site should be able to drive clearing via process k_2 , but only direct excitation of the trap leads to clearing via processes k_3 and k_4 . We note that light-enhanced trap-clearing is ~ 10 times faster in dCH dBr PDI than dEO PDI.

A film of dEO PDI drop-cast on bare SiO_2 was the only sample to show enhanced rates of trap clearing with a significantly different lineshape than the neutral PDI absorption (Fig. 4.9e-f). Compared with the trap-clearing spectrum in the same PDI on HMDS-treated SiO_2 , the main peak in the trap-clearing spectrum is blue-shifted, and there is a new low-energy feature. This blue-shifted absorption might be consistent with excitation of a 1,6 instead of the 1,7 isomer, as has been observed in pyrrolidine core-substituted PDI derivatives [144], although it is unclear why an isomer would play an important role in trap-clearing for

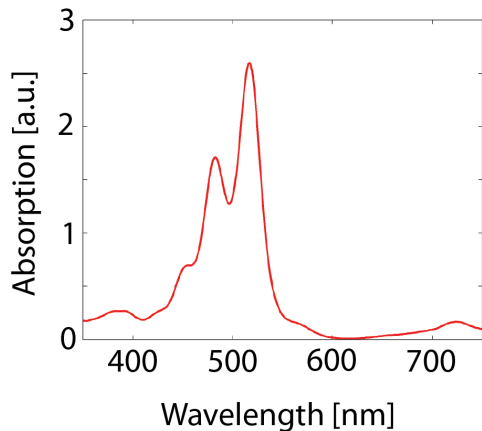


Figure 4.11: Solution absorption spectrum of dEO PDI anion radical; dEO PDI was reduced by fluoride ions in DMSO (Braunschweig group).

the same material on one substrate but not another. The low energy feature could indicate absorption by the PDI anion radical (Fig. 4.11) [145].

We note that in dEO PDI evaporated on bare SiO_2 , thermal trap-clearing was slower, and there was not a strong light-induced rate enhancement for single exponential rates (Fig. 4.9g-h). A weak wavelength dependence is observable in the longer-time linear slopes, with a similar lineshape as the film of dEO PDI drop-cast on bare SiO_2 (Fig. 4.10). Film preparation method has been shown to have a strong effect on trap distribution and formation in pentacene derivatives [28], so it is reasonable that different film preparations of the same PDI would show different thermal trap-clearing rates. However, as an intermediate case between the apparently light-insensitive traps in dPyr PDI and dCH dEO PDI, and light-sensitive traps in dCH dBr PDI and other samples of dEO PDI, this sample suggests that films with slower thermal trap-clearing rates are also slower to respond to light.

Between films of dEO PDI evaporated on bare or HMDS-treated SiO_2 , traps are cleared much faster both thermally and with light in the film on HMDS. This observation seems consistent with the observation of faster rates of trap-clearing in OTS-treated versus bare SiO_2 *p*-type transistors [46]. Thermal and light-enhanced trap-clearing rates in drop-cast

dEO PDI are on the same order as dEO PDI evaporated onto HMDS-treated SiO_2 . The more crystalline morphology of the drop-cast film may be partially responsible for these faster trap-clearing rates in drop-cast dEO PDI (Fig. 4.2b vs. Fig. 4.3a).

Comparing the spectral lineshapes for trap-clearing in dEO PDI evaporated on HMDS-treated SiO_2 and drop-cast on bare SiO_2 , the traps on HMDS/ SiO_2 seem to be cleared via excitation of the neutral PDI (k_1 and k_2), the shifted peak on bare SiO_2 may be evidence for excitation of another chemical species (k_3 and k_4). These differences in the trap-clearing spectra could indicate that light-enhanced trap-clearing processes are different for the same PDI on HMDS-treated versus bare SiO_2 . Different trap-clearing processes would suggest that trap chemistry could be different for electron traps in PDI thin films on HMDS-treated versus bare SiO_2 , but whether the traps on bare SiO_2 arise from silanol groups ($-\text{SiO}^-$) is not clarified by these measurements. Further computational study would help revise our peak assignments and aid interpretation of these spectra; however, calculations for PDIs and their anion radicals will be more demanding than those performed for pentacene cation radicals [25], due to their larger size.

4.3 Trap formation kinetics and surface treatments

Since our trap-clearing spectroscopy did not offer decisive information regarding the chemical mechanism of trapping in PDI transistors, we thought a kinetics study of the trap formation process might shed light on the trapping process reaction order for the free charge carrier, anion radical PDI^- . Here, we focus on the trapping process in thermally deposited dEO PDI transistors on three different substrates: bare SiO_2 , HNO_3 -soaked SiO_2 , and HMDS-treated SiO_2 . These substrates were selected for their different silanol concentrations. HNO_3 treatment increases the silanol concentration on SiO_2 but also increase surface roughness

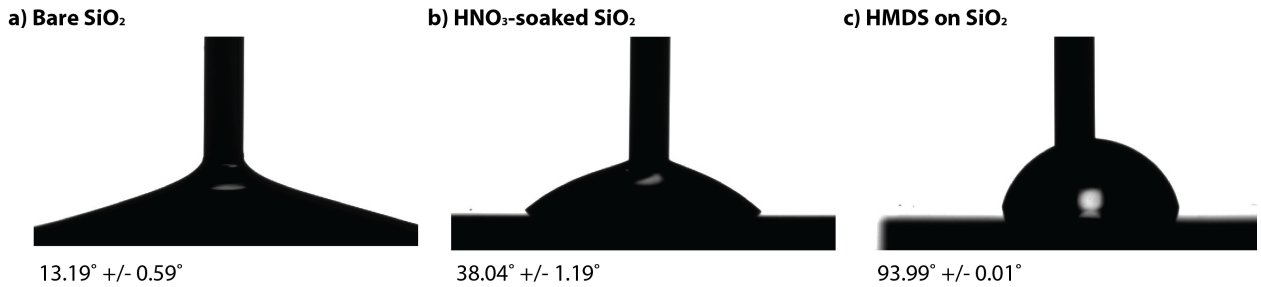


Figure 4.12: Water contact angle measured for (a) bare SiO₂, (b) HNO₃-soaked SiO₂, and (c) HMDS on SiO₂ bottom-contact transistor chips. Angles were measured on the Rame-Hart 500 Contact Angle Goniometer in the Nanobiotechnology Center (NBTC) at CNF.

[146, 147]. HMDS treatment should passivate silanol groups [129].

The water contact angles for the three different substrates studied are shown in Fig. 4.12. Since the acid soak increases the SiO₂ roughness, the water contact angle is increased despite the increased surface hydrophilicity. Our measured contact angle of 38° is consistent with literature values [147]. We anticipated that if mechanisms like as Eqs. 4.1-4.17 were at play, increasing the silanol concentration on the transistor dielectric surface would increase trap formation rates.

4.3.1 Trap formation rate experiment

To measure trap formation rates, we employ an alternating series of gate bias pulses and surface potential measurements. When the gate is on, trap states in the channel are being filled. When the gate is off, traps are not shielded by free charge, and a surface potential measurement reflects the amount of trapped charge [26–28]. This scheme is sketched in Fig. 4.13. We employ tip voltage-cantilever frequency shift parabolas to measure the surface potential in the few hundred-millisecond pauses when the gate is off, Fig. 4.13a. Since we know the length of t_{pulse} , we can plot the surface potential as a function of the time the

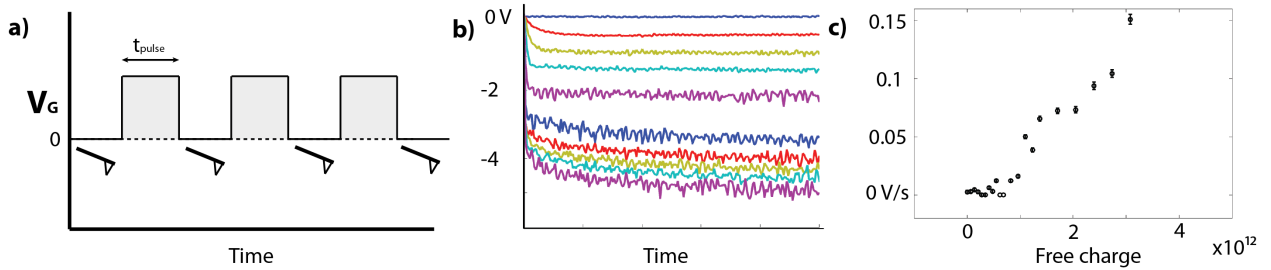


Figure 4.13: (a) Alternate gate pulse and measurement scheme used in trap formation kinetics measurements. The gate is repeatedly pulsed on for a duration t_{pulse} ; when the gate is off, the trapped charge is measured. Since t_{pulse} is known, the potential versus gate “on” duration can be extracted, as shown in (b). For each gate voltage, the trap formation rate is extracted from the surface potential transient. These rates can be plotted versus free charge calculated from the gate voltage and dielectric capacitance, as in (c). (b) and (c) do not correspond to the same dataset.

gate bias is turned on, Fig. 4.13b. Finally, by fitting the raw transients, we can extract the trap formation rates versus gate voltage, Fig. 4.13c (b and c do not correspond to the same dataset). These measurements are all performed in high vacuum.

4.3.2 Trap formation rate results and discussion

Example raw data sets from this trap formation kinetics experiment are shown in Fig. 4.14 for trap formation in dEO PDI on bare SiO_2 , HNO_3 -soaked SiO_2 , and HMDS-treated SiO_2 . We measured substantial noise in the surface potential at higher gate voltages in the HNO_3 -soaked SiO_2 sample, but this noise was determined to be related to a malfunction in our microscope, not the sample (at the end of its lifetime, our interferometer laser diode was unstable, perhaps mode hopping frequently, causing intermittent lapses in our surface potential parabola tracking). Looking at all three data sets, the surface potentials all generally decrease over time as traps form, and the overall magnitude of trapping is generally larger for greater gate voltages. These trends are consistent with our expectation that electron trap formation rates depend in part on the concentration of available free charge in the channel.

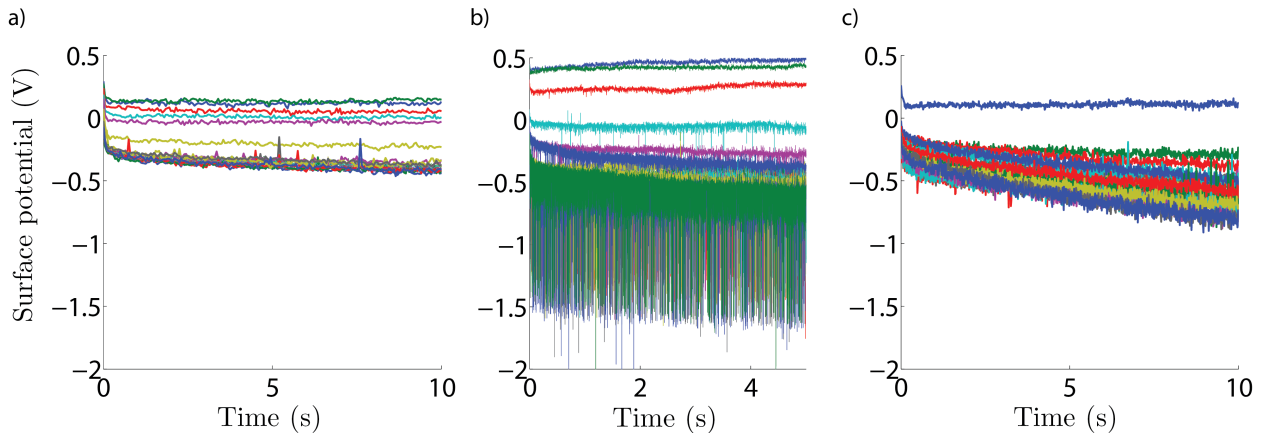


Figure 4.14: Sample raw trap formation surface potential transients collected from dEO PDI transistors on (a) bare SiO_2 , (b) HNO_3 -soaked SiO_2 , and (c) HMDS-treated SiO_2 .

At first glance, it is also apparent that trap formation rates are not identical between the three data sets.

We collected at least one, but usually a few trap-formation transient surface potential data sets for dEO PDI films on these treated SiO_2 substrates. The best fit for these surface potential transients was, again, an assumed two-exponential process where the slow portion is fit to a line and the fast portion is fit to an exponential decay, as in Eq. 2.3. Intriguingly, the slow portion of this trapping process contains a gate bias dependence, while the fast portion does not. The electron trapping mechanism we are observing appears to be a combination of a fast and a slow trapping process. This finding might be consistent with the Yoon *et al.* mechanism in Eq. 4.2, but could also reflect a different process, such as a fast chemical trapping in the PDI that is slowly transferred to silanols.

We focus here on the slow process that shows a dependence on the amount of available charge. To obtain the free charge at each gate voltage, the applied gate bias was converted to a free charge concentration via the dielectric capacitance:

$$\text{Free Charge} = C \times V_g \times e = \frac{\epsilon_0 \epsilon_r V_g e}{d} \quad (4.18)$$

where C is the SiO_2 dielectric capacitance, V_g is the gate bias, e is the elementary charge of

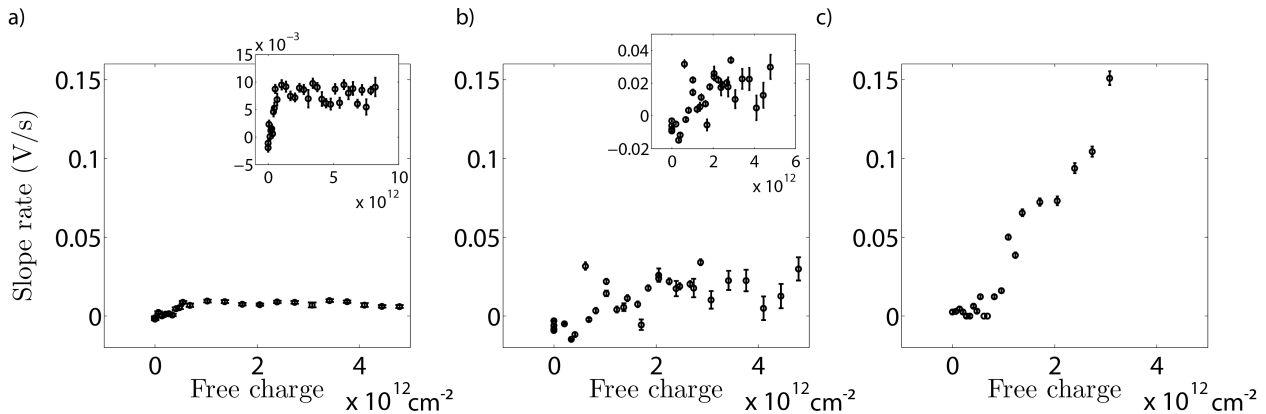


Figure 4.15: Sample trap formation rates versus free charge collected from dEO PDI transistors on (a) bare SiO_2 , (b) HNO_3 -soaked SiO_2 , and (c) HMDS-treated SiO_2 . These plots correspond to the raw data in Fig. 4.14. The insets in (a) and (b) are zoomed-in plots of the same data for clearer viewing on an expanded y-axis.

an electron, ϵ_0 is the vacuum dielectric constant, ϵ_r is the dielectric constant ($\epsilon_r = 3.9$ for SiO_2), and d is the dielectric thickness (typically ~ 300 nm thermal SiO_2). This calculation assumes that all the applied voltage is converted to free charge, or in other words, that threshold voltage $V_{th} = 0$ V. To incorporate V_{th} , V_g should be replaced with $V_g - V_{th}$ in Eq. 4.18.

The slow trap formation rates as a function of free charge are shown in Fig. 4.15, corresponding to the raw data sets in Fig. 4.14. For these example data sets, the rates of trap formation exhibit some unexpected behavior. First, the rates of trap formation on bare SiO_2 (Fig. 4.15a) are low compared with the other samples. Not only are these rates low, but they also exhibit a saturation around $V_g = 2\text{V}$ (see inset)- in other words, the rate of trap formation is constant as free charge increases- despite the evident presence of silanol groups on the surface.

The trap formation in dEO PDI on HNO_3 -soaked SiO_2 (Fig. 4.15b) reaches rates twice as great as the rates in dEO PDI on bare SiO_2 . This observation is consistent with our expectations for the greater concentration of silanols on this acid-treated surface. However,

the greatest surprise was the high rate of trap formation on HMDS-treated SiO₂ (Fig. 4.15c). Not only are these rates much faster than the other samples, but they also continue to increase as the amount of free charge increases, whereas the rates on the other substrates saturate at larger gate biases. This finding suggests that trapping rates in dEO PDI on HMDS-passivated SiO₂ are not decreased by the decreased number of silanols on the substrate, and are instead strongly related to the amount of available charge in the working device.

The faster rates of trap formation in HMDS-treated devices might actually be consistent with our observations of increased trap-clearing rates in HMDS-treated sample, as discussed in Ch. 4.2.3. Traps in HMDS-treated devices may be shallower than traps on bare SiO₂. The observation that these HMDS-related trap states are also filled faster than traps on bare SiO₂ could fit with this overall picture.

With these surprising results in mind, we found it was important to collect the trap-formation rate information from all the experiments we performed in one plot. This data is presented in Fig. 4.16; Fig. 4.16a shows a zoomed in view of the same data shown in Fig. 4.16b. The solid lines are linear fits to individual data sets and are meant only as guides to the eye. The datasets with connecting lines represent data that was collected without gate randomization.

Clearly, the first measurements we made (Fig. 4.15) are not representative of general device behavior. Instead, Fig. 4.16 shows that we essentially have a scatter plot of trap formation rate dependence on free charge. We may observe a general trend of faster trap formation rates for samples with silanol groups (black circles, bare SiO₂, and blue squares, HNO₃-soaked) versus passivated samples (red triangles, HMDS-treated), but this trend is contradicted by some particularly slow-trapping SiO₂ samples and an outlying measurement of very high trap formation rates in an HMDS-treated sample (Fig. 4.16b).

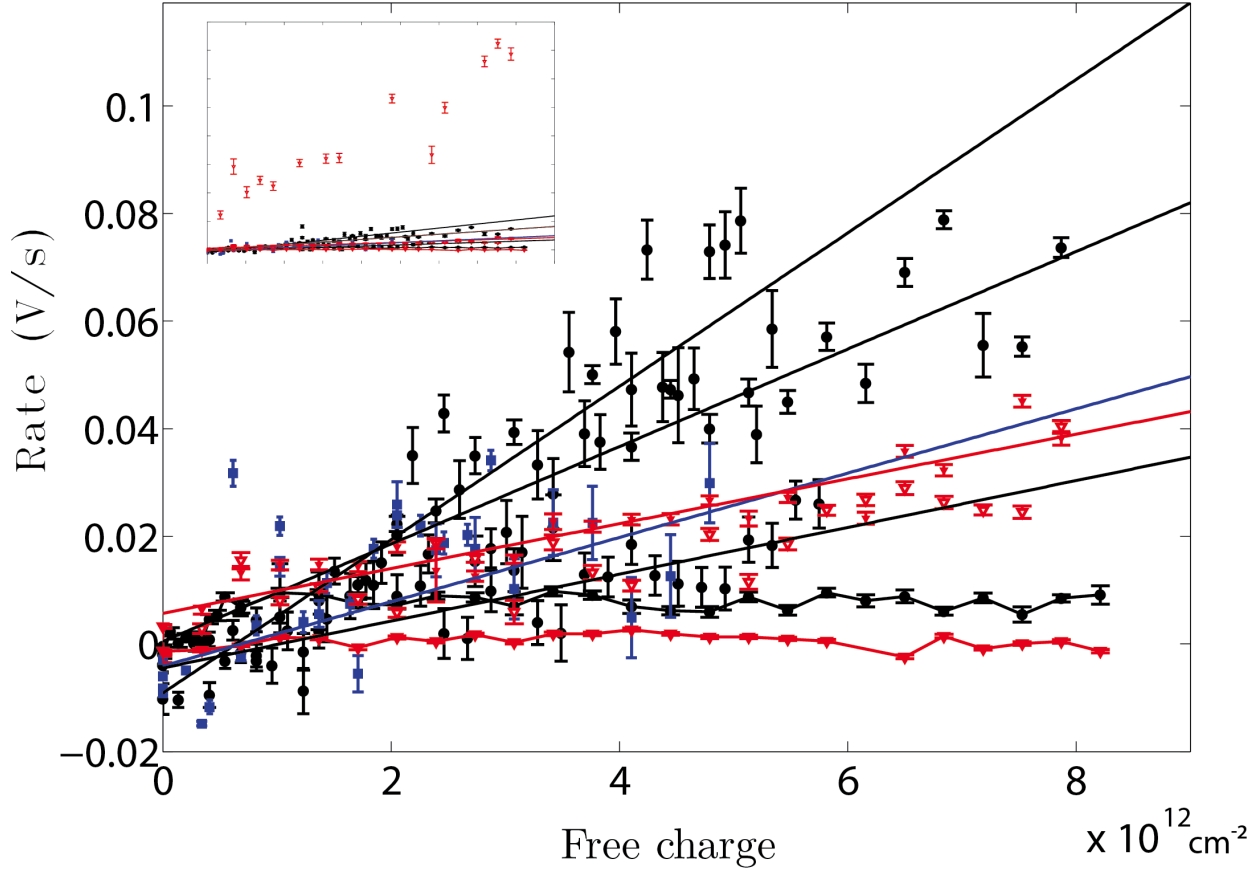


Figure 4.16: All the trap formation kinetics data are plotted in (a) and (b). Black circles represent bare SiO_2 , blue squares represent HNO_3 -soaked SiO_2 , and red triangles represent HMDS-treated SiO_2 . (a) is a zoomed-in version of (b) to show the variation in the lower-rate portions of the data. The solid lines are guides to the eye. Different values of t_{pulse} were used to generate many of these data sets, but accounting for t_{pulse} does not reveal any trends.

Evidently, our manipulation of dielectric surface chemistry is not controlling the rates of trap formation in these dEO PDI transistors. We expected that increasing or decreasing the concentration of silanol groups on the substrate would correspondingly increase or decrease trap formation rates in the transistors. However, we cannot conclude that such a dependence exists, a finding that seems to refute the silanol trapping mechanism. Instead, another factor that we do not control here must be more important; candidates for this factor could include humidity [128] (although HMDS treatment would be expected to decrease the amount of water in the film), interfacial disorder in our amorphous films, or the formation of long-lived intermediate species.

If an intermediate species is preventing the reproducible measurement of initial trap formation rates, a new device geometry might improve this trap formation kinetics experiment. Instead of using the same device for repeated measurements, an array of smaller devices could be fabricated on the same chip. Trap formation rates could be measured for one gate bias in each single device. This “fresh reaction vessel” approach would avoid residual trap intermediates arising from device reuse. Such a multi-device chip would require modification to the microscope to enable wiring of multiple devices, as well as an improved sample positioning system to make sure the different devices are simple to find.

4.4 Conclusions

In this chapter, we have presented the results of two experiments exploring the chemistry of trapping in PDI films. First, we used trap-clearing spectroscopy to learn whether other chemical species besides the semiconducting PDIs were involved in light-assisted trap-clearing. In dEO PDI transistors on bare SiO₂, the trap-clearing rate enhancement around 720 nm suggests that the PDI anion radical might be involved in trap-clearing. These devices also

exhibit the fastest trap-clearing rates at wavelengths slightly blue-shifted relative to the neutral PDI absorption; further theoretical study is required to determine whether this shift could be attributed to a different species such as a protonated PDI anion radical or a PDI isomer. This experiment also revealed that dEO PDI transistors on HMDS-treated SiO₂ exhibit *more* trapping than devices on bare SiO₂, but that these HMDS traps clear faster than traps on SiO₂, consistent with observations in F8T2 on OTS-treated SiO₂ [46].

Second, we performed measurements of trap-formation rates in dEO PDI transistors with different channel dielectric chemistries (bare SiO₂, HNO₃-soaked SiO₂, and HMDS-treated SiO₂). We were unable to discern a strong trend based on dielectric chemistry in the trap formation rates versus free charge concentration data. We conclude that despite the regular citation of silanols as an important source of electron trapping in *n*-channel devices [3, 129, 131, 148], passivation of the dielectric surface with monolayers like HMDS does not seem to slow the formation of traps. In future work, a new multi-device sample geometry and a reliable method for locating these devices without breaking vacuum are needed to carefully investigate trap formation kinetics.

4.5 Acknowledgements

The PDI derivatives used for drop-casting were synthesized and purified by Dr. Zhong Li. The dCH dBr PDI used for thermal deposition was synthesized and purified by Dr. Zhong Li. The dEO PDI used for thermal deposition was synthesized and purified by Dr. David Ley. Drop-cast PDI transistors were prepared by Dr. Zhong Li. The solution and thin film absorption spectra for PDI derivatives shown in Figs. 4.8 and 4.9 were collected by Dr. David Ley. The water contact angles were measured using a Rame-Hart 500 Contact Angle Goniometer in the NanoBiotechnology Center (NBTC) at the Cornell Nanoscale Science

and Technology Facility (CNF). This work made use of the Cornell Center for Materials Research Shared Facilities which are supported through the NSF MRSEC program (DMR-1120296): the mass spectrometry data was collected using a Waters MALDI Micro MX time-of-flight benchtop mass spectrometer with a 10 Hz N₂ UV laser as described in Ch. 2.5.2. 50-70 individual spectra from each sample were combined for data analysis. This work was supported by an NSF graduate research fellowship as well as funding from NSF-DMR 1006633 and NSF-DMR 1309540.

CHAPTER 5

POSITION-MODULATED FM-KELVIN PROBE FORCE MICROSCOPY

5.1 Introduction

High-quality local measurements of electric fields are critical to understanding charge injection and transport in organic semiconducting materials. In this chapter, we report a new variation of frequency-modulated Kelvin probe force microscopy (FM-KPFM) that enables local measurements of electric field by employing position modulation and lock-in detection instead of the usual numeric differentiation of the surface potential. We present, to the best of our knowledge, the first formal expressions for the electric field signal-to-noise in both the numeric-differentiation and position-modulation methods. As we will show, these methods can in principle yield similar results in terms of the overall electric field noise (δE_{rms}) if treated carefully and with attention to detail.

5.1.1 Motivation

Charge transport theory predicts device behavior as a function of electric field. Making local measurements of electric fields is especially important for understanding local performance in less ordered materials like organic semiconductors. Scanning probe techniques that are sensitive to electrostatic forces usually measure contact potential differences between the cantilever tip and the sample, not electric fields. These voltage measurements can be transformed into lateral electric fields by taking the numeric spatial derivative [30, 34], yielding electric field line scans.

Electric field profiles obtained by differentiating local potentials can shed light on charge

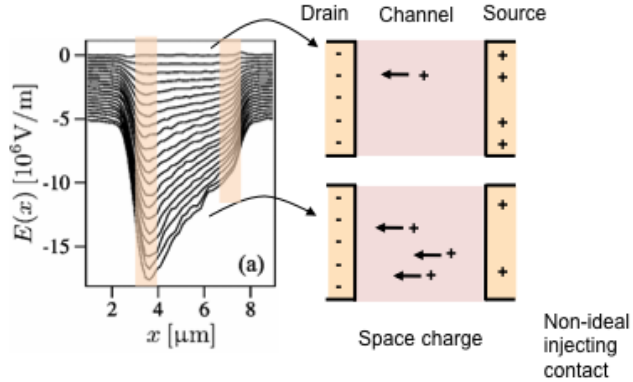


Figure 5.1: Electric field profiles across a two-terminal TPD-PS device at different channel biases [16] and sketches of corresponding charge distributions. The electric field steps at the contacts correspond to charge density at the electrodes, and the difference in electric field at the contacts corresponds to space charge in the channel. The size of the electric field at the injecting contact is a measure of the contact quality; an ideal contact would not require a field to inject charge into the channel.

injection and transport in organic devices. If a scanning probe measurement of surface potentials reveals a minimal voltage drop at the injecting contact, charge transport is often assumed to be bulk-limited, rather than injection-limited. However, even in the “bulk-limited” case, there can be substantial variation in the quality of the injecting contact [16].

$$\sigma = \epsilon E \quad (5.1)$$

The quality of injection can be assessed by measuring the local electric field between two contacts. We can then use a simple Gauss’ law relationship (Eq. 5.1) to sketch the amount of charge on each contact (Fig. 5.1). The difference in the amount of charge on each contact is space charge in the channel. The key point here is that there is a nonzero electric field at the injecting contact, meaning that the contact is not ideal. Measuring the electric field at the injecting contact as a function of channel voltage can offer a metric for the quality of charge injection that is not accessible from simple surface potential profiles.

Variations in contact quality are often thought to be the result of energetic barriers to

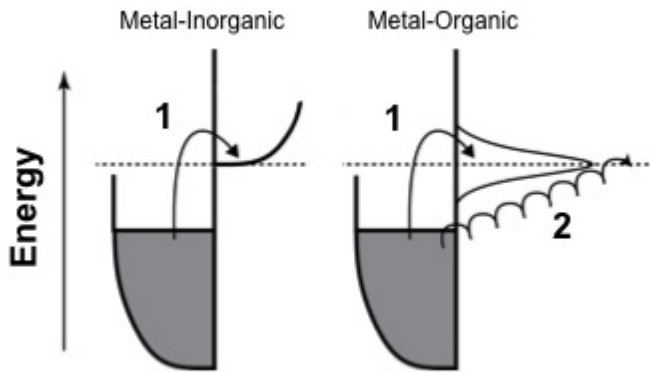


Figure 5.2: Injection processes for a traditional metal-inorganic semiconductor interface (left) and a metal-organic interface (right). In traditional models, injection is considered an activated process (1). On the other hand, organic semiconductors can have a range of possible energy band widths based on the degree of disorder in the system. If the organic energy band is narrow, injection can be an activated process (1), but if the tail states extend down to the metal states then injection can appear activationless (2).

charge injection, but for organic semiconductors, the energetic picture can be more complex (Fig. 5.2). Injection is usually an activated process for metal-inorganic semiconductor junctions, and may also be an activated process for metal-organic junctions if the organic energy band is narrow and offset from the metal band. However, organic semiconductors are often much more disordered than inorganic materials, and this disorder can lead to broadening of the organic material's energy bands. In this limit, charge injection can be essentially activationless if the organic tail states overlap with the filled metal states. Measurements of electric field profiles at various channel voltages and temperatures can help determine which limiting case best describes charge injection in a given device [14, 29].

Electric fields are crucially important to charge transport as well as charge injection. Even when injection is poor, it is often of great interest to evaluate the semiconducting material itself. Scanning probe measurements can help decouple material performance from device performance. Transistor current can be defined as:

$$I_{SD} = WC_i(\phi(x) - V_G)\mu E \quad (5.2)$$

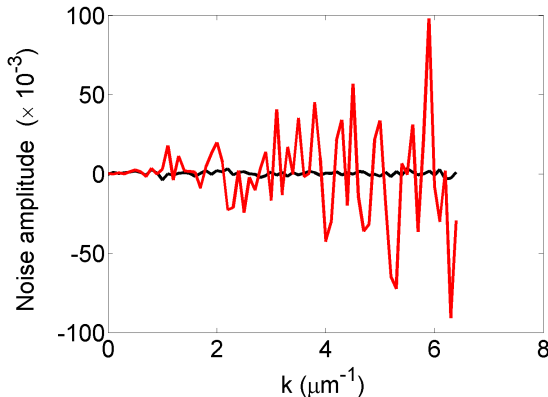


Figure 5.3: Voltage noise versus position in k-space, before (black) and after amplification by a spatial derivative (red).

where I_{SD} is source-drain current, W is channel width, C_i is the dielectric capacitance, $\phi(x)$ is the measured surface potential, V_G is the gate voltage, μ is mobility, and E is electric field [30, 31]. Surface potential profiles can be measured and differentiated to obtain calculated electric fields, leaving mobility as the only unknown [30]. An example of such a measurement is shown in Chapter 3, Fig. 3.6. This method of calculating material mobility is powerful because it extracts local material properties from a bulk current and does not need to address any poor performance due to charge injection. The charge density dependence, temperature dependence, and electric field dependence of the mobility can all be studied independent of charge injection [30].

In most electrical scanning probe measurements, like those discussed above, the electric field is calculated from the surface potential with a numeric derivative. However, this method inherently introduces noise into the electric field measurement. To see this, we can write the surface potential versus position as a Fourier transform and take the spatial derivative in k-space:

$$-\frac{d}{dx}\phi(x) = -\frac{d}{dx} \int \hat{\phi}(k)e^{ikx}dk = \int (\hat{\phi}(k)\textcolor{red}{ik})e^{ikx}dk \quad (5.3)$$

The spatial derivative leads to multiplication by k , amplifying signals at high spatial fre-

quencies. In Fig. 5.3, the original signal is show in black, and the noise-amplified signal is shown in red. The amplification translates to increased noise in the potential signal when the inverse Fourier transform is applied. This brief explanation illustrates why derivatives act as high-pass filters.

The inherent noise in obtaining electric fields via potential differentiation could help explain why such scanning probe measurements are rarely employed for material studies. The potential linescans must be obtained in high vacuum to be clean enough to obtain reasonable electric fields [30, 31]. Some efforts have been made to calculate electric fields from potential measurements taken in air, but these fields are quite noisy and difficult to interpret in detail [32, 33]. In this chapter, we set out to modify the usual FM-KPFM to enable direct spatial imaging of electric fields while avoiding numeric derivatives.

5.2 Concept: Position Modulated FM-KPFM

Our approach to avoiding taking the numeric derivative is to allow the charged cantilever to take the spatial derivative of the potential for us (Fig. 5.4). Rather than simply scanning the tip continuously across the sample in the x direction, a small oscillation on the order of 50-150 nm in the x direction is added to the scan position. This position modulation means that the surface potential, ϕ , is now a function of both position and time, as in Eq. (5.4), where ω is the frequency of the position modulation.

$$\phi(x, t) = \phi(x) + \frac{\partial \phi}{\partial x} \delta x \cos(\omega t) \quad (5.4)$$

The time-dependent portion of the surface potential measurement can then be rewritten in terms of the local electric field, as in Eq. 5.6. By adding a small oscillating component to the cantilever scanning position, the local electric field can be extracted from the surface

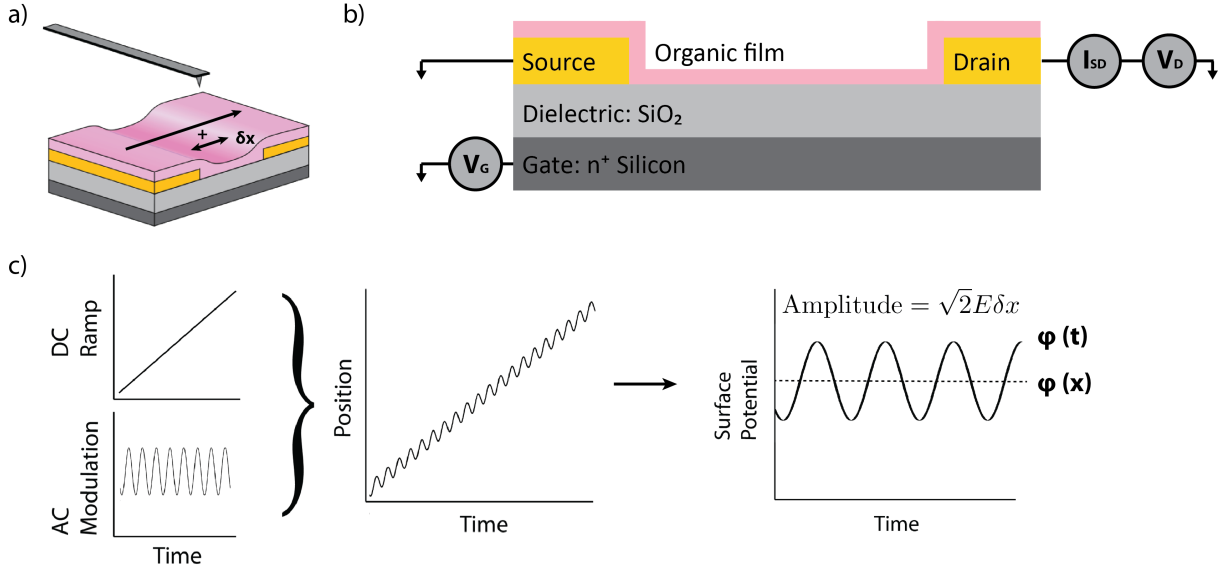


Figure 5.4: (a) Sketch of cantilever above transistor channel with scan direction and modulation. (b) Schematic of transistor cross-section, illustrating connections to ground and voltage/current sources. (c) Sketch of DC ramp and AC position modulation summed to give the overall scanning motion used. This motion yields an oscillating surface potential in time, also sketched. The amplitude of this signal is related to the electric field.

potential signal.

$$\phi(x, t) = \phi(v_{\text{tip}}t + x_m \cos(\omega t)) \quad (5.5)$$

$$\phi(x, t) \approx \phi(x) - E\delta x \cos(\omega t) \quad (5.6)$$

We note that the expression in Eq. 5.6 is an approximation. We have recently discovered that an exact analytical expression can be written for the expansion of $\phi(x, t)$, which will be discussed in a future publication.

$$\phi(v_{\text{tip}}t + x_m \cos(\omega t)) = \sum_{k=0}^{\infty} e^{ikv_{\text{tip}}t} e^{ikx_m \cos(\omega t)} \hat{\phi}(k) \quad (5.7)$$

In practice, the position-modulated EFM surface potential signal oscillates in time. The local electric field is extracted from the amplitude of this signal as in Eq. (5.8), where A is the zero-to-peak amplitude of the oscillating surface potential. The surface potential for a

given position is the average value of the oscillating signal.

$$E \propto \frac{A}{\partial x} \quad (5.8)$$

As we show in our derivations below, for this relationship to hold it is very important that the change in surface potential due to the position modulation is tracked in real time and not cut off by any of the lock-in detectors in the experiment. When the oscillating potential is measured accurately, the experiment avoids artifacts in the electric field arising from position-dependent capacitance changes. This caveat limits the speed of the experiment because the position modulation must be slow enough to pass through the tip modulation lock-in detector and feedback loop.

5.3 Data workup process

We process our position-modulated potential signal in Python, using the Marohn group “freqdemod” package [<http://freqdemod.readthedocs.org/en/latest/intro.html>]. Although in principle it is possible to use a third lock-in detection step to read in the position-modulated term, in practice it can be difficult to track this signal in real time with small modulations and large lock-in bandwidths. In this work, we instead consider the data a function of time and use filters in Fourier space at 0 Hz and $\omega_x/2\pi$ Hz to examine the DC and AC components of the signal, respectively. We use the DC signal obtained in this manner as a direct constant-time comparison with the position-modulation method. In this section, we illustrate an example data workup process.

Figure 5.5 illustrates the transformation of the raw signal in time into the Fourier domain. We first perform several small adjustments to the raw data to facilitate this transformation. We shift the baseline of the potential scan to zero, and we double the size of the dataset to

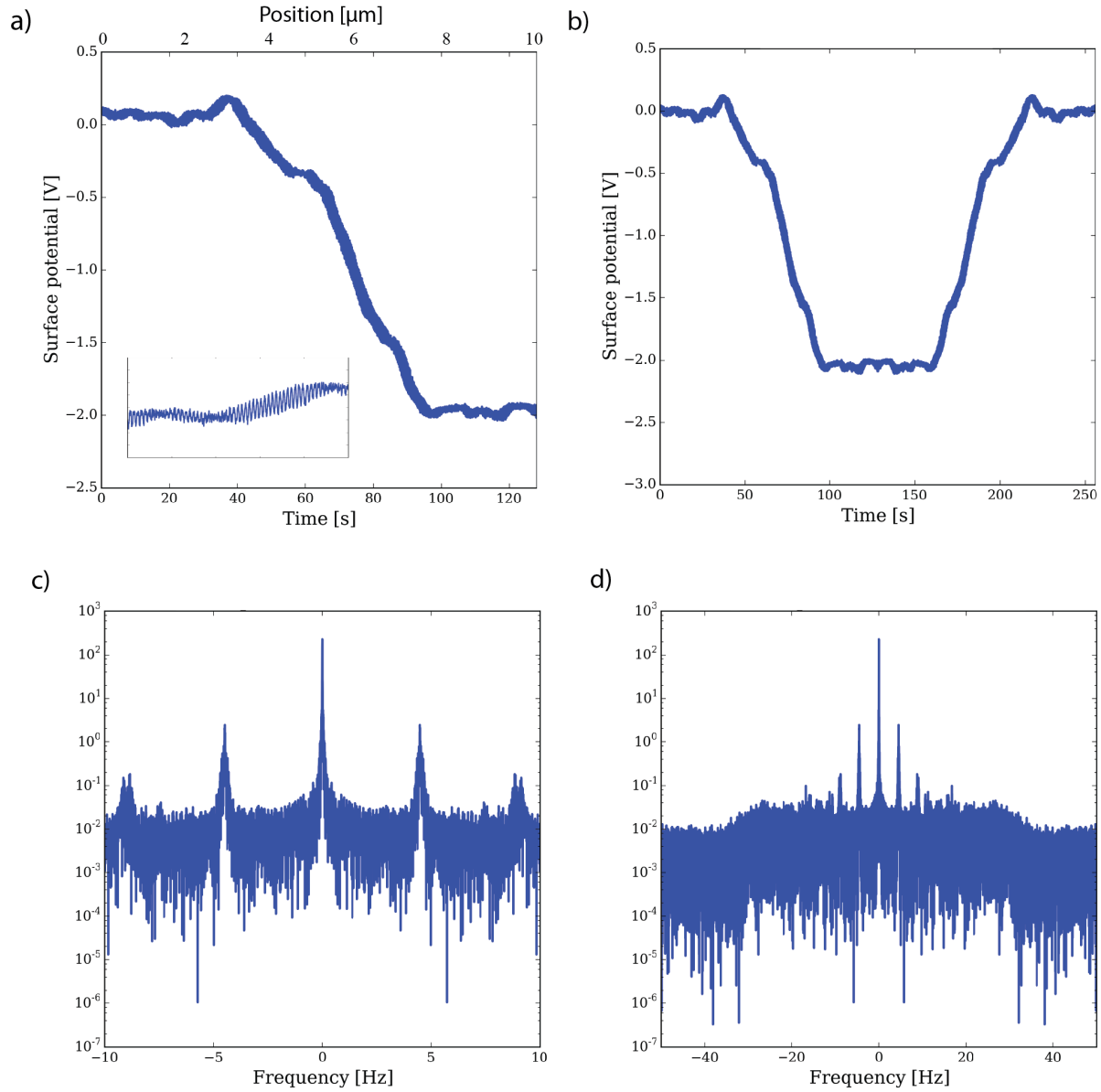


Figure 5.5: (a) Raw surface potential signal as a function of time and position. Inset shows a few seconds' worth of data, where the modulation oscillations are visible. (b) The raw data is shifted to a zero baseline and symmetrized. (c-d) Fourier transformed symmetrized data; (c) shows the DC, ω_x , and $2\omega_x$ components of the signal; (d) shows a zoomed out view of the DC and modulation peaks.

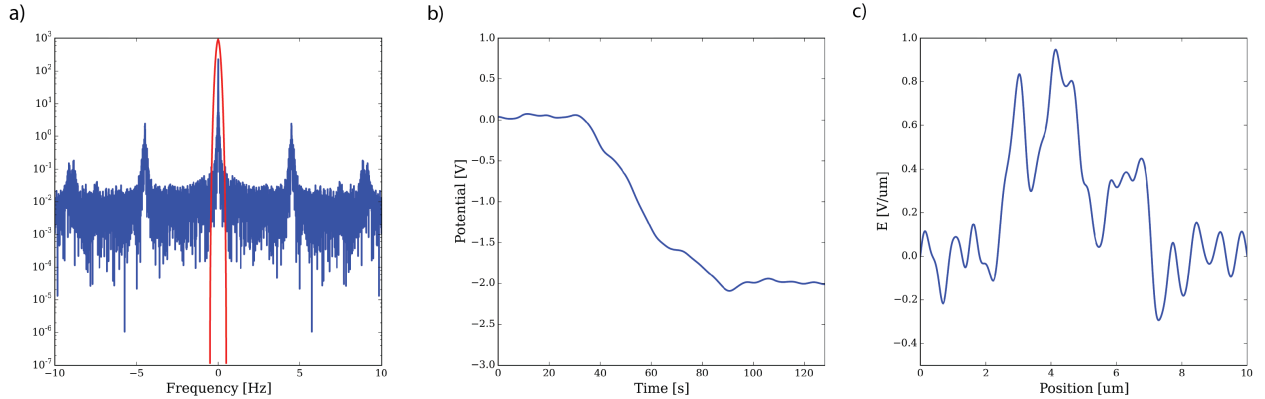


Figure 5.6: (a) Fourier transformed, symmetrized data with filter at 0 Hz. (b) Inverse Fourier transforming the filtered data yields the surface potential profile with no modulation. The spatial numeric derivative of (b) produces the electric field profile in (c).

create a symmetric signal. The number of data points collected is chosen to be a power of two to speed up the Fourier transform, but the length of the data set can be trimmed at this point if the data set is not a power of two in length. The signal can then be Fourier transformed.

To obtain the surface potential with no modulation component, we apply a filter at 0 Hz. Inverse Fourier transforming this filtered data yields the surface potential profile that would be measured in typical FM-KPFM. We can take the numeric derivative of this signal to obtain an electric field profile in the conventional manner. These steps are shown in Fig. 5.6.

In contrast, Fig. 5.7 shows the process for working up the position modulation signal. We apply a filter at the modulation frequency, $\omega_x/2\pi$ Hz, and inverse Fourier transform this filtered signal. We obtain an oscillating signal whose amplitude corresponds to the size of the electric field. We obtain the envelope of this oscillating potential and scale it by $2x_m$ to obtain the electric field profile. This approach can be improved by implementing a true “software lock-in” to accurately track the sign of the electric field signal.

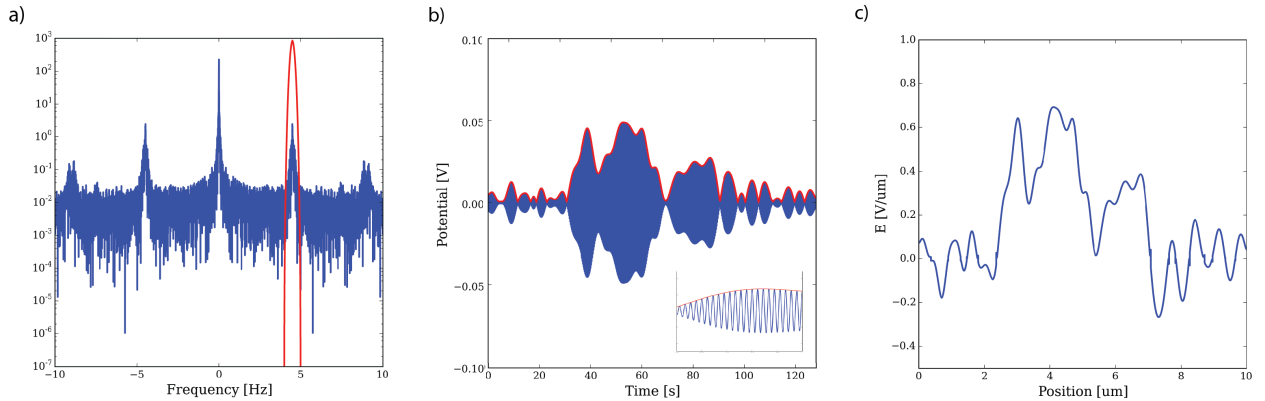


Figure 5.7: (a) Fourier transformed, symmetrized data with filter at $\omega_x = 4.5$ Hz. (b) Inverse Fourier transforming the filtered data yields only the modulated surface potential. The amplitude envelope of (b), shown in red, is scaled by the size of the modulation to give the electric field profile in (c).

5.4 Experimental details

The block diagram for the experiment is shown in Fig. 5.8. The cantilever frequency shift (RHK Δf) is obtained with an RHK PLL Pro frequency demodulator. The cantilever frequency shift is tracked at the cantilever tip voltage modulation frequency ω_{tip} with an SRS 830 Lock-in amplifier, and at twice the tip voltage modulation frequency ($2\omega_{\text{tip}}$) with a Perkin-Elmer Lock-in amplifier. The $2\omega_{\text{tip}}$ frequency shift tracked by the Perkin-Elmer Lock-in is related to the second derivative of the tip-sample capacitance with respect to height, so this term is read in by the computer. The SRS 830 Lock-in amplifier generates the oscillating tip voltage at ω_{tip} , and sends the frequency component $f(\omega_{\text{tip}})$ to the PID feedback loop. The PID loop nullifies $f(\omega_{\text{tip}})$ with a DC voltage output equal to the surface potential. This DC bias and the SRS 830 AC bias at ω_{tip} are summed to generate the cantilever tip bias. The output of the PID loop is the surface potential, which is read into the computer. The setup thus far is generally consistent with a typical FM-KPFM experiment.

In position-modulation, a third lock-in amplifier is used to generate the oscillating position. An AC voltage at ω_x is generated by a Signal Recovery lock-in and summed with the

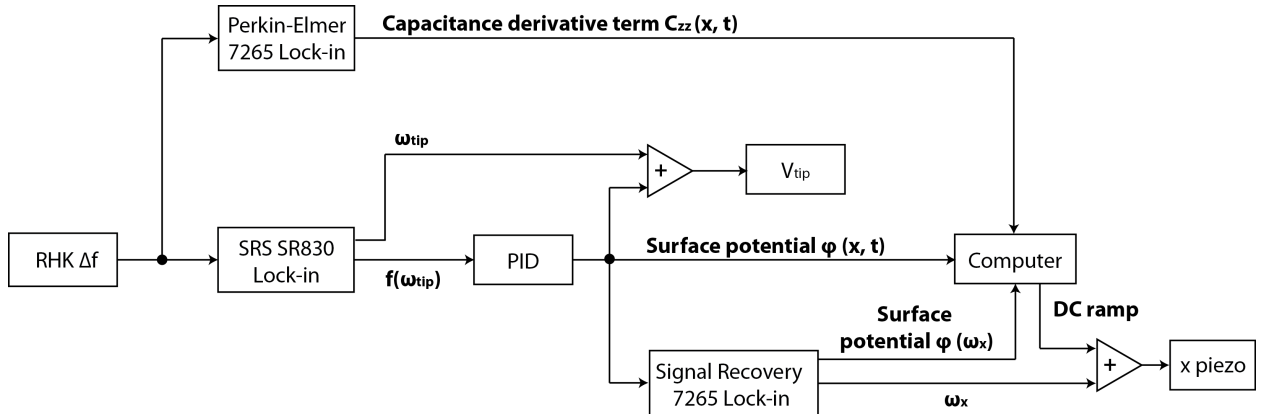


Figure 5.8: Block diagram of position modulated FM-KPFM experiment. The setup is similar to standard FM-KPFM, with the addition of a third lock-in amplifier and a second summing circuit.

DC ramp that is generated in Labview and output through a National Instruments DAQ board. This combined ramp and oscillating voltage is sent to the x piezo to create the position modulation. The modulation is thus in the same direction of the overall scan, so the probe backtracks over the same areas as it scans. This modulation is what generates the time-dependent component of the surface potential. If desired, the same lock-in can be used to track the surface potential at ω_x and extract the amplitude directly. For the data discussed in this chapter, we instead use the Python freqdemod package as described above to obtain the DC and AC components of the surface potential from the output of the PID loop.

5.4.1 Instrument settings

Several important experimental details must be considered in order to obtain accurate position-modulated FM-KPFM signal. I shall list instrument settings here for the experiment outlined in the block diagram above. Below, I will discuss the general considerations that led us to choose these settings.

SRS 830 Lock-in

- Input = Δf RHK
- $\omega_{tip} = 160$ Hz, 0.5-3 V_{rms}; typically 1.5 V_{rms}
- $\hat{f}(\omega_{tip})$ = channel 1; use x output (not display)
- TC = 10 ms
- slope = 6dB/oct
- sync filter ON

Perkin-Elmer Lock-in

- Input = Δf RHK
- Reference = SRS 830 Lock-in channel 1 output, $f(\omega_{tip})$
- TC = 50 ms
- slope = 6dB/oct

Signal Recovery Lock-in

- Input = surface potential, $\phi(x,t)$
- $\omega_{tip} = 4.5$ Hz, 0.01-0.1 V_{rms}; typically 0.07 V_{rms}
- $\phi(\omega_x)$ = channel 1, if using lock-in detection to measure ϕ
- TC = 10 ms
- slope = 6dB/oct

PID

- P = 0.1 to 10; typically ~ 3

- $I = 50 \text{ rad/s}$
- $D = 5E-5 \text{ s}$

5.4.2 Choosing a position modulation frequency and amplitude

There are two important considerations when choosing the position modulation frequency ω_x . First, the frequency of the position modulation must be lower than the tip-modulation lock-in time constant cutoff (the SR830 in Fig. 5.8). If this condition is exceeded, the modulation signal will be severely attenuated or lost. In our experiments, this limiting time constant is usually set at 10 ms ($1/\text{TC} = 100 \text{ rad/s} = 15.9 \text{ Hz}$). Note that the lock-in bandwidth set by the time constant is in rad/seconds, not Hz!

Second, the position modulation frequency should be relatively noise-free. In other words, ω_x should be chosen from a minimum in the frequency noise spectrum. In Fig. 5.9a, we plot frequency noise for a variety of tip voltages swept from low to high voltage and back again. The tip voltage dependence of the frequency noise reveals whether cantilever frequency noise arises from mechanical or sample (dielectric fluctuations) sources: mechanically-derived frequency noise is quartic in tip voltage (V_{tip}^4) while sample-derived frequency noise is quadratic in tip voltage (V_{tip}^2) [149]. In Fig. 5.9b-d, we show that the frequency noise at 1 Hz (b) and 9 Hz (b) arises from mechanical vibrations because it has a quartic tip voltage dependence. The frequency noise at 4 Hz (Fig. 5.9c) is not strongly tip-voltage dependent, suggesting that there are no major peaks in mechanical or sample noise at this frequency. In most of the data in this chapter, we used a modulation frequency of 4 or 4.5 Hz.

One might guess that the size of the position modulation should be optimized so that the modulation is as large as possible without compromising the resolution of the surface potential image, in order to maximize the measured signal. However, the size of the position

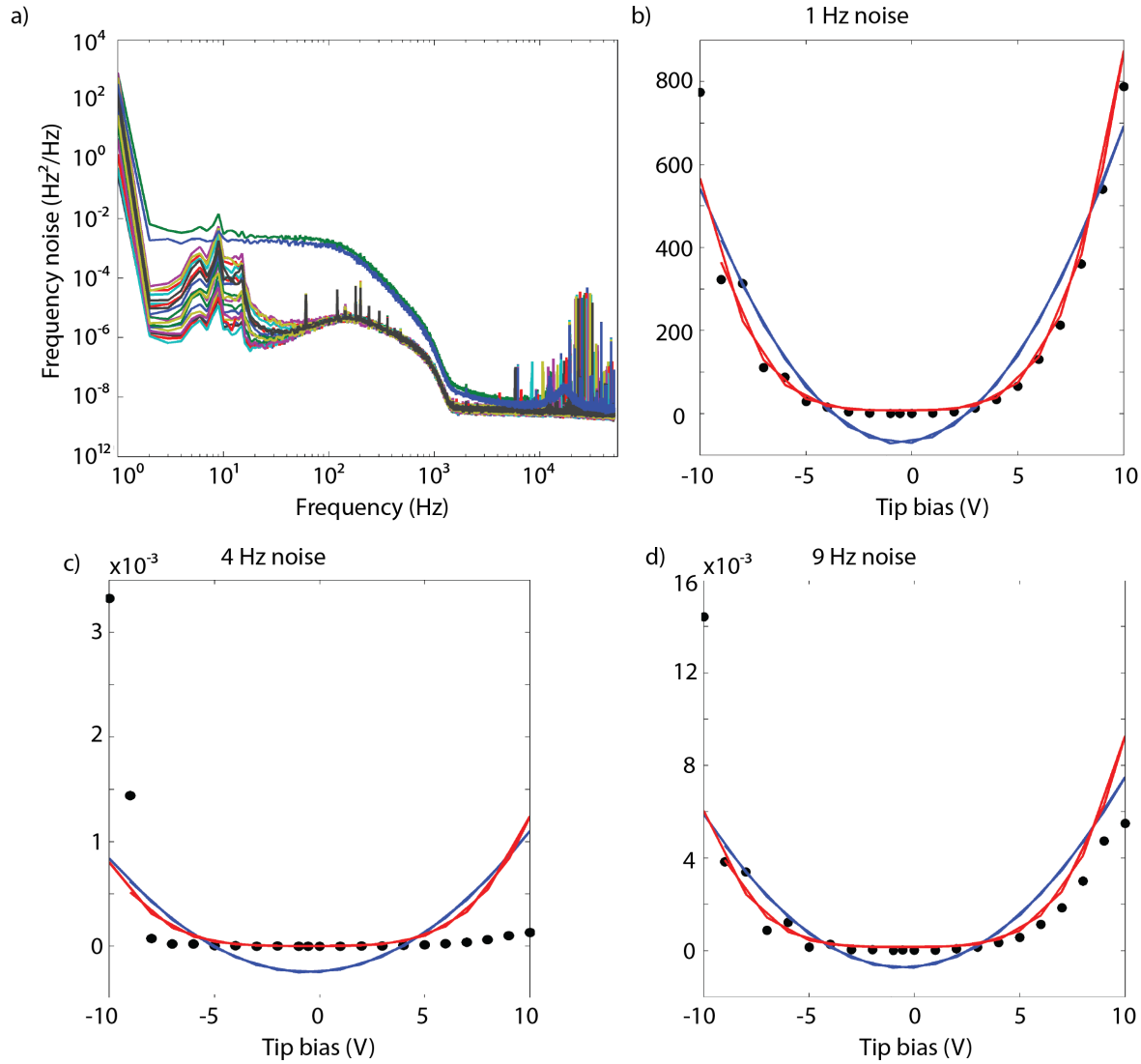


Figure 5.9: (a) Tip voltage-dependent frequency power spectra for a cantilever 60 nm above a transistor sample. (b-d) Black dots represent frequency noise versus tip voltage at (b) 1 Hz, (c) 4 Hz, and (d) 9 Hz. Red lines represent a quartic fit and blue lines represent a quadratic fit to the data.

modulation also sets the bandwidth for filtering out the AC and DC components in Fourier space; too large a modulation results in too narrow a filter. It turns out that a smaller modulation is desirable to maximize the amount of signal passed through the filter in Fourier space; the signal lost in this filtering step explains why the position-modulation signal appears smaller than the derivative signal at high spatial frequencies (see Fig. 5.16). An optimal size for this filter will be discussed in future publications, since it has to do with the full expression for the surface potential with position modulation; if this filter shape can be analytically described, it may also be possible to correct for this loss in the position modulated signal.

For transistor samples, where the electric field is on the order of $1 \text{ V}\mu\text{m}^{-1}$, I have found that the position modulation can be set as large as 140 nm (0-pk) for a $10\times 10 \mu\text{m}$ scan, but the electric field measurement is cleaner for smaller modulations (50-75 nm 0-pk). The conversion for our x piezo is 100 nm/V, and our bipolar amplifier has a gain of 15. The lock-in rms output must also be accounted for. I show an example conversion between lock-in voltage and nanometers to assist in the conversion between lock-in output and physical position modulation. The factor of 95% comes from the resistance of the PCB summing circuit output, which can be corrected by replacing the output resistors (see section B.2).

$$\begin{aligned} 0.035 \text{ V}_{\text{rms}} \text{ (0-pk)} \times \sqrt{2} &= 0.049 \text{ V (0-pk)} \times 15 \times 100 \text{ nm/V} \\ &= 74.2 \text{ nm (0-pk)} [\times 0.95] = 70.5 \text{ nm (0-pk)} \end{aligned} \quad (5.9)$$

5.4.3 Feedback gains

It is critically important for the success of this position modulation technique that the feedback loop and all gains within the circuitry controlling the tip voltage are accurately characterized. The electric field measured by the position-modulation method depends on the amplitude of the oscillating component of the surface potential, so it is essential that the

surface potential is not attenuated at the position modulation frequency.

Ideally, in position-modulation, the tip voltage feedback loop will have a constant gain for both the DC frequency shift and the position modulation frequency. If the feedback is not carefully tracked, *i.e.*, if the gains are not the same at 0 Hz and 4.5 Hz, then small changes in the magnitude of the frequency shift will cause large changes in the electric field measured via position modulation. Two key factors that can influence the magnitude of the frequency shift are tip-sample separation and the tip voltage:

$$\hat{f}(\omega_{\text{tip}}) = \frac{f_0 V_{\text{AC}}}{2k_0} C_{zz}(V_{\text{DC}} - \phi) \quad (5.10)$$

The frequency shift is increased for smaller tip-sample separations, since these result in larger tip-sample capacitances C_{zz} , and is increased at greater AC tip biases. If feedback is not correctly enabled, these dependencies of the frequency shift will manifest themselves as height- and tip-dependent measured electric fields.

In Figs. 5.10 and 5.11, we illustrate the dramatic importance of proper feedback in position-modulation measurements of electric field. Fig. 5.10 shows the electric field dependence on tip-sample separation for attenuated feedback at the position modulation frequency ω_x . Note that the measured electric fields, 5.10d, are greater at close tip-sample separations, as are the measured capacitance terms 5.10b.

Similarly, Fig. 5.11 shows the electric field dependence on tip AC bias (V_{AC}) for attenuated feedback at the position modulation frequency. The measured electric field is greater for larger tip AC biases. The largest measured electric fields in this experiment came from a moderate tip bias that coincided with a drift closer to the sample, as seen in the capacitance values (5.11b).

The feedback gains can be evaluated by measuring the frequency response of the feedback loop over a range of frequencies and viewing the results as gain and phase Bode plots. We

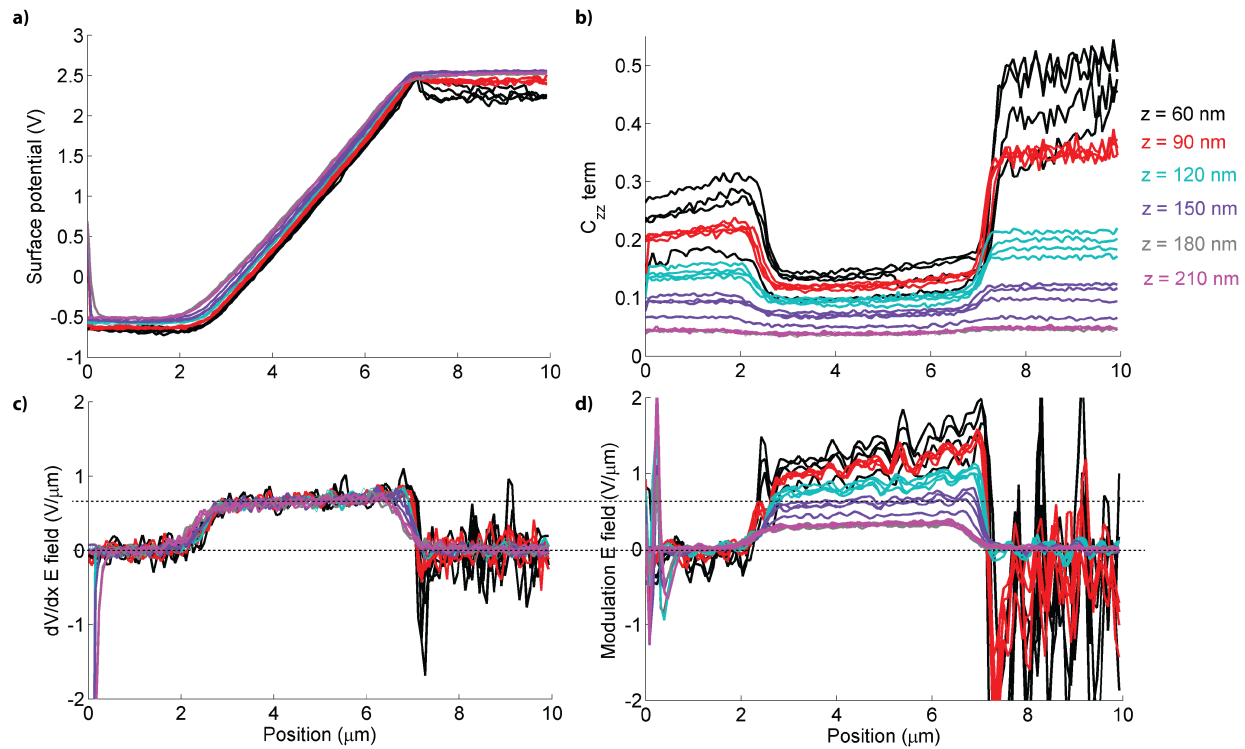


Figure 5.10: (a) Surface potential profiles, (b) capacitance derivative profiles, (c) electric fields calculated from the numeric derivative of the surface potential, and (d) electric fields determined using the position-modulation signal, for different tip-sample separations.

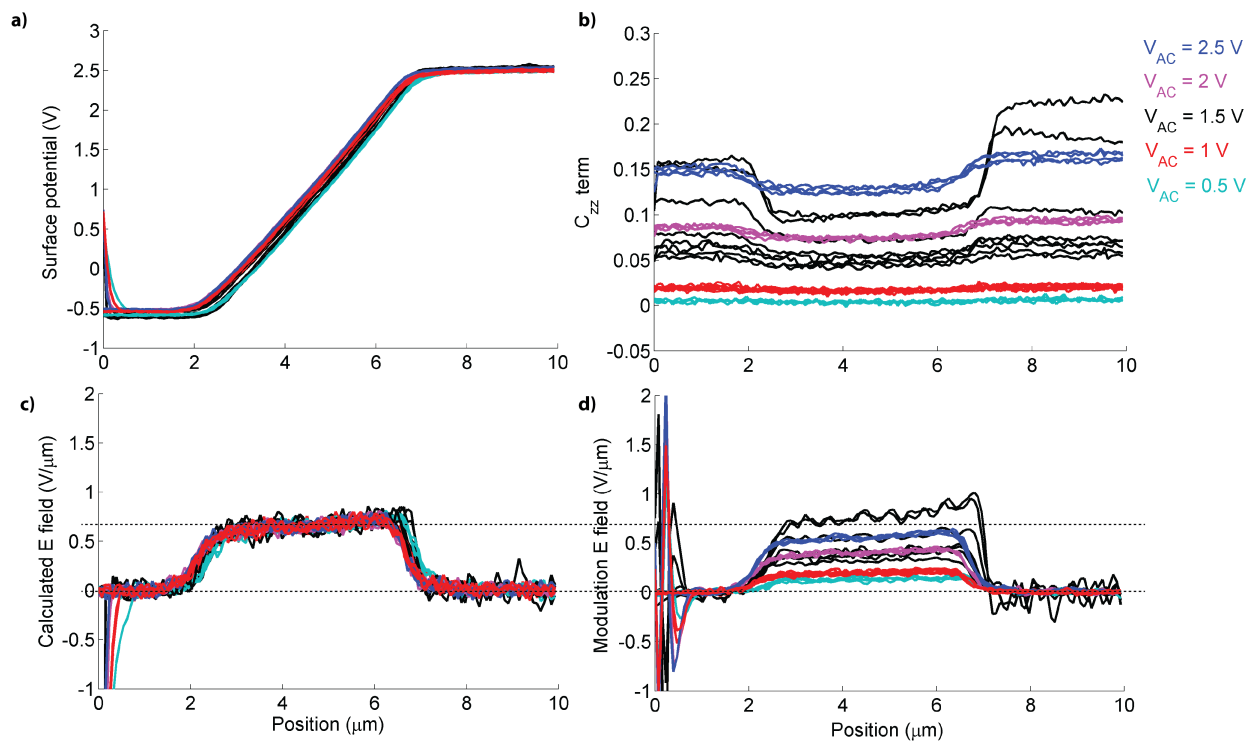


Figure 5.11: (a) Surface potential profiles, (b) capacitance derivative profiles, (c) electric fields calculated from the numeric derivative of the surface potential, and (d) electric fields determined using the position-modulation signal, for different tip voltages V_{AC} .

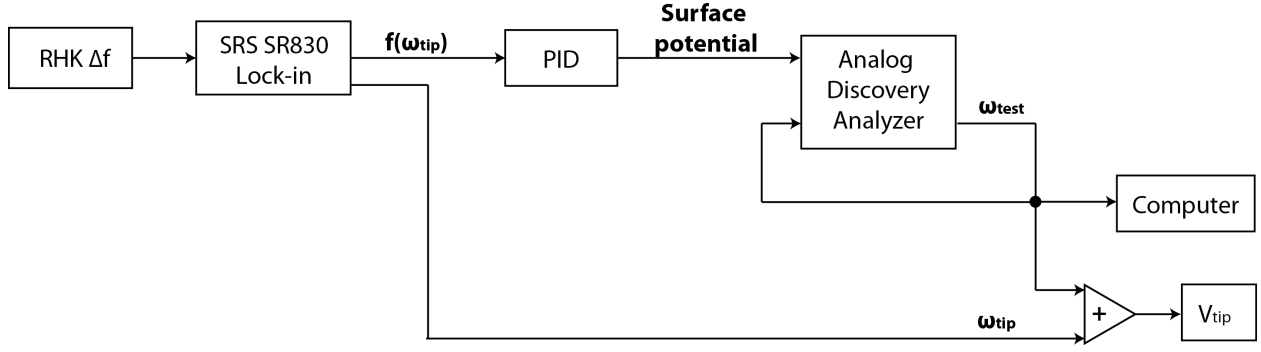


Figure 5.12: Block diagram for feedback network frequency analysis (Bode plots). The cantilever is driven, and the tip-sample separation should be in a relevant experimental range (60-180 nm).

employed an Analog Discovery Network Analyzer to make these measurements. A block diagram illustrating the wiring for position-modulation closed-loop feedback analysis is shown in Fig. 5.12.

The results of our network analysis are shown in gain and phase Bode plots in Fig. 5.13. We have overlaid the Bode plots for our standard FM-KPFM feedback settings (blue) with the updated feedback settings for position modulation (black). In standard FM-KPFM feedback, the gain response at 4.5 Hz is clearly not constant, but is rather dramatically sloping. In addition, the phase response in standard FM-KPFM feedback at 4.5 Hz is approaching instability at -180° . In contrast, the position modulation gain response is constant beyond 10 Hz, and the phase response is much more stable at low frequencies.

In practice, the settings of the PID loops should be adjusted for each sample studied. The I and D terms are usually small, so the major adjustment to be made is in the P term. To tune the feedback, the P term should be increased until the feedback loop is unstable; this value should be noted so that P can then be decreased to half this value where instability begins. P will need to be adjusted for different tip-sample separations or AC tip biases, but when the feedback loop is properly tuned, the position-modulation electric field is no longer height-dependent (Fig. 5.14)

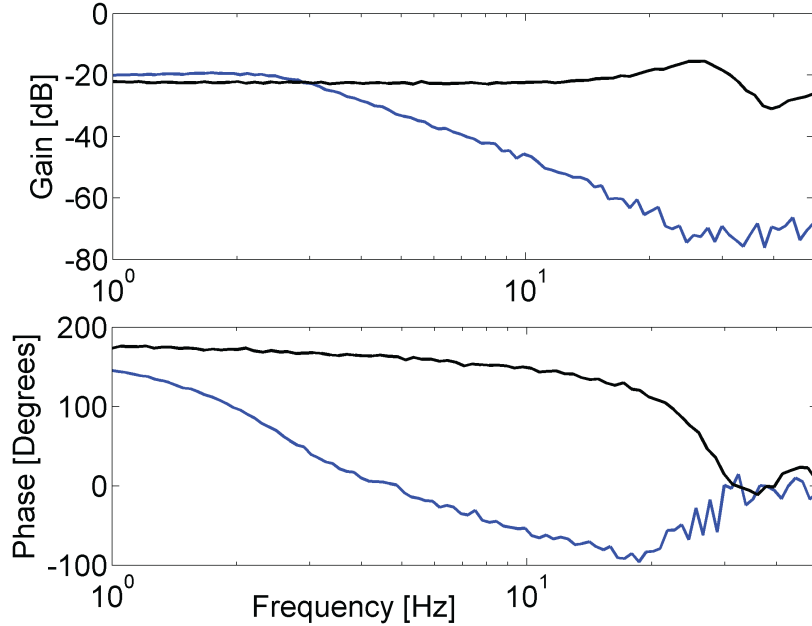


Figure 5.13: Gain (top) and phase shift (bottom) for typical FM-KPFM tip voltage feedback (blue) and position-modulated FM-KPFM tip voltage feedback (black).

5.4.4 Choosing a tip-sample separation

As discussed above in section 5.4.3, changes in the overall size of the cantilever frequency shift signal (Eq. 5.10) will change the frequency response of the tip voltage feedback loop (*i.e.*, change/shift the Bode plots in Fig. 5.13). If the size of the frequency shift signal changes dramatically during an experiment, the tip voltage feedback loop will become unstable. In practice, the AC tip bias is constant throughout a single scan, but the capacitance derivative is both tip height- and sample-dependent. Avoiding large changes in C_{zz} is therefore a critical parameter in maintaining stable feedback.

Two factors in a sample influence the measured C_{zz} : topography, for its influence on tip-sample separation, and the material itself. In practice, this means that scanning from an organic semiconductor to gold can increase the capacitance enough to destabilize the feedback loop. Feedback is thus usually most stable at slightly larger tip-sample separations. We found

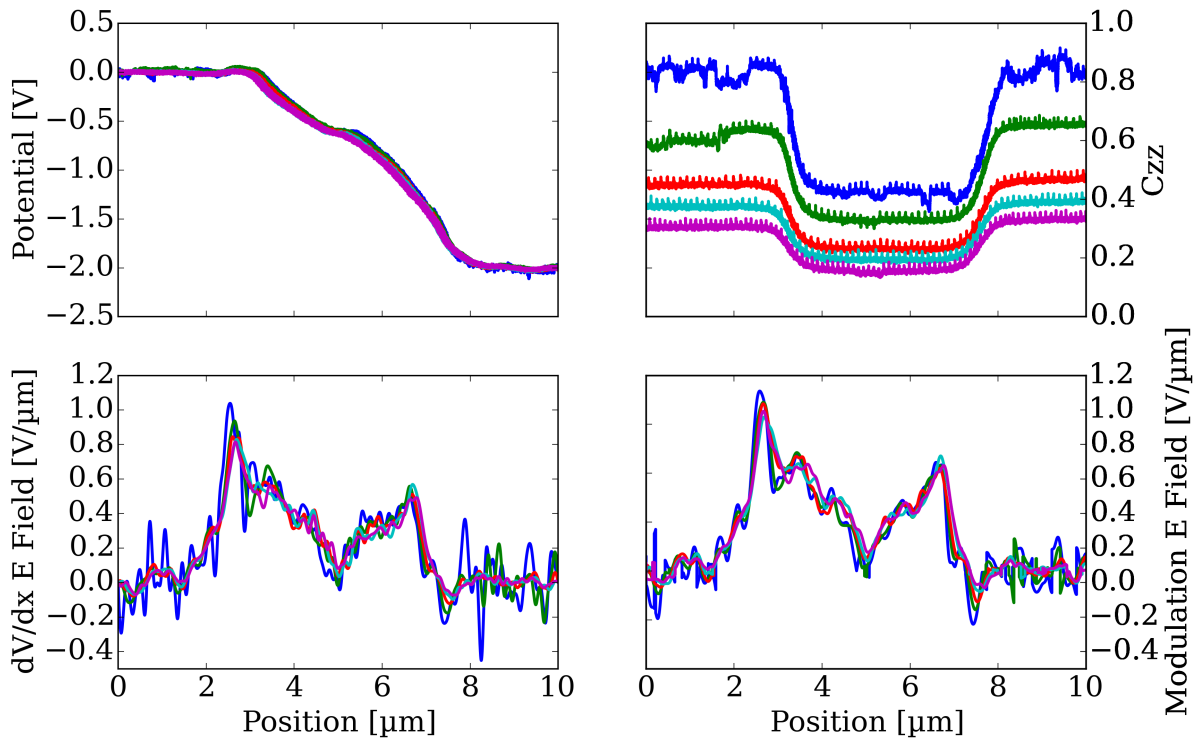


Figure 5.14: (a) Surface potential profiles, (b) capacitance derivative profiles, (c) electric fields calculated from the numeric derivative of the surface potential, and (d) electric fields determined using the position-modulation signal, for different tip-sample separations (90–210 nm, 30 nm steps). The capacitance derivative clearly shows that different tip-sample separations are used, but the electric fields measured in each method agree well.

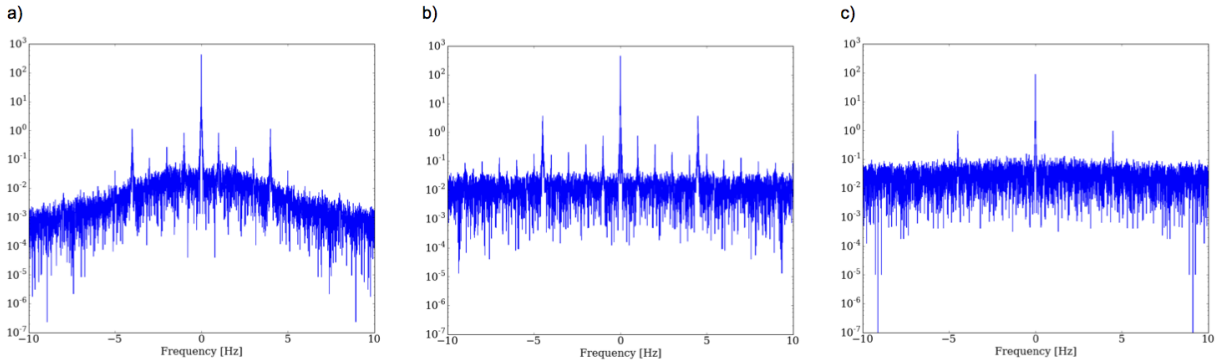


Figure 5.15: Fourier transforms of position modulated surface potential for different scanning step sizes. (a) Large step sizes at low frequency cause noise that can interfere with the position modulation. Here the step size is 78 nm at 1 Hz, with a 4 Hz position modulation; the 1 Hz sidebands overlap with the 4 Hz signal. (b) Same step size and frequency as (a), but the position modulation has been moved to 4.5 Hz, avoiding the 1 Hz sidebands. (c) Step size has been decreased to 0.038 nm with a step frequency of 2.048 kHz. The 4.5 Hz position modulation signal is now clean.

the range 120-150 nm to be an empirically nice operating distance. Tracking topography while scanning would likely improve feedback stability by mitigating the varying tip-sample separations, but would not remove the challenge of neighboring materials with very different capacitances.

5.4.5 Scanning speed and spatial grid

If too large a step grid is used, the low frequency of these spatial steps adds mechanical vibration sidebands to the DC and position-modulation signals. For example, in preliminary experiments using a step frequency of 1 Hz, these 1 Hz sidebands are evident in the Fourier transformed signal. In Fig. 5.15a, a 1 Hz step frequency causes sidebands that overlap with a 4 Hz modulation. The position modulation frequency can be shifted slightly to avoid contributions from these sidebands (Fig. 5.15b), but a better solution to avoid this step-frequency noise is to use a much smaller spatial step size (Fig. 5.15c).

We created a very fine grid of 2^{18} position steps for each linescan, yielding an almost continuous spatial output. Of course, the NI-DAQ board cannot give a perfectly continuous output since it is a 16-bit system; in addition, we are not using the full range of the NI-DAQ, so we are probably operating on the order of 2^{12} bits. Our output ramp signal therefore is composed of tiny steps in voltage, and is not exactly a smooth continuous ramp. However, this near-continuity is sufficient to prevent any low-frequency position-step sidebands from interfering with the position-modulation signal. In the future, an analog filter could be added to the NI-DAQ output to blur these steps into a more continuous function if desired.

The scanning speed in points/second needs to be relatively slow to accommodate the position modulation. As we will show in our derivations below, the tip velocity is the conversion factor between the surface potential as a function of time versus a function of space. For our grid of 2^{18} steps and a data read-in rate of 2048 Hz, each line scan is completed in 128 seconds. For a $10 \mu\text{m}$ scan, the tip velocity for these grid conditions is $\sim 78 \text{ nm/s}$.

5.5 Interconverting signals and noise measured as functions of time and position

As we have discussed above, our experimental surface potential signal is a function of both time and position. Before we can explore the theoretical noise in each of the electric field measurement methods, we will demonstrate that the signal as a function of time can be converted to a function of position through the tip velocity. We will show that this conversion factor is also valid for changing variables in Fourier space and for changing variables of power spectra.

We begin by defining a signal measured in time, $V(t)$. The signal is measured over a

distance x , for a measurement velocity $v_{\text{tip}} = x/t$. Fourier transforming this signal, we obtain:

$$\hat{V}(f) = \int_{-\infty}^{\infty} dt V(t) e^{2\pi i f t} \quad (5.11)$$

We can write the measurement time t in terms of position x and the velocity:

$$t = \frac{x}{v_{\text{tip}}} \quad (5.12)$$

$$dt = \frac{1}{v_{\text{tip}}} dx \quad (5.13)$$

Substituting back into Eq. 5.11, we can write $\hat{V}(f)$ in terms of x :

$$\hat{V}(f) = \int_{-\infty}^{\infty} dx \frac{1}{v_{\text{tip}}} V\left(\frac{x}{v_{\text{tip}}}\right) e^{2\pi i \frac{f}{v_{\text{tip}}} x} \quad (5.14)$$

We can also consider the same signal $V(t)$ as a function of x , $V(x)$. We can write down the Fourier transform of $V(x)$ as in Eq. 5.11:

$$\hat{V}(k) = \int_{-\infty}^{\infty} dx V(x) e^{2\pi i k x} \quad (5.15)$$

We can see by inspection that Eq. 5.11 = Eq. 5.15 if:

$$k = \frac{f}{v_{\text{tip}}} \quad (5.16)$$

In other words, comparing our signal versus time and position in Fourier space:

$$v_{\text{tip}} \hat{V}(f) = \hat{V}(k) \quad (5.17)$$

$$\hat{V}(k) = \hat{V}(f = v_{\text{tip}} k) v_{\text{tip}} \quad (5.18)$$

The units for this equivalence work since $\hat{V}(f)$ has units of V/Hz and v_{tip} has units of m/s, giving $\hat{V}(k)$ the correct units of V/m⁻¹.

Can we use these Fourier space relationships to define a relationship between the power spectra of the noise in a measured signal in terms of the frequencies f and k ? The rms-squared noise in the signal V_T is defined as:

$$\delta V_T^2_{rms} = \lim_{T \rightarrow \infty} \frac{1}{2T} \int_{-T}^T \delta V_T(t)^2 dt \quad (5.19)$$

V_T is the signal measured over a finite time T and δV_T is the noise in signal V_T . In addition, the power spectrum of voltage noise in terms of frequency for a finite time measurement from $-T$ to T is defined as:

$$P_{\delta V}(f) = \lim_{T \rightarrow \infty} \frac{1}{2T} |\hat{\delta V}_T(f)|^2 \quad (5.20)$$

where $\hat{\delta V}_T(f)$ is the Fourier transform of the noise δV_T .

We need to confirm that the relationships in Eqs. 5.73-5.18 hold for a finite measurement (from time $-T$ to T or position $-X$ to X). We write the Fourier transforms:

$$\hat{V}_T(f) = \int_{-\infty}^{\infty} dt V_T(t) e^{2\pi i f t} \quad (5.21)$$

$$\hat{V}_T(f) = \int_{-\infty}^{\infty} dx \frac{1}{v_{\text{tip}}} V_T\left(\frac{x}{v_{\text{tip}}}\right) e^{2\pi i \frac{f}{v_{\text{tip}}} x} \quad (5.22)$$

$$\hat{V}_X(k) = \int_{-\infty}^{\infty} dx V_X(s) e^{2\pi i k s} \quad (5.23)$$

For finite time measurements, we see that we again recover relationships between f and k Fourier space through the measurement velocity v_{tip} :

$$T = \frac{X}{v_{\text{tip}}} \quad (5.24)$$

$$k = \frac{f}{v_{\text{tip}}} \quad (5.25)$$

$$\hat{V}_X(k) = \hat{V}_T(f = v_{\text{tip}}k) v_{\text{tip}} \quad (5.26)$$

If we move from the Fourier relationship in Eq. 5.26 to a power spectrum of voltage in terms of frequency as defined in Eq. 5.20, we obtain:

$$\hat{V}_T(f = v_{\text{tip}}k) = \hat{V}_X(k) \frac{1}{v_{\text{tip}}} \quad (5.27)$$

$$\frac{1}{2T} |\hat{V}_T(f = v_{\text{tip}}k)|^2 = \frac{1}{2T} |\hat{V}_X(k)|^2 \frac{1}{v_{\text{tip}}^2} \quad (5.28)$$

$$P_{\delta V}(f) = \lim_{T \rightarrow \infty} \frac{1}{2T} |\hat{V}_T(f = v_{\text{tip}}k)|^2 = \lim_{T \rightarrow \infty} \frac{1}{2T} \frac{1}{v_{\text{tip}}^2} |\hat{V}_X(k)|^2 \quad (5.29)$$

Using the equivalence in Eq. 5.24, we can simplify 5.29:

$$\frac{1}{2T v_{\text{tip}}^2} = \frac{1}{2} \frac{v_{\text{tip}}}{X} \frac{1}{v_{\text{tip}}^2} = \frac{1}{2X} \frac{1}{v_{\text{tip}}} \quad (5.30)$$

$$P_{\delta V}(f) = \lim_{X \rightarrow \infty} \frac{1}{2X} |\hat{V}_X(k)|^2 \frac{1}{v_{\text{tip}}} \quad (5.31)$$

$$P_{\delta V}(f) = P_{\delta V}(k) \frac{1}{v_{\text{tip}}} \quad (5.32)$$

Just as the signal could be converted in Fourier space between f and k , we also find that the power spectra of the noise can be interconverted through the scanning speed v_{tip} . The units for the power spectra are V^2/Hz for frequency and V^2/m^{-1} for k-space; sure enough, the unit conversion works when the tip velocity is employed ($\text{V}^2/\text{Hz} \times \text{m/s} = \text{V}^2/\text{m}^{-1}$). These relationships will be helpful as we proceed.

5.6 Overview of electric field noise derivations

In the following two sections, we will describe the noise in the measured electric field for the numeric derivative of standard FM-KPFM and for the electric field extracted from our position-modulated FM-KPFM experiment. For each derivation, we will first define the measured signal and the potential noise δV_n in terms of the cantilever frequency shift noise δf . In the numeric derivative case, we will use δV_n to obtain a power spectrum of the potential noise $P_{\delta V_n}$ in terms of f and k . We will show mathematically that taking a derivative in x is equivalent to multiplying by k in Fourier space, leading to a power spectrum for the electric field noise that is proportional to k^2 , or an rms-squared noise proportional to $\frac{1}{x^3}$.

In the position modulation case, we examine the Fourier transformed signal and separately treat the filtered components at 0 Hz and the modulation frequency f_x . We will show that the position modulation electric field noise depends on both the physical size of the position modulation and the size of the filter used to extract the signal. When the derivative

of potential is treated with the same spatial filter as the position modulation size, the rms-squared electric field noise is comparable between the two methods. However, the methods have very different responses to high frequency components of the electric field.

5.7 Electric field noise in the potential derivative from standard FM-KPFM

5.7.1 Signal and voltage noise in terms of frequency noise

In standard tip voltage-modulated EFM, an AC and a DC voltage are summed and applied to the cantilever tip while the cantilever resonance frequency shift (Δf) arising from electrostatic interactions with the sample is monitored at the AC modulation frequency by lock-in detection. The resulting cantilever frequency shift can be written as in Eq. 5.33, and the first harmonic of this frequency shift can be written as Eq. 6.2.

$$\Delta f = f_0 - \frac{f_0}{4k_0} \frac{\partial^2 C}{\partial z^2} (V_{DC} - \phi + V_{AC} \cos(\omega t))^2 \quad (5.33)$$

$$\hat{f}(\omega) = \frac{f_0 V_{AC}}{2k_0} \frac{\partial^2 C}{\partial z^2} (V_{DC} - \phi) \quad (5.34)$$

where V_{AC} is the AC tip voltage, k_0 is the effective cantilever spring constant, $\partial^2 C / \partial z^2$ is the second derivative of the tip-sample capacitance (C) in terms of the tip-sample separation (z), V_{DC} is the DC tip voltage, and ϕ is the surface potential [25, 26, 28]. By feeding back on the DC tip voltage to nullify the first harmonic in Eq. 6.2, the surface potential ϕ is obtained as the output of the feedback loop. In our measurements, the tip is normally held at a constant height z above the sample surface while scanning. In this discussion, we refer to the fast “linescan” direction as x and the slow lateral scan direction as y (*i.e.*, a 2D image would be built up in the y direction of many scans in the x direction).

We now need to include a term in Eq. 5.33 for the frequency noise, $\delta f_n(t)$.

$$\Delta f_{\text{shift}} = -\frac{f_0}{4k_0} \frac{\partial^2 C}{\partial z^2} (V_{\text{DC}} - \phi + \sqrt{2}V_{\text{AC,rms}} \cos(\omega_v t))^2 + \delta f_n(t) \quad (5.35)$$

This expression for the cantilever frequency shift signal can be expanded into:

$$\begin{aligned} \Delta f_{\text{shift}} = & -\frac{f_0}{4k_0} \frac{\partial^2 C}{\partial z^2} \{(V_{\text{DC}} - \phi)^2 \\ & + 2\sqrt{2}(V_{\text{DC}} - \phi)V_{\text{AC,rms}} \cos(\omega_v t) + 2V_{\text{AC,rms}}^2 \cos^2(\omega_v t)\} + \delta f_n(t) \end{aligned} \quad (5.36)$$

where only the red terms contain components at the tip voltage modulation frequency, ω_v .

A lock-in amplifier referenced to ω_v will only detect these terms in red.

5.7.2 Defining a lock-in operator

Let us review the mathematical operations that lead to lock-in detection at a frequency ω_v .

If we define V_s as:

$$V_s = -\frac{f_0}{4k_0} \frac{\partial^2 C}{\partial z^2} (V_{\text{DC}} - \phi) 2V_{\text{AC,rms}} \quad (5.37)$$

we can rewrite the cantilever signal read into the lock-in:

$$\Delta f_{\text{shift-lockin}} = \sqrt{2}V_s \cos(\omega_v t) + \delta f_n(t) \quad (5.38)$$

We read this signal into the lock-in detector, where it is multiplied by $\sqrt{2} \cos(\omega_v t)$ (the factor of $\sqrt{2}$ comes from the lock-in rms output), giving the product:

$$2V_s \cos^2(\omega_v t) + \sqrt{2}\delta f_n(t) \cos(\omega_v t) = 2V_s \left(\frac{1}{2} + \frac{1}{2} \cos(2\omega_v t) \right) + \sqrt{2}\delta f_n(t) \cos(\omega_v t) \quad (5.39)$$

We drop the $2\omega_v$ term since it gets filtered out by the lock-in reference and time constant.

When we resubstitute Eq. 5.37 for V_s , we obtain the lock-in output as:

$$\hat{f}(\omega_v) = \Delta f_{LI}(\omega_v) = -\frac{f_0}{4k_0} \frac{\partial^2 C}{\partial z^2} (V_{\text{DC}} - \phi) 2V_{\text{AC,rms}} + \delta f_n(t) \sqrt{2} \cos(\omega_v t) \quad (5.40)$$

This result confirms that the lock-in operator can be described as $\sqrt{2} \cos(\omega t)$, and that the lock-in output is what we would expect from the input signal:

$$V_{\text{out}} = \text{Low-Pass } [V_{\text{in}} \times \sqrt{2} \cos(\omega_v t)] \quad (5.41)$$

5.7.3 Potential noise in FM-KPFM feedback

When we perform PID loop feedback in standard FM-KPFM, we set the lock-in output in Eq. 5.40 equal to zero by adjusting V_{DC} . When this output is zero, our measured signal V_{DC} equals ϕ , the surface potential. If we then solve for the $(V_{\text{DC}} - \phi)$ term, representing the difference between the real and measured signal, we obtain the potential noise δV_n :

$$\delta V_n = (\phi - V_{\text{DC}}) = \frac{2k_0}{f_0 V_{\text{AC,rms}} C_{zz}} \delta f_n(t) \sqrt{2} \cos(\omega_v t) \quad (5.42)$$

where we have inverted the sign of the difference term and eliminated the leading negative sign. What we now need is an expression for the power spectrum of this voltage noise. (We cannot define it precisely as a function of time, but we can define it as a function of frequency.) The power spectrum of a value fluctuating in time is equal to the square of the Fourier transform of the noise, normalized by the measurement time. Changing units from angular momentum to frequency, and taking the Fourier transform of Eq. 5.42, I obtain:

$$\delta \hat{V}_n = \frac{\sqrt{2}k_0}{f_0 V_{\text{AC,rms}} C_{zz}} [\delta \hat{f}_n(f - f_v) + \delta \hat{f}_n(f + f_v)] \quad (5.43)$$

where the Fourier transform of $\cos(2\pi f_v t) = \frac{1}{2}[(f + f_v) + (f - f_v)]$.

As described in John's group report "Frequency Noise (2008)," moving from the Fourier transform of the noise to a power spectrum requires a limit corresponding to the measurement time T . We have written the definition of this power spectral transformation in Eq. 5.20. Applying this definition to Eq. 5.43, we find:

$$P_{\delta V_n}(f) = \lim_{T \rightarrow \infty} \frac{1}{2T} \delta \hat{V}_n \delta \hat{V}_n^* \quad (5.44)$$

$$P_{\delta V_n}(f) = \lim_{T \rightarrow \infty} \frac{1}{2T} \left(\frac{\sqrt{2}k_0}{f_0 V_{\text{AC,rms}} C_{zz}} \right)^2 [\delta \hat{f}_n(f - f_v) + \delta \hat{f}_n(f + f_v)] \\ \times [\delta \hat{f}_n^*(f - f_v) + \delta \hat{f}_n^*(f + f_v)] \quad (5.45)$$

$$P_{\delta V_n}(f) = \lim_{T \rightarrow \infty} \frac{1}{2T} \left(\frac{\sqrt{2}k_0}{f_0 V_{\text{AC,rms}} C_{zz}} \right)^2 [\delta \hat{f}_n(f - f_v) \delta \hat{f}_n^*(f - f_v) + \delta \hat{f}_n(f + f_v) \delta \hat{f}_n^*(f + f_v)] \\ + \lim_{T \rightarrow \infty} \frac{1}{2T} \left(\frac{\sqrt{2}k_0}{f_0 V_{\text{AC,rms}} C_{zz}} \right)^2 [\delta \hat{f}_n(f - f_v) \delta \hat{f}_n^*(f + f_v) + \delta \hat{f}_n(f + f_v) \delta \hat{f}_n^*(f - f_v)] \quad (5.46)$$

$$P_{\delta V_n}(f) = \frac{2k_0^2}{f_0^2 V_{\text{AC,rms}}^2 C_{zz}^2} [P_{\delta f_n}(f + f_v) + P_{\delta f_n}(f - f_v)] + \text{Cross terms} \rightarrow 0 \quad (5.47)$$

The cross terms moving from 5.46 to Eq. 5.47 do not survive averaging at long times T , as summarized in the report “Frequency Noise (2008).” This expression of potential noise in terms of frequency noise (5.47) is a key finding.

The terms in Eq. 5.47 are all either known or measurable. The power spectrum of the surface potential noise ($P_{\delta V_n}(f)$) can be computed from the residual noise in a steady-state surface potential versus time measurement. The cantilever resonance frequency and spring constant are measurable from the cantilever Brownian motion. The AC tip bias is known (set as an rms voltage on the SRS 830 lock-in amplifier) and the tip-sample capacitance derivative term C_{zz} is usually measured simultaneously with the surface potential. The $P_{\delta f_n}(f \pm f_v)$ terms can be computed from measurements of δf versus time (as in regular FM-KPFM, with the feedback off and the DC tip voltage adjusted to match the surface potential).

When the surface potential is measured for a finite time T , the rms-squared value of the surface potential in time is related to the power spectrum of surface potential fluctuations in frequency:

$$\delta V_{\text{rms}}^2 = \int_0^{1/(2T)} P_{\delta V_n}(f) df \quad (5.48)$$

Analogously, the rms-squared value of the surface potential in space is related to the power spectrum of surface potential fluctuations in k-space. Converting measured time to

measured position using the tip velocity v_{tip} :

$$\delta V_{rms}^2(f) = \int_0^{1/2T} \frac{P_{\delta V_n}(k)}{v_{\text{tip}}} dk \times v_{\text{tip}} \quad (5.49)$$

$$\delta V_{rms}^2(k) = \int_0^{k/2v_{\text{tip}}} P_{\delta V_n}(k) dk \quad (5.50)$$

where $k = 1/X$, with $X = T \times v_{\text{tip}}$ being the distance measured. In principle, Eq. 5.48 = Eq. 5.50. Both versions of this expression are valid and we can interconvert between them using the tip velocity.

5.7.4 Relationship between power spectra of electric field noise and voltage noise in k -space

We next need to use our knowledge of the surface potential noise δV_n to determine the expected noise in the electric field arising from the derivative of the surface potential (Eq. 5.52). This derivation is analogous to the derivation of frequency shift noise from phase noise in John's 2008 "Frequency Noise" report. We define the electric field in terms of potential as:

$$E(x) = -\frac{d}{dx}\phi(x) \quad (5.51)$$

where $\phi(x)$ is the local surface potential. Analogously, we can write the noise in the electric field in terms of the potential noise, $\delta V_n(x)$:

$$\delta E_n(x) = -\frac{d}{dx}\delta V_n(x) \quad (5.52)$$

Instead of considering the measurement as a function of time, we treat the noise as a function of position, having shown that these expressions in frequency and k -space are interconvertible. We can write the correlation function for electric field noise at position x versus $x + X$, and substitute our expression for the electric field in Eq. 5.52. This argument is analogous

to writing the signal over a finite time T , but in this case we use a finite distance X .

$$\begin{aligned} C_{\delta E_n}(\chi) &= \lim_{X \rightarrow \infty} \frac{1}{2X} \int_{-\infty}^{+\infty} \langle \delta E_n(x) \delta E_n(x + \chi) \rangle dx \\ &= \lim_{X \rightarrow \infty} \frac{1}{2X} \int_{-\infty}^{+\infty} \left\langle -\frac{d}{dx} \delta V_n(x) \left(-\frac{d}{dx} \delta V_n(x + \chi) \right) \right\rangle dx \end{aligned} \quad (5.53)$$

where χ is an arbitrary position and X is the total measurement length.

Next we will show that the position derivative of the surface potential requires multiplication by k in position Fourier space. We write the Fourier transform of $V_n(x)$ and take the spatial derivative for a position x and a position $x + \chi$:

$$\delta V_n(x) = \int_{-\infty}^{+\infty} \widehat{\delta V_n}(k) e^{(-2\pi j k x)} dk \quad (5.54)$$

$$\frac{d}{dx} \delta V_n(x) = \int_{-\infty}^{+\infty} \widehat{\delta V_n}(k) (-2\pi j k) e^{(-2\pi j k x)} dk = -2\pi j \int_{-\infty}^{+\infty} \widehat{\delta V_n}(k) k e^{(-2\pi j k x)} dk \quad (5.55)$$

Similarly,

$$\frac{d}{dx} \delta V_n(x + \chi) = -2\pi j \int_{-\infty}^{+\infty} \widehat{\delta V_n}(k) k e^{(-2\pi j k (x + \chi))} dk \quad (5.56)$$

We have changed the Fourier coefficients but this has not changed the Fourier transform term at all. Substituting back into Eq. 5.53, we obtain

$$C_{\delta E_n}(\chi) = \lim_{X \rightarrow \infty} \frac{1}{2X} \int_{-\infty}^{+\infty} -4\pi^2 dx \int_{-\infty}^{+\infty} \widehat{\delta V_n}(k) k e^{(-2\pi j k x)} dk \int_{-\infty}^{+\infty} \widehat{\delta V_n}(k') k' e^{(-2\pi j k' x)} e^{(-2\pi j k' \chi)} dk' \quad (5.57)$$

$$C_{\delta E_n}(\chi) = \lim_{X \rightarrow \infty} \frac{1}{2X} - 4\pi^2 \int_{-\infty}^{+\infty} e^{(-2\pi j k x)} e^{(-2\pi j k' x)} dx \int_{-\infty}^{+\infty} \widehat{\delta V_n}(k) k dk \int_{-\infty}^{+\infty} \widehat{\delta V_n}(k') k' e^{(-2\pi j k' \chi)} dk' \quad (5.58)$$

The first integral term in the above expression collapses to 1 as an integral over the delta function if $k + k' = 0$, *i.e.*, $k' = -k$. We then rewrite, converting the k' integral to an integral over k and passing the limit into the integral:

$$C_{\delta E_n}(\chi) = 4\pi^2 \int_{-\infty}^{+\infty} k^2 e^{(2\pi j k \chi)} \left[\lim_{X \rightarrow \infty} \frac{1}{2X} \widehat{\delta V_n}(k) \widehat{\delta V_n}(-k) \right] dk \quad (5.59)$$

The term in brackets is the definition of the power spectrum of spatial surface potential fluctuations.

$$C_{\delta E_n}(\chi) = 4\pi^2 \int_{-\infty}^{+\infty} k^2 e^{(2\pi j k \chi))} [P_{\delta V_n}(k)] dk \quad (5.60)$$

We would normally write the Fourier transform of $C_{\delta E_n}(\chi)$ as:

$$C_{\delta E_n}(\chi) = \int_{-\infty}^{+\infty} e^{(-2\pi j k \chi))} [P_{\delta E_n}(k)] dk \quad (5.61)$$

Setting Eqs. 5.60 and 5.61 equal, we observe:

$$e^{(-2\pi j k \chi))} P_{\delta E_n}(k) = 4\pi^2 k^2 e^{(2\pi j k \chi))} P_{\delta V_n}(k) \quad (5.62)$$

or

$$P_{\delta E_n}(k) = 4\pi^2 k^2 P_{\delta V_n}(-k) \quad (5.63)$$

The relationship in Eq. 5.63, relating the power spectrum of electric field position noise to the power spectrum of potential position noise, is the main finding of this section.

5.7.5 Electric field noise in derivative of FM-KPFM potential

The result in Eq. 5.63 relates the power spectrum of the electric field noise to the power spectrum of the surface potential noise in k -space. This result should be generally valid for both electric field measurements we explore in this chapter (numeric derivative and position modulation). If we can find an expression for the power spectrum of the potential noise in k -space, then we can also write the power spectrum of electric field noise in k -space. We will now examine the electric field noise for the numeric derivative case, defining the error signal simply as:

$$\delta V_{\text{DC}}(x, t) = V_{\text{DC}(x,t)} - \phi(x) = \delta V_n(t) \quad (5.64)$$

where $V_{\text{DC}(x,t)}$ is the measured surface potential signal, ϕ is the actual surface potential, $\delta V_n(t)$ is the potential noise. A full expression for δV_n is written in Eq. 5.42. In this notation, the power spectrum of the potential noise as a function of frequency is $P_{\delta V_n}(f)$.

From Eq. 5.48, the definition of the rms-squared potential noise is related to the power spectrum of potential noise by:

$$\delta V_{n \text{ rms}}^2 = \int_0^{1/(2\Delta t_{\text{pt}})} P_{\delta V_n}(f) df \quad (5.65)$$

where we have written the total time T as the time per point, Δt_{pt} (*i.e.*, the dwell time of the cantilever at each spatial grid point). We can approximate the rms-squared potential noise per point as the product of the power spectrum at a constant frequency $f = kv_{\text{tip}}$ and the measurement bandwidth b :

$$\delta V_{n \text{ rms}}^2 = \int_0^{1/(2\Delta t_{\text{pt}})} P_{\delta V_n}(f = kv_{\text{tip}}) \simeq P_{\delta V_n}(f = kv_{\text{tip}}) \int_0^{1/(2\Delta t_{\text{pt}})} df \quad (5.66)$$

$$\delta V_{n \text{ rms}}^2 \simeq P_{\delta V_n}(f = kv_{\text{tip}})b = \frac{P_{\delta V_n}(f = kv_{\text{tip}})}{2\Delta t_{\text{pt}}} \quad (5.67)$$

$$b = \frac{1}{2\Delta t_{\text{pt}}} \quad (5.68)$$

where b is the measurement bandwidth and Δt_{pt} is the measurement time per point (*i.e.*, how long the potential is measured at each spatial grid point). Removing the power spectrum term from the integration reflects the assumption that the noise is constant over the integration.

Similarly, we can also relate the potential noise per point to the spatial power spectrum of potential noise:

$$\delta V_{n \text{ rms}}^2 \simeq P_{\delta V_n}(k = f/v_{\text{tip}}) \int_0^{1/2\Delta x_{\text{pt}}} dk = \frac{P_{\delta V_n}(k = f/v_{\text{tip}})}{2\Delta x_{\text{pt}}} \quad (5.69)$$

$$P_{\delta V_n}(k = f/v_{\text{tip}}) = \delta V_{n \text{ rms}}^2 2\Delta x_{\text{pt}} \quad (5.70)$$

where Δx_{pt} is the spatial grid step size. For our finest position grids, $x_{\text{pt}} = 10\mu\text{m}/2^{18} = 0.038$ nm. With a tip velocity of $v_{\text{tip}} = 10\mu\text{m}/128\text{s} = 78.125$ nm/s, $t_{\text{pt}} = 0.5$ ms.

Combining Eqs. 5.67 and 5.70, and solving for $P_{\delta V_n}(k = 0)$, we find:

$$P_{\delta V_n}(k = f/v_{\text{tip}}) = P_{\delta V_n}(f = kv_{\text{tip}}) \frac{\Delta x_{\text{pt}}}{\Delta t_{\text{pt}}} = P_{\delta V_n}(f = kv_{\text{tip}}) \times v_{\text{tip}} \quad (5.71)$$

where v_{tip} is the tip velocity. This is a nice result, confirming that the power spectra of the potential noise in time and position are related through the scanning speed as we demonstrated in section 5.5.

If our experiment noise were white, we approximate the power spectra using the noise at zero frequency:

$$P_{\delta V_n}(k = 0) = P_{\delta V_n}(f = 0) \times v_{\text{tip}} \quad (5.72)$$

In practice, however, the noise δV_{DC} is correlated point-to-point by the RHK PLLPro frequency demodulation, and therefore the noise is bandwidth limited as in Eq. 5.71. The correlation time τ_c is the inverse of the RHK frequency filter cutoff, $1/f_{\text{RHK}}$. For our usual 400 Hz filter, $\tau_c = 2.5$ ms. As we have seen, the spatial frequency k is related to the time frequency f through the tip velocity v_{tip} :

$$f = kv_{\text{tip}} \quad (5.73)$$

We can use Eq. 5.73 convert the RHK frequency cutoff to a spatial frequency roll-off. For a 400 Hz f_{RHK} and $v_{\text{tip}} = 10\mu\text{m}/128\text{s} = 78.125 \text{ nm/s}$, $k_{\text{RHK}} = 5.12 \text{ nm}^{-1}$, corresponding to a spatial blurring width of 0.2 nm.

Using the result we found in Eq. 5.63, we can use Eq. 5.71 to write a power spectrum for the spatial electric field noise:

$$P_{\delta E_n}(k) = 4\pi^2 k^2 P_{\delta V_n}(f = kv_{\text{tip}}) \times v_{\text{tip}} \quad (5.74)$$

This expression should be true for any k .

As we showed in Eqs. 5.3 and 5.55, taking a derivative in potential leads to a multiplication by k in spatial Fourier space. For the power spectrum of the electric field, which is the square of the Fourier transform, we expect a k^2 dependence on the noise (Eq. 5.74). We also expect a 1-pole filter roll-off due to the RHK at $\sim 5\text{nm}^{-1}$. Finally, in our workup

we are applying a spatial filter k_{FILT} the same size as our zero-to-peak position modulation, for a fair comparison between the two methods. We have tried k_{FILT} values in the range 0.007-0.056 nm⁻¹, corresponding to 0-to-peak position modulation values (Δx_{FILT}) in the range 141-17.6 nm.

Assuming the filter is produces a hard cutoff in frequency, we can write the expression for the electric field rms-squared noise from Eq. 5.74 as:

$$\begin{aligned}\delta E_{n \text{ rms}}^2 &= 4\pi^2 \int_0^{k_{\text{FILT}}} P_{\delta V_n}(f = kv_{\text{tip}}) v_{\text{tip}} k^2 dk \\ &\simeq 4\pi^2 P_{\delta V_n}(f = kv_{\text{tip}}) v_{\text{tip}} \int_0^{k_{\text{FILT}}} k^2 dk \\ &= 4\pi^2 P_{\delta V_n}(f = kv_{\text{tip}}) v_{\text{tip}} \left[\frac{1}{3} \frac{1}{\Delta x_{\text{FILT}}^3} \right] = \frac{4}{3} \pi^2 P_{\delta V_n}(f = kv_{\text{tip}}) v_{\text{tip}} \frac{1}{\Delta x_{\text{FILT}}^3} \quad (5.75)\end{aligned}$$

Since the spatial frequency filter Δk_{FILT} is small, we can approximate the power spectrum of the potential noise at $f = kv_{\text{tip}}$ as the power at $f = 0$. We then find:

$$\delta E_{n \text{ rms}}^2 = \frac{4}{3} \pi^2 P_{\delta V_n}(f = 0) v_{\text{tip}} \frac{1}{\Delta x_{\text{FILT}}^3} \quad (5.76)$$

However, the assumption of a hard filter cutoff at k_{FILT} is not exactly what we do in practice. The real filter, as shown in Figs. 5.6-5.7, is curved using a cosine to avoid ringing in the inverse Fourier transform. An expression for the electric field rms-squared noise that reflects what we do in practice is:

$$\delta E_{n \text{ rms}}^2 = 4\pi^2 \int_0^{k_{\text{FILT}}} P_{\delta V_n}(f = kv_{\text{tip}}) v_{\text{tip}} \cos\left(\frac{k}{k_{\text{FILT}}} \frac{\pi}{2}\right) k^2 dk \quad (5.77)$$

Again, we approximate the power spectrum of potential noise as constant, moving it outside the integration:

$$\begin{aligned}\delta E_{n \text{ rms}}^2 &\simeq 4\pi^2 P_{\delta V_n}(f = kv_{\text{tip}}) v_{\text{tip}} \int_0^{k_{\text{FILT}}} \cos\left(\frac{k}{k_{\text{FILT}}} \frac{\pi}{2}\right) k^2 dk \\ &= 4\pi^2 P_{\delta V_n}(f = kv_{\text{tip}}) v_{\text{tip}} \left[\frac{2(\pi^2 - 8) k_{\text{FILT}}^3}{\pi^3} \right] \\ &= 4\pi^2 P_{\delta V_n}(f = kv_{\text{tip}}) v_{\text{tip}} \left[\frac{2(\pi^2 - 8)}{\Delta x_{\text{FILT}}^3 \pi^3} \right] \quad (5.78)\end{aligned}$$

and again, we further approximate the power spectrum of potential noise as the noise at zero frequency:

$$\delta E_{n \text{ rms}}^2 = \frac{8(\pi^2 - 8)}{\pi} P_{\delta V_n}(f = 0) v_{\text{tip}} \frac{1}{\Delta x_{\text{FILT}}^3} \quad (5.79)$$

The definition of the rms-squared electric field noise for the numeric derivative of potential in Eq. 5.79 is the main finding of this section. We see that changing the definition of the filter in frequency space changed the numeric constant in calculating the rms-squared electric field noise from Eq. 5.76 to Eq. 5.79, but the $1/\Delta x_{\text{FILT}}^3$ dependence was unchanged. In the next section, we will find an analogous expression for the rms-squared electric field noise in the position modulation case for comparison.

5.8 Electric field noise in position-modulated FM-KPFM

5.8.1 Definition of position modulated signal and voltage noise in terms of frequency noise

To begin, we need an expression for the potential noise in the position-modulated FM-KPFM experiment. We first rewrite the cantilever frequency shift from Eq. 5.35, adding terms (in blue) to describe the frequency shifts arising from the position-dependent capacitance and position-dependent surface potential (electric field term).

$$\Delta f_{\text{shift}} = -\frac{f_0}{4k_0}(C_{zz} + \cancel{\sqrt{2}x_m \cos(\omega_x t)} C_{zxx}) \times \\ (V_{\text{DC}} - \phi \cancel{-E_x} \sqrt{2}x_m \cos(\omega_x t) + \sqrt{2}V_{\text{AC,rms}} \cos(\omega_v t))^2 + \delta f_{\text{n}}(t) \quad (5.80)$$

where x_m is the zero-to-peak amplitude of the position modulation, ω_x is the frequency of the position modulation, C_{zxx} is the position-dependent tip-sample capacitance, and E_x is the electric field. When we expand Eq. 5.80, we obtain Eq. 5.81. Only the term in red

depends on the tip-modulation voltage alone (ω_v), and is passed through the lock-in that modulates the tip voltage.

$$\Delta f_{\text{shift}} = -\frac{f_0}{4k_0}(C_{zz} + \sqrt{2}x_m \cos(\omega_x t)C_{zxx})[(V_{\text{DC}} - \phi - E_x \sqrt{2}x_m \cos(\omega_x t))^2 + 2\sqrt{2}V_{\text{AC,rms}}(V_{\text{DC}} - \phi - E_x \sqrt{2}x_m \cos(\omega_x t)) \cos(\omega_v t) + 2V_{\text{AC,rms}}^2 \cos^2(\omega_v t)] + \delta f_n(t) \quad (5.81)$$

The signal read in by the tip voltage-modulation lock-in is then:

$$\Delta f(\omega_v) = -\frac{f_0}{4k_0}(C_{zz} + \sqrt{2}x_m \cos(\omega_x t)C_{zxx}) \times [2\sqrt{2}V_{\text{AC,rms}}(V_{\text{DC}} - \phi - E_x \sqrt{2}x_m \cos(\omega_x t))] \cos(\omega_v t) + \delta f_n(t) \quad (5.82)$$

As we can see, the tip voltage modulation and position modulation signals mix, yielding harmonics in the signal at $\omega_v \pm \omega_x$.

We now consider the case where the position modulation frequency is small enough to pass through the tip-modulation lock-in filter. In other words, this derivation assumes that the tip feedback is correctly tracking the surface potential in time.

If ω_x , the position modulation frequency, is less than the inverse of the lock-in time constant (*i.e.*, $\omega_x < 1/TC$), then the harmonics at $\omega_v \pm \omega_x$ will not be cut off and the entire signal in Eq. 5.82 is passed through the lock-in amplifier. In this case, the tip voltage feedback tracks the local potential as the tip is moved back and forth in space, yielding an oscillating voltage in time. This makes some physical sense: the average value of the oscillating surface potential signal is the local surface potential, and the amplitude of the oscillating signal is proportional to the local electric field, as shown in Eq. 5.8.

By analogy to the arguments in Eq. 5.37-5.40, we can write the lock-in output signal as:

$$\Delta f_{LI}(\omega_v) = -\frac{f_0}{4k_0}(C_{zz} + \sqrt{2}x_m \cos(\omega_x t)C_{zxx}) [2V_{\text{AC,rms}}(V_{\text{DC}} - \phi - E_x \sqrt{2}x_m \cos(\omega_x t))] + \sqrt{2}\delta f_n(t) \cos(\omega_v t) \quad (5.83)$$

Expanding this expression yields

$$\begin{aligned}\Delta f_{LI}(\omega_v) = & -\frac{f_0 V_{AC,rms}}{2k_0} [C_{zz}(\phi - V_{DC}) - E_x \sqrt{2} x_m C_{zz} \cos(\omega_x t) \\ & + \sqrt{2} x_m C_{zzx} \cos(\omega_x t)(\phi - V_{DC}) - E_x 2 x_m^2 C_{zzx} \cos^2(\omega_x t)] + \sqrt{2} \delta f_n(t) \cos(\omega_v t)\end{aligned}\quad (5.84)$$

Setting the output in Eq. 5.83 equal to zero and solving for $(\phi - V_{DC})$, with $a = \frac{f_0 V_{AC,rms}}{2k_0}$, we find the potential noise δV_n :

$$\delta V_n = -\frac{a \sqrt{2} C_{zz} E_x x_m \cos(\omega_x t) + 2a E_x x_m^2 C_{zzx} \cos^2(\omega_x t) + \sqrt{2} \delta f_n(t) \cos(\omega_v t)}{a C_{zz} + a \sqrt{2} x_m C_{zzx} \cos(\omega_x t)} \quad (5.85)$$

Or, with simplification:

$$\delta V_n = -\sqrt{2} E_x x_m \cos(\omega_x t) - \frac{\sqrt{2} \delta f_n(t) \cos(\omega_v t)}{C_{zz} + \sqrt{2} x_m C_{zzx} \cos(\omega_x t)} \frac{2k_0}{f_0 V_{AC,rms}} \quad (5.86)$$

Equation 5.86 describes the measured potential noise in the position-modulation experiment, and is the main finding of this sub-section. Perhaps counterintuitively, if feedback is properly maintained, then capacitive effects do not influence the measured amplitude of the oscillating field and therefore the measured electric field.

5.8.2 Electric field noise in position-modulated FM-KPFM

We would now like to find the rms electric field noise for the position-modulation case. We will begin by writing down the measured signal, as it is read out of the tip voltage feedback loop (similar to Eq. 5.86):

$$V_{signal}(t) = \phi\left(t = \frac{x}{v_{tip}}\right) - \sqrt{2} E_x \left(t = \frac{x}{v_{tip}}\right) x_m \cos(2\pi f_x t) + \delta V_n(t) \quad (5.87)$$

where V_s is the overall position modulation signal, ϕ is the usual KPFM surface potential, E_x is the electric field, x_m is the zero-to-peak amplitude of the position modulation, f_x is the frequency of the position modulation, and $\delta V_n(t)$ is the time-dependent noise in the

measured potential. Since we wish to obtain a power spectrum and an expression for the rms-squared noise in each component of this signal, we need to pass into Fourier space; the integrals are defined from time zero to finite time T .

$$\hat{V}_s(f) = \int_0^T V_s(t) e^{2\pi i f t} dt \quad (5.88)$$

$$\begin{aligned} \hat{V}_s(f) &= \int_0^T \phi\left(t = \frac{x}{v_{\text{tip}}}\right) e^{2\pi i f t} dt \\ &\quad - \sqrt{2}x_m \int_0^T E_x\left(t = \frac{x}{v_{\text{tip}}}\right) \cos(2\pi f_x t) e^{2\pi i f t} dt + \int_0^T \delta V_n(t) e^{2\pi i f t} dt \end{aligned} \quad (5.89)$$

$$\hat{V}_s(f) = \hat{\phi}(f = kv_{\text{tip}}) - \sqrt{2} \int_0^T E_x\left(t = \frac{x}{v_{\text{tip}}}\right) \cos(2\pi f_x t) e^{2\pi i f t} dt + \delta \hat{V}_n(f = kv_{\text{tip}}) \quad (5.90)$$

Since in practice we filter the first term (DC) and second term (modulation) separately in Fourier space, we will treat them separately here. We have already described the electric field noise that arises from a derivative of the filtered DC signal in section 5.7.5. Let us now focus on the signal at f_x , the second term in Eq. 5.90. Using the definition the cosine, we can rewrite the Fourier transform of this term:

$$\begin{aligned} \hat{V}_s(f)^{\text{2nd term}} &= -\sqrt{2}x_m \int_0^T E_x\left(t = \frac{x}{v_{\text{tip}}}\right) \frac{1}{2} (e^{2\pi i f_x t} + e^{-2\pi i f_x t}) e^{2\pi i f t} dt \\ &= -\sqrt{2}x_m \int_0^T E_x\left(t = \frac{x}{v_{\text{tip}}}\right) \left[\frac{1}{2} e^{2\pi i (f+f_x)t} + \frac{1}{2} e^{2\pi i (f-f_x)t} \right] dt \end{aligned} \quad (5.91)$$

This expression is equivalent to:

$$\hat{V}_s(f)^{\text{2nd term}} = -\sqrt{2}x_m \left[\frac{1}{2} \hat{E}_x(f + f_x) + \frac{1}{2} \hat{E}_x(f - f_x) \right] \quad (5.92)$$

Equation 5.92 shows that the Fourier transform of the position modulated signal at the modulation frequency f_x is related to the Fourier transform of the electric field at $+f_x$ and $-f_x$. This result makes sense intuitively since we expect copies of the modulation signal at $+f_x$ and $-f_x$ in Fourier space. We note that filtering out this second term to extract the

electric field information assumes that $E_x(f)$ has no information outside the frequency range $+f_x$ to $-f_x$. For our typical position modulation frequencies of 4.5 Hz and tip velocities of $v_{\text{tip}} = 10\mu\text{m}/128\text{s} = 78.125 \text{ nm/s}$, the relevant spatial frequency cutoff is $\sim 0.06 \text{ nm}^{-1}$, or in space, about 17 nm. Since the spatial resolution of our FM-KPFM apparatus is on the order of $\sim 10\text{-}20 \text{ nm}$, this is a fair assumption: we do not expect to measure electric field features smaller than this.

For a small frequency step ν away from f_x , the Fourier transform of the modulated potential in Eq. 5.92 is:

$$\hat{V}_s(f_x + \nu)^{\text{2nd term}} = -\sqrt{2}x_m \left[\frac{1}{2}\hat{E}_x(2f_x + \nu) + \frac{1}{2}\hat{E}_x(\nu) \right] \quad (5.93)$$

$$\hat{V}_s(f_x + \nu)^{\text{2nd term}} \simeq -\sqrt{2}x_m \frac{1}{2}\hat{E}_x(\nu) \quad (5.94)$$

We assume that the electric field component at $2f_x + \nu$ is negligible, giving 5.94. Solving for the electric field term, we obtain:

$$\hat{E}_x(\nu) \simeq -\frac{\sqrt{2}}{x_m} BP \left[\hat{V}_s(f_x + \nu) \right] \quad (5.95)$$

where the band-pass operation BP requires multiplying the signal by a filter around f_x . This filtering procedure corresponds to (a) in the position modulation signal workup chain illustrated in Fig. 5.7. We use the same filter as described in Eq. 5.77, defined formally as:

$$BP(f) = \begin{cases} 0 & : f < f_x - f_{\text{FILT}} \\ \cos \left(\frac{\pi}{2} \frac{f - f_x}{f_{\text{FILT}}} \right) & : f_x - f_{\text{FILT}} < f < f_x + f_{\text{FILT}} \\ 0 & : f_x + f_{\text{FILT}} < f \end{cases} \quad (5.96)$$

We can write the Fourier transform of the electric field *noise* in terms of frequency in the same form as Eq. 5.95:

$$\delta\hat{E}_x(\nu) \simeq -\frac{\sqrt{2}}{x_m} BP(f_x + \nu) \left[\delta\hat{V}_s(f_x + \nu) \right] \quad (5.97)$$

The power spectrum of the electric field noise in terms of frequency for the position modulated electric field is then:

$$P_{\delta E_x}(\nu) = \frac{2}{x_m^2} BP^2(f_x + \nu) P_{\delta V_n}(f_x + \nu) \quad (5.98)$$

$$P_{\delta E_x}(k) = P_{\delta E_x}(\nu = kv_{\text{tip}}) v_{\text{tip}} = \frac{2v_{\text{tip}}}{x_m^2} BP^2(f_x + kv_{\text{tip}}) P_{\delta V_n}(f_x + kv_{\text{tip}}) \quad (5.99)$$

where we have passed to spatial frequency using the relationships defined in section 5.5. As a check that we are still in reasonable territory, the units are still correct: $P_{\delta E_x}(k)$ has units of V^2/m^{-1} , and the units on the right side of Eq. 5.99 turn out to be $(\text{m}/\text{s})(1/\text{m}^2)(\text{V}^2/\text{Hz}) = \text{V}^2\text{m}$ or V^2/m^{-1} .

Finally, we can convert the power spectrum for the electric field noise to the rms-squared noise. This procedure is analogous to the derivation in Eqs. 5.78-5.79.

$$\delta E_x^2 \text{ rms} = \int_{-\infty}^{\infty} P_{\delta E_x}(\nu) d\nu = \int_{-\infty}^{\infty} \frac{2}{x_m^2} BP^2(f_x + \nu) P_{\delta V_n}(f_x + \nu) d\nu \quad (5.100)$$

$$\delta E_x^2 \text{ rms} \simeq \frac{2}{x_m^2} P_{\delta V_n}(f = f_x) \int_{-\infty}^{\infty} BP^2(f_x + \nu) d\nu \quad (5.101)$$

We assume in Eq. 5.101 that the power spectrum of potential noise in the filter window around f_x is constant, allowing us to move this term outside the integration. Setting the limits of integration to the filter size, and using the definition of the filter from Eq. 5.96, we evaluate:

$$\delta E_x^2 \text{ rms} \simeq \frac{2}{x_m^2} P_{\delta V_n}(f = f_x) \int_0^{f_{\text{FILT}}} BP^2(f_x + \nu) d\nu \quad (5.102)$$

$$\begin{aligned} \delta E_x^2 \text{ rms} &\simeq \frac{2}{x_m^2} P_{\delta V_n}(f = f_x) \int_0^{f_{\text{FILT}}} \cos^2\left(\frac{\pi}{2} \frac{\nu}{f_{\text{FILT}}}\right) d\nu \\ &= \frac{2}{x_m^2} P_{\delta V_n}(f = f_x) \int_0^{f_{\text{FILT}}} \left(\frac{1}{2} + \frac{1}{2} \cos\left(\pi \frac{\nu}{f_{\text{FILT}}}\right)\right) d\nu \\ &= \frac{2}{x_m^2} P_{\delta V_n}(f = f_x) \int_0^{f_{\text{FILT}}} \frac{1}{2} d\nu + \int_0^{f_{\text{FILT}}} \frac{1}{2} \cos\left(\pi \frac{\nu}{f_{\text{FILT}}}\right) d\nu \end{aligned} \quad (5.103)$$

$$\delta E_x^2 \text{ rms} \simeq \frac{2}{x_m^2} P_{\delta V_n}(f = f_x) \frac{f_{\text{FILT}}}{2} \quad (5.104)$$

The units here are accurate: V^2/m^2 does indeed equal $(1/m^2)(V^2/\text{Hz})(1/\text{s})$. We convert the filter frequency to a spatial frequency via the tip velocity, and finally to a spatial position filter:

$$\delta E_x^2 \text{ rms} \simeq \frac{1}{x_m^2} P_{\delta V_n}(f = f_x) k_{\text{FILT}} v_{\text{tip}} \quad (5.105)$$

$$\delta E_x^2 \text{ rms} \simeq \frac{v_{\text{tip}}}{x_m^2} P_{\delta V_n}(f = f_x) \frac{1}{\Delta x_{\text{FILT}}} \quad (5.106)$$

The rms-squared electric field noise for the position-modulation experiment in Eq. 5.106 is the main finding of this section.

5.9 Discussion: comparing electric field noise in standard and position-modulated KPFM

Let us compare the results of sections 5.8 and 5.8 by examining the electric field noise expected for the two measurements we have discussed. For the numeric derivative of a standard FM-KPFM measurement, blurred in space by the size of the derivative step Δx_{FILT} , we found Eq. 5.79:

$$\delta E^2 \text{ rms} \simeq \frac{8(\pi^2 - 8)}{\pi} P_{\delta V_n}(f = 0) v_{\text{tip}} \frac{1}{\Delta x_{\text{FILT}}^3} \quad (5.107)$$

Whereas for the position-modulation experiment, we found Eq. 5.106:

$$\delta E^2 \text{ rms} \simeq P_{\delta V_n}(f = f_x) \frac{v_{\text{tip}}}{x_m^2} \frac{1}{\Delta x_{\text{FILT}}} \quad (5.108)$$

We observe that the rms-squared noise of the electric field in both methods depends on a factor of $1/x^3$. In the limit that x_{FILT} , the spatial filter size, is set equal to x_m , the size of the position modulation, the main difference between the two expressions is the frequency dependence of the voltage noise. If these values are comparable, *i.e.*, if $P_{\delta V_n}(f = 0)$ equals

$P_{\delta V_n}(f = f_x)$, then the two methods should give rms-squared electric field noise comparable to within a numerical factor of ~ 5 .

In what limit would position modulation give a much cleaner electric field signal than a numeric derivative? If $P_{\delta V_n}(f = 0)$ is much greater than $P_{\delta V_n}(f = f_x)$ - in other words, if the surface potential noise at low frequencies is much greater than the potential noise at the position modulation frequency- then the position modulation experiment is expected to yield a less noisy electric field. In our current microscope, we operate closer to the limit where the rms-squared electric field noise is fairly comparable, since the surface potential noise is not too different for $f = 0$ Hz and $f = 4.5$ Hz.

The spatial resolution is limited by the position modulation frequency f_x and our assumption that no electric field information lies below that frequency. If we could operate at a much greater position modulation frequency, the theoretical spatial resolution of the measurement would be increased. However, our detector (the photodiode that registers the cantilever position, the signal that we demodulate to obtain the cantilever frequency shift) suffers from noise proportional to f^2 that sets in around 12 Hz (see Fig. 5.9).

When choosing f_x for a position-modulation experiment, we see that there are several constraints to balance. The first goal is to minimize the surface potential noise at f_x as compared with $f = 0$, to minimize the rms-squared electric field noise. The second goal is to maximize f_x , which improves the position modulation spatial resolution, while still maintaining real-time tip voltage feedback. In other words, as f_x is increased, the entire modulation signal must still pass through the tip-voltage feedback loop, without being cut off by the lock-in time constant for the tip voltage feedback. One must also work around mechanical vibration peaks in the apparatus.

5.10 Varying size of position modulation

In our experiment, the frequency noise (Fig. 5.9) has a minimum around 4-5 Hz. Therefore, our position modulation frequency of 4.5 Hz should place us in the limit where the potential noise at the modulation frequency is smaller than the potential noise at 0 Hz. In practice, whether the position modulation method yields a less noisy electric field than the derivative method depends on the size of the position modulation.

In Fig. 5.16, we show electric fields measured using the numeric derivative and our position modulation method for a pentacene (*p*- type) bottom-contact transistor. The gate bias is set to zero, and the source-drain bias is set to -2 V. The top row of figures shows the DC potential linescan extracted as shown in Fig. 5.6. The bottom row of figures shows the electric fields measured in each method overlaid with one another. As expected from the potential profile, we find a small peak in the electric field at the injecting contact (left) where there is a small potential drop, and a large electric field peak at the extracting contact (right) where the potential drop is large.

For large position modulations, as seen in the left-most plots ($dx = 141\text{nm}$), the electric field features in both methods are blurred. On the other hand, when the position modulation is small (right-hand plots, $dx = 35$ or 17 nm), the electric field in both methods is quite noisy. This result is not surprising since a small modulation in space corresponds to a large filter window in frequency space and therefore more noise. The pleasing result in Fig. 5.16 is the plot second from the left, for $dx = 70\text{ nm}$. When an appropriate modulation size is chosen, the position modulation method does indeed appear to yield a cleaner signal than the numeric derivative method.

Note that the magnitude of the electric field peaks appears to increase as the size of the modulation decreases. Since the electric field is defined as a potential difference over

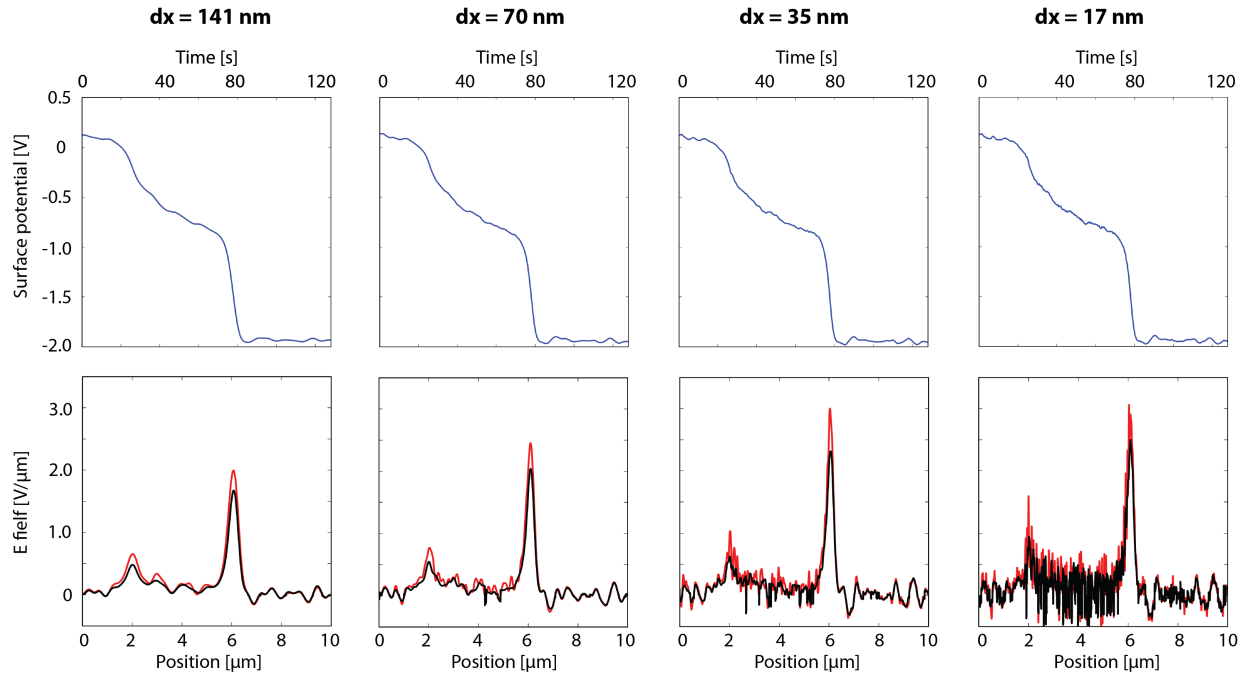


Figure 5.16: Comparison of derivative and position modulated electric fields for different size modulations. Top row: DC surface potential profiles. Bottom row: Electric fields obtained via numeric derivative (red) and position modulation (black).

a spatial distance, it makes sense that the field appears larger when the spatial distance considered is smaller. We also note that both methods of obtaining electric fields distort the “real” electric field. The numeric derivative amplifies high-frequency noise, as we have seen. On the other hand, while the position modulation method avoids a great deal of high frequency noise by filtering the signal through the position modulation f_x , it underestimates the magnitude of sharp features in space due to details of the filtering in Fourier space (to be expanded in future publication). In addition, we only measure the component of the signal at f_x , yet we know that the Fourier transform of a square edge has components at a range of frequencies. One method overestimates noise; the other underestimates real signal. If we were to use these electric field profiles to estimate local mobilities, the position-modulation method would overestimate mobility since $E \propto 1/\mu$.

5.11 Conclusions and future directions

We have demonstrated that position-modulation can be combined with FM-KPFM to extract electric fields from surface potential measurements without taking a derivative. We have defined the electric field noise as a function of the potential noise for both the numeric derivative and position modulation methods. We show that in order to measure smaller electric field features, a higher modulation frequency is needed. Faster measurements would also be enabled by faster position modulation. Our position modulation frequency is currently limited by our photodetector, where noise increases as f^2 at high frequencies. The method in general is also limited by the requirement that the position modulation signal pass cleanly through the tip feedback loop in real time. We note again that a full analytical expression for the surface potential in position modulation is forthcoming, which will help explain the different frequency-dependence of the derivative and position-modulated electric fields obtained in this chapter.

We anticipate that this simple modification of FM-KPFM will be useful for electric field measurements in a variety of systems. When clean electric field profiles are accessible via the derivative method, such as for high-voltage transistor measurements in high vacuum, position modulation may not offer a substantial improvement in the electric field noise. However, for systems where electric fields are small, such as organic donor-acceptor solar cell blends, position modulation could be a useful technique.

In addition, if lateral position modulation measurements are made in perpendicular directions, it should be possible to produce 2D images of the electric field. Such 2D E field images would be a great advance from lateral E field linescans. In the future, we hope to apply this technique to measuring local electric fields in bulk heterojunction solar cell blends.

5.12 Acknowledgements

Many thanks to Ryan Dwyer for his assistance designing and building the second summing circuit needed for the x -modulation, and especially for his help testing and improving the tip voltage feedback loop. Thanks to Ryan Dwyer and John Marohn for their help implementing the freqdemod package in Python for analyzing the position-modulation data. Thanks to John Marohn for the many discussions of theoretical noise in both standard and position-modulated FM-KPFM. This work was supported by NSF-DMR 1309540.

CHAPTER 6

COLLABORATIVE WORK: PRELIMINARY EFM MEASUREMENTS ON PHOTOVOLTAIC MATERIALS

6.1 Introduction

A strength of EFM is the wide variety of materials it can be used to study. At Cornell, I have had the opportunity to work on a range of samples prepared in collaboration with other researchers. In this chapter, details are provided for two of the most promising collaborations I worked on during this thesis: studies of covalent organic frameworks with the Dichtel group and experiments on lead-halide perovskites with Dr. David Moore. None of this data has been published, but I hope that the background literature and preliminary experiments detailed here will stimulate future localized measurements via scanned probe microscopy of these exciting systems.

6.2 EFM of Covalent Organic Frameworks

6.2.1 Introduction: Chemistry of COFs

Covalent organic frameworks, or COFs, are a relatively new class of materials featuring porous, crystalline, regular structures with potential applications in gas storage [150, 151], catalysis [152], and organic semiconducting devices [153, 154]. Similar to metal-organic frameworks (MOFs), which are usually composed of metal atoms linked in a regular pattern by organic ligands, COFs are generally composed of two monomer species covalently bonded in long-range porous networks. Two-dimensional networks with hexagonal [155, 156] or

square pores [157] and three-dimensional networks with tetrahedral pores have all been synthesized [158, 159]. The covalent bonds are usually boronate esters, but imine bonded COFs have also been demonstrated [160]. This study will focus on 2D COFs with boronate ester bonds prepared by the Dichtel group, who have shown that it should be possible to build a wide range of structures by varying the COF building blocks functionalized with either the diboronic acid or the polycatechols [161, 162]. The particular COF of interest in these initial studies will be the 2D, hexagonal-pore HHTP-DPB COF synthesized by the Dichtel group [163].

A major challenge in COF synthesis is the decreasing solubility of the COF network as it grows [158]. Of the several examples of COFs that have been synthesized, most have been purified as powders. The growth of macroscopic, continuous COFs is an important step towards incorporating these materials into functional electronic devices. One general approach to growing COF films is vacuum-deposited surface assembly. For example, 2-D COFs can be grown by polymerization on a metal surface, often Au(111), by annealing a vacuum-deposited layer of monomer precursors [164, 165], or by direct vacuum deposition onto heated well-ordered noble metal surfaces [166]. Taking a different approach, Colson *et al.* recently demonstrated that 2D COFs can be grown from solution in a layered, highly ordered fashion on single-layer graphene [167]. This is a promising development for incorporation of these materials into devices.

6.2.2 Characterization Techniques for COFs

Several characterization techniques are commonly employed to characterize COFs. Adsorption isotherms, usually with nitrogen, argon, or CO₂, are regularly used as a measure of a material's porosity. By measuring the gas uptake as a function of pressure, metrics such as cumulative surface area and pore size distribution can be calculated using Brunauer-

Emmett-Teller (BET) theory [155]. Experimental gas adsorption isotherms are commonly compared to those predicted by DFT calculations to estimate the percentage of “activated” material [153, 163].

Current-voltage characteristics of an arene-based COF have been measured by placing a sample of material across two platinum electrodes and measuring current as a function of source-drain bias [153]. Very simple photocurrent measurements on COF powders sandwiched between two metal electrodes have been made in arene-based [153] and metallophthalocyanine-based COFs [154, 168], and one wavelength-dependence of photogenerated current measurement has been made [154].

Flash photolysis time-resolved microwave conductivity (FP-TRMC) experiments are another common characterization metric for two-dimensional COFs [154, 168, 169]. In FP-TRMC measurements, a sample in a microwave cavity is irradiated with a laser pulse that generates charge carriers in the sample; the interaction of the charge carriers with the microwave field changes the microwave power and this change can be related to the sample conductivity [170]. These experiments have the advantages of accessing extremely short time scales and not requiring electrodes. However, since photogenerated charge carriers move such a tiny distance on the time scale of the high microwave frequencies used for conductivity detection, FP-TRMC experiments tend to overestimate conductivity. These measurements are most sensitive to ordered regions and insensitive to bulk phenomena like grain boundaries and domain edges; in addition, the charge carrier mobilities cannot be deconvoluted from one another or from the photogenerated carrier quantum yield.

6.2.3 COFs for Devices

As yet there are no examples of COFs in working transistors or photovoltaics. The current-voltage characteristics measured by Wan *et al.* demonstrated that the COF in question was conductive with an applied bias [153], and the existing photocurrent measurements show that some COFs can generate charge carriers under illumination [153, 154, 168]. Blunt *et al.* have shown that a COF thin film can capture C₆₀ clusters in its pores [164], but these films could not be made into solar cells since the COF was grown on a non-transparent Cu(111) substrate. With so much promise and so few measurements made, COFs are an excellent candidate for further study with scanning-probe techniques.

6.2.4 Scanning-Probe Microscopy for COFs

Scanning-probe microscopy (SPM) techniques have the major advantage of allowing correlation between topographic and electronic properties like current, surface potential, and photovoltage. The only SPM data on COFs thus far are scanning tunneling microscopy (STM) images of thin COF films on highly ordered metal substrates; these measurements have been used to identify several COF growth defects [165, 166, 171, 172] and verify the presence of C₆₀ clusters in the COF pores [164]. Here, I propose several SPM experiments that each will be the first measurement of its type on COF thin films, each yielding quantities not measurable by the current COF characterization techniques; I also present some preliminary data.

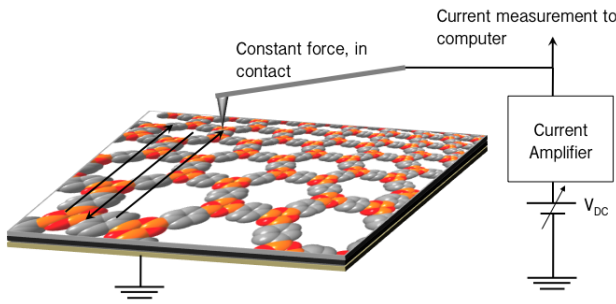


Figure 6.1: Schematic of conductive-probe atomic force microscopy experiment. The sample is composed of a conductive substrate such as ITO topped with graphene and ~ 100 nm COF. The cantilever is scanned across the sample, in contact with the surface, while tip-sample current is measured for a set tip-sample bias.

6.2.5 Conductive-Probe AFM for COFs

In conductive-probe atomic force microscopy (cp-AFM), a metal-coated cantilever tip is brought in contact with a sample surface, a tip-sample bias is applied, and current is measured locally while the probe is scanned at constant force across the sample (Fig. 6.1). To study COFs with cp-AFM, a conductive substrate is required. The graphene used in templating COF growth may be sufficient [167], or the graphene can be transferred to a conductive substrate before COF growth.

Initial cp-AFM measurements were made by Dr. James O'Dea on the Veeco AFM system maintained by the Cornell Center for Materials Research (CCMR). This setup requires imaging in ambient atmosphere and offers the choice of an opaque hood (dark) or ambient lighting. This study used HHTP-DPB COF [163] on graphene on a fused silica substrate, with silver-painted electrical connections to the underlying graphene. We anticipated that current collection would be fairly homogeneous across the COF film. It is unlikely that a cantilever tip would give sensitive enough resolution to distinguish between the conductive

COF framework and the nonconductive pores since the pores in HHTP-DPB COF are 4.7 nm wide (although this seems like a small feature size, these are the largest COF pores to date) [163].

The measurements in Fig. 6.2 show generally low conductivity with small scattered regions of higher conductivity. The high-conductivity regions appear to be correlated with regions of lower topography, and may represent conduction through graphene. Also, some of the measured morphology is artificially lowered by attraction between the tip and the sample. Exposing the sample to ambient lighting did not increase the conductivity. The graphene substrate is \sim 1000 times more resistive than the usual conductive substrates such as ITO; this may explain the low measured currents through the COF. Another possible explanation for the low COF current is chemical degradation. COFs break down upon exposure to moisture. The sample was stored in air for a few days before cp-AFM experiments and the cp-AFM experiments themselves are performed in ambient atmospheric conditions.

6.2.6 Electric Force Microscopy for COFs

Electric force microscopy (EFM) is a technique that measures the potential between a metal-coated cantilever tip and the sample surface. For fastest 2D imaging, modulated EFM is often used. In modulated EFM, an AC modulation voltage and a DC bias are summed and applied to the cantilever tip. The interaction of the biased cantilever tip with charges in the sample causes the cantilever frequency to shift; the component of the cantilever frequency shift at the modulation frequency ω can be written as in Equation (6.2) [27]:

$$\hat{f}(\omega) = -\frac{f_0 V_{AC}}{2k_0} \frac{\partial^2 C}{\partial z^2} (V_{DC} - \phi) \quad (6.1)$$

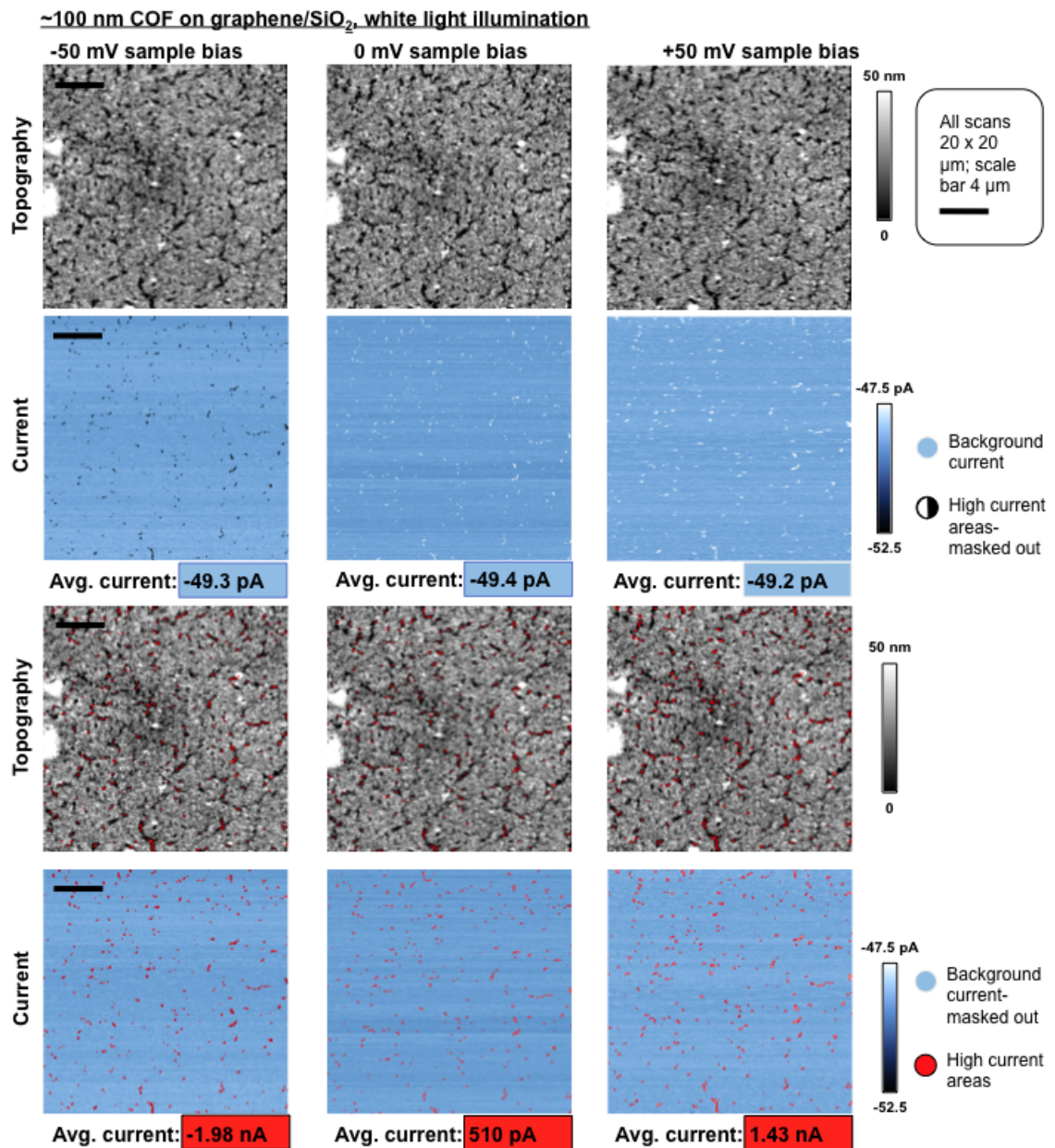


Figure 6.2: Preliminary cp-AFM data on a COF/graphene/fused silica sample, collected by Dr. James O'Dea. Data was collected under white light illumination. From left to right, the three columns represent -50 mV, 0 mV, and +50 mV tip-sample bias. Topography is mapped in the first and third row. The currents collected from the COF film at different biases are mapped in the second and fourth rows. The average COF currents are listed in the blue boxes below row 2, while the average low-topography currents are listed in the red boxes below row 4. The high current areas are masked out in the fourth row, and when overlaid with topography in row three, it is clear that the high currents come from regions of low topography.

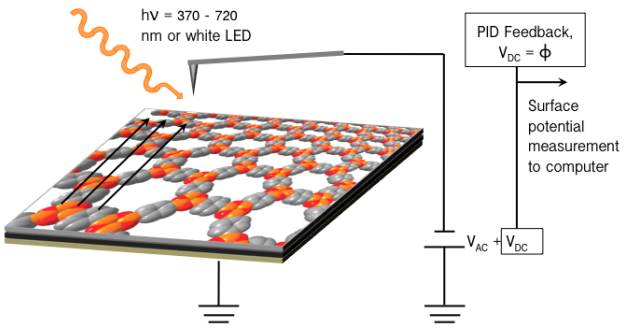


Figure 6.3: Schematic of electric force microscopy experiment. The sample is composed of a conductive substrate such as ITO topped with graphene, ~ 100 nm COF film. The cantilever is scanned in the plane 60 nm above the sample while the tip voltage is adjusted to track the surface potential (modulated EFM).

with f_0 the cantilever resonance frequency, V_{AC} the modulation voltage, k_0 the cantilever spring constant, $\partial^2 C / \partial z^2$ the second derivative of the tip-sample capacitance with respect to tip height z , V_{DC} the DC tip bias, and ϕ the surface potential. A feedback loop is used to adjust the tip bias V_{DC} to nullify $\hat{f}(\omega)$, at which bias $V_{DC} = \phi$. By tracking V_{DC} while the tip is raster-scanned in close proximity (60 nm) to the sample surface, ϕ is measured as a function of position.

Preliminary AFM and EFM measurements of a 100 nm HHTP-DPB COF film on graphene on fused silica, with silver paint contacts to the graphene, are shown in Fig. 6.4. The film is grainy; there are clearly visible particles of a fairly uniform height (70-80 nm), with scattered tall spires (>125 nm). The surface potential is roughly constant around -0.45 V in a large scale scan ($10 \times 10 \mu\text{m}$), but on a smaller scale ($1 \times 1 \mu\text{m}$) the surface potential is clearly seen to vary with morphology. There is an overall slow, negative shift in surface potential under white LED illumination; this shift is slowly recovered when the LED is turned off. The sign of this shift suggests that holes are extracted by the graphene under illumination,

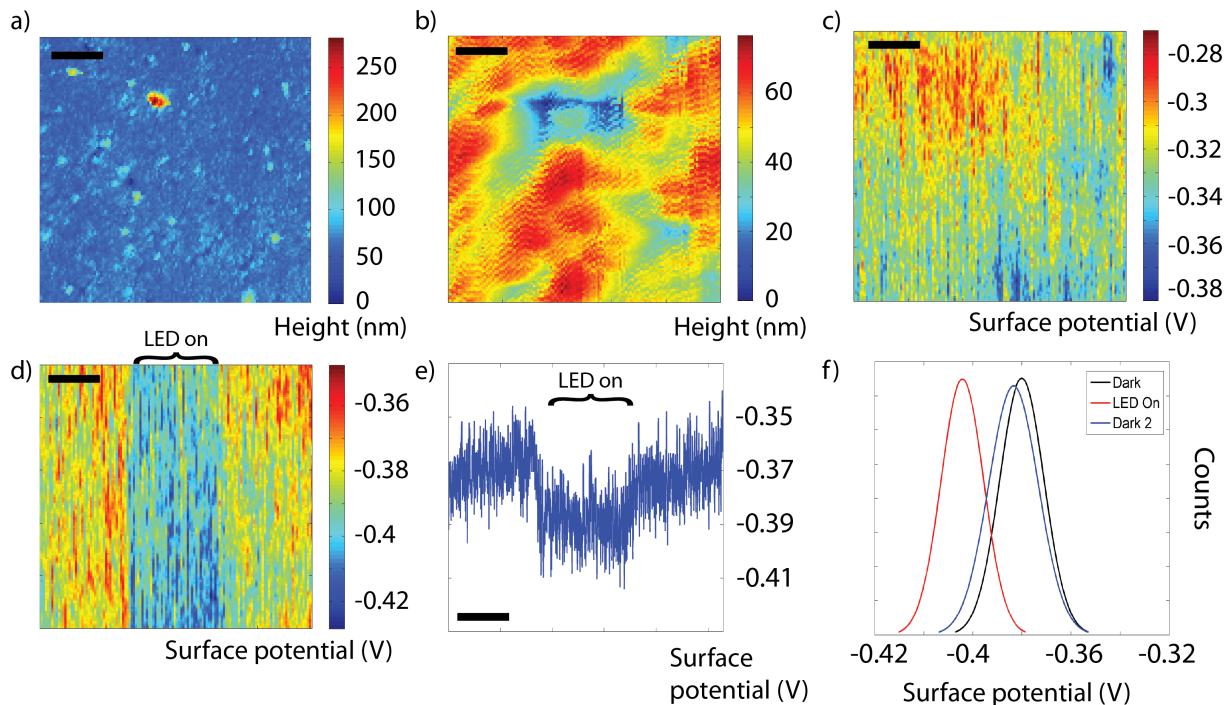


Figure 6.4: Preliminary EFM on HHTP-DPB COF on graphene. Topography of a (a) $10 \times 10 \mu\text{m}$ and (b) $1 \times 1 \mu\text{m}$ region of the film. (c) Surface potential of same region as (b). (d) Surface potential in dark, under white light, and in dark again (left to right). (e) Surface potential data versus position, average of data in (d). (f) Histograms of photovoltage data in (d). The scale bar in (a) is $2 \mu\text{m}$ and $0.2 \mu\text{m}$ in (b-e).

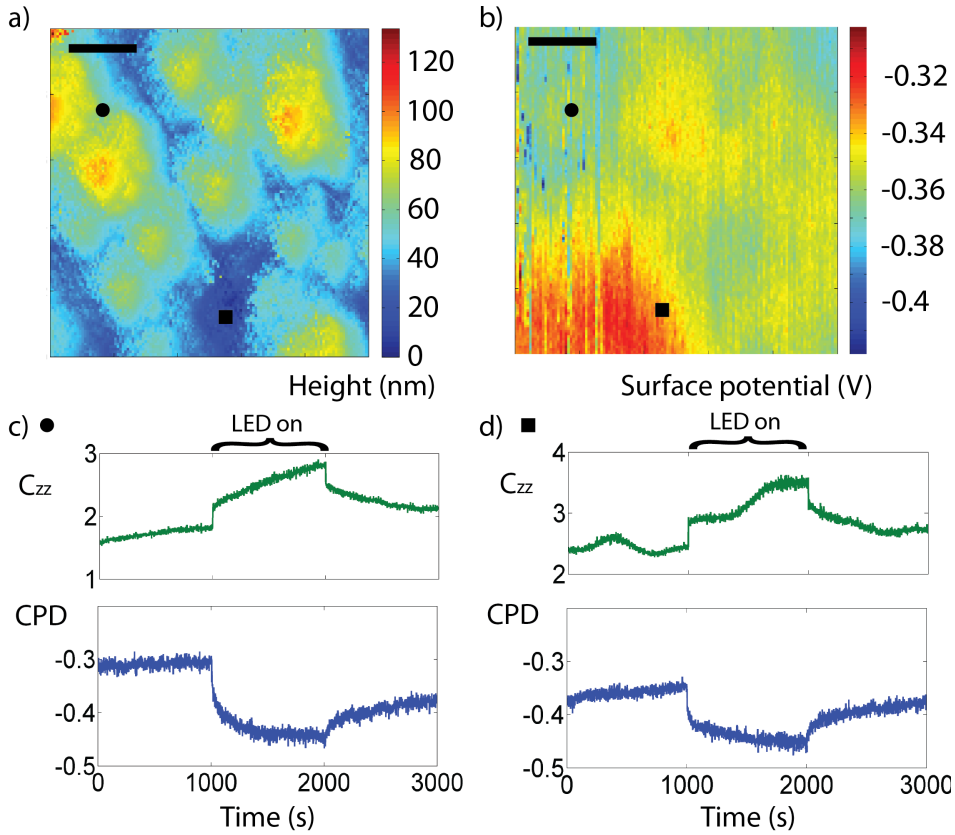


Figure 6.5: Preliminary EFM on COF-5 on ITO. (a) Topography of a $1 \times 1 \mu\text{m}$ region of the film. (b) Surface potential of same region as (a). Scale bar in (a-b) is $0.2 \mu\text{m}$. (c-d) Capacitance derivative and surface potential (V) measured as a function of time in dark, under LED light, and returned to dark, for the point marked with the circle (c) and square (d).

leaving excess electrons in the COF film.

I made similar AFM and EFM measurements of an approximately 100 nm COF-5 film on an ITO substrate. I used silver paint to make contact to the ITO. The data is shown in Fig. 6.5. Although the COF grains in this film are larger, I observe a similar correlation between lower topography and more positive surface potential. The sign of the photovoltage under a white LED is negative again, and the magnitude of the photovoltage is comparable or smaller (about 150 mV in COF-5 on ITO versus 200 mV in HHTP-DPB COF on graphene). In this sample, the surface potential recovers much more slowly after exposure to light,

suggesting that hole transfer back into the COF-5 from ITO is more difficult than the HHTP-DPB COF/graphene case. The surface potential can be restored to its “neutral” potential by biasing the ITO.

6.2.7 Future COF Experiments

It would be extremely interesting to compare the photovoltage behavior of a COF film with and without a layer of an electron acceptor like a fullerene. If the fullerene efficiently accepts electrons from the COF, I would expect to observe a more negative photovoltage in such a donor-acceptor bilayer sample. Holes would still be extracted by ITO, but electrons would be transferred to the top fullerene layer. The photovoltage would be more negative because there would be a greater charge separation distance between the electrons in the sample and the grounded substrate, essentially forming a larger dipole for the probe to measure.

Luria predicted that for samples with laterally invariant surface potential, the surface potential shift under illumination for a bilayer donor-acceptor film is expected to depend on the electron donor film thickness:

$$\phi = -\frac{1}{2\epsilon_0}(\sigma_{\text{ex}}d_{\text{ex}} + \sigma_{\text{sep}}t + \frac{\rho_{\text{trap}} - \rho_{\text{free}}}{2}) \quad (6.2)$$

with ϵ_0 the dielectric constant, σ_{ex} the exciplex planar density, d_{ex} the depth of the exciplex concentration, σ_{sep} the planar density of separated charge, t the donor film thickness, ρ_{trap} the volume density of trapped charge, and ρ_{free} the volume density of free charge.

If this relationship holds, the determination of $\sigma_{\text{ex}}d_{\text{ex}}$, σ_{sep} , and $\rho_{\text{net free}}$ would all be new measurements in a COF + fullerene system. For the most recent COF films fabricated, the morphology is probably too rough to yield a consistent lateral surface potential. Tightly

controlling COF film thickness is also a sample preparation challenge. Unfortunately, donor-acceptor COF bilayer samples did not become available during the thesis period.

6.2.8 COF Acknowledgements

HHTP-DPB COF on graphene and COF-5 on ITO were prepared by John Colson in the Dichtel group. Dr. James O'Dea collected the cp-AFM data for the HHTP-DPB COF on graphene. This work was supported by an NSF graduate research fellowship as well as funding from NSF-DMR 1006633 and NSF-DMR 1309540.

6.3 EFM of Perovskites

The term “perovskite” refers to an ABX_3 crystal structure, not to any particular materials, although recently the term has been used increasingly to refer to organometallic halide materials- especially methylammonium lead halides (usually trioxide). These organometallic perovskites are extremely exciting photovoltaic materials. I will refer to methylammonium lead halide perovskites simply as “perovskites” in the remainder of this chapter.

Photovoltaic devices using perovskites started out using perovskite as the dye in a TiO_2 dye sensitized solar cell (DSSC) architecture. It was then found that meso-structuring the perovskite and removing the TiO_2 worked even better, calling into question the role of the TiO_2 . Most recently, *p-i-n* photovoltaic devices with vapor deposited perovskites as the active layers have also produced high efficiencies [173]. A typical device composition is ITO/ TiO_2 /perovskite/Hole Transport Material (usually spiro-OMeTad)/gold.

6.3.1 Perovskite performance pros and cons

The reason for perovskites' strong photovoltaic performance remains somewhat of an open question. The high performance is probably due in part to long (greater than 1 μm) exciton diffusion lengths and long recombination lifetimes. These exciton behaviors have been characterized using photoluminescence in mixed halide perovskite films [174]. On the other hand, perovskite excitons are fairly weakly bound [175], so less energy may be lost in splitting excitons compared with the larger exciton binding energies in organic photovoltaics. The question of whether photovoltaic perovskites should be considered ferroelectric, and what influence any ferroelectricity has on solar cell performance, also remains unanswered.

On the other hand, optimizing perovskite photovoltaics does pose several challenges. First, although perovskites are relatively easy to prepare from solutions of precursors, processing conditions strongly influence film morphology and performance. Dr. David Moore has shown that the choice of counterion in perovskite fabrication is extremely important because it sets the time frame for film formation; acetate yields the slowest film formation so far. Second, perovskite photovoltaic performance can be difficult to accurately report since current-voltage curves often suffer from hysteresis which might come from halide ion migration in the film [176]. Finally, perovskite solar cells suffer from long-term performance instability, due perhaps to water sensitivity and/or UV light sensitivity in the presence of TiO_2 . The interfaces in the solar cell are extremely important in determining overall performance.

6.3.2 Previous scanning probe microscopy of perovskites

Two scanning Kelvin probe studies have examined the surface potential at perovskite grain boundaries. A mixed iodide/chloride perovskite on TiO_2/ITO showed increased band bend-

ing (sharper, more negative surface potential) at the grain boundaries compared with the iodide-only device; the authors concluded that the presence of chloride gave rise to this difference [177]. A second study examined the influence of annealing on iodide-only perovskites, and proposed that annealing creates a layer of lead iodide around each grain, reducing recombination and yielding a more uniform surface potential [178].

Two other scanning Kelvin probe studies have looked at cross-sections of perovskite devices [179, 180]. Both papers measure potential profiles (and numerically differentiated electric fields) across working devices. Electron extraction is clearly more efficient than hole extraction since positive charge builds up in the film under illumination, but when light is turned off electron traps yield a negative surface potential. These microscopic measurements are consistent with macroscale Kelvin probe measurements of perovskite surface potentials [181]. The macroscale Kelvin probe study also measured the spectral dependence of the surface potential, revealing the band absorption edge.

6.3.3 Preparing a perovskite transistor

With the help of Dr. David Moore, we prepared the precursor solutions for a perovskite solar cell and spun-cast the film onto transistor substrates. ITO substrates are normally prepared by sonicating in DI + Aquet, then DI water, followed by scrubbing, sonicating in acetone and then isopropanol. The chips are rinsed with IPA, dried with nitrogen, and UV-ozone cleaned.

We prepared methylammonium lead iodide perovskites from lead chloride (PbCl_2) and methylammonium iodide (MAI). To remove water arising from air exposure, it is good practice to rinse the MAI with ether on a Buchner funnel. Methylammonium iodide turns yellowish when water is present. Perovskites can also be made from a lead acetate precursor;

this precursor should be rinsed with ether to remove hydrates. The precursors were weighed out in a 3:1 MAI:PbCl₂ ratio. There should be a slight excess of MAI to ensure that all the lead is used. We used 0.149 g PbCl₂ and 0.276 g MAI for a total of 0.425 g solids.

	MW (g/mol)	Ratio	Amount used
MAI	158.97	3	0.276 g
PbAc2	325.29	1	n/a
PbCl2	278.10	1	0.149 g

Table 6.1: Molecular weights, ratios, and amounts used in preparing the perovskite transistor studied below.

Dimethylformamide (DMF) should be added to the solids in a 6:4 solvent:solids ratio by mass. We added 0.638 g dry DMF, as Dr. Moore recommends rounding up when adding solvent for spin-casting these materials. Be cautious in preparing this solution, since DMF is an efficient carrier for lead through the skin. The resulting solution was sonicated to dissolve the solids.

$$0.425\text{g} = 0.4x \quad (6.3)$$

$$x = 1.6025\text{g} \quad (6.4)$$

$$x - 0.425\text{g} = 0.6375\text{g} \quad (6.5)$$

The substrates were moved straight from UV-ozone cleaning to the spinner. The perovskite solution was spun-cast at 2000 rpm for 30 seconds with a 0.5 second ramp. Immediately after spinning, the chip with perovskite film was moved to a 100°C hot plate, where it was annealed in air for 5 minutes. Water will incorporate into the lattice if the film is annealed below 50°C. Note that the methylammonium chloride (MACl) byproduct is not removed by annealing at 100°C (it evaporates at 200-250°C, and the perovskite cannot be heated to such high temperatures); it is unclear what the role of MACl is in the active film.

Dr. Moore recommends that toluene is the best anti-solvent for perovskite films if one

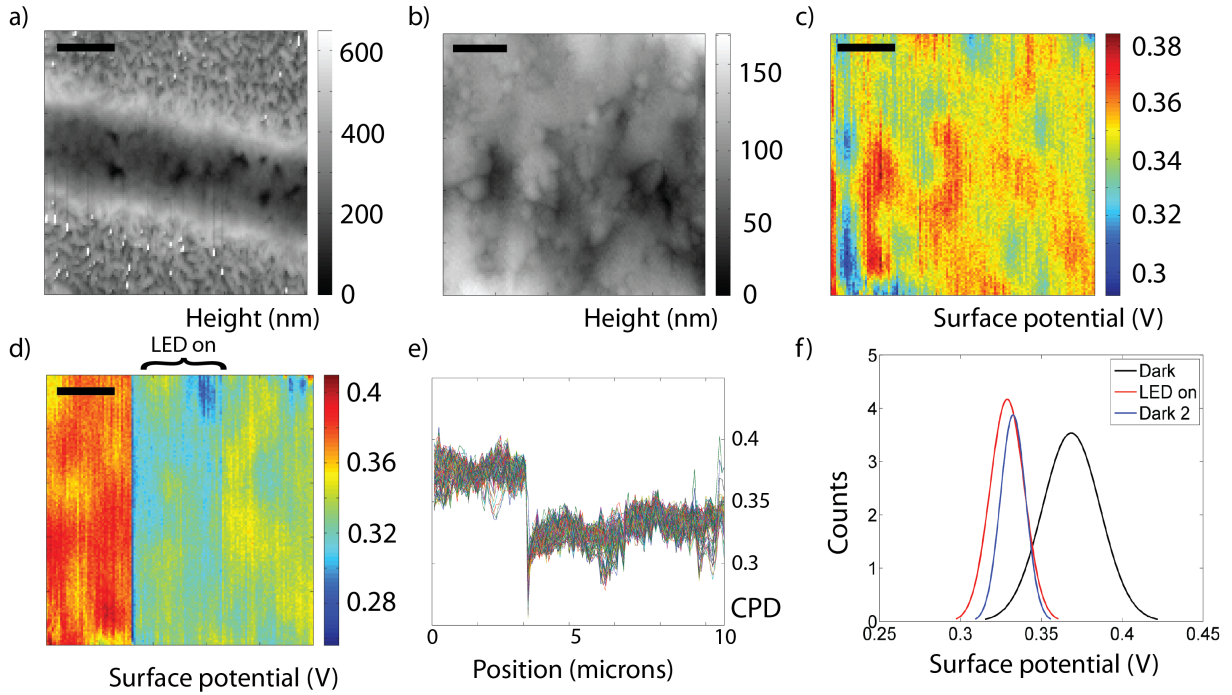


Figure 6.6: Topography of (a) $10 \times 10 \mu\text{m}$ and (b) $2 \times 2 \mu\text{m}$ regions of a perovskite transistor. (b) shows the center of the transistor channel. (c) Surface potential of same region as (b). (d) Dark, light, and dark surface potentials in same region as (b). Scale bar in (a) is $2 \mu\text{m}$ and $0.4 \mu\text{m}$ in (b-d). (e) Horizontal linescans of surface potential in (d). (f) Histograms of dark, light, and dark surface potential regions in (d).

needs to clean the film from a section of the substrate. However, the toluene must be dry, or water will attack the perovskite. Lead acetate (PbAc) produces smoother perovskite films, but the grains are smaller [182, 183]. Dr. Moore suggested that annealing perovskites made with PbAc for several minutes at a lower temperature (but above 50°C), followed by a short annealing period at 95°C to remove the methylammonium acetate (MAAc) byproduct might produce larger grains.

6.3.4 EFM of a perovskite transistor

Our scanning-probe results are collected in Figure 6.6. The film formed relatively large grains in the transistor channel, although the coverage does not appear to be continuous across the

channel (Fig. 6.6a-b). Regions of higher surface potential (Fig. 6.6c) appear to be correlated with regions of lower topography. The film responds to white LED light by exhibiting a negative surface potential shift of around 50 mV (Fig. 6.6d-f). The surface potential does not recover quickly when the light is turned off.

The negative photovoltage is consistent with hole extraction by gold and the residual negative charge when light is turned off suggests electron trapping. Both these conjectures are consistent with previous scanning probe measurements of perovskite solar cells. We had hoped to perform charge transport studies in the perovskite film by placing it on a transistor substrate. However, spin-casting the perovskite film led to large (~ 200 nm) ridges in the film topography along the transistor channel edges. These features made it impossible to obtain electric force microscopy measurements without tracking topography.

6.3.5 Future experiments

No microscopic and spectrally resolved surface potential measurements have yet been made on a perovskite photovoltaic film. Such a measurement appears feasible, does not require specialized substrate processing, and might be an interesting way to approach the electron traps in the perovskite film, if a trap-clearing spectrum could be obtained.

Obtaining transport characteristics of perovskite films remains of strong interest. If a smoother film can be prepared on a transistor substrate, Sirringhaus-style potential linescans across the transistor channel can be collected at different gate and drain voltages. When the device current is collected alongside this information, local mobilities can be calculated throughout the channel independent of the contact effects. Since the contacts are known to have a strong effect on photovoltaic device performance, it would be helpful to learn what mobility is inherent to the material. This type of experiment might be a good application

of position-modulated EFM since the electric field is needed to calculate the mobility.

6.3.6 Perovskite Acknowledgements

Many thanks to Dr. David Moore for his advice and assistance in fabricating the perovskite transistor. Thanks to Sarah Nathan for her help collecting the AFM and EFM data presented above. This work was supported by an NSF graduate research fellowship as well as funding from NSF-DMR 1006633 and NSF-DMR 1309540.

APPENDIX A

GLOVE BOX AND EVAPORATOR PROTOCOLS

In this Appendix, I describe the requirements for installing the glove box. Details are provided regarding the maintenance and operation of the custom glove box and evaporator. I also recommend future upgrades to the equipment.

A.1 Glove box and evaporator requirements

The glove box and evaporator system in the Marohn lab was custom-fabricated by Trovato Mfg., Inc., located in Victor, NY. The system is hard-wired to the building; it requires a 40 Amp line to the built-in transfer box built into the back of the computer cabinet. This transformer unit is required to have a 3 foot clearance between it and the wall behind it.

The box can be run from a nitrogen tank, but requires two separate regulators. A high-pressure regulator (80-100 psi) should be used at the nitrogen tank. A second, low-pressure regulator (10-20 psi) is located behind the evaporator and supplies the shutter switching mechanism. The box is vented into the upper level of the fume hood. A turbo vacuum pump is built into the evaporator chamber, but an external roughing pump is required to evacuate the antechamber and pull an initial vacuum for the evaporator chamber.

The glove box operations are controlled by a non-networked Windows computer. The pumping and venting operations are controlled from “GMC 1-10.vi,” a proprietary LabView program written by Trovato. The deposition operations are controlled and monitored with the program “SQM242CoDep.”

A.2 Glove box and evaporator operation

This operating information is also available in abbreviated form on the group wiki site. For visual identification of some of the glove box parts mentioned, see Fig. A.1.

A.2.1 Operating the transfer antechamber

Transferring materials into the glove box

1. Turn on the roughing pump via computer using the “Rough pump” button in the “GMC 1-10.vi” program. The button is red when the pump is off and turns green when the pump is turned on.
2. Fill the antechamber with N₂ from the glovebox by opening the small red valve (Fig. A.1E) under the antechamber. As the box refills with N₂, you will need to open this valve briefly for a second time to fully release the pressure.
3. Open the antechamber to load/unload materials from lab side; close and latch when finished.
4. Evacuate the chamber with the roughing pump by opening the blue valve (Fig. A.1D) under the antechamber. The pressure should reach ~ -0.9 bar.
5. Close the chamber to the roughing pump (blue valve, Fig. A.1D) and open the chamber to N₂ (red valve, Fig. A.1E) to purge the chamber: fill until the pressure reaches ~ -0.4 bar. Repeat process of evacuating and purging with N₂ for a minimum of three times total.
6. If leaving samples in antechamber, move on to the next step. If moving samples into the glove box, you can now do so from inside the box. You will need to fill the antechamber

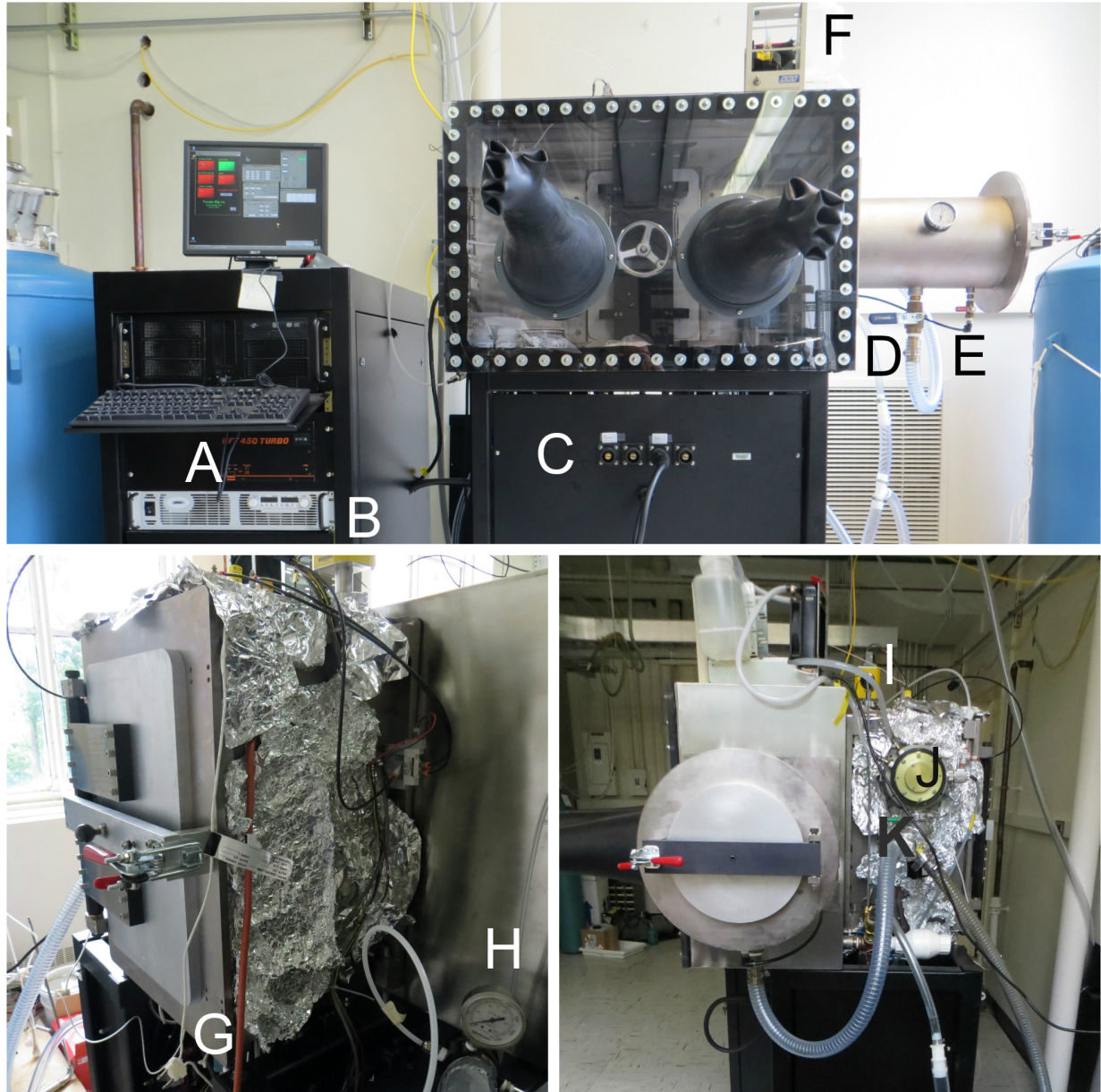


Figure A.1: A: Turbo fan controller. B: Power source for deposition heating. C: Selection of deposition source. D: Rough pump to antechamber valve. E: Glove box nitrogen to antechamber valve. F: Turbo fan water cooling system. G: Plug for heating tape. H: Low pressure regulator. I: Evaporator pressure sensor. J: Turbo fan. K: Green valve to shut off antechamber from evaporator chamber.

with N₂ first, making sure the pressure is fully released before putting your arms inside the box.

7. Turn roughing pump off when finished.

It is good practice to leave a slight negative pressure on the antechamber when it has been purged with nitrogen, to indicate its status to others and as an easy visual confirmation that the antechamber seal has not been broken.

Note: The round door to the antechamber can come loose over time. If it is not sealing well when pumping down, the hex screw in the center of the door should be tightened.

A.2.2 Evacuating, venting, and baking out the evaporator

The yellow pressure gauge on top of the evaporator chamber tends to give a more stable reading than the GMC 1-10.vi software.

How to pump down the evaporator chamber

1. Make sure that everything you might need to move or store while the evaporator is running is inside the glove box or stored in the antechamber. When the evaporator chamber is being under vacuum, the antechamber cannot be evacuated. Make sure there is a slight negative pressure in the antechamber to seal it thoroughly.
2. Close the large green valve (Fig. A.1K) that connects the roughing pump line to the antechamber (behind the antechamber).
3. Plug in and turn on the water cooling system (Fig. A.1F) for the turbo pump. Add tap water to the reservoir if the level is more than an inch below the shoulder of the container.

4. If the roughing pump is not on, turn it on via computer.
5. Open the backing valve by clicking the “Backing valve” button in the GMC 1-10.vi program. The roughing pump will start to pump out the evaporator chamber.
6. Wait until the pressure is in the low 10^{-2} to high 10^{-3} torr range. This should not take more than 15-20 minutes. If it does, the chamber probably needs to be baked out and dehydrated (leave some desiccant in the chamber overnight).
7. Turn on turbo power by clicking the “Turbo power” button in the GMC 1-10.vi program. This does not start the turbo pump, it only supplies the turbo pump controller with power.
8. The control panel for the turbo pump is located under the computer keyboard (Fig. A.1A). Flick the “start” switch. It will snap back in place, but a light should come on as the turbo pump comes up to speed.
9. Wait for the chamber to reach its lowest pressure. Ideally, the pressure will be less than 5×10^{-6} torr. This should not take more than 20-30 minutes. When the chamber is clean, this will only take 5-10 minutes and the pressure can reach the 10^{-8} torr range.
10. The chamber is now ready for a deposition or to start baking out.

How to vent the evaporator chamber

After a deposition or baking out, wait at least 15-30 minutes for the chamber to cool before venting. When ready to vent, look over the steps and be prepared to go through them in sequence without taking any long breaks.

1. Using the panel under the computer keyboard, flick the turbo “stop” switch. The light on this panel should go off.

2. Turn off the turbo power by clicking the “Turbo power” button in the GMC 1-10.vi program. Quickly after turning off the turbo power, close the backing valve by clicking the “Backing valve” button in the GMC 1-10.vi program.
3. Quickly after closing the backing valve, open the vent by clicking the “Vent” button in the GMC 1-10.vi program. When the pressure in the chamber has equilibrated with the pressure in the glove box (usually around 9×10^2 torr), you will hear clicking as the glove box starts cycling N₂. You can then close the vent by clicking the “Vent” button again.
4. Turn off roughing pump via the GMC 1-10.vi program.
5. Turn off and unplug the water cooling system and re-open the green valve to the antechamber. The system is now back to normal.

How to bake out the evaporator chamber

The evaporator should be baked out between deposition of different organic materials. I have not baked out the chamber when switching back and forth between organics and metals.

1. Make sure quartz crystal monitors (QCMs) are working and have a reasonable lifetime remaining.
2. Pump down the chamber to at least 5×10^{-6} torr as described above. If the heating tapes are turned on before the pressure gets low enough, there is a risk of bursting one of the nitrogen lines.
3. When the evaporator chamber is stable at low pressure, plug in one heating tape (Fig. A.1G) using a surge protector.

4. If there is a lot of material on the chamber walls, the heat will cause the pressure to rise. Wait until pressure stabilizes before plugging in the next tape; repeat for the third tape.
5. If desired, the substrate heater and/or an empty organic crucible can also be heated during bake-out to clean them out.
6. Heat the chamber until pressure is in the 10^{-5} torr range, or as high as possible.
7. While the chamber is heating, monitor the QCM readings. Material will be deposited as the chamber heats; the object of baking out is to heat the chamber until no further material is being deposited.
8. When no more material is being deposited, cool down the chamber by unplugging the heating tapes. Wait until the pressure has decreased again.
9. If the substrate heater and/or the crucible were heated, turn these off. Keep pumping down until low pressure (ideally in the 10^{-7} torr range or less) has stabilized. Be sure to allow everything to cool for at least 15-30 minutes.
10. Vent the chamber following the steps above. The chamber is now cleaned and ready for a new organic material.

If the chamber is vented while it is still warm after baking out, it can pull vacuum as it cools. Check the pressure gauge at the chamber and be sure it is around 9×10^2 torr before attempting to open the evaporator door. Re-vent the chamber via the “Vent” button if the pressure is low.

A.2.3 Depositions in the Trovato evaporator

General deposition information and tips

Only one source can be powered at a time. The four sources on the front of the box, from left to right, are Metal I (front), Metal 2 (back), Organic I (front), and Organic 2 (back; not set up).

Do not enter a value for the power greater than 100 in the SQM242 front panel. This will crash the SQM242 program, and when it is reopened, the output power will be reset to zero, ruining your deposition rate. This also risks breaking crucibles and boats by not ramping down the power slowly. If the SQM242 program does crash, ramp down the power output manually on the power supply before reopening the SQM242 program.

Make sure that the blue box under “Thickness” on the SQM242 front panel has a value greater than the amount you want to deposit, plus an extra hundred kÅ or so. The units of this thickness are kÅ. If this thickness is reached during the deposition, the SQM242 program will stop the deposition and ramp down the power automatically. This might be an annoyance for organics, but could crack a metal boat since the ramp is not very slow.

General deposition procedure

1. Clean substrates appropriately and move them into the glove box.
2. Open the chamber door from inside glove box: Tightening the wheel opens the door. Stabilize it with one hand while you tighten the wheel, then lift the latch on the upper right and slide the door to the left. Remove the sample holder.
Warning: The opening to the turbo pump blades is on the upper right side of the chamber. Do not under any circumstances put anything near it!
3. Load substrates into the sample holder, facing down. Kapton tape can help hold small chips in place.
4. Set the sample holder above the desired material source (metal or organic). The metal “ears” on the four corners of the sample holder should be parallel to the sides of the

evaporator chamber. Move the substrate heater to the other source if it is in the way, being careful not to jostle the wire connections.

5. If using the substrate heater in your deposition, gently lift it and set it down on top of your substrates. Be careful not to jostle the wire connections to the block, especially the thermocouple on the left side. Be careful not to let wires go near the turbo fan entrance, and do not pinch any wires underneath the heater block.
6. If needed, load material into the appropriate boat or crucible.
7. Close the chamber door gently; it should latch into place. Stabilizing the door with one hand, loosen the wheel to tightly seal the chamber door.
8. On the computer, open the program “SQM242 CoDep.” Make sure only one copy of the software is running. The box “Input Readings” shows information from the QCMs on either side of the chamber. Check the crystal lifetime for the appropriate sensor (organics = 3, metals = 4). If the QCM has been jostled during sample loading, it will say “Fail;” now is a good time to fix that. If the lifetime is low, this is also a good time to replace the crystal.
9. Follow normal steps for pumping down the chamber.
10. While pumping, make sure the correct source is being powered by the large high voltage cable on the front of the glove box. It takes a lot of force to unplug and plug in this cable. It helps to know that it uses a twist-lock mechanism.
11. If using the substrate heater, when chamber pressure reaches 10^{-6} torr, raise the set-point of the temperature controller PID. The PID temperature is in units of °F. Choose a lower temperature than the goal by several degrees to minimize overshoot. Slowly increase the setpoint as the temperature rises until the desired temperature is reached. Allow substrate temperature to stabilize before beginning the deposition.

12. On the computer, check that the shutter button in the GMC 1-10.vi is set to the side that should be **open**. If the shutter says metal, the organic side is closed, and vice versa. Click the shutter button to switch the shutter position.
13. Go back to the program “SQM242 CoDep.” Check that the blue box under ”thickness” is much greater than the amount you want to deposit.
14. In SQM242 CoDep, open the windows at View > Card setup and View > Input setup.
 - (a) In “Input setup,” check that the density, z factor, and tooling factors are correct for the material you are depositing. Make sure the “monitor” column is only checked next to the sensor you are using. Click update.
 - (b) Change the filename in the “Card setup” box and hit update. The data in the “input readings” box over time (deposition rate over time, total amount of material deposited, etc.) will automatically save to this filename when the deposition is over.
 - (c) On the SQM242 CoDep front panel, click “Edit” at the bottom of the left hand panel. This will also open a new window. Make sure that the sensor you want to monitor is checked and that output is disabled and click update. Now the information from the sensor will be read into the front panel input readings so it can be saved at the end of the run. The monitor panel should say “Trovato” next to the sensor you are using, not just “monitor.”
15. On the power supply (grey panel under the keyboard, brand “Lambda”, Fig. A.1B), turn on the power and press “out” for output.
16. On the SQM242 CoDep front panel, make sure the Trovato column is set to manual and power is set to zero, and that the thickness is zero, then click start.
17. Raise the power by entering a value in the grey box under the “power” setting and hitting enter. Increase the power slowly in increments of 0.1 until the desired deposition

rate is reached (keep an eye on the rate for your sensor in the input readings box). Don't trust the rate reading, though: rather, watch the time it takes to deposit 1 Å of material. $1 \text{ \AA} / 10 \text{ sec} = 0.1 \text{ \AA/sec}$ which is a good rate for organics and for metals. Let the rate stabilize.

18. Open the shutter and deposit the desired amount of material. If you are depositing metal onto an organic film, alternate between opening and closing the shutter every 5 Å (or more frequently) to prevent the hot metal from damaging the organic.
19. Close the shutter. Slowly ramp the power down in the SQM242 CoDep front panel. Turn off the output and power on the Lambda front panel. Press stop in the SQM242 CoDep panel.
20. If the substrate heater was on, lower the PID setpoint on the temperature controller. Wait at least 15 minutes to let the substrate heater cool down.
21. Vent the chamber. You may want to let the substrate heater cool further before opening the chamber and removing your samples.

Details: depositing organics

1. The ceramic crucible is housed for deposition in a metal RADAK furnace. The outer shell is twisted counter-clockwise to loosen and clockwise to replace. Take care not to apply torque to the thermocouple leads coming out the bottom of the furnace; do not tighten the metal cover more than a gentle finger-tight.
2. Substrates are often heated when depositing organic semiconductors- check the literature. Substrates are usually heated to 60 °C for pentacene and 110-125 °C for PDIs. Note that the set point of the PID controller is in units of °F.
3. Check that the density, z factor, and tooling factors are correct for the material you are depositing. For pentacene these values are 1.31, 1, and 100, respectively.

Material	Density	z-ratio	Power for constant rate with W boat s(arbitrary software units)
Titanium	4.5	0.628	24
Gold	19.3	0.381	13
Aluminum	2.7	1.08	18

Table A.1: Common metal densities, z-ratios, and deposition powers.

Details: depositing metals

1. If you are using the top-contact mask, use copper tape to stick the samples face down onto the back of the mask. The channel widths are $75 \mu\text{m}$ and $125 \mu\text{m}$.
2. The commercially available boats for depositing metals are too long for our system. They need to be gently trimmed (scissors work if you are careful, they shatter easily) before being screwed in place in the evaporator. We have tungsten and molybdenum boats; the molybdenum boats are expected to be more robust.
3. **Be careful not to drop metal pellets!** It is fine to remove the metal spacer fans so the boat is easier to see. Replace these spacers when the boat is loaded.
4. Note that if depositing metal onto an organic, you will have to pause every few angstroms, so make sure the total thickness is the SQMCoDep is bigger than *twice* your desired final thickness!
5. Check that the density, z factor, and tooling factors are correct for the material you are depositing. See Table A.1 for some common values.

A.3 Maintenance and parts

A.3.1 Glove box and evaporator upkeep

The glove box and evaporator system is relatively low-maintenance. The most important item is that the glove box requires approximately one nitrogen cylinder per month. The water chamber in the turbo cooling system should be topped off with tap water every few months. The roughing pump is not run for extended periods of time, but its oil level and cleanliness should be monitored.

Evaporation does require some consumable supplies. The quartz crystal resonators in the evaporator need to be replaced after their lifetime drops below 70%. Metal deposition requires boats that have a finite lifetime and metal pellets as a material source. Organic deposition uses ceramic crucibles that can be reused if cleaned thoroughly with solvents, dried, and baked out with the evaporator chamber. Table A.2 lists supplies for evaporation that have been purchased, including the quartz crystal resonators.

A.3.2 Glove box parts: setup, repairs, and upgrades

In Table A.3, I list manufacturers and part numbers for some key parts used in setting up the glove box and evaporator. A spreadsheet detailing all purchases, including tubing and connectors, made for the glove box and evaporator (“LouisaGloveBoxPurchases.xlsx”) can also be found on the group Dropbox account in the folder “Glove box and evaporator.”

The major upgrade I made to the glove box was to replace all the old O-rings. The previous O-rings were made from oil-resistant Buna-N, the typical O-ring material, which is only rated to 250° F. After several rounds of baking out the chamber, these O-rings would

Item	Supplier	Part number
General deposition supplies		
Inficon QCM crystals, 6MHz, gold coated, 10/pkg	Kurt J. Lesker	008-010-G10
Metal deposition supplies		
Molybdenum boats, 3" long by 3/4" wide by 1/8" deep	Kurt J. Lesker	EVS7010MO
Tungsten boats, 3.5" long by 0.5" wide by 1/8" deep	Kurt J. Lesker	EVS2A005W
Gold pellets, 1/8" x 1/8" long, 99.999% pure	Kurt J. Lesker	EVMAUXX50G
Titanium pellets, 1/8" x 1/8" long, 99.995% pure	Kurt J. Lesker	EVMTI45EXE-A
Aluminum pellets, 1/8" x 1/8" long, 99.99% pure	Kurt J. Lesker	EVMAL40EXEA
Organic deposition supplies		
Alumina crucible for RADAQ I, 1" H X 0.495" OD	Luxel Corporation	10300-1L

Table A.2: Supplies purchased for metal and organic depositions.

Item	Supplier	Part number
Nitrogen cylinder		
High pressure cylinder regulator: 1 state general purpose plated brass 3500 PSI inlet (1/4" FNPT) /100 PSI outlet (CGA 580)	Airgas	Y11-215D580
Ball valve	McMaster-Carr	47865K21
High-Pressure Brass Threaded Pipe Fitting 1/4" NPT, Male Tee	McMaster-Carr	4757T152
Med-Pressure Brass Threaded Pipe Fitting 1/4" NPT, Hex Coupling	McMaster-Carr	50785K92
PVC Tubing for rough pump exhaust: 1"ID x 1.25" OD x 0.125" wall	McMaster-Carr	Masterkleer, 5233K72
Evaporator chamber		
Silicone O-ring, AS568A-114, Pack of 100 (-60° to 400° F)	McMaster-Carr	9396K27
Corrosion-Resistant Type 304 Stainless Steel Woven Wire Cloth, 12x12", 5x5 mesh	McMaster-Carr	85385T818
Glove box		
Pressure switch	Dwyer Instruments	ADPS-05-2-N

Table A.3: Some key parts used in setting up the glove box.

fail and prevent the chamber from reaching low pressures. I replaced these O-rings with high-temperature silicone rated to 400° F ([A.3](#)). Screws on the outside of the evaporator chamber that are marked with a dab of red nail polish have been upgraded. I did not disassemble the seals for any of the feedthroughs such as the pressure gauge, so these seals may need upgrades in the future.

A.3.3 Replacing the pressure switches

Thus far, the most common repair for the glove box has been the replacement of the pressure switches ([Table A.3](#)). These have been replaced twice in the past four years. There are two

pressure switches; one controls when the box vents old nitrogen and the other controls when it draws in fresh nitrogen. When a pressure switch is not working, the box stops venting and filling with nitrogen on its own. Instructions from the manufacturer for installing these switches can be found at www.dwyer-inst.com. Sarah Nathan has compiled the steps as they apply to our glove box; these are summarized here and on the group wiki page.

How to replace pressure switches

1. Turn off the power to the glove box by flipping all the breakers at the box (in the cabinet behind the glove box computer). Turn off N₂ at the tank.
2. Take the panels off the right side of the box (facing the front of the box), under the antechamber.
3. There will be a blue gas line visible that goes into the two round pressure switches. Take off the clear plastic housing from the pressure switch(es) being replaced with a Philips screwdriver. Notice that the upper switch is labeled “Exhaust” and the lower switch is labeled “N₂,” and that they have different pressure settings.
4. Check with a multimeter that there is no AC or DC voltage or current between the leads on each switch. If there is, ground to outer frame of the box. It may take some time to discharge completely. The DC voltage may be in the mV range so be sure to turn the multimeter to that setting to check.
5. Unscrew the wire leads from the switch(es) being replaced; unthread the leads and set aside. Unscrew the old switch from the mount.
6. Remove the blue gas line from the switch via the quick-release connection, noting that it should be replaced into the back-most “gas-in” line on the switch.
7. On the new switch, put the included screw connections onto the copper pins.

8. Push the quick release connection from the blue gas line into the proper “gas-in” line on the new switch as far as it will go.
9. Screw the new switch back onto mount.
10. Replace the wiring for the new switch. Thread the wire through the provided hole on the left side of the switch.
 - (a) For **Exhaust** switch (upper switch): Red connects to the top pin, blue to the bottom.
 - (b) For **N₂** switch (bottom switch): Red connects to top pin, yellow to the side.
11. Set pressure on the new switch by rotating the dial. Exhaust is set to 2.40 and N₂ is 2.00.
12. Screw plastic housing back on the new switch.
13. Turn on power to the glove box and nitrogen at the tank. Gloves should fill and some clicking heard as the box fills and vents properly. Put side panels back on.

A.4 Recommended upgrades

The vent to the turbo pump inside the evaporator chamber is not covered. To protect the turbo blades, a mesh screen should be installed over this opening. A stainless steel mesh was purchased for this purpose (Table A.3) but has not yet been installed. It should be possible to affix this mesh to the inside of the evaporator chamber using Torr Seal without detrimental effects.

The high-voltage copper posts that power the organic crucibles and the metal posts are only separated from the metal of the evaporator chamber by a small (few mm) air gap. If a metal pellet or other flake of metal were to fall and touch this area, it could short the post to

the evaporator chamber. To prevent this issue, the bottom of the posts should be insulated with a wider ceramic spacer (such as Macor).

There is a post available to install a second organic crucible in the back of the evaporator chamber. If desired, 10 AWG solid copper leads are recommended for installing the RADA^K crucibles from the Luxel Corporation. Further information on the design and installation of RADA^K crucibles can be found at Luxel.com.

APPENDIX B

MICROSCOPE UPGRADES

In this Appendix, I describe changes made to the microscope during the course of this thesis period.

B.1 Laser diode replacement

In summer 2014, the 1310 nm laser diode for the interferometer in the microscope reached the end of its lifetime. The first symptom of this problem was instability in the raw interferometer signal. It was extremely difficult to keep the cantilever driving on resonance, and when it was driven, the amplitude was very noisy and jumpy. From these symptoms, it appeared as if the cantilever drive piezo or laser mode hopping might be the problem, but in the following weeks of troubleshooting, we noticed that the laser diode current was also fluctuating a great deal. Soon after, temperature-tuning the laser diode output became impossible at low temperatures. Eventually, the diode output wavelength stopped responding to any temperature adjustments. We then tested another diode in the system and saw that everything behaved normally, leading us to conclude that our laser diode was finished.

The requirements for choosing a new diode are growing more challenging to meet from commercially available stock. Our diode driver uses a 14-pin DIL mount, a standard which has become less popular since our microscope was initially built. In addition, we require a laser with both a narrow spectral linewidth and a moderate temperature coefficient. The temperature coefficient ($\text{nm}/^\circ\text{C}$) needs to be large enough for temperature tuning the laser diode to stay on the sensitive slope of an interferometer fringe, but not so large that the diode becomes sensitive to room temperature fluctuations. The temperature coefficient T_c

is given by:

$$T_c = \frac{\Delta\lambda}{\Delta T} \quad (\text{B.1})$$

where $\Delta\lambda$ is the spectral linewidth and ΔT is the temperature shift in °C. Some manufacturers report ΔT and others report T_c , so it is important to pay attention to units when researching diodes.

The spectral linewidth determines the coherence length of the laser. We need the coherence length to reach from the cleaved fiber to the cantilever and back, setting the fiber-cantilever working distance. The coherence length L is given by:

$$L = \frac{2\ln(2)}{\pi n} \frac{\lambda^2}{\Delta\lambda} \quad (\text{B.2})$$

where n is the refractive index of the fiber, λ is the wavelength of the laser, and $\Delta\lambda$ is the spectral linewidth (at full-width half-maximum) of the laser, which all manufacturers I surveyed reported. Our interferometer fiber is a single mode optical fiber (Corning 9/125; 9 μm diameter core and 125 μm diameter cladding). For this fiber, $n = 1.46$. The smaller the linewidth, the longer the coherence length.

We replaced our 1310 nm diode with a 1490 nm diode from QPhotonics (QFLD-1490-5S with FC/APC connector). If future laser diodes are to be purchased from QPhotonics, it is a good idea to contact the company first to see what the specifications are for their present diodes; the linewidths on these diodes vary substantially from batch to batch. The specifications for our specific laser diode are summarized in Table B.1.

Wavelength, λ	1490 nm
Linewidth, $\Delta\lambda$	0.2 nm
Calculated coherence length	3.36 mm
Temperature coefficient, T_c	0.5 nm/C

Table B.1: QPhotonics laser diode specs for unit purchased 8/2014.

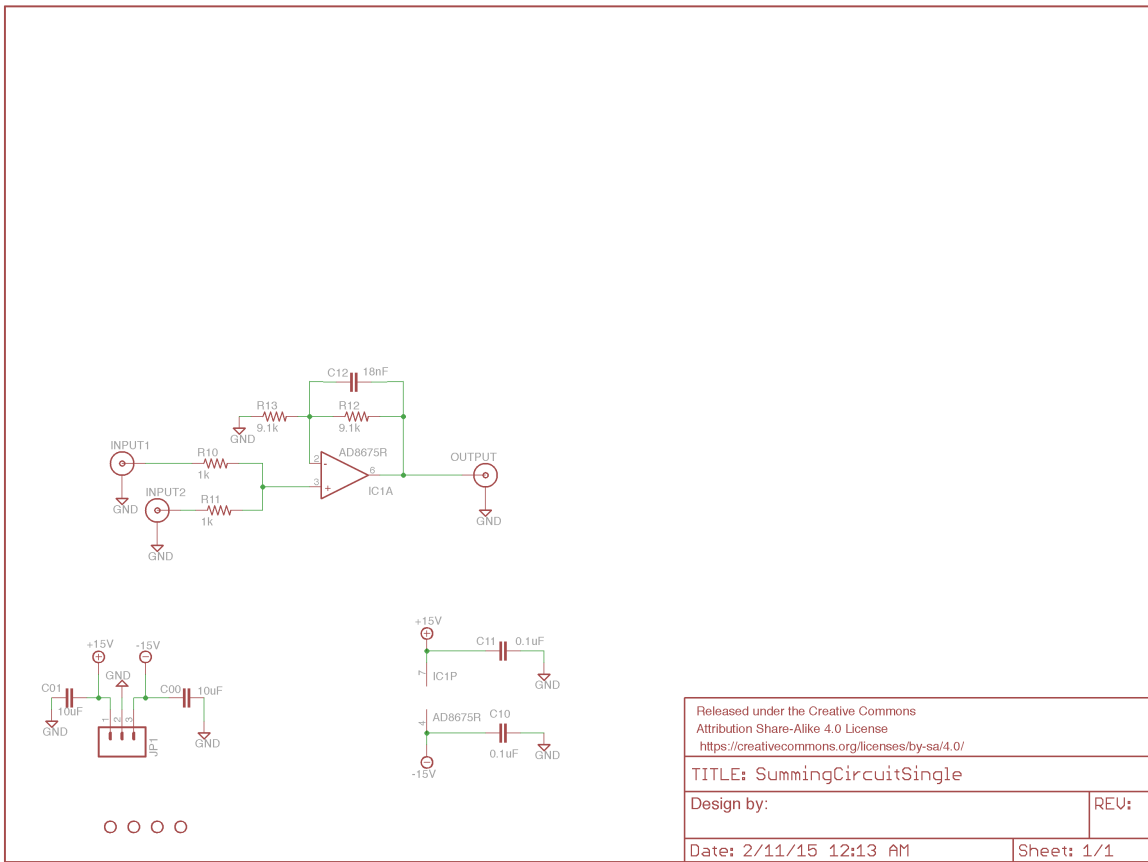


Figure B.1: Single summing circuit, schematic.

B.2 Summing circuit

For the position modulation experiment, a second summing circuit was required to add the DC ramp voltage to the position modulation voltage. A summing circuit built on a breadboard was sufficient for preliminary work, but breadboards are not suited for permanent installation in the microscope. With substantial assistance from Ryan Dwyer, a printed circuit board (PCB) summing circuit was designed for use in the position modulation experiment. Here, I record the circuit board layouts for a one-sum and a two-sum design. The circuits and boards were designed in EAGLE; the plans can be found on the group Dropbox in the folder labeled Circuits.

Note that the input resistors as labeled on the board schematic are actually too small.

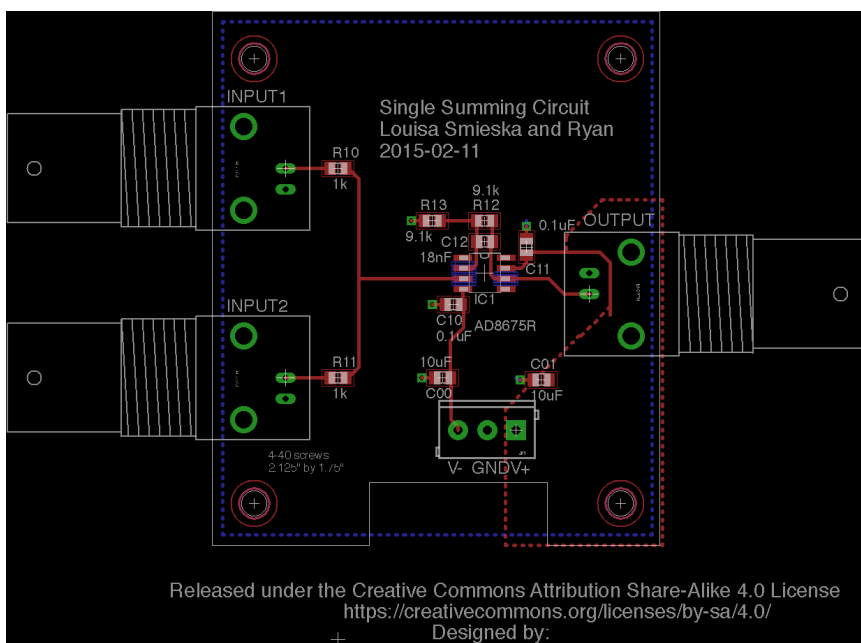


Figure B.2: Single summing circuit, board layout.

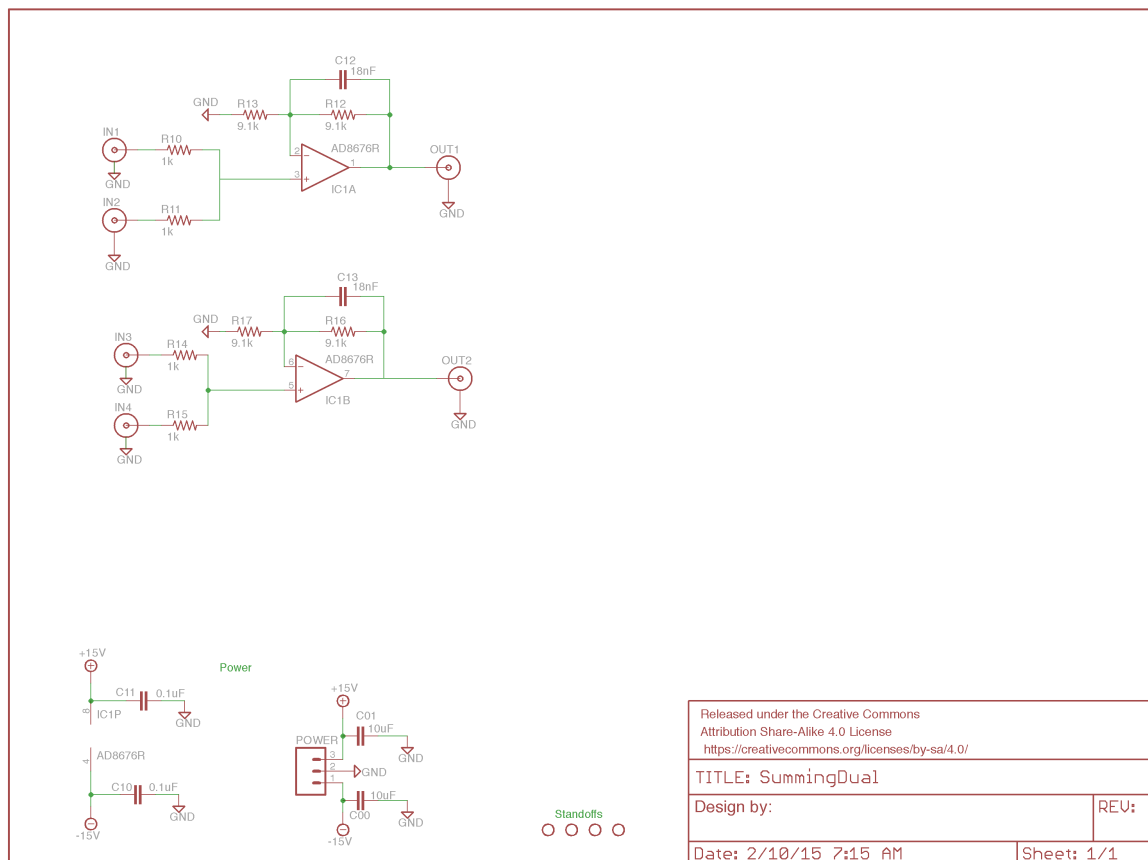


Figure B.3: Dual summing circuit, schematic.

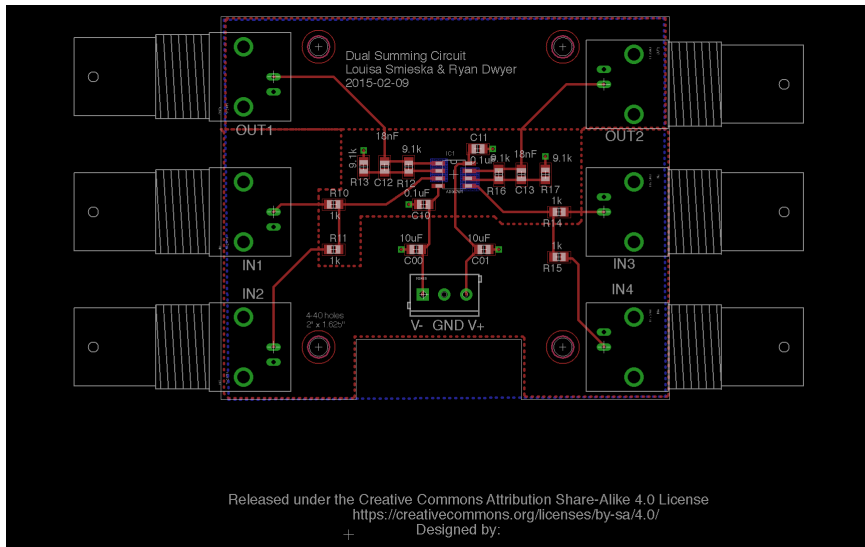


Figure B.4: Dual summing circuit, board layout.

When $1\text{ k}\Omega$ resistors are used here, the summing circuit output is actually 95% of the expected value. A better value for these resistors would be $100\text{k}\Omega$. At the time of writing, $1\text{ k}\Omega$ resistors are still installed on the PCB, and should be replaced.

Single and dual summing circuit boards were fabricated by OSH Park. I use a single summing circuit board for position-modulation experiments. This board is shown in Fig. B.5.

B.3 Temperature diode

At the beginning of this thesis period, the temperature diode in the microscope was not operational. A replacement was not needed; re-soldering the disconnected wire lead to the temperature diode returned it to functionality. If this part requires replacement in the future, a good option might be DT-670B-SD from LakeShore Cryogenics. This model can measure temperatures between 1.4 K and 500 K, to a precision of 0.5 K below 305 K or 0.33 % of the temperature above 305 K. Fig. B.6 shows the temperature diode on its own (left) and

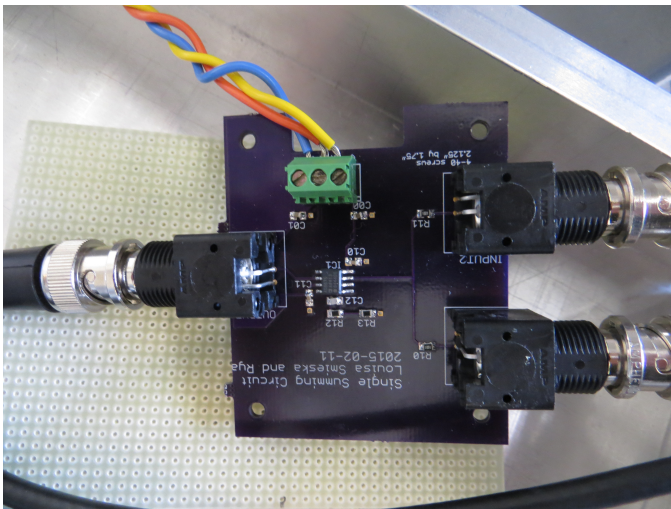


Figure B.5: Printed circuit board summing circuit in use for position modulation.

properly mounted in its housing (right).

B.4 Monochromator Labview Code

The manufacturer of the monochromator, Mikropak, has been purchased by Ocean Optics. The original software that was supplied with the monochromator is no longer supported, so when the microscope computer was upgraded to 64-bit Windows 7, we could no longer run the monochromator via Labview. It is possible to communicate with the monochromator directly through the RS232 connection using ASCII commands, but calibrating the monochromator step size for each wavelength would be quite tedious. Instead, Ocean Optics was kind enough to supply us with a .dll library for the monochromator in x86 and x64 versions. In Labview, this library is considered a .NET assembly and should be loaded using a .NET constructor node (Fig. B.7). Comparing the programmed output of the monochromator with the wavelength measured with a USB OceanOptics spectrometer, we find that the Monoscan output is low by a few nm across the visible spectrum. This correction factor can be hard-wired into future Labview code.

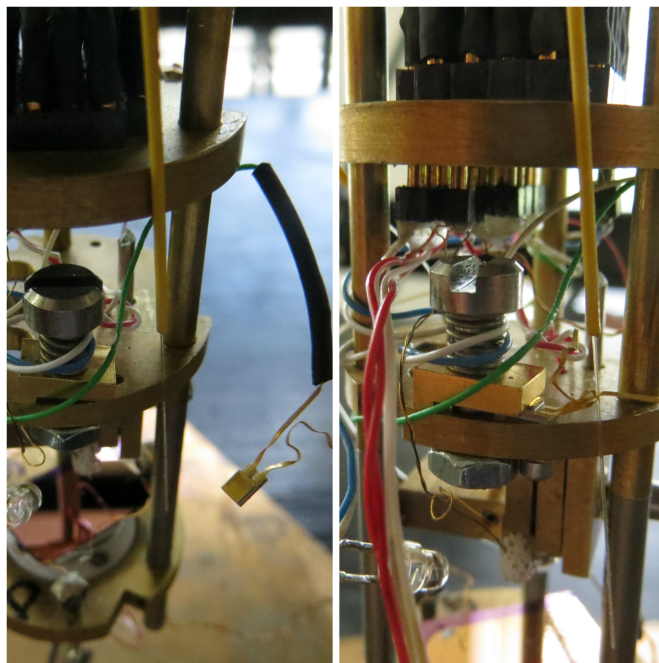


Figure B.6: Temperature diode removed from mount (left) and properly mounted (right).

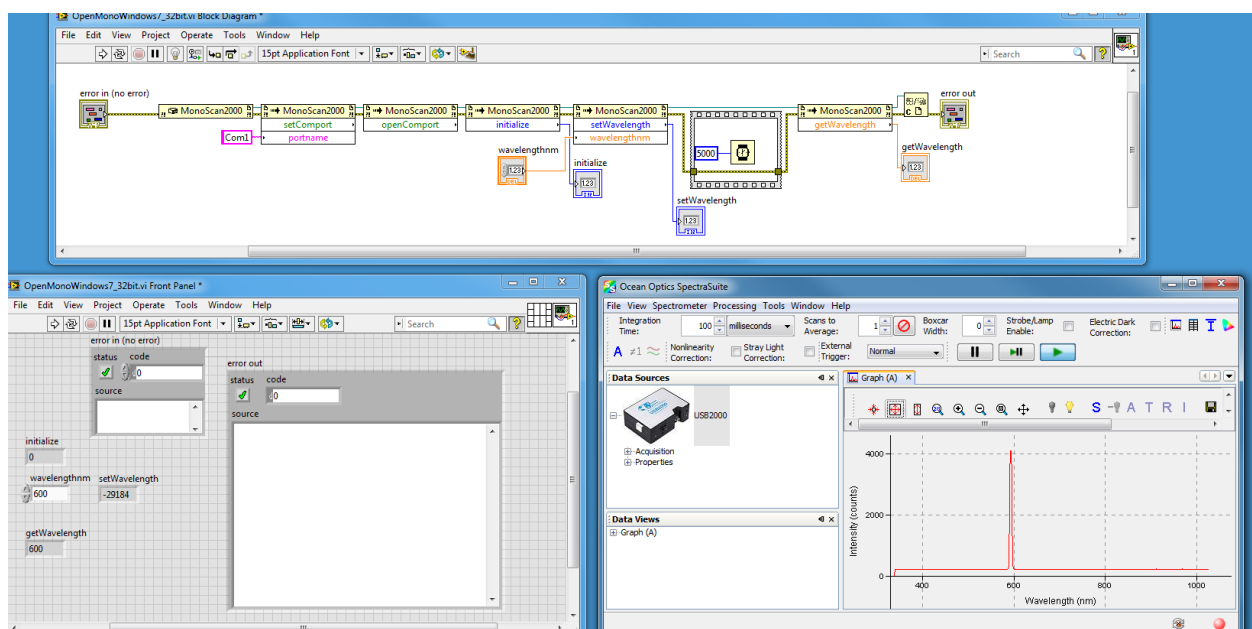


Figure B.7: Example code using the new Ocean Optics library for controlling the Monoscan in Windows 7.

The chemists are a strange class of mortals, impelled by an almost insane impulse to seek their pleasures amid smoke and vapor, soot and flame, poisons and poverty; yet among all these evils I seem to live so sweetly...

- Johann Joachim Becher, 1635 - 1682

Progress is made by trial and failure; the failures are generally a hundred times more numerous than the successes; yet they are usually left unchronicled.

- William Ramsay, 1852-1916

And so, after many years, victory has come, and the romance of exploration, of high hopes and bitter disappointment, will in a few years simply be recorded in the text-books of organic chemistry in a few terse sentences.

- Sir Ian Morris Heilbron, 1886 - 1959

BIBLIOGRAPHY

- [1] C. Dimitrakopoulos and P. Malenfant, *Adv. Mater.* **14**, 99 (2002). [1.1](#)
- [2] H. Klauk, U. Zschieschang, J. Pflaum, and M. Halik, *Nature* **445**, 745 (2007).
- [3] X. Zhan et al., *Adv. Mater.* **23**, 268 (2011). [2.7](#), [3.1](#), [4.1.1](#), [4.4](#)
- [4] H. Usta, A. Facchetti, and T. J. Marks, *Acc. Chem. Res.* **44**, 501 (2011). [1.1](#)
- [5] Z. Zhu, J. Mason, R. Dieckmann, and G. Malliaras, *Appl. Phys. Lett.* **81**, 4643 (2002).
[1.1](#)
- [6] B. Gregg, *J. Phys. Chem. B* **107**, 4688 (2003). [1.1](#)
- [7] S. Guenes, H. Neugebauer, and N. S. Sariciftci, *Chem. Rev.* **107**, 1324 (2007). [1.1](#)
- [8] O. Jurchescu, J. Baas, and T. Palstra, *Appl. Phys. Lett.* **87**, 052102 (2005). [1.1](#), [2.1](#)
- [9] M. Kytka, A. Gerlach, F. Schreiber, and J. Kovac, *Appl. Phys. Lett.* **90**, 131911 (2007).
[1.1](#)
- [10] F. D. Angelis, G. Das, and E. D. Fabrizio, *Chem. Phys. Lett.* **462**, 234 (2008). [1.1](#)
- [11] P. Coppo and S. Yeates, *Adv. Mater.* **17**, 3001 (2005). [1.1](#), [2.1](#)
- [12] F. D. Angelis, M. Gaspari, A. Procopio, G. Cuda, and E. D. Fabrizio, *Chem. Phys. Lett.* **468**, 193 (2009). [1.1](#), [2.1](#)
- [13] L. M. Smieska et al., *Adv. Funct. Mater.* **22**, 5096 (2012). [1.1](#), [1.1.1](#), [2.8](#), [4.1](#), [4.2.2](#),
[4.2.2](#)
- [14] A. L. Burin and M. A. Ratner, *J. Chem. Phys.* **113**, 3941 (2000). [1.1](#), [5.1.1](#)
- [15] T. N. Ng, W. R. Silveira, and J. A. Marohn, *Phys. Rev. Lett.* **98**, 066101 (2007). [1.1](#),
[1.1.1](#), [3.4](#)

- [16] W. Silveira and J. Marohn, Phys. Rev. Lett. **93**, 116104 (2004). [1.1](#), [1.1.1](#), [5.1](#), [5.1.1](#)
- [17] R. Chesterfield et al., J. Appl. Phys. **95**, 6396 (2004). [1.1](#), [3.7.2](#), [4.1.1](#), [4.2.2](#)
- [18] X. Cheng et al., Adv. Funct. Mater. **19**, 2407 (2009). [1.1](#)
- [19] G. Horowitz, P. Lang, M. Mottaghi, and H. Aubin, Adv. Funct. Mater. **14**, 1069 (2004). [1.1](#)
- [20] V. Coropceanu et al., Chemical Reviews **107**, 926 (2007). [1.1](#)
- [21] Y. Hosoi and Y. Furukawa, Mol. Cryst. Liq. Cryst. **471**, 189 (2007), Korea-Japan Joint Forum on Organic Materials for Electronics and Photonics, Niigata, JAPAN, OCT 02-05, 2006. [1.1](#), [4.1.1](#)
- [22] A. Saeki, S.-i. Ohsaki, S. Seki, and S. Tagawa, J. Phys. Chem. C **112**, 16643 (2008). [1.1](#)
- [23] L. Bürgi, T. J. Richards, R. H. Friend, and H. Sirringhaus, Journal of Applied Physics **94**, 6129 (2003). [1.1](#), [3.4](#), [3.5](#)
- [24] O. G. Reid, G. E. Rayermann, D. C. Coffey, and D. S. Ginger, J. Phys. Chem. C **114**, 20672 (2010). [1.1.1](#), [2.1](#)
- [25] J. L. Luria, K. A. Schwarz, M. J. Jaquith, R. G. Hennig, and J. A. Marohn, Adv. Mater. **23**, 624 (2011). [1.1.1](#), [2.1](#), [2.2](#), [2.1](#), [2.2.2](#), [2.8](#), [2.4.1](#), [2.4.2](#), [2.7](#), [4.2.2](#), [4.2.2](#), [4.2.3](#), [5.7.1](#)
- [26] E. Muller and J. Marohn, Adv. Mater. **17**, 1410 (2005). [1.1.1](#), [4.2.1](#), [4.3.1](#), [5.7.1](#)
- [27] M. Jaquith, E. M. Muller, and J. A. Marohn, J. Phys. Chem. B **111**, 7711 (2007). [1.1.1](#), [2.1](#), [6.2.6](#)

- [28] M. J. Jaquith, J. E. Anthony, and J. A. Marohn, *J. Mater. Chem.* **19**, 6116 (2009). [1.1.1](#), [2.1](#), [2.6.2](#), [4.2.3](#), [4.3.1](#), [5.7.1](#)
- [29] T. N. Ng, W. R. Silveira, and J. A. Marohn, *Organic Field-Effect Transistors V* **6336**, 63360A (2006). [1.1.1](#), [5.1.1](#)
- [30] L. Bürgi, H. Sirringhaus, and R. Friend, *Appl. Phys. Lett.* **80**, 2913 (2002). [1.1.1](#), [3.1](#), [3.4](#), [3.4](#), [3.4](#), [3.6](#), [5.1.1](#), [5.1.1](#), [5.1.1](#)
- [31] L. Bürgi, T. Richards, M. Chiesa, R. Friend, and H. Sirringhaus, *Synth. Met.* **146**, 297 (2004), Symposium on Organic Field-Effect Transistors - Towards Molecular Scale held at the 2004 Annual E-MRS Spring Meeting, Strasbourg, FRANCE, MAY 24-28, 2004. [3.4](#), [5.1.1](#), [5.1.1](#)
- [32] F. Lüttich, D. Lehmann, H. Graaf, D. R. T. Zahn, and C. von Borczyskowski, *Phys. Status Solidi C* **7**, 452 (2010). [3.1.1](#), [5.1.1](#)
- [33] F. Lüttich et al., *Phys. Status Solidi A* **209**, 585 (2012). [1.1.1](#), [3.1.1](#), [4.1.1](#), [5.1.1](#)
- [34] X. Li et al., *Phys. Rev. Lett.* **108**, 066601 (2012). [1.1.1](#), [5.1.1](#)
- [35] E. Muller, *Electric Force microscopy of charge trapping in thin-film Pentacene Transistors*, PhD thesis, Cornell University, 2005. [1.2.1](#)
- [36] M. J. Jaquith, *The Kinetics of Charge Trapping in Polycrystalline Pentacene and Ion Migration in Light Emitting Electrochemical Cells Studied by Time- and Temperature-Resolved Electric Force Microscopy*, PhD thesis, Cornell University, 2009. [1.2.1](#), [1.2.2](#), [1.2.3](#)
- [37] W. R. Silveira, *Microscopic view of charge injection in a model organic semiconductor*, PhD thesis, Cornell University, 2005. [1.2.1](#)

- [38] J. L. Luria, *Spectroscopic Characterization of Charge Generation and Trapping in Third-Generation Solar Cell Materials Using Wavelength- and Time-resolved Electric Force Microscopy*, PhD thesis, Cornell University, 2011. [1.2.1](#)
- [39] A. Kikukawa, S. Hosaka, and R. Imura, Appl. Phys. Lett. **66**, 3510 (1995). [1.2.2](#), [1.2.3](#), [3.4](#)
- [40] W. R. Silveira, E. M. Muller, T.-N. Ng, D. H. Dunlap, and J. A. Marohn, *Scanning Probe Microscopy: Electrical and Electromechanical Phenomena at the Nanoscale Vol. II*, Springer, New York, 2007. [1.2.2](#), [1.2.2](#)
- [41] G. G. Malliaras, V. Krasnikov, H. J. Bolink, and G. Hadzioannou, Appl. Phys. Lett. **66**, 1038 (1995). [2.1](#)
- [42] W. You, Z. Hou, and L. Yu, Adv. Mater. **16**, 356 (2004). [2.1](#)
- [43] S. Wang, C.-W. Leung, and P. K. L. Chan, Org. Electron. **11**, 990 (2010). [2.1](#)
- [44] V. Bliznyuk et al., Macromolecules **32**, 361 (1999). [2.1](#)
- [45] L. J. Soltzberg et al., J. Am. Chem. Soc. **128**, 7761 (2006). [2.1](#)
- [46] T. N. Ng, J. A. Marohn, and M. L. Chabinyc, J. Appl. Phys. **100**, 084505 (2006). [2.1](#), [4.2.3](#), [4.4](#)
- [47] D. V. Lang, X. Chi, T. Siegrist, A. M. Sergent, and A. P. Ramirez, Phys. Rev. Lett. **93**, 076601 (2004). [2.1](#), [2.4.2](#), [4.2.2](#)
- [48] C. Goldmann, D. J. Gundlach, and B. Batlogg, Appl. Phys. Lett. **88**, 063501 (2006). [2.1](#)
- [49] W. L. Kalb, K. Mattenberger, and B. Batlogg, Phys. Rev. B **78**, 035334 (2008). [2.1](#)
- [50] B. Stevens, S. Perez, and J. Ors, J. Am. Chem. Soc. **96**, 6846 (1974). [2.1](#)

- [51] A. Maliakal, K. Raghavachari, H. Katz, E. Chandross, and T. Siegrist, *Chem. Mater.* **16**, 4980 (2004). [2.1](#)
- [52] A. Reddy and M. Bendikov, *Chem. Commun. –*, 1179 (2006). [2.1](#)
- [53] S. Chien, M. Cheng, K. Lau, and W. Li, *J. Phys. Chem. A* **109**, 7509 (2005). [2.1](#)
- [54] L. Tsetseris and S. T. Pantelides, *Phys. Rev. B* **75**, 153202 (2007). [2.1](#)
- [55] H. Najafov, D. Mastrogiovanni, E. Garfunkel, L. C. Feldman, and V. Podzorov, *Adv. Mater.* **23**, 981 (2011). [2.1](#)
- [56] L. Tsetseris and S. T. Pantelides, *Phys. Rev. B* **78**, 115205 (2008). [2.1](#)
- [57] L. Tsetseris and S. Pantelides, *Org. Electron.* **10**, 333 (2009). [2.1](#)
- [58] M. Yamada, I. Ikemoto, and H. Kuroda, *Bull. Chem. Soc. Jpn.* **61**, 1057 (1988). [2.1](#)
- [59] J. Northrup and M. Chabinyc, *Phys. Rev. B* **68**, 041202 (2003). [2.1](#), [2.1](#), [2.5.2](#), [2.7](#)
- [60] C. C. Mattheus et al., *Acta Crystallogr., Sect. E: Struct. Rep. Online* **58**, o1229 (2002). [2.1](#)
- [61] L. Roberson et al., *J. Am. Chem. Soc.* **127**, 3069 (2005). [2.1](#)
- [62] B. H. Northrop, J. E. Norton, and K. N. Houk, *J. Am. Chem. Soc.* **129**, 6536 (2007). [2.1](#)
- [63] O. Jurchescu, J. Baas, and T. Palstra, *Appl. Phys. Lett.* **84**, 3061 (2004). [2.1](#)
- [64] E. Gomar-Nadal, B. R. Conrad, W. G. Cullen, and E. A. Willams, *J. Phys. Chem. C* **112**, 5646 (2008). [2.1](#), [2.1](#), [2.4.1](#), [2.5.2](#)
- [65] B. R. Conrad et al., *Phys. Rev. B* **77**, 205328 (2008). [2.1](#)
- [66] I. Salzmann et al., *Phys. Rev. B* **75**, 174108 (2007). [2.1](#), [2.1](#)

- [67] I. Salzmann, S. Duhm, R. Opitz, J. P. Rabe, and N. Koch, *Appl. Phys. Lett.* **91**, 051919 (2007). [2.1](#)
- [68] O. Berg et al., *J. Phys. Chem. A* **103**, 2451 (1999). [2.1](#)
- [69] B. Purushothaman, S. R. Parkin, and J. E. Anthony, *Org. Lett.* **12**, 2060 (2010). [2.1](#)
- [70] M. Kiguchi, M. Nakayama, T. Shimada, and K. Saiki, *Phys. Rev. B* **71**, 035332 (2005). [2.1](#)
- [71] R. Ruiz, A. Papadimitratos, A. Mayer, and G. Malliaras, *Adv. Mater.* **17**, 1795 (2005).
- [72] B.-N. Park, S. Seo, and P. G. Evans, *J. Phys. D: Appl. Phys.* **40**, 3506 (2007).
- [73] H. Yang et al., *J. Phys. Chem. C* **112**, 16161 (2008).
- [74] M. Fiebig, D. Beckmeier, and B. Nickel, *Appl. Phys. Lett.* **96**, 083304 (2010). [2.1](#)
- [75] A. Shehu et al., *Phys. Rev. Lett.* **104**, 246602 (2010). [2.1](#)
- [76] O. D. Jurchescu, M. Popinciuc, B. J. van Wees, and T. T. M. Palstra, *Adv. Mater.* **19**, 688 (2007). [2.4.1](#), [2.4.2](#)
- [77] M. Tello, M. Chiesa, C. M. Duffy, and H. Sirringhaus, *Adv. Funct. Mater.* **18**, 3907 (2008). [2.4.1](#), [2.4.2](#)
- [78] A. Sharma et al., *Appl. Phys. Lett.* **96**, 103306 (2010). [2.4.2](#)
- [79] A. Sharma et al., *Phys. Rev. B* **82**, 075322 (2010). [2.4.2](#)
- [80] B. Lee et al., *Phys. Rev. B* **82**, 085302 (2010). [2.4.2](#)
- [81] M. Faggin and M. Hines, *Rev. Sci. Instrum.* **75**, 4547 (2004). [2.5.3](#)
- [82] S. Langhoff, *J. Phys. Chem.* **100**, 2819 (1996). [2.5.3](#)

- [83] C. W. Bauschlicher, Jr. et al., *Astrophys. J. Supp. Ser.* **189**, 341 (2010). [2.5.3](#)
- [84] D. Hudgins and S. Sandford, *J. Phys. Chem. A* **102**, 344 (1998). [2.5.3](#)
- [85] C. W. Bauschlicher, E. Peeters, and L. J. Allamandola, *Astrophys. J. Supp. Ser.* **678**, 316 (2008). [2.5.3](#)
- [86] A. J. Athans, J. B. Briggs, W. Jia, and G. P. Miller, *J. Mater. Chem.* **17**, 2636 (2007). [2.5.3, 2.6.1](#)
- [87] Y. Hosoi, K. Okamura, Y. Kimura, H. Ishii, and M. Niwano, *Appl. Surf. Sci.* **244**, 607 (2005), 12th International Conference on Solid Films and Surface (ICSF-12), Hamamatsu, JAPAN, JUN 21-25, 2004. [2.5.3](#)
- [88] K. Queeney et al., *J. Appl. Phys.* **87**, 1322 (2000). [2.5.3](#)
- [89] Gaussian 09 Revision A.1, Gaussian Inc., Wallingford, CT (2009). [2.5.3](#)
- [90] R. Bauernschmitt and R. Ahlrichs, *Chem. Phys. Lett.* **256**, 454 (1996). [2.5.3](#)
- [91] A. D. Becke, *J. Chem. Phys.* **98**, 5648 (1993). [2.5.3](#)
- [92] S. Miertus, E. Scrocco, and J. Tomasi, *Chem. Phys.* **55**, 117 (1981). [2.5.3](#)
- [93] P. K. Nayak and N. Periasamy, *Org. Electron.* **10**, 1396 (2009). [2.5.3](#)
- [94] N. Vets, M. Smet, and W. Dehaen, *Tet. Lett.* **45**, 7287 (2004). [2.6.1](#)
- [95] T. R. Criswell and B. H. Klanderman, *J. Org. Chem.* **39**, 770 (1974). [2.6.1](#)
- [96] M. Tamano and J. Koketsu, *Bull. Chem. Soc. Jpn.* **58**, 2577 (1985). [2.6.1](#)
- [97] C. Newman et al., *Chem. Mater.* **16**, 4436 (2004). [2.7](#)
- [98] Y.-C. Chang, M.-Y. Kuo, C.-P. Chen, H.-F. Lu, and I. Chao, *J. Phys. Chem. C* **114**, 11595 (2010). [2.7, 4.1, 4.1.1](#)

- [99] B. Jones et al., *Angew. Chem. Int. Ed.* **43**, 6363 (2004). [2.7](#), [3.1](#)
- [100] B. A. Jones, A. Facchetti, M. R. Wasielewski, and T. J. Marks, *Adv. Funct. Mater.* **18**, 1329 (2008). [4.1.1](#), [4.1.1](#)
- [101] J. E. Anthony, A. Facchetti, M. Heeney, S. R. Marder, and X. Zhan, *Adv. Mater.* **22**, 3876 (2010). [3.1](#)
- [102] V. Palermo et al., *J. Am. Chem. Soc.* **130**, 14605 (2008). [3.1](#)
- [103] M. Li et al., *Phys. Chem. Chem. Phys.* **16**, 4528 (2014). [3.1](#)
- [104] S. Rieth et al., *J. Phys. Chem. C* **117**, 11347 (2013). [3.1](#), [4.1](#)
- [105] D. Ley, C. X. Guzman, K. H. Adolfsson, A. M. Scott, and A. Braunschweig, *J. Am. Chem. Soc.* **136**, 7809 (2014). [3.1](#), [4.1.1](#)
- [106] B. A. Jones, A. Facchetti, M. R. Wasielewski, and T. J. Marks, *J. Am. Chem. Soc.* **129**, 15259 (2007). [3.1](#), [3.3](#), [4.1.1](#)
- [107] V. Palermo et al., *Small* **3**, 161 (2007). [3.1.1](#)
- [108] A. Liscio et al., *Small* **7**, 634 (2011). [3.1.1](#)
- [109] J. N. Haddock et al., *Organic Electronics* **7**, 45 (2006). [3.3](#)
- [110] F. Chiarella, M. Barra, L. Ricciotti, A. Aloisio, and A. Cassinese, *Electronics* **3**, 76 (2014). [3.3](#), [4.1.1](#)
- [111] S. Locci, M. Morana, E. Orgiu, A. Bonfiglio, and P. Lugli, *IEEE Trans. Electr. Dev.* **55**, 2561 (2008). [3.3](#)
- [112] Y. Chen and I. Shih, *J. Mater. Sci.* **44**, 280 (2009). [3.4](#)
- [113] S. Fabiano et al., *Adv. Funct. Mater.* **21**, 4479 (2011). [3.4](#)

- [114] M. L. Chabinyc et al., J. Appl. **96**, 2063 (2004). [3.4](#)
- [115] Y.-S. Lin et al., Proc. SPIE 7778 **7778**, 77781E (2010). [3.5](#), [4.1.1](#)
- [116] S. M. Sze, *Physics of Semiconductor Devices*, John Wiley and Sons, New York, NY, 2nd edition, 1981, p. 250-254. [3.5](#)
- [117] Y. Kim and D. Jeon, J. Appl. Phys. **108**, 016101 (2010). [3.7.1](#)
- [118] C.-H. Wang et al., J. Phys. Chem. C **119**, 14593 (2015). [3.7.1](#)
- [119] J. H. Oh, S. Liu, Z. Bao, R. Schmidt, and F. Wuerthner, Appl. Phys. Lett. **91**, 212107 (2007). [3.7.2](#)
- [120] R. T. Weitz et al., J. Am. Chem. Soc. **130**, 4637 (2008). [4.1.1](#)
- [121] K. Vasseur et al., J. Phys. Chem. C **114**, 2730 (2010).
- [122] J. H. Oh, P. Wei, and Z. Bao, Appl. Phys. Lett. **97**, 243305 (2010). [3.7.2](#)
- [123] F. Liscio et al., ACS Nano **7**, 1257 (2013). [3.7.2](#)
- [124] D. de Leeuw, M. Simenon, A. Brown, and R. Einerhand, Synth. Met. **87**, 53 (1997). [4.1](#), [4.1.1](#)
- [125] R. Di Pietro and H. Sirringhaus, Adv. Mater. **24**, 3367 (2012). [4.1.1](#)
- [126] R. Di Pietro, D. Fazzi, T. B. Kehoe, and H. Sirringhaus, J. Am. Chem. Soc. **134**, 14877 (2012). [4.1.1](#)
- [127] H. Z. Chen et al., Chem. Mater. **19**, 816 (2007). [4.1.1](#)
- [128] M. Barra et al., The Journal of Physical Chemistry C **114**, 20387 (2010). [4.1.1](#), [4.1.1](#), [4.3.2](#)

- [129] M.-H. Yoon, C. Kim, A. Facchetti, and T. J. Marks, *J. Am. Chem. Soc.* **128**, 12851 (2006). [4.1.1](#), [4.3](#), [4.4](#)
- [130] W. Olthuis and P. Bergveld, *IEEE Trans. Electr. Insul.* **27**, 691 (1992), 7TH INTERNATIONAL SYMP ON ELECTRETS (ISE7), BERLIN, GERMANY, SEP 25-27, 1991. [4.1.1](#)
- [131] L. Chua et al., *Nature* **434**, 194 (2005). [4.1.1](#), [4.1.1](#), [4.4](#)
- [132] M. Sulpizi, M.-P. Gaigeot, and M. Sprik, *J. Chem. Theory Comput.* **8**, 1037 (2012). [4.1.1](#), [4.1.1](#)
- [133] E. V. Anslyn and D. A. Dougherty, *Modern Physical Organic Chemistry*, University Science Books, Sausalito, California, 2006. [4.1.1](#), [4.1.1](#)
- [134] C. M. Cardona, W. Li, A. E. Kaifer, D. Stockdale, and G. C. Bazan, *Adv. Mater.* **23**, 2367 (2011). [4.1.1](#)
- [135] T. Suga, M. Iizuka, S. Kuniyoshi, K. Kudo, and K. Tanaka, *Synthetic Metals* **102**, 1050 (1999). [4.1.1](#)
- [136] C. Piliego et al., *Adv. Mater.* **21**, 1573 (2009). [4.1.1](#)
- [137] F.-C. Chen and C.-H. Liao, *Appl. Phys. Lett.* **93**, 103310 (2008). [4.1.1](#)
- [138] J. H. Park et al., *Phys. Chem. Chem. Phys.* **14**, 14202 (2012). [4.1.1](#)
- [139] K. P. Pernstich, D. Oberhoff, C. Goldmann, and B. Batlogg, *Applied Physics Letters* **89**, 213509 (2006). [4.1.1](#)
- [140] W. L. Kalb, S. Haas, C. Krellner, T. Mathis, and B. Batlogg, *Phys. Rev. B* **81**, 155315 (2010). [4.1.1](#)

- [141] H. L. Gomes, P. Stallinga, M. Colle, D. M. de Leeuw, and F. Biscarini, *Appl. Phys. Lett.* **88**, 082101 (2006). [4.1.1](#)
- [142] J. Rivnay et al., *Nat. Mater.* **8**, 952 (2009). [4.1.1](#)
- [143] H. Graaf and D. Schlettwein, *J. Appl. Phys.* **100**, 126104 (2006). [4.1.1](#)
- [144] R. K. Dubey, A. Efimov, and H. Lemmetyinen, *Chem. Mater.* **23**, 778 (2011). [4.2.3](#)
- [145] F. S. Goodson et al., *Org. Biomol. Chem.* **11**, 4797 (2013). [4.2.3](#)
- [146] H. K. Jang et al., *J. Vac. Sci. Technol. A* **19**, 267 (2001). [4.3](#)
- [147] S. Guhathakurta and A. Subramanian, *J. Electrochem. Soc.* **154**, P136 (2007). [4.3](#), [4.3](#)
- [148] D. Kumaki, T. Umeda, and S. Tokito, *Appl. Phys. Lett.* **92**, 093309 (2008). [4.4](#)
- [149] N. Hoepker, S. Lekkala, R. F. Loring, and J. A. Marohn, *J. Phys. Chem. B* **115**, 14493 (2011). [5.4.2](#)
- [150] E. Klontzas, E. Tylianakis, and G. E. Froudakis, *J. Phys. Chem. C* **113**, 21253 (2009). [6.2.1](#)
- [151] C. J. Doonan, D. J. Tranchemontagne, T. G. Glover, J. R. Hunt, and O. M. Yaghi, *Nat. Chem.* **2**, 235 (2010). [6.2.1](#)
- [152] S.-Y. Ding et al., *J. Am. Chem. Soc.* **133**, 19816 (2011). [6.2.1](#)
- [153] S. Wan, J. Guo, J. Kim, H. Ihee, and D. Jiang, *Angew. Chem. Int. Ed.* **48**, 5439 (2009). [6.2.1](#), [6.2.2](#), [6.2.3](#)
- [154] X. Ding et al., *J. Am. Chem. Soc.* **133**, 14510 (2011). [6.2.1](#), [6.2.2](#), [6.2.3](#)
- [155] A. Cote et al., *Science* **310**, 1166 (2005). [6.2.1](#), [6.2.2](#)

- [156] R. W. Tilford, W. R. Gemmill, H.-C. zur Loyer, and J. J. Lavigne, *Chem. Mater.* **18**, 5296 (2006). [6.2.1](#)
- [157] E. L. Spitler and W. R. Dichtel, *Nat. Chem.* **2**, 672 (2010). [6.2.1](#)
- [158] H. M. El-Kaderi et al., *Science* **316**, 268 (2007). [6.2.1](#)
- [159] J. R. Hunt, C. J. Doonan, J. D. LeVangie, A. P. Cote, and O. M. Yaghi, *J. Am. Chem. Soc.* **130**, 11872 (2008). [6.2.1](#)
- [160] F. J. Uribe-Romo et al., *J. Am. Chem. Soc.* **131**, 4570+ (2009). [6.2.1](#)
- [161] E. L. Spitler, M. R. Giovino, S. L. White, and W. R. Dichtel, *Chem. Sci.* **2**, 1588 (2011). [6.2.1](#)
- [162] E. L. Spitler et al., *Angew. Chem. Int. Ed.* **51**, 2623 (2012). [6.2.1](#)
- [163] E. L. Spitler et al., *J. Am. Chem. Soc.* **133**, 19416 (2011). [6.2.1](#), [6.2.2](#), [6.2.5](#)
- [164] M. O. Blunt, J. C. Russell, N. R. Champness, and P. H. Beton, *Chem. Comm.* **46**, 7157 (2010). [6.2.1](#), [6.2.3](#), [6.2.4](#)
- [165] T. Faury et al., *J. Phys. Chem. C* **116**, 4819 (2012). [6.2.1](#), [6.2.4](#)
- [166] O. Ourdjini et al., *Phys. Rev. B* **84**, 125421 (2011). [6.2.1](#), [6.2.4](#)
- [167] J. W. Colson et al., *Science* **332**, 228 (2011). [6.2.1](#), [6.2.5](#)
- [168] X. Ding et al., *Angew. Chem. Int. Ed.* **50**, 1289 (2011). [6.2.2](#), [6.2.3](#)
- [169] S. Wan et al., *Chem. Mater.* **23**, 4094 (2011). [6.2.2](#)
- [170] G. Dicker, M. de Haas, L. Siebbeles, and J. Warman, *Phys. Rev. B* **70**, 045203 (2004). [6.2.2](#)
- [171] N. A. A. Zwanenveld et al., *J. Am. Chem. Soc.* **130**, 6678+ (2008). [6.2.4](#)

- [172] J. F. Dienstmaier et al., ACS Nano **5**, 9737 (2011). [6.2.4](#)
- [173] H. J. Snaith, J. Phys. Chem. Lett **4**, 3623 (2013). [6.3](#)
- [174] S. D. Stranks et al., Science **342**, 341 (2013). [6.3.1](#)
- [175] K. Tanaka et al., Solid State Commun. **127**, 619 (2003). [6.3.1](#)
- [176] E. L. Unger et al., Energy & Environ. Sci. **7**, 3690 (2014). [6.3.1](#)
- [177] M. Jiang et al., J. Mater. Chem. A **3**, 963 (2015). [6.3.2](#)
- [178] Q. Chen et al., Nano Lett. **14**, 4158 (2014). [6.3.2](#)
- [179] V. W. Bergmann et al., Nat. Commun. **5**, 5001 (2014). [6.3.2](#)
- [180] A. Guerrero, E. J. Juarez-Perez, J. Bisquert, I. Mora-Sero, and G. Garcia-Belmonte, Appl. Phys. Lett. **105**, 133902 (2014). [6.3.2](#)
- [181] L. Barnea-Nehoshtan, S. Kirmayer, E. Edri, G. Hodes, and D. Cahen, J. Phys. Chem. Lett. **5**, 2408 (2014). [6.3.2](#)
- [182] D. T. Moore, H. Sai, K. Wee Tan, L. A. Estroff, and U. Wiesner, APL Mater. **2**, 081802 (2014). [6.3.3](#)
- [183] D. T. Moore et al., J. Am. Chem. Soc. **137**, 2350 (2015). [6.3.3](#)